

**DEVELOPMENT OF PHOTOELASTIC METHODS
TOWARDS STUDY OF MECHANICAL AGING OF
2-DIMENSIONAL GRANULAR ASSEMBLIES**

by

Thaweesak Jirathanathaworn

A dissertation submitted in partial fulfillment
of the requirements for the degree of
Doctor of Philosophy
(Civil Engineering)
in The University of Michigan
2009

Doctoral Committee:

Professor Roman D. Hryciw, Co-Chair
Associate Professor Russell A. Green, Co-Chair
Professor James R. Barber
Professor Radoslaw L. Michalowski

© **Thaweesak Jirathanathaworn** 2009

All Rights Reserved

This dissertation is dedicated to my parents

ACKNOWLEDGEMENTS

First and foremost, the author fully expresses the his gratitude to Co-Chairs, Associate Professor Russell A. Green and Professor Roman D. Hryciw, for their insight, thoughtful guidance and continuous assistance throughout the research project. For their hard work, expertise and dedication, I am very grateful for having such mentors and advisors for the development of my Ph.D. dissertation at the University of Michigan, Ann Arbor. Much of the research presented in this dissertation would not have come together without their patience and perseverance. Recommendations for the test programs and discussions of experimental results with in-depth understandings in soil mechanics were always valuable. They explained difficult theories in understandable ways. The opportunities give to me and the sincere instructions I obtained from my advisors are gratefully acknowledged.

Again, my sincere gratitude is reserved for Professor Hryciw's enthusiastic academic interests and continuous encouragement throughout the course of my study at Michigan, especially in the early stage of the formation of the research topic, and in the final stage for the write-up of this dissertation. Explanations, suggestions and discussions were always useful and very much appreciated.

I extended my sincere gratitude to the other advisory committee members, Professor James R. Barber and Professor Radoslaw L. Michalowski, for providing advice and guidance. Thanks also my CU-Boulder advisor, Professor Stein Sture, who advised the independent research study for my master's degree. Professor Sture's sincere instructions and recommendations that encouraged me for Ph.D. study at the University of Michigan are acknowledged. The acknowledgements are also extended to Assistant Professor Dimitrios Zekkos and Assistant Professor Adda Athanasopoulos-Zekkos who offered me opportunities for presenting a part of my Ph.D. research to the UM geotechnical group, and for discussing my work via Geotechnical Seminar.

Thanks is given for all useful technical assistance from Harald Eberheart, Bob Fischer, Jan Pantolin, Bob Spence, Murrick Burch, Kimberly Gauss and Kimberly Smith. Without them, many parts of this research project would have taken longer than they did. Appreciation is extended to fellow geotechnical graduate students and visiting scholars: Dr. Jongwon Lee, David Saftner, Yongsub Jung, Theresa White, Srinivasa Siddhartha Nadukuru, Kate Gunberg, Wanda Cameron, Dr. Ayman Ibrahim Eltahrany, Mustafa Saadi, Adam Lobbetael, Yuyou Yang, and others; for sharing space in 1358 G.G. Brown (office) and in 1331 G.G. Brown (F.E. Richart Soil Dynamics laboratory) and for discussing many fruitful topics in geotechnical engineering and other applications. Special thanks are extended to Thai friends: Dr. Kittinun Sirijaroonchai, Monthian Setkit, Chutimon Sindhuprama, Naszha Pimpawatin; who made me enjoyable during my Ph.D. study.

The partial support for this research that was provided by the National Science Foundation (NSF) under the Grant No. CMMI 0530378 is thankfully acknowledged. I also gratefully acknowledged the Royal Thai Government for financial assistance for my studies and stay in the United States from Fall 2004 to Summer 2009.

Last but not least, I am fully indebted to my beloved family: my father, mother and sisters. Their support, love, understanding and encouragement motivated me to complete this dissertation. Thanks to my father and mother who were waiting for the completion of this advanced degree throughout these years. Words cannot express my thankful feeling to my beloved family, especially to my respected parents, but I do wish that they are happy for the completion of this work. Finally, I wish to extend a very special thanks to Ommy Chutimon Srinavakatrakul for friendship, understanding and perseverance throughout these years.

Thaweesak Jirathanathaworn

July, 2009

TABLE OF CONTENTS

DEDICATION.....	ii
ACKNOWLEDGEMENTS.....	iii
LIST OF FIGURES.....	x
LIST OF TABLES.....	xx
LIST OF APPENDICES.....	xxi
LIST OF TERMS.....	xxii
ABSTRACT.....	xxv
CHAPTERS	
I. INTRODUCTION.....	1
1.1 Introduction	1
1.2 Research objectives	3
1.3 Organization of dissertation	4
1.4 Terminology	5
II. REVIEW OF RELEVANT LITERATURE.....	8
2.1 Introduction	8
2.2 Reduction of strength and stiffness of sands due to vibrations.....	9

2.3	Aging effects on increases in strength and stiffness in sands.....	13
2.4	Proposed mechanisms of sand aging from previous studies.....	15
2.4.1	Mechanical aging process.....	15
2.4.2	Chemical aging process.....	18
2.4.3	Other potential aging mechanisms.....	19
2.4.3.1	Mechanism of blast gas dissipation.....	19
2.4.3.2	Biological aging mechanism.....	21
2.5	Aging effects on horizontal effective stress in granular soils.....	22
2.6	Theory of photoelasticity	28
2.6.1	Polarized light	28
2.6.2	Plane and circular polariscopes	29
2.6.3	Double refraction (birefringence)	33
2.6.4	Compensator (tint plate or full wave plate)	35
III.	TESTING MATERIALS AND TEST APPARATUS.....	38
3.1	Introduction	38
3.2	Facilities for preparing the glass particles	39
3.3	Glass particles	41
3.3.1	Cylindrical particles with smooth contact surface	43
3.3.2	Cylindrical particles with rough contact surface	43
3.3.3	Angular prism particles with rough contact surface	44
3.4	Test apparatus and hardware components	44
3.4.1	Test apparatus	44
3.4.2	Hardware components	45

3.5 Digital image processing	52
IV. CALIBRATION OF GLASS PLATE PHOTOELASTIC SENSORS.....	54
4.1 Introduction	54
4.2 Experimental setup.....	55
4.3 Results and discussion.....	56
4.3.1 Color intensities in a 6 mm x 6 mm stressed glass plate	56
4.3.2 Calibration of glass plate photoelastic sensors.....	59
4.3.3 Calibration charts	62
4.4 Assessment of temperature effects on red intensity values.....	67
4.4.1 Discussion of results from Test #T1.....	67
4.4.2 Discussion of results from Test #T2.....	69
4.5 Concluding remarks.....	72
V. APPLICATION OF PHOTOELASTICITY FOR MEASURING HORIZONTAL STRESS IN 2-DIMENSIONAL GRANULAR ASSEMBLIES.....	74
5.1 Introduction.....	74
5.2 Experimental setup.....	75
5.3 Results and discussion.....	77
5.3.1 Stiffness of granular assemblies and possibility of particle seating and sliding in 2D granular assemblies.....	77
5.3.2 Coefficient of lateral earth pressure at rest (K_0).....	86
5.3.3 Time-dependent horizontal stress in 2D granular assemblies..	91
5.3.3.1 Preliminary study.....	92

5.3.3.2 Parametric study of time-dependent surface settlement tests	101
(1) Discussion on results of specimens under constant vertical stress.....	101
(2) Discussion of particle shape effects.....	104
(3) Discussion of particle surface roughness effects.....	113
5.3.3.3 Analysis of Bowman’s hypothesis.....	120
VI. CONCLUSIONS AND RECOMMENDATIONS	128
6.1 Conclusions.....	128
6.2 Recommendations for future research.....	133
APPENDICES	135
REFERENCES.....	218

LIST OF FIGURES

FIGURE

1-1	Two particles in contact: (a) after deposition with unstable contact, and (b) formation of more stable contact with better seating and improved micro-interlocking of surface roughness.....	6
1-2	Two particles in contact: (a) before sliding, (b) after sliding.....	7
2-1	Example of sand deposit with possible drainage constraints.....	10
2-2	Diagram presenting collapse of initial structure (loose sands) and disruption of past-aging effects due to vibrations.....	12
2-3	Increased penetration resistance with time following vibrocompaction at Jebba dam site (after Mitchell and Solymar, 1984; figure from Baxter, 1999).....	13
2-4	Changes in penetration resistance with time following explosive compaction at Jebba dam site (Mitchell and Solymar, 1984, figure by Baxter, 1999).....	14
2-5	Plan view of arching effects (hoop stress) around a pile shaft initially after pile installation (Chow et al., 1988).....	17
2-6	Dissolution rate of silica as a function of time (Wilding et al., 1977).....	19
2-7	Silica dissolution and precipitation under contact stress (Sheldon et al., 2003).....	20
2-8	Grains under constant pressure: (a) initial state (b) precipitated silica around grains providing cementation between grains (after Sheldon et al., 2003).....	20
2-9	Blast-gas bubble producing arching of particles and loose sand pockets (Hryciw, 1986; labels added by the author).....	21

2-9	Increase in lateral stress coefficient (K) in loose dry sand during 17 hrs without wall movement from d to e (after Terzaghi, 1934)	23
2-10	Void elongation parallel to the direction of major principal stress (after Oda et al., 1985)	25
2-11	Model of microdeformation mechanism of dilatancy in a shear band by the combination of buckling of columns and particle rotations during loading approaching failure (after Oda and Kazama, 1998).....	26
2-12	Mechanism of how strong and weak force networks may change with time via particle rotation in granular materials under loads (i.e., creep), resulting in a strong self-supporting network (after Bowman, 2002).....	27
2-13	Diagram representing the production of polarized light by a polarizer (after Frocht, 1946).....	29
2-15	Simple setup for visually observing photoelastic fringes in a glass specimen.....	30
2-16	Schematic light wave transmitting through a quarter wave plate producing a phase difference (or retardation) of $\lambda/4$ (after McKenzie and Hand, 1999).....	31
2-17	Arrangement of plane polariscope illustrating an isoclinic fringe (after McKenzie and Hand, 1999).....	32
2-18	Arrangement of circular polariscope (after McKenzie and Hand, 1999)....	32
2-19	Photoelastic fringes in discs subjected to diametral compression; (a) image observed through a plane polariscope illustrating isoclinics (black band), (b) image observed through circular polariscope (isoclinics removed) (McKenzie and Hand, 1999).....	33
2-20	Light wave behavior entering and passing through a double refractive material (after McKenzie and Hand, 1999).....	34
2-21	Color sequences produced in dark-field circular polariscope, corresponding retardation (δ) values and principal stress difference $ \sigma_1 - \sigma_2 $ of borosilicate glass; using Eq. 2-2 to calculate $ \sigma_1 - \sigma_2 $ by assuming $C_B = 2.93$ Brewsters and $t = 0.125$ in (Courtesy: Strainoptics, Inc.).....	36
3-1	(a) Dymax UV curing adhesive and (b) UV light for curing the adhesive.....	40

3-2	(a) Glass rods to be cut using the alignment-cutting template incorporation with the diamond saw (b) glass particles after cutting.....	40
3-3	Glass particles assembled to a holding frame for polishing.....	41
3-4	LECO polishing machine.....	42
3-5	Oven in the glass laboratory.....	42
3-6	Glass particles in the shapes of cylinders and angular prisms.....	43
3-7	Test apparatus used for the research project.....	45
3-8	Schematic of the photoelasticity system.....	46
3-9	Test box	47
3-10	Red intensity at the center of the light source versus supplied voltage.....	49
3-11	Strainoptics A-100 analyzer and RP-100 tint plate.....	50
3-12	User interface of Nikon Camera Control Pro version 2.0.....	52
3-13	Procedure for obtaining three independent matrices for R , G and B intensities.....	53
4-1	Test setup with light eliminated at the surrounding area the test station	56
4-2	Thin black aluminum plate with small openings at the regions of interests..	57
4-3	Test setup with the 6mm x 6mm glass plate.....	58
4-4	Applied vertical stress versus R , G , B intensity values from the central zone (1 mm x 1 mm) of 6mm x 6mm glass plate.....	58
4-5	Applied vertical and corresponding R , G and B intensities from the central zone (1 mm x 1 mm) of the 6 mm x 6 mm glass plate.....	60
4-6	Glass plate sensors and schematic test setup for the calibration.....	61
4-7	Example of an image from calibration tests.....	62
4-8	Test box attached with the glass plate sensors at the sidewalls	63
4-9	Calibration charts for S1 at points L (top) and R (bottom)	65

4-10	Calibration charts for S2 at points L (top) and R (bottom).....	66
4-11	Test setup for assessment of temperature effects on red intensity values for pilot Tests #T1 and #T2.....	68
4-12	Red intensity and temperatures versus time at the measurements from sensors S3 and S8 from Test #T1.....	70
4-13	Red intensity and temperatures versus time at the measurements from sensors S3 and S8 from Test #T2.....	71
5-1	Test box with the calibrated glass plate sensors at the sidewalls.....	76
5-2	Typical setup for experiments in this chapter.....	77
5-3	1.5" x 5.0" specimens: (a) 550 cylinders and (b) 300 angular prisms.....	78
5-4	1D strain model for cohesionless soils (Hardin, 1987).....	80
5-5	Surface settlements at left and right sides of a 1.5"x5.0" specimen with 300 angular prisms during loading and unloading	81
5-6	Surface settlements at left and right sides of a 4.5"x5.0" specimen with 1810 smooth cylinders during loading and unloading.....	82
5-7	1D strain model with variations of p and r^2 for 1.5" x 5.0" specimen (300 angular prism particles) and 4.5" x 5.0" specimen (1810 smooth cylindrical particles).....	83
5-8	Particle sliding and appearance of load chains (photos from Test #5-2) in a specimen with 550 cylindrical particles.....	85
5-9	Horizontal versus vertical stress on loading and unloading from sensors S1 and S6 from Test #5-1.....	88
5-10	Horizontal versus vertical stress on loading and unloading from sensors S1 and S6 from Test #5-2.....	89
5-11	Horizontal versus vertical stress on loading and unloading from sensors S2 and S7 from Test #5-7.....	90
5-12	Relative red intensity and horizontal stress versus time for Test #5-8.....	95
5-13	Horizontal stress and surface settlement versus time for Test #5-9.....	96
5-14	Horizontal stress and surface settlement versus time for Test #5-10.....	97

5-15	Changes in horizontal stress versus surface settlement for Test #5-10.....	99
5-16	Changes in horizontal stress versus surface settlement for Test #5-13.....	100
5-17	Surface settlement versus time for 7.5" x 5.0" specimens with smooth cylinders under different vertical stresses.....	102
5-18	Surface settlement versus time for 7.5" x 5.0" specimens with angular prisms under different vertical stresses.....	103
5-19	Surface settlement of 7.5" x 5.0" specimens with cylinders and angular prisms during loading.....	106
5-20	Hardin's 1D strain model for 7.5" x 5.0" specimens with (a) smooth cylinders and (b) angular prisms.....	107
5-21	Surface settlement of 7.5" x 5.0" specimens with cylinders and angular prisms during incremental loading and under sustained vertical stress of 23.3 psi and during unloading.....	109
5-22	Surface settlement of 7.5" x 5.0" specimens with cylinders and angular prisms during incremental loading, under sustained vertical stress of 40.9 psi and during unloading.....	110
5-23	Surface settlement versus time for 7.5" x 5.0" specimens with smooth cylinders and angular prisms under a constant vertical stress of 23.3 psi ..	111
5-24	Surface settlement versus time for 7.5" x 5.0" specimens with smooth cylinders and angular prisms under a constant vertical stress of 40.9 psi	112
5-25	Surface settlement of 7.5" x 5.0" specimens with smooth and rough cylinders during loading.....	114
5-26	Surface settlement of 7.5" x 5.0" specimens with smooth and rough cylinders during incremental loading, under sustained vertical stress of 23.3 psi and during unloading.....	116
5-27	Surface settlements of 7.5" x 5.0" specimens with smooth and rough cylinders during incremental loading, under sustained vertical stress of 40.9 psi and during unloading.....	117
5-28	Surface settlement versus time for 7.5" x 5.0" specimens with smooth and rough cylinders under a constant vertical stress of 23.3 psi.....	118
5-29	Surface settlement versus time for 7.5" x 5.0" specimens with smooth and rough cylinders under a constant vertical stress of 40.9 psi.....	119

5-30	Selected regions for observing force chains in the specimen during loading and during aging.....	121
5-31	Formations of force chains in the direction of major principal (vertical) stress in region #1 during loading from 0 psi to 23.3 psi (see also Figure 5-30 for the location of region #1).....	124
5-32	Force chains versus time in region #1 under a constant vertical stress of 23.3 psi (see also Figure 5-30 for the location of region #1).....	125
A-1	Calibration charts for sensor S3 at points L (top) and R (bottom).....	137
A-2	Calibration charts for sensor S4 at points L (top) and R (bottom).....	138
A-3	Calibration charts for sensor S5 at points L (top) and R (bottom).....	139
A-4	Calibration charts for sensor S6 at points L (top) and R (bottom).....	140
A-5	Calibration charts for sensor S7 at points L (top) and R (bottom).....	141
A-6	Calibration charts for sensor S8 at points L (top) and R (bottom).....	142
A-7	Calibration charts for sensor S9 at points L (top) and R (bottom).....	143
A-8	Calibration charts for sensor S10 at points L (top) and R (bottom).....	144
A-9	Red intensity and temperatures versus time at the measurements from sensors S1 and S2 from Test #T1.....	145
A-10	Red intensity and temperatures versus time at the measurements from sensors S4 and S5 from Test #T1.....	146
A-11	Red intensity and temperatures versus time at the measurements from sensors S6 and S7 from Test #T1.....	147
A-12	Red intensity and temperatures versus time at the measurements from sensors S9 and S10 from Test #T1.....	148
A-13	Red intensity and temperatures versus time at the measurements from sensors S1 and S2 from Test #T2.....	149
A-14	Red intensity and temperatures versus time at the measurements from sensors S4 and S5 from Test #T2.....	150
A-15	Red intensity and temperatures versus time at the measurements from sensors S6 and S7 from Test #T2.....	151

A-16	Red intensity and temperatures versus time at the measurements from sensors S9 and S10 from Test #T2.....	152
B-1	Horizontal versus vertical stress on loading and unloading from sensors S1 and S6 in Test #5-3.....	154
B-2	Horizontal versus vertical stress on loading and unloading from sensors S1 and S6 in Test #5-4.....	155
B-3	Horizontal versus vertical stress on loading and unloading from sensors S1 and S6 in Test #5-5.....	156
B-4	Horizontal versus vertical stress on loading and unloading from sensors S1 and S6 in Test #5-6.....	157
B-5	Horizontal versus vertical stress on loading and unloading from sensors S1 and S6 in Test #5-7.....	158
B-6	Horizontal versus vertical stress on loading and unloading from sensors S3 and S8 in Test #5-7.....	159
C-1	Relative red intensity versus time from S1, S2, S3 (left) and S6, S7, S8 (right) from Test #5-10.....	161
C-2	Relative red intensity versus time from sensors S1, S2 (left) and S6, S7 (right) from Test #5-11.....	162
C-3	Relative red intensity versus time from sensors S3, S4 (left) and S8, S9 (right) from Test #5-11.....	163
C-4	Relative red intensity versus time from sensors S5 (left) and S10 (right) from test #5-11.....	164
C-5	Horizontal stress versus time from sensors S1, S2 (left) and S6, S7 (right) from Test #5-11.....	165
C-6	Horizontal stress versus time from sensors S3, S4 (left) and S8, S9 (right) from Test #5-11.....	166
C-7	Horizontal stress versus time from sensors S5 (left) and S10 (right) from Test #5-11.....	167
C-8	Changes in horizontal stress versus surface settlement from Test #5-11.....	167
C-9	Relative red intensity versus time from sensors S1, S2 (left) and S6, S7 (right) from Test #5-12.....	168

C-10	Relative red intensity versus time from sensors S3, S4 (left) and S8, S9 (right) for Test #5-12.....	169
C-11	Relative red intensity versus time from sensors S5 (left) and S10 (right) for Test #5-12.....	170
C-12	Surface settlements during loading and under a constant vertical stress of 23.3 psi for 10 days for Test #5-12.....	170
C-13	Changes in horizontal stress versus surface settlement for Test #5-12 (black plate with pin hole was not used during the test).....	171
C-14	Horizontal stress versus time from sensors S1, S2 (left) and S6, S7 (right) for Test #5-12.....	172
C-15	Horizontal stress versus time from sensors S3, S4 (left) and S8, S9 (right) for Test #5-12.....	173
C-16	Horizontal stress versus time from sensors S5 (left) and S10 (right) for Test #5-12.....	174
C-17	Relative red intensity versus time from sensors S1, S2 (left) and S6, S7 (right) for Test #5-13.....	175
C-18	Relative red intensity versus time from sensors S3, S4 (left) and S8, S9 (right) for Test #5-13.....	176
C-19	Relative red intensity versus time from sensors S5 (left) and S10 (right) For Test #5-13.....	177
C-20	Changes in horizontal stress versus surface settlement for Test #5-13.....	178
C-21	Horizontal stress versus time from sensors S1, S2 (left) and S6, S7 (right) For Test #5-13.....	179
C-22	Horizontal stress versus time from from sensors S3, S4 (left) and S8, S9 (right) for Test #5-13.....	180
C-23	Horizontal stress versus time from sensors S5 (left) and S10 (right) for Test #5-13.....	181
C-24	Relative red intensity versus time from sensors S1, S2 (left) and S6, S7 (right) for Test #5-14.....	182
C-25	Relative red intensity versus time from sensors S3, S4 (left) and S8, S9 (right) for Test #5-14.....	183

C-26	Relative red intensity versus time from sensors S5 (left) and S10 (right) for Test #5-14.....	184
C-27	Horizontal stress versus time from sensors S1, S2 (left) and S6, S7 (right) for Test #5-14.....	185
C-28	Horizontal stress versus time from sensors S3, S4 (left) and S8, S9 (right) for Test #5-14.....	186
C-29	Horizontal stress versus time from sensors S5 (left) and S10 (right) from test #5-14.....	187
C-30	Surface settlement during loading, under sustained vertical stress of 23.3 psi for 7 days and during unloading for Test #5-14.....	188
C-31	Relative red intensity versus time from sensors S1 (left) and S6 (right) For Test #5-15	189
C-32	Relative red intensity versus time from sensors S2, S3 (left) and S7, S8 (right) for Test #5-15.....	190
C-33	Relative red intensity versus time from sensors S4, S5 (left) and S9, S10 (right) for Test #5-15.....	191
C-34	Horizontal stress versus time from sensors S1 (left) and S6 (right) for Test #5-15.....	192
C-35	Horizontal stress versus time from sensors S2, S3 (left) and S7, S8 (right) for Test #5-15.....	193
C-36	Horizontal stress versus time from sensors S4, S5 (left) and S9, S10 (right) for Test #5-15.....	194
C-37	Surface settlement during loading, under sustained vertical stress of 40.90 psi for 7 days, and unloading for Test #5-5.....	195
C-38	Relative red intensity versus time from sensors S1, S2 (left) and S6, S7 (right) for Test #5-16.....	196
C-39	Relative red intensity versus time from sensors S3, S4 (left) and S8, S9 (right) for Test #5-16.....	197
C-40	Relative red intensity versus time from sensors S5 (left) and S10 (right) for Test #5-16.....	198

C-41	Horizontal stress versus time from sensors S1, S2 (left) and S6, S7 (right) for Test #5-16.....	199
C-42	Horizontal stress versus time from sensors S3, S4 (left) and S8, S9 (right) For Test #5-16.....	200
C-43	Horizontal stress versus time from sensors S5 (left) and S10 (right) for Test #5-16.....	201
C-44	Surface settlement during loading, under sustained vertical stress of 23.28 psi for 7 days and during unloading for Test #5-16.....	202
C-45	Surface settlement for 7.5" x 5.0" specimens under a constant vertical stress of 23.3 psi.....	203
C-46	Surface settlement for 7.5" x 5.0" specimens under a constant vertical stress of 40.9 psi.....	204
D-1	Photos of particles at the left wall of the specimen on loading for Test #5-2.....	206
D-2	Photos of particles at the left wall of the specimen during loading and unloading for Test #5-2.....	208
D-3	Photos of particles at the right wall of the specimen during loading for Test #5-2.....	209
D-4	Photos of particles at the right wall of the specimen on loading and unloading for Test #5-2	211
D-5	Formations of force chains in region #2 from the specimen during loading from 0 psi to 23.3 psi (see Figure 5-30 for the location of region #2).....	212
D-6	Force chains versus time in region #2 from the specimen under a constant vertical stress of 23.3 psi (see Figure 5-30 for the location of region #2).....	213
D-7	Formations of force chains in region #3 from the specimen during loading from 0 psi to 23.3 psi (see Figure 5-30 for the location of region #3).....	215
D-8	Force chains versus time in region #3 from the specimen under a constant vertical stress of 23.3 psi (see Figure 5-30 for the location of region #3).....	216

LIST OF TABLES

TABLE

4-1	Empirical coefficients a and b for calibrations of sensors S1 to S10	67
5-1	Initial conditions of test specimens for the study of K_o values.....	87
5-2	Initial conditions of specimens for time-dependent surface settlement tests.....	93
6-1	Summary of K_o values.....	130

LIST OF APPENDICES

APPENDIX

A	CALIBRATION CHARTS FOR SENSORS S3 TO S10 AND TEST RESULTS FROM CHAPTER 4.....	136
B	COEFFICIENT OF LATERAL EARTH PRESSURE AT REST (K_o).....	153
C	TEST RESULTS FROM CHAPTER 5 (RED INTENSITY, HORIZONTAL STRESS AND SURFACE SETTLEMENT VERSUS TIME).....	160
D	PHOTOS FROM CHAPTER 5	205

LIST OF TERMS

2D	Two-dimensional
3D	Three-dimensional
a	Dimensionless coefficient a in the equation of calibration charts
b	Dimensionless coefficient b in the equation of calibration charts
B	Blue intensity
C_B	Brewster's photoelastic constant (1 Brewster = 10^{-6} MPa)
CPT	Cone penetration test
e	Void ratio
e_o	Initial void ratio
G	Green intensity
K	Lateral stress coefficient
K_a	Coefficient of active earth pressure
K_p	Coefficient of passive earth pressure
K_o	Coefficient of lateral earth pressure at rest
N	Fringe order ($\delta = N\lambda$)
p	Exponent on the term (σ_v/P_a) in Hardin's 1D strain model
P_a	Atmospheric pressure ($P_a \cong 14.69$ psi)
R	Red intensity

R_o	Red intensity of stress-free glass
R_σ	Red intensity of stressed glass
R_{rel}	Relative red intensity ($R_{rel} = R_o - R_\sigma$)
r^2	Correlation coefficient
S1	Glass plate sensor #S1
S2	Glass plate sensor #S2
S3	Glass plate sensor #S3
S4	Glass plate sensor #S4
S5	Glass plate sensor #S5
S6	Glass plate sensor #S6
S7	Glass plate sensor #S7
S8	Glass plate sensor #S8
S9	Glass plate sensor #S9
S10	Glass plate sensor #S10
S_{1D}	Dimensionless stiffness coefficient from Hardin's 1D strain model
t	Thickness of photoelastic materials
Δ_y	Surface settlement of specimens
δ	Retardation (or phase difference) of light wave
γ	Shear strain
λ	Wavelength of white light ($\lambda \approx 565$ nm in glass according to ASTM standard)
μ	Coefficient of frictional resistance
σ	Stress applied on the top of glass plate sensors
σ_1	Major principal stress

σ_2	Minor principal stress
σ_v	Vertical stress
σ_h	Horizontal stress
σ'_v	Vertical effective stress
σ'_h	Horizontal effective stress
σ'_θ	Hoop effective stress (around the perimeter of a pile shaft)
σ'_r	Radial effective stress (confining pressure)

ABSTRACT

DEVELOPMENT OF PHOTOELASTIC METHODS TOWARDS STUDY OF MECHANICAL AGING OF 2-DIMENSIONAL GRANULAR ASSEMBLIES

by

Thaweesak Jirathanathaworn

Co-Chairs: Roman D. Hryciw and Russell A. Green

Phototelasticity is a well-known method for experimental stress analysis of solid transparent materials. It has commonly been used to measure stresses from the analysis of photoelastic fringes. In this study, a test apparatus was built for geotechnical engineering research in which both the specimen and sensors were of photoelastic material. Digital image processing of light color intensities was used to analyze stress in the specimens. Glass particles were used to model the sand grains. The shapes of the particles included cylinders and angular prisms.

Glass plates with a central hole were manufactured and used as sensors for determining horizontal stresses in 2D assemblies of glass particles. The horizontal stresses in the 2D granular assemblies were measured during loading and unloading, and with elapsed time under constant vertical stress. The horizontal stress was determined through changes in relative red intensity of the sensors. Experimental results show

potential uses of the relative red intensity for measuring horizontal stress, and estimating K_o of particulate assemblies. Results showed that the values of K_o ranged from 0.30 to 0.84. Variations of the K_o values were attributed to unbalanced loading during the tests and swinging of a load frame. The use of the relative red intensity in glass plate sensors may be adapted to other engineering applications and scientific uses.

The calibrated sensors were used to monitor time-dependent increases in horizontal stress in 2D granular assemblies. Time-dependent surface settlement as a result of particle rearrangement in granular assemblies may be a critical factor in mechanical aging. Particle rearrangement results in time-dependent increases in horizontal stress in granular assemblies possibly via the formation of particle arches, through which forces are transferred horizontally.

Time-dependent changes under constant vertical stress depended on vertical stress, particle shape and particle surface roughness. In 2D granular assemblies, individual particles move as a response to forces transferred from the specimen surface. The angular prisms used in this study were observed to pack very efficiently. Particle surface roughness inhibits particle motions, but micro-interlocking in the granular assemblies may be developed with time.

An earlier hypothesis by Bowman and Soga (2003) that buckling of strong force chains due to disappearance of lateral support from weak force networks was supported by observation of time-dependent changes in shapes of force chains. Experiments using larger specimens are recommended because they may allow better observance of the buckling of the force chains.

CHAPTER I

INTRODUCTION

1.1 Introduction

For decades, there has been evidence of time-dependent increases in strength and stiffness in recently deposited/densified sands. The process has been called *sand aging*. Aging effects are manifested as increases in small-strain shear modulus (observed through increases in shear wave velocity) and penetration resistance (e.g., cone penetration resistance) with time.

Hypothesized aging mechanisms have included both *mechanical* and *chemical* processes. However, the investigations into aging mechanisms have been inconclusive, sometimes raising more questions than they resolved. Questions also arise whether aging mechanisms involve mainly mechanical processes, chemical processes, or possibly their combination (Afifi and Woods, 1971; Anderson and Stokoe, 1978; Mitchell and Solymar, 1984; Hryciw, 1986; Dowding and Hryciw, 1986; Chow et al., 1988; Hryciw and Dowding, 1988; Mesri et al., 1990; Schmertmann, 1991; Charlie et al., 1992; Barton, 1993; Joshi et al., 1995; Baxter, 1999; Bowman, 2002; Bowman and Soga, 2003; Baxter and Mitchell, 2004; Green et al., 2008; Mitchell, 2008).

Possible mechanical aging processes involve readjustment of sand particles after deposition/densification of soils. This slight time-dependent movement of sand

particles under constant pressure encompasses particle sliding and rolling. Although sand density does not significantly increase as a result of time-dependent particle rearrangement and reorientation, the process is significant enough to cause intergranular stress redistribution. Ultimately, the sand particles reorient into more stable positions with possibly an increased number of particle contacts, better micro-interlocking of grain asperities and reduced shear stress at contacts (Terzaghi, 1934; Mesri et al., 1990; Schmertmann, 1991; Bowman, 2002; Bowman and Soga, 2003).

The hypothesized chemical mechanism is precipitation of dissolved silica (i.e., *silica acid gel*) and/or carbonates at particle contacts. The dissolution of silica is caused by chemical interaction between pore fluid and soil grains, possibly enhanced by contact stresses. Above equilibrium solution, the dissolved silica and carbonates will precipitate and may cement sand particles together, thereby increasing strength and stiffness of the sand (De Boer, 1977; Mitchell and Solymar, 1984; Hryciw, 1986; Barton, 1993; Joshi et al., 1995; Sheldon and Wheeler, 2003; Sheldon et al., 2003).

Aging in sands ultimately increases strength and stiffness of sands. Many past studies showed increases in cone penetration resistance with time (Mitchell and Solymar, 1984; Mesri et al., 1990; Charlie et al., 1992). The increases in cone penetration resistance indicate increase of strength, stiffness and *probably horizontal stress* (i.e., confining pressure) in sands.

The objectives of this study are observation of possible changes in horizontal stresses in granular assemblies during loading-unloading and during aging under constant vertical stress. For uniform soil profiles with level ground surface subjected to vertical pressure, macroscopic strains occur only in the vertical direction, i.e., one-dimensional settlement. Lateral strain is globally zero although local horizontal strains (at the particle level) must be occurring for vertical compression to occur. In this state,

vertical and horizontal effective stresses are in an "at-rest" condition. The ratio of horizontal to vertical effective stress in this case is the coefficient of lateral earth pressure at-rest or K_o .

The research presented in this dissertation also focuses on explaining the mechanical aging mechanisms which may result in increases in horizontal stress in granular assemblies. A photoelasticity test system was developed for the study. Glass particles were used to model sand grains. The test system was used for: (1) determining horizontal stresses in 2-dimensional granular assemblies during loading and unloading, and (2) observing horizontal stress of specimens with time. The focus and objectives of this research are outlined further in Section 1.2.

1.2 Research objectives

This research used cylindrical and angular prism glass particles as a model for sand grains. In this dissertation, specimens with assemblies of the glass particles are also called "*2D granular assemblies*" or "*2D assemblies of glass particles*". Instead of using 3D assemblies of glass particles, this study used 2D granular assemblies to allow for observation of the patterns of developing force chains in the specimens due to loading-unloading, and during aging by use of photoelasticity.

The objectives of the research were to develop a photoelasticity test apparatus and to use the apparatus in conjunction with digital image processing. Glass plate photoelastic sensors were manufactured for measuring horizontal stress in 2D granular assemblies during loading-unloading, and as a function of time under constant vertical stress. This research also used photoelasticity to observe force chains in the 2D granular assemblies. The patterns of force chains were used to examine an aging mechanism hypothesized by Bowman and Soga (2003).

1.3 Organization of dissertation

This dissertation consists of 6 chapters. In Chapter 1, an overview of sand aging is presented. The objectives of the research and the organization of the dissertation are also outlined in Chapter 1.

Chapter 2 reviews relevant literature on sand aging. The field evidence of sand aging and previously proposed aging mechanisms are summarized. The review of the relevant literature on sand aging disclosed gaps in knowledge which became the objectives of this study to search for better understanding of aging mechanisms and possible time-dependent increases in horizontal stress in granular assemblies. In Chapter 2, the background and theory of photoelasticity are presented. The background of photoelasticity was helpful in the design and construction of the test apparatus. The summary of photoelasticity theory also served as a guideline for the experimental studies.

Chapter 3 presents the preparation technique and processes for manufacturing the testing material (i.e., glass particles). The setup of the test apparatus with associated hardware is shown in this chapter.

Chapter 4 discusses calibration of the glass plate photoelastic sensors. In Chapter 4, “*relative red intensity (or $R_{rel} = R_o - R_\sigma$)*” was used for tracking changes in stress applied to the sensors. Calibration charts were developed as the relationship between relative red intensity (R_{rel}) and dimensionless applied vertical stress (σ/P_a).

Chapter 5 presents the application of photoelasticity using the calibrated glass plate sensors for measuring horizontal stress in 2D granular assemblies. In Chapter 5, glass particles in the shape of cylinders and angular prisms were used to simulate sand grains. The calibrated glass plate sensors were attached to both sides of the test box for determining horizontal stresses. The values of horizontal stresses in the specimens

were determined through the relative red intensity (R_{rel}) in the glass plate sensors. The application of photoelasticity for determining horizontal stress in 2D granular assemblies was used: (1) to measure horizontal stress of specimens during loading and unloading, and (2) to obtain the values of horizontal stress in 2D granular assemblies with time.

Finally, a brief summary of the research presented in this dissertation and recommendations for future research are presented in Chapter 6.

1.4 Terminology

In this dissertation, the following terms or phrases are often used:

Aging of sand: Time-dependent phenomenon where the strength and stiffness in sand increases. The increases in strength and stiffness are often surmised from increases in *in situ* penetration resistance.

Aging mechanism: Mechanism(s) underlying the *aging of sand*. Hypothesized mechanism includes mechanical and chemical aging. Mechanical aging is particle rearrangement (i.e., particle rolling, sliding and seating) and reorientation into a more stable position with improved micro-interlocking. Chemical aging involves dissolution and precipitation of silica and carbonate.

Aging effect: Manifestation of the *aging mechanisms* (e.g., the formation of micro-interlocking of grain asperities due to particle rolling, sliding and seating and the formation of cementation at particle contacts which be enhanced by contact pressure).

Particle seating: Improved micro-interlocking of particle asperities occurs at small unstable contacts that exist primarily at low confining pressure. Particle seating may happen instantaneously to form stable contacts after initial deposition of the particulate assembly.

Particle sliding: Translational motion of particles that happens instantaneously upon a change in loading but may also continue to occur gradually with time. Particle sliding should happen particularly under high confining pressure at which stable contacts are formed.

Figure 1-1 shows two particles in contact after initial deposition with possibly small unstable contacts. Overburden pressure transferred through the particle contacts could overcome the frictional resistance at particle contact and better seat the particles with improved micro-interlocking of surface roughness. This would contribute to an increase in stiffness and strength of the particulate assembly.

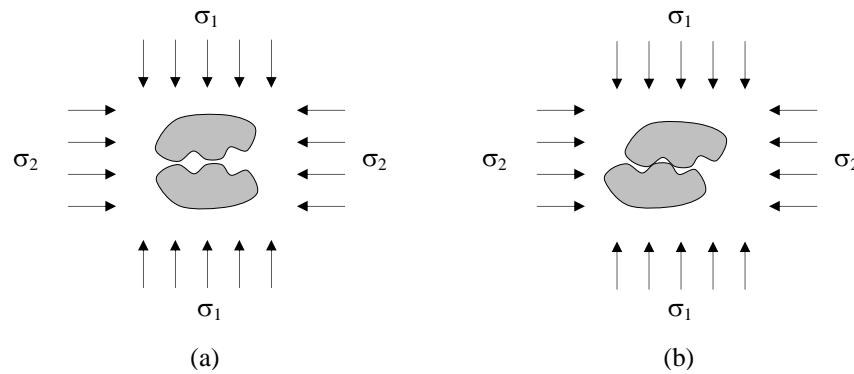


Figure 1-1 Two particles in contact: (a) after deposition with unstable contact, and (b) formation of more stable contact with better seating and improved micro-interlocking of surface roughness

Figure 1-2 shows two particles in contact before and after sliding. At constant confining stress, this motion could be considered as "creep". The two particles have a stable contact. Sliding may continue to occur with time and result in overall reduction of porosity of the particulate assembly. This interface creep, as confirmed by time-dependent surface settlement of the ground surface, could result in the formation of particle arches and time-dependent increase in horizontal stress in the particulate assembly as will be discussed in Chapter 5.

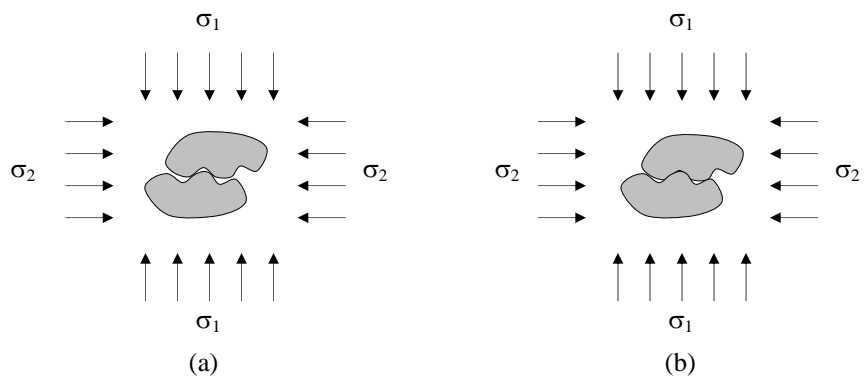


Figure 1-2 Two particles in contact: (a) before sliding, (b) after sliding

CHAPTER II

REVIEW OF RELEVANT LITERATURE

2.1 Introduction

The review of relevant literature on aging of sands is summarized in this chapter. Unlike in clayey soils, excess pore water pressure due to volume changes in clean sands dissipates rapidly, primary consolidation in sands after disturbance/deposition is insignificant. The first well-documented case study of sand aging was the Jebba Dam project on the Niger River in Nigeria (Mitchell and Solymar, 1984). In the Jebba dam project, despite obvious densification, several unexpected results related to sand aging were observed. For example, an initial loss in penetration resistance was observed following mechanical disturbance by explosive compaction. Large increases in penetration resistance were found over periods of several weeks and months after the densification.

Following these surprising observations of sand aging, the number of studies on sand aging increased as questions arose regarding what mechanisms underlie the time-dependent increase strength and stiffness of sands under constant vertical pressure.

In this chapter, Section 2.2 discusses the effects of vibrations on decreases in strength and stiffness of sands. Section 2.3 discusses the effects of aging as manifested by increases in strength and stiffness of sands. Section 2.4 summarizes

proposed aging mechanisms from previous research. Section 2.5 discusses aging effects on changes in horizontal effective stress in granular soils. A discussion in Section 2.5 presents the objective of this study, which is the development of a better understanding of the aging mechanisms that cause time-dependent increase in horizontal effective stress in granular assemblies. Section 2.6 summarizes the theory of photoelasticity, which is the method for determining horizontal stress of 2D granular assemblies used in this research.

2.2 Reduction of strength and stiffness of sands due to vibrations

Vibrations from vibrocompaction, explosive compaction, and earthquake shaking produce shear strains in sand. If loose, these vibrations result in collapse of the soil skeleton, which ultimately cause volumetric contraction (i.e., decrease in void ratio). When the collapse of the soil skeleton occurs rapidly, pore water pressures above hydrostatic values (i.e., excess pore water pressure) are generated.

The excess pore water pressure reduces effective stress in sands, thereby decreasing soil stiffness, strength, and cone penetration resistance. However, the excess pore pressure dissipates quickly in well-draining clean sands. Therefore, excess pore pressure in these sands should not be the cause of reduction of the penetration resistance after densification of sands.

However, in some cases (e.g., in Figure 2-1), excess pore water pressure in clean sand cannot drain easily due to impermeable layers at the top and bottom of sand layer. Here, the dissipation of excess pore pressure may require up to months after the deposition of the soil skeleton because the clay cap does not allow excess pore pressure to quickly dissipate. Therefore, in such a case as shown in Figure 2-1, the excess pore pressure could actually be the reason for penetration resistance being lower than that prior to disturbance. However, if the sand would likely densify with a

water film formed between the sand and clay layers, time-dependent increases in strength and stiffness would have been observed. With the water film, initially loads from overburden are not transferred into the sand layer. With time, the water film disappears. The loads from overburden gradually transfer into the sand layer. Therefore, degrees of mechanical particle rearrangement and chemical dissolution/precipitation increases with the increased load transferred from the overburden.

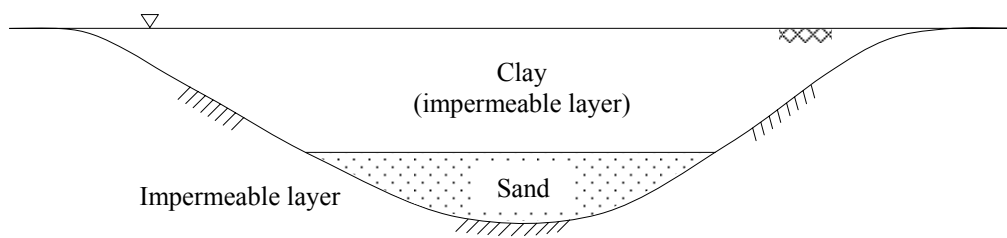


Figure 2-1 Example of sand deposit with possible drainage constraints

Ground surface settlement is an indication of sand densification. Mitchell and Solymar (1984) reported surface settlement between 0.3 and 1.1 meters occurring immediately after the completion of blasting in the Jebba dam project. In this project, the sand layer specified for the explosive compaction was about 15-m thick at a depth between 25 and 40 meters below the ground surface. Even though the densification of sand was clearly evident by subsidence of the ground surface, the post-blast penetration resistances were found to be lower than the pre-blast values several days to weeks after explosive compaction, but ultimately the pre-disturbance resistance was regained with time, and finally exceeded.

After explosive compaction in loose sand, there is an increase in sand density due to collapse of the initial loose structure. The redeposited soil, albeit denser, may contain unstable contacts on which micro-shearing and sliding can occur over some period of time. Low penetration resistance shortly after explosive compaction may be

attributed to destruction of past aging effects. Thomann and Hryciw (1992) show that even shear strain greater than 10^{-3} % could cause loss in small-strain shear modulus of soils. They showed that the time required to regain the values of stiffness that existed prior to the disturbance is controlled by the magnitude of shear strain. Therefore, even small vibrations could produce shearing at contacts of sand grains, thereby destroying the past aging effects, i.e., micro-interlocking and cement bonding (see Figure 2-2).

Unlike the results from explosive compaction, Mitchell and Solymar (1984) found, in the same project, no reduction of penetration resistance in sands after vibrocompaction (see Figure 2-3). Mitchell and Solymar explained that this is due to the additional backfilling associated with this technique (i.e., vibrocompaction) for soil densification. The backfill material directly increases sand density. Vibrocompaction (vertical and lateral compaction) of sands also cause an increase in horizontal effective stress.

In summary, although large vibration in loose sands causes an immediate increase in sand density, as manifested by ground surface settlement, past aging effects (i.e., micro-interlocking and cement bonding) could be destroyed due to shearing strains at particle contacts larger than 10^{-3} % (i.e., $\gamma > 10^{-3}$ %). The disappearance of micro-interlocks between grain asperities and the disruption of chemical cement bonding reduces strength and stiffness of sands. Reduction of sand strength and stiffness is indicated by the cone penetration resistance being lower than pre-vibration.

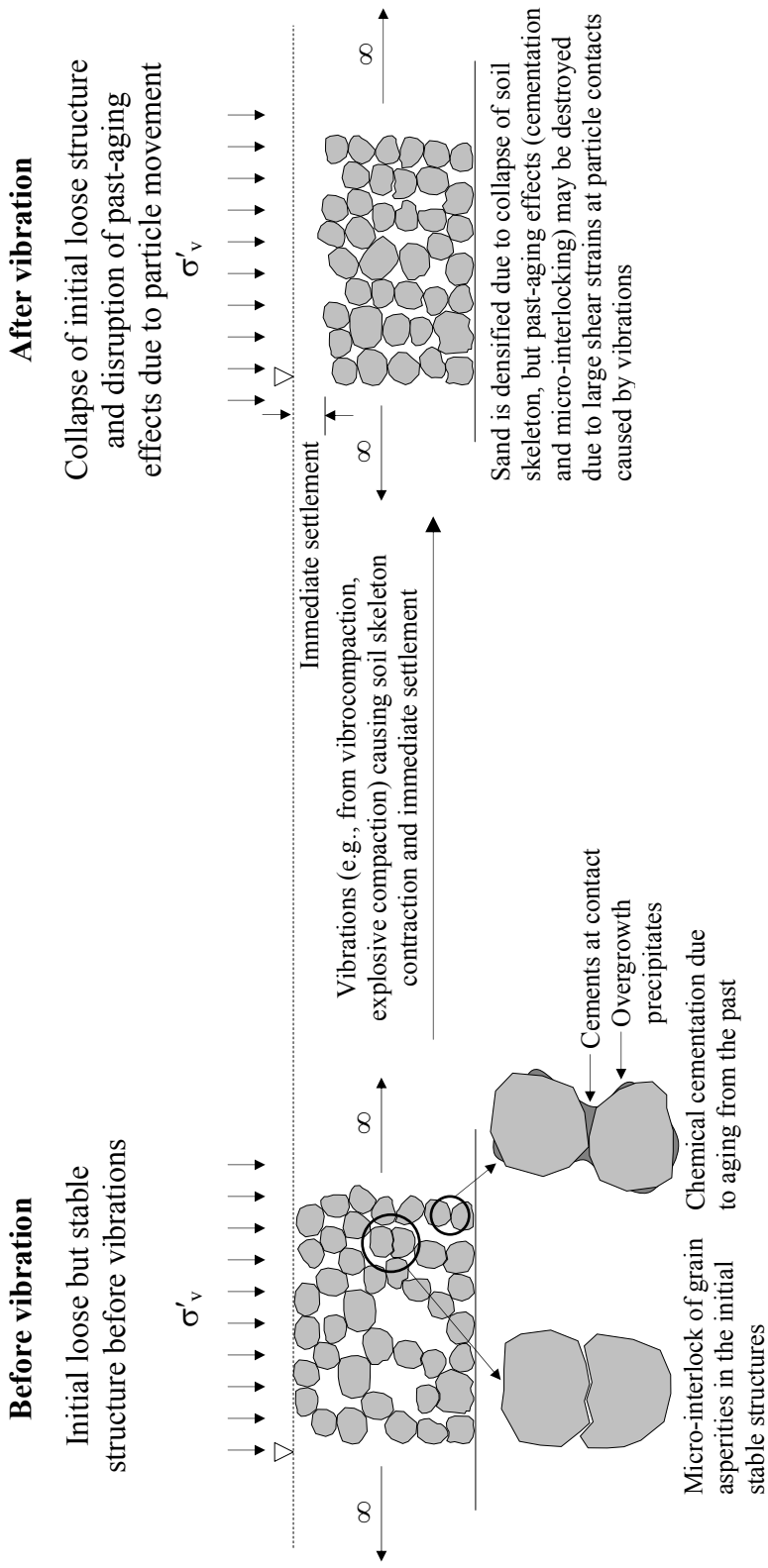


Figure 2-2 Diagram presenting collapse of initial structure (loose sands) and disruption of past-aging effects due to vibrations

2.3 Aging effects as manifested as increases in strength and stiffness in sands

The Jebba dam project was the construction of a large embankment dam for hydroelectric purposes. The site consisted of loose, clean alluvial sand. To preclude excessive settlement of the main dam, the upper 25 meters of the river alluvium was densified by vibrocompaction. At the depth of 25-40 meters, explosive compaction was used to densify the sand. Figures 2-3 and 2-4 show time-dependent increases in penetration resistance after vibrocompaction and explosive compaction, respectively.

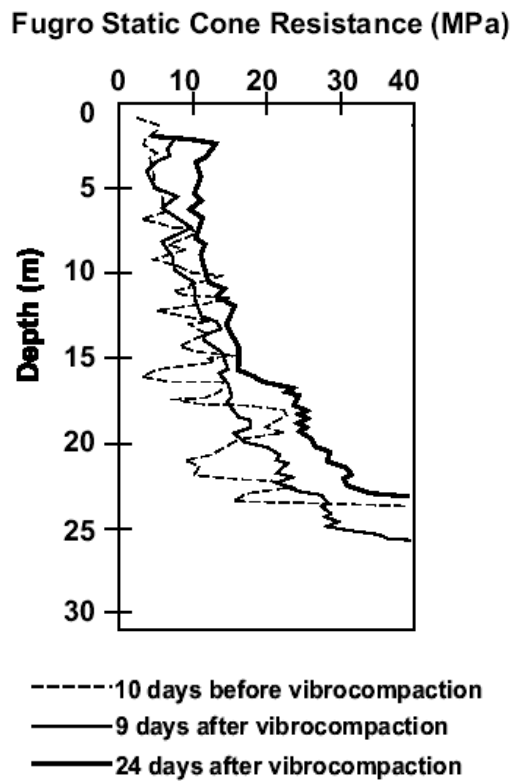


Figure 2-3 Increased penetration resistance with time following vibrocompaction at Jebba dam site (after Mitchell and Solymar, 1984; figure from Baxter, 1999)

Increase in cone penetration resistance of sands signifies increases in strength and stiffness. This manifestation probably indicates increases in horizontal stress in sands (Mitchell and Solymar, 1984; Houlsby and Hitchman, 1988; Ashford et al., 2004). Similar *in situ* results on increases in cone penetration resistance can be found in Mesri et al. (1990) and Charlie et al. (1992).

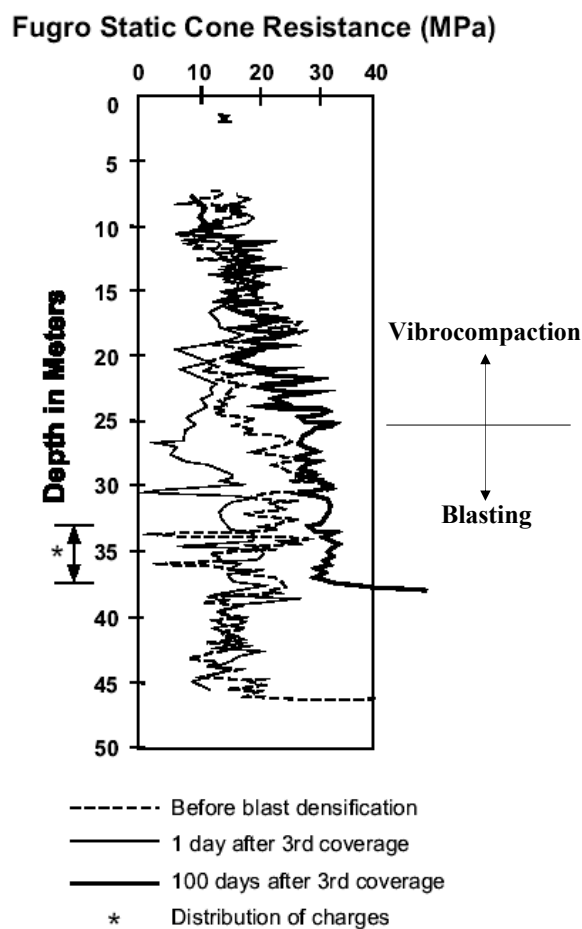


Figure 2-4 Changes in penetration resistance with time following explosive compaction at Jebba dam site (Mitchell and Solymar, 1984, figure by Baxter, 1999)

Increases in stiffness in sands with time were found using shear wave propagated through the sands. Time-dependent increases in shear wave velocity were also observed

in aged sands by Anderson and Stokoe, 1978; Afifi and Woods, 1971, Baxter and Mitchell, 2004; Thomann and Hryciw, 1990. The increased shear wave velocity manifested indicated in small-strain shear modulus. Aging mechanisms that possibly explains these observations include time-dependent mechanical and chemical processes as discussed in the Section 2.4.

2.4 Proposed mechanisms of sand aging from previous studies

Mechanical aging probably occurs over a period of weeks to months (Terzaghi, 1934; Mesri et al., 1990; Schmertmann, 1991; Bowman and Soga, 2003). For longer durations (e.g., years), chemical mechanisms may play a more significant role. Cementation is enhanced by pressure solution (Weyl, 1959; De Boer, 1977; Mitchell and Solymar, 1984; Barton, 1993; Sheldon and Wheeler, 2003; Sheldon et al., 2003). This section summarizes and discusses aging mechanisms from previous research.

2.4.1 Mechanical aging process

Mechanical aging occurs due to particle rearrangement in granular assemblies (i.e., creep). The rearrangement of particles results in time-dependent increases in sand strength and stiffness (Terzaghi, 1934; Mesri et al., 1990; Schmertmann, 1991; Bowman and Soga, 2003). Under constant loading, particles begin to move when intergranular limiting frictional resistances are reached or exceed. Particles rearrange into stable position with better micro-interlocking. Via this process, particle contacts in granular assemblies gradually develop lower intergranular shearing stress, thereby improving the soils' capacity to carry shear forces compared to that before soil improvement.

Mesri et al. (1990) suggested that mechanical aging occurs because of slight movements of individual sand particles with time. Continuing rearrangement of particles takes place by particle sliding, rolling and/or slipping. This process results in increases in macro-interlocking of associated sand particles. Increases in micro-interlocking may occur locally in aged sands. Time-dependent formation of micro-interlocking is believed to cause an increase in stiffness of sands with time.

Similar to Mesri et al. (1990), Schmertmann (1991) explained that time-dependent mechanical process in aged sands occurs because of particle reorientation. Although the reorientation of particles is not significant enough to increase sand density, the process causes stress redistribution (i.e., stress relaxation) at contacts of sand particles. As a result of time-dependent particle reorientation, the stress redistribution results in reductions of frictional (shearing) stress and probably increases in micro-interlocking at the associated particle contacts. Schmertmann explained that small movements of sand particles and grain slippage result in a more compact configuration in sands (i.e., without large increases in sand density). This process finally produces an increased shearing resistance of sands, particularly at particle contacts.

Bowman and Soga (2005) proposed a sand aging mechanism called displacement pile setup. The mechanism of displacement pile setup can be categorized as a form of mechanical aging in sands. They hypothesized that there is an increase in radial stress (i.e., horizontal effective stress) around a pile shaft after installation. Chow et al. (1988) explained that the horizontal stress around the pile decreases due to disturbance of the soil around the pile shaft during processes of driving the pile into the ground.

Chow et al. (1988) explained that initially after the installation of piles into the ground, a thin layer of loose sand around the pile is created. Particle arching (with hoop stress, σ'_θ) appears in the surrounding denser sand as shown in Figure 2-5. This circumferential (hoop) arching stress limits the radial (confining/horizontal) stress from acting on the pile shaft. With time after pile installation, a reduction of arching effects (or the breakdown of the hoop stress) produce continuous increase in the pile capacity due to the time-dependent increases in the radial (i.e., horizontal) stress that acts on the pile shaft.

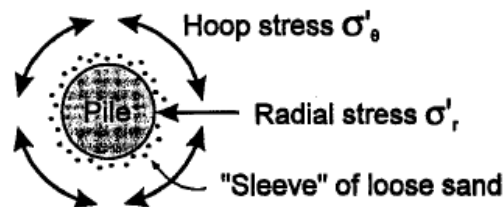


Figure 2-5 Plan view of arching effects (hoop stress) around a pile shaft initially after the pile installation (Chow et al., 1988)

After the process of driving the piles into sands, Bowman and Soga (2005) proposed that displacement pile setup or restrained dilation occurs with time. With the presence of a pile in the ground, sand particles adjacent to the pile shaft tend to rearrange (i.e., creep) relative to the pile shaft. This process causes redistribution of the loads imposed on individual sand particles. In this process, dense sand around the pile initially tends to contract, and with time, it dilates under constrained volume.

This slow dilation in sands near the pile shaft is a type of particle rearrangement and/or particle reorientation (i.e., creep), which probably causes time-dependent increase in horizontal stress (confining pressure) around the pile shaft. Increases in the horizontal

stress with time around the pile shaft would result in time-dependent increases in capacity of the pile to carry the loads (Chow et al., 1988; Bowman and Soga, 2005; Bowman, 2002).

2.4.2 Chemical aging process

Chemical aging in sands was initially postulated by Mitchell and Solymar (1984) to explain the Jebba dam's results of time-dependent increases in cone penetration resistance in sands. The time-dependent chemical process or pressure solution mechanism in sands occurs by dissolution of silica (i.e., sand grains) at particle contacts with time. At solution equilibrium, dissolved silica begins to precipitate, and chemical cement bonding is produced at grain contacts, thereby ultimately increasing strength and stiffness of sands (Weyl, 1959; De Boer, 1977; Sheldon and Wheeler, 2003; Sheldon et al., 2003).

Mitchell and Solymar (1984) postulated that the increases in penetration resistance are attributed cementation at contacts from precipitation of dissolved silica. As shown in Figure 2-6, Mitchell and Solymar pointed out that silica solubility would reach the equilibrium within weeks to a few months. The time frame for reaching equilibrium of silica solubility (see Figure 2-6) is consistent with the time period of the observed increases in cone penetration resistance at the Jebba dam site. Cementation of precipitated silica causes an improvement in cohesion of sands, thereby improving shearing resistance of sands (Weyl, 1959; De Boer, 1977; Hryciw, 1986; Barton, 1993; Joshi et al., 1995; Dittes and Labuz, 2002; Sheldon and Wheeler, 2003; Sheldon et al., 2003).

Figure 2-7 presents the process of silica dissolution between two sand (quartz) grains under sustained normal stress. Contact stress accelerates localized dissolution of silica at the contact of the associated particles. In this Figure 2-7, the applied normal stress transfers the load to the contact of the two particles. The contact stress causes dissolution of silica from the two grains. Dissolved silica diffuses away from the contact area toward the pore fluid, and precipitates coats the surface of the sand grains. At the edge between the sand grains, silica precipitates to cement the grains together as shown in Figure 2-8.

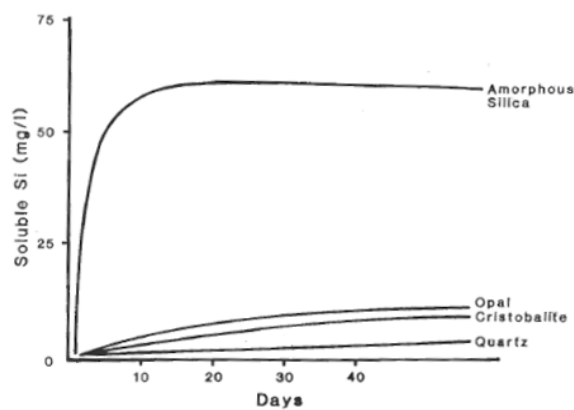


Figure 2-6 Dissolution rate of silica as a function of time (Wilding et al., 1977)

2.4.3 Other potential aging mechanisms

2.4.3.1 Mechanism of blast gas dissipation

Blast gases are produced during the detonation of the buried charges. The blast gases are trapped underground. Hryciw (1986) hypothesized that the blast gases exist in the form of bubbles entrapped underground. Some of these gas bubbles may have diameters larger than the diameters of sand grains.

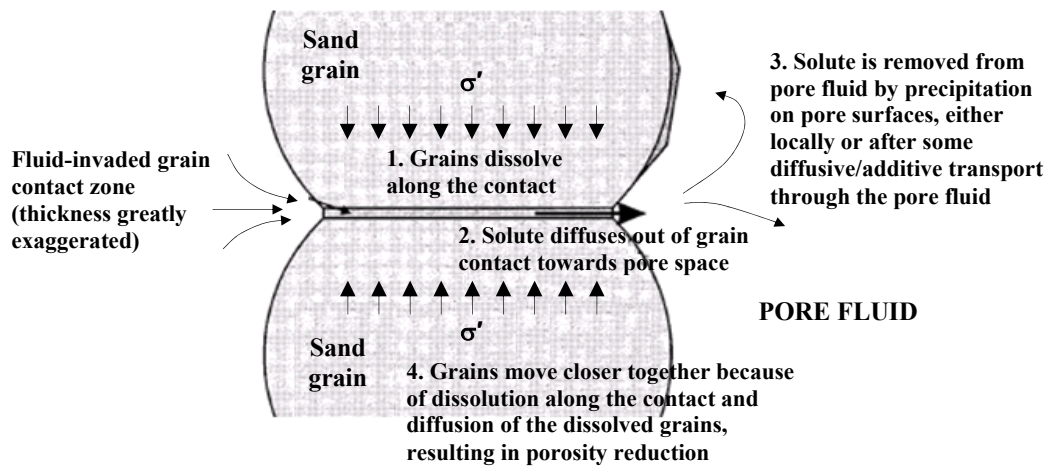


Figure 2-7 Silica dissolution and precipitation under contact stress
(after Sheldon et al., 2003)

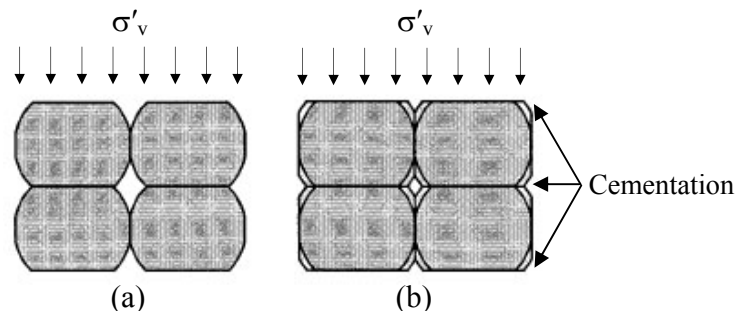


Figure 2-8 Grains under constant pressure: (a) initial state (b) precipitated silica around grains providing cementation between grains (after Sheldon et al., 2003)

The large gas bubbles inhibit sand particles from settling immediately after blasting, thereby creating particle arches as shown in Figure 2-9. With time under constant sustained pressure, the trapped gas bubbles dissolve, and/or escape to the ground surface. The disappearance of the gas bubbles may allow some individual sand particles to rearrange into a more compact configuration. It is also possible that the trapped gas bubbles may impede pore fluid flow, and thus prolong the dissipation of excess pore

water pressures (Hryciw, 1986; Hryciw and Dowding, 1986; Dowding and Hryciw, 1988; Mesri et al., 1990).

2.4.3.2 Biological aging mechanism

Recent research in biology and earth science has enabled a better understanding of microbiological processes in soils. The process could explain a time-dependent increase in the cohesion of sands from the by-products of microbiological activities. Therefore, this process may be called geo-biological process. The geo-biological process occurs by biological activity in the soil pore space. In the pore space where bacteria dwell they produce biomass, slimes and/or viscous gels. These by-products (as cementing materials) generally consist of precipitates of magnesium and calcium carbonate. These cohesive materials from bacteria activity coat the surfaces of sand grains. The precipitates at particle contacts results in increases in cohesions in aged sands.

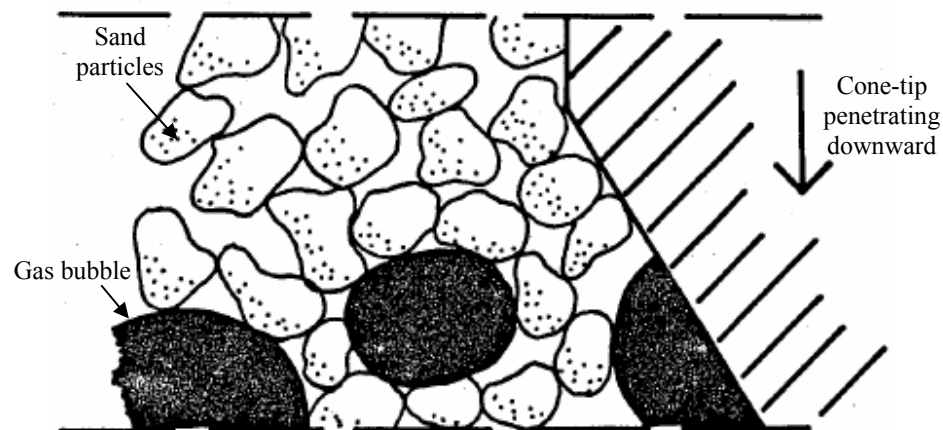


Figure 2-9 Blast-gas bubble producing arching of particles and loose sand pockets (adapted from Hryciw, 1986)

Mitchell and Santamarina (2005) summarized that bacterial growth and its reproduction rates depend on availability of nutrients, water and/or pore space. They mentioned that the absence of biological activity in old deposits is because of the lack in nutrients for the bacteria to dwell. Additional information on the microbiological processes for soil improvement can be found in Stocks-Fischer et al (1999), Mitchell and Santamarina (2005) and Mitchell (2008).

DeJong et al. (2006) performed extensive experiments to study the effects of *Bacillus pasteurii* on increases in strength and stiffness of sands. They found that *Bacillus pasteurii* produced calcite (i.e., calcium carbonate), which creates a cement bonding at the sand particle contacts. Time-dependent performance of the bacteria activities that produce calcite was assessed by an increase in small-strain shear modulus. Increases in cohesion of the soils were also observed from experimental results of isotropic consolidated undrained compression (CIUC) tests. In this experimental study, the cement bonding at particle contacts was verified as calcite by scanning electron micrographs and x-ray compositional mapping. Similar electron scanning micrographs of calcite cementation in aged sands were also found by Joshi et al. (1995).

2.5 Aging effects on horizontal effective stress in granular soils

Both soil strength (ultimate stress) and stiffness depend on confining pressure. Therefore, an investigation into aging mechanisms on the increase in horizontal effective stress (σ'_h) is an important component in this present study.

There were many previous studies investigating and developing instruments for measuring horizontal stress of soils, especially at zero lateral strain (K_o) conditions (Dyvik et al., 1985; Mesri and Castro, 1987; Thomann, 1990; Thomann and Hryciw,

1990; Mesri and Hayat, 1993; Mesri and Vardhanabhuti, 2007). This research proposes a new approach for measuring horizontal stress in 2-dimensional granular assemblies using photoelasticity. The application of photoelasticity for measuring horizontal stress of 2D granular assemblies is presented and discussed in Chapter 5.

Mesri and Castro (1987) found time-dependent increases in σ'_h in normally consolidated clays. For sands, Terzaghi (1934) performed experiments using rigid retaining walls to measure the lateral earth pressure of dry Plum Island sand. After deposition, Terzaghi found a marked increase in σ'_h in spite of the fact that the position of the wall did not change. The increase in σ'_h was found over a period of 17 hours as shown in Figure 2-10 (from point d to point e).

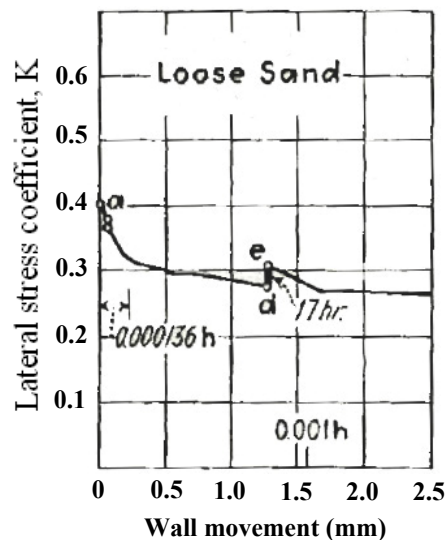


Figure 2-10 Increase in lateral stress coefficient (K) in loose dry sand during 17 hrs without wall movement from d to e (after Terzaghi, 1934)

Terzaghi (1934) explained that the time-dependent increase in σ'_h in sand was attributed to the continuous rearrangement of individual particles after deposition.

Particle rearrangement under constant pressure causes individual sand grains to move into more stable positions with reduced frictional (shear) stress at contacts of sand grains. In brief, Terzaghi's explanations suggest that decreases in shearing stresses at individual contacts in aged sands causes an increase in σ'_h . Decreases in the contact shear stresses as described by Terzaghi could be explained by continuous slight movements of particles. At microscopic levels (i.e., interaction of particles), Kuhn and Mitchell (1993) suggested that particles translate (or slide) based on numerical results, while Bowman and Soga (2003) proposed that the particles rotate (or roll) based on experimental results of fabric tests.

From the review of literature, it may be concluded that while time-dependent increase in sand strength and stiffness is due to both particle rearrangement and/or chemical bonding, time-dependent increase in σ'_h is hypothesized to be caused only by mechanical rearrangement of particles rather than by cement bonding at contacts (Terzaghi, 1934; Mesri et al., 1990; Schmertmann, 1991). This hypothesis was supported in experiments by Clark et al. (1993). Clark et al. measured σ'_h of sands mixed with Portland cement. They found no time-dependent change in lateral stress in the cemented sands under constant vertical pressures up to 400 kPa. Cementation at grain contacts inhibits particle rearrangement, thereby resulting in no change of σ'_h in the cemented sands.

As shown in Figure 2-11, loads are transferred through granular assemblies via particle chains. The force chains (i.e., force columns) are formed parallel to the direction of major principal stress (σ_1). With increased macroscopic load approaching failure of a laboratory specimen, the number of force chains increases before finally buckling at

failure (Oda, 1972). Oda and Kazama (1998) stated that “*Development of the columnar structure is a common feature prevailing in the strain-hardening (pre-peak) process of granular soils.*” When loads increase in the direction of σ_1 (with σ_2 held constant), the specimen approaches failure. At this moment particles move and begin to form force chains that are parallel to the direction of the increased loads. As macro-failure approaches voids in the loaded specimen, the longest dimension of the voids grows nearly parallel to the direction of σ_1 as shown in Figure 2-11. In Figure 2-12, during buckling of the force chains, particles roll and slide in the buckling zone, shear bands begin to form. In the end, the loaded specimen fails along this zone of buckling of force chains.

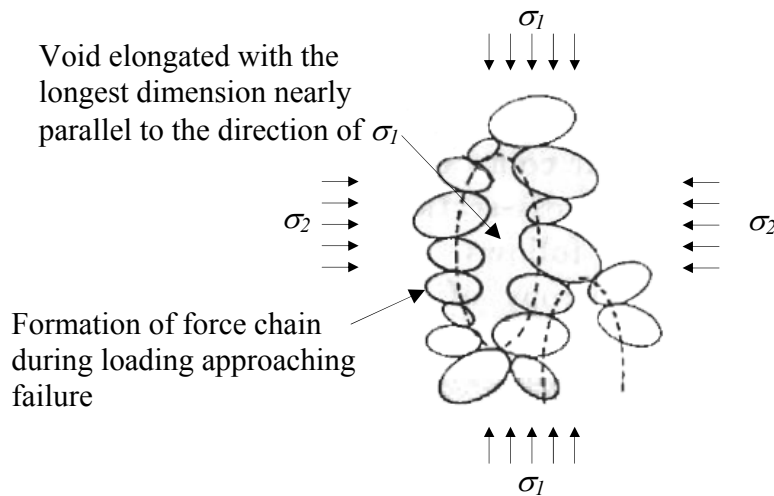


Figure 2-11 Void elongation parallel to the direction of major principal stress
(after Oda et al., 1985)

According to Radjai et al. (1998), there are “strong” and “weak” force networks in an assembly of granular materials. Bowman (2002) stated that “*The strong force network carries the deviatoric load with high normal to frictional contact forces*” and

“...contacts in the weak force network carry very low normal forces and relatively high frictional forces.”

During aging, Bowman (2002) stated that “Creep essentially begins in the weak force network because contacts are at limiting frictional equilibrium and any perturbation in applied load at the contacts (i.e., either reduction in normal force or increase in frictional force), or time-dependent change in material strength can lead to sliding or yield at grain asperities.”

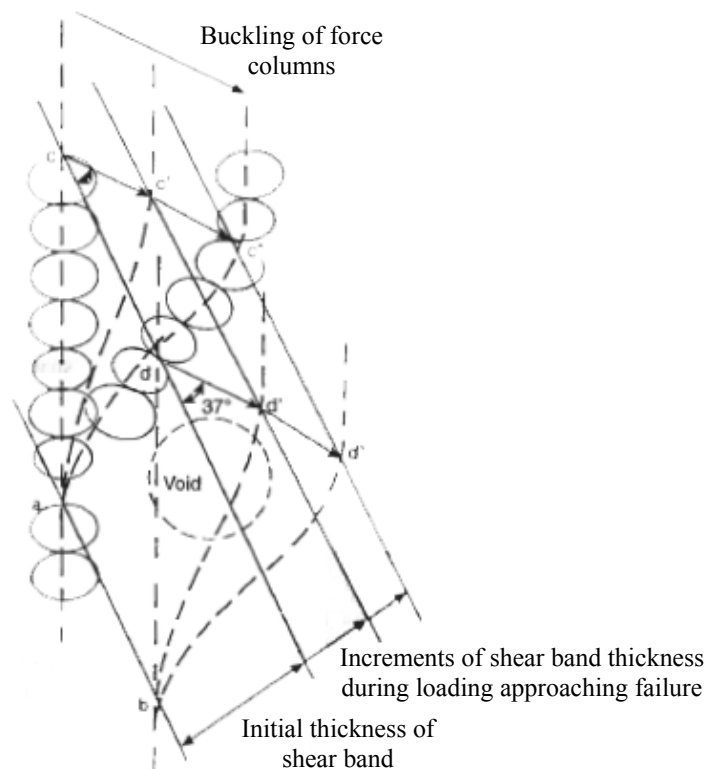


Figure 2-12 Model of microdeformation mechanism of dilatancy in a shear band by the combination of buckling of columns and particle rotations during loading approaching failure (after Oda and Kazama, 1998)

Figure 2-13 illustrates an aging mechanism via particle rotation as hypothesized by Bowman and Soga (2003). They explain that strong force chains are initially

supported by nearby weak force networks. Some particles in the weak force networks begin to rotate when the contacts are at or exceed the frictional resistance at particle contacts. If this happens, the weak force networks stop laterally supporting the strong force chains (columns), and the strong force chains (columns) buckle.

Bowman (2002) stated that *“As particles slip, this leads to the release of propped strong force network columns which buckle via particle rolling.”* At the frictional resistance of individual contacts, particles readjust themselves to minimize shear stress at the contacts. Kuhn and Mitchell (1993) write that *“As deformation proceeds during creep, particles undergo slight rearrangements that reduce the tangential components and/or increase the normal components of the contact forces.”*

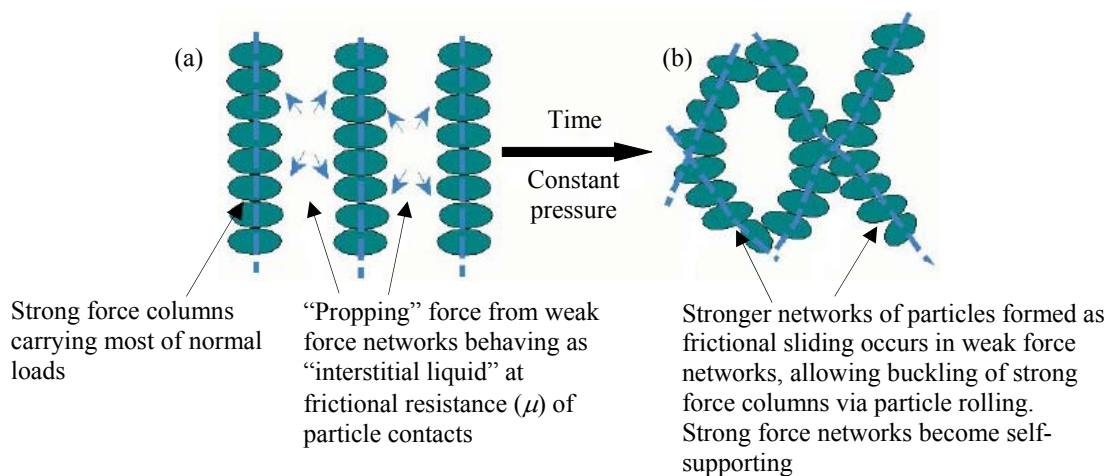


Figure 2-13 Mechanism of how strong and weak force networks may change with time via particle rotation in granular materials under loads (i.e., creep), resulting in a strong self-supporting network (after Bowman, 2002)

When particles move (i.e., rotate or translate) in the weak force networks, this results in volumetric contraction in the weak force networks and collapse of soil skeleton. The weak force networks temporarily cease to laterally support the strong force columns. Due to the disappearance of lateral supports from weak force networks, the strong force

columns may buckle, and new stronger self-supporting networks may be formed. Figure 2-13(b) shows the self-supporting networks.

From the review of literature, the study presented in this dissertation further hypothesizes that via the force chain buckling, self-supporting networks are formed as arches of particles, which occur locally and result in increases in horizontal stress in the granular assemblies. 2D granular assembly used in this present study allows the transmission patterns of force chain columns to be observed. Details of changes in patterns of force chains are discussed in Chapter 5.

For the present research, photoelasticity was employed for determining horizontal stress in granular assemblies in an attempt to find experimental evidence to test Bowman's proposed hypothesis, and to observe possible increases in σ'_h in granular assemblies.

2.6 Theory of photoelasticity

2.6.1 Polarized light

Unpolarized light consists of a stream of extremely small particles projected in all directions from a light source. The projected directions of unpolarized light can be expressed by light vectors. The light vectors represent the direction of vibration of light particles. These light vectors are perpendicular to the direction of light propagation.

Polarized light can be obtained by passing the unpolarized light through a polarization filter (or polarizer) so that light particles vibrating in the direction of the polarizing axis are allowed to pass through the polarizer. A schematic representation for obtaining the polarized light is shown in Figure 2-14. In Figure 2-14, the vertically

oriented polarizer allows the light particles to vibrate only in the vertical direction when the lights pass through (Frocht, 1946).

2.6.2 Plane and circular polariscopes

A polariscope (or polarimeter) is an instrument for observing photoelastic fringes appearing in stressed photoelastic materials. The fringe patterns are used to determine/analyze stresses in the photoelastic materials.

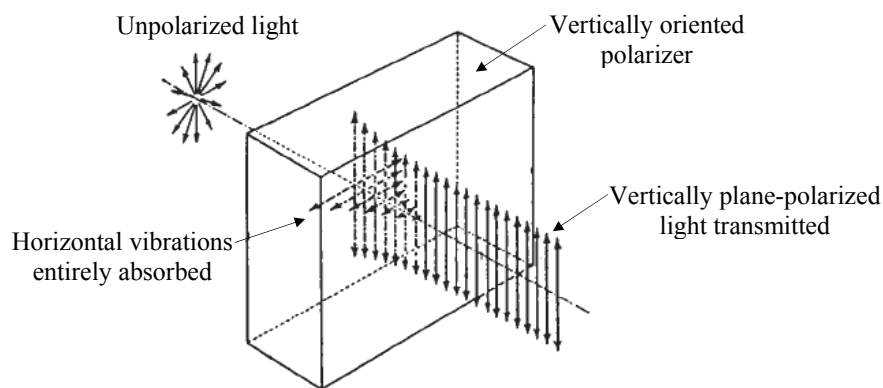


Figure 2-14 Diagram representing the production of polarized light by a polarizer (after Frocht, 1946)

A “*plane polariscope*” is the simplest arrangement for photoelastic observations. The plane polariscope consists of a light source and two linear (plane) polarizers. The first linear polarizer is placed in front of the light source to produce the polarized light. The other linear polarizer (also called an analyzer or strain viewer) is placed in front of a viewing screen (see also Figure 2-17 for locations of each component in the plane polariscope).

Generally, the polarizing axis of the analyzer is rotatable. Rotation of the polarizing axis of the analyzer produces two different fields of photoelastic observations. When the polarizing axis of the analyzer is parallel with the polarizing axis of the first polarizer, the light-field for photoelastic observations is obtained. When the polarizing axis of the analyzer is perpendicular to the polarizing axis of the first polarizer, the dark-field for photoelastic observations is achieved.

In a test, the photoelastic specimen is placed between the polarized light and the analyzer. The polarized light is used for illuminating the specimen, while the analyzer with rotatable polarizing axis is employed to view the photoelastic fringe patterns in the specimen (see Figure 2-15).

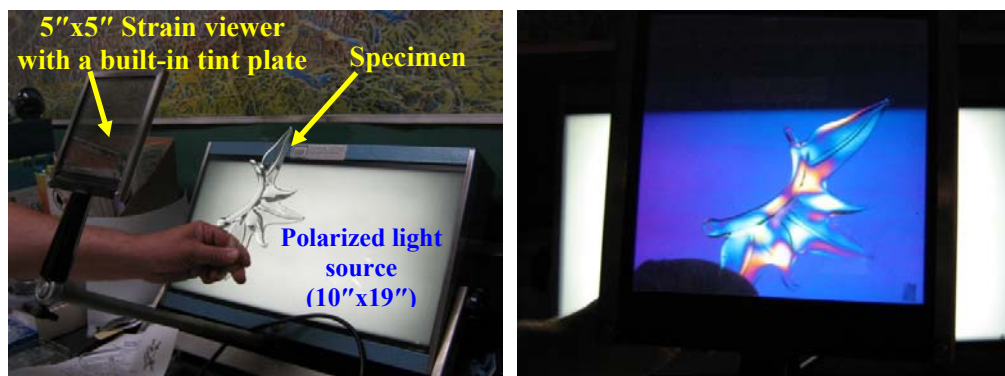


Figure 2-15 Simple setup for visually observing photoelastic fringes in a glass specimen

Colors observed in the photoelastic stressed specimens represent magnitudes of principal stress difference. Each color in the stressed specimen is quantified by a retardation (δ) value. However, the estimation of stresses from the retardation values could vary greatly. Therefore, interpretation of colors and their intensities in the photoelastic material depends greatly on the experience of the photoelastic experimentalist.

The other type of polariscope is a “*circular polariscope*” The circular polariscope consists of two polarizers. The arrangement of the two polarizers in a circular polariscope is similar to the arrangement of the plane polariscope. The first linear polarizer is placed in front of the light source to obtain polarized light. The other linear polarizer has a rotatable axis and includes a quarter wave plate. The quarter wave plate is a birefringent material that generates an additional $\frac{1}{4}$ phase difference (i.e., retardation, $\delta = \frac{1}{4}$) of the light wave (wavelength of white light, λ , is equal to 565 nm for glass according to ASTM standard). When polarized light passes through a quarter wave plate, the polarized light splits with $\frac{1}{4}$ retardation parallel to the direction of fast and slow axes of the quarter wave plate as shown in Figure 2-16. Figures 2-17 and 2-18 illustrate the arrangements of plane and circular polariscopes, respectively.

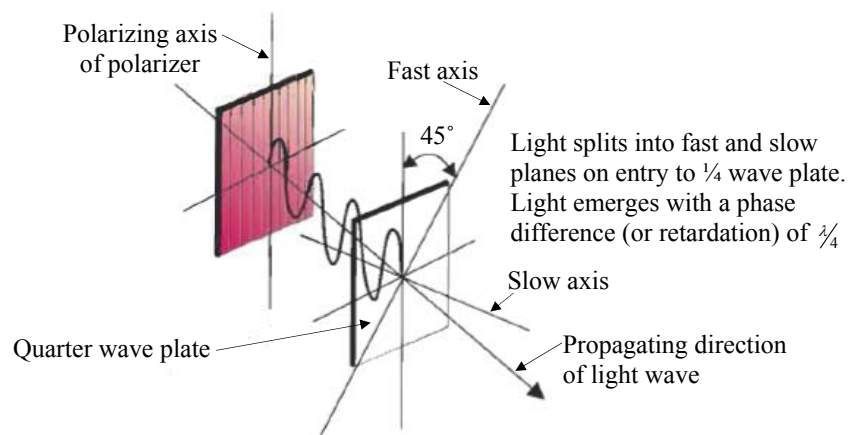


Figure 2-16 Schematic light wave transmitting through a quarter wave plate producing a phase difference (or retardation) of $\lambda/4$ (after McKenzie and Hand, 1999)

With polarized light as a source of illumination, the plane polariscope enables two different types of photoelastic fringes: isoclinics and isochromatics as shown in Figure 2-19(a). The isoclinics are the black fringes which represent the locus of points having

the same principal stress direction. The isochromatics are the photoelastic fringes with the same color bands, representing the zone of equal principal stress difference.

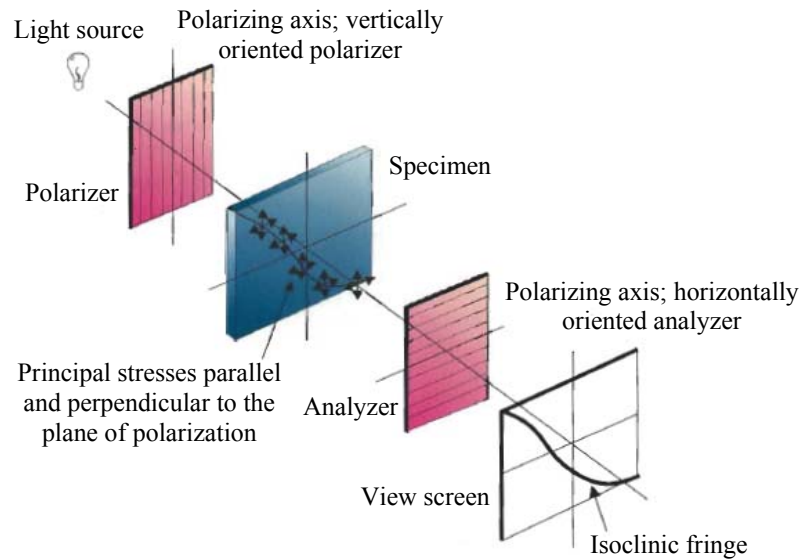


Figure 2-17 Arrangement of plane polariscope illustrating an isoclinic fringe (after McKenzie and Hand, 1999)

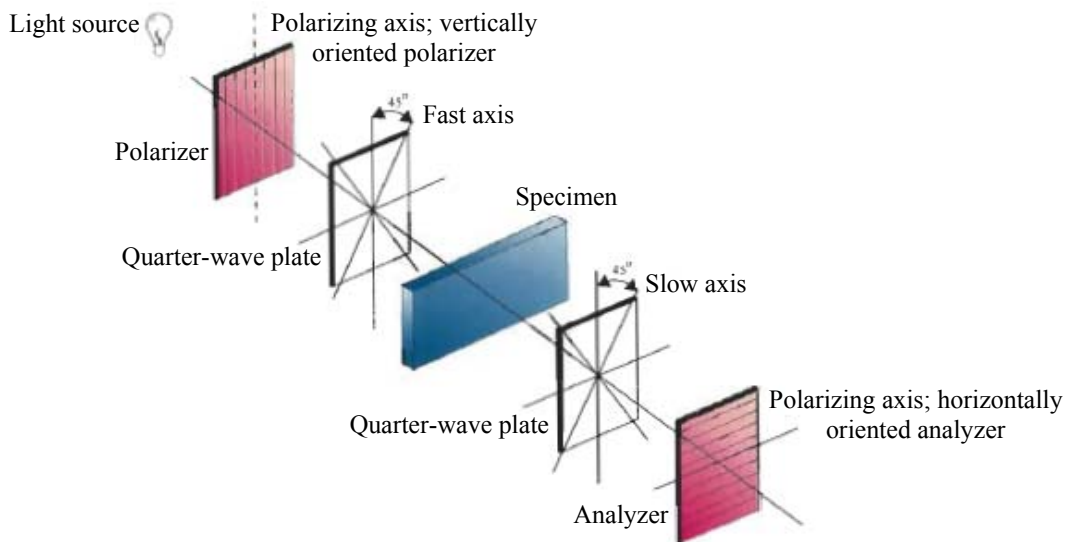


Figure 2-18 Arrangement of circular polariscope (after McKenzie and Hand, 1999)

To see the full color bands of the photoelastic fringes, the isoclinics need to be removed. A circular polariscope eliminates the isoclinics. The quarter wave plate in front of the rotatable linear polarizer in the circular polariscope removes the isoclinic fringes, thereby allowing full multicolored bands of isochromatics to be observed as shown in Figure 2-19(b).

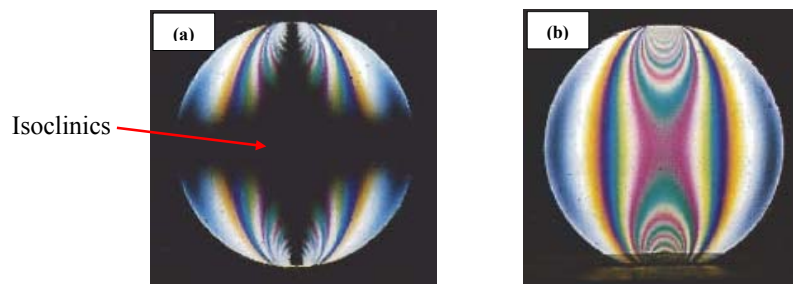


Figure 2-19 Photoelastic fringes in discs subjected to diametral compression; (a) image observed through a plane polariscope illustrating isoclinics (black band), (b) image observed through circular polariscope (isoclinics removed) (McKenzie and Hand, 1999)

2.6.3 Double refraction (birefringence)

Double refraction or birefringence (definition quoted from wikipedia.com) is “...the decomposition of a [ray of light](#) into two rays when it passes through certain types of material...” When transparent materials such as glass are subjected to stresses, they behave as doubly refractive (birefringent) materials. In Figure 2-20, when polarized light enters the double refractive materials, the polarized light splits into two directions. They are perpendicular to each other and correspond to the directions of major (σ_1) and minor (σ_2) principal stress. The two components of the light wave travel at different velocities, thereby developing a retardation or phase difference (δ) between them as shown in Figure 2-20 (Frocht, 1946; Hendry, 1948; Allersma, 1987; Aben and Guillemet, 1993; McKenzie and Hand, 1999; Allersma, 2005). The retardation of the light wave can be

calculated by Eq. (2-1). According to the stress-optic law, the difference in magnitudes of σ_1 and σ_2 can be calculated using Eq. (2-2).

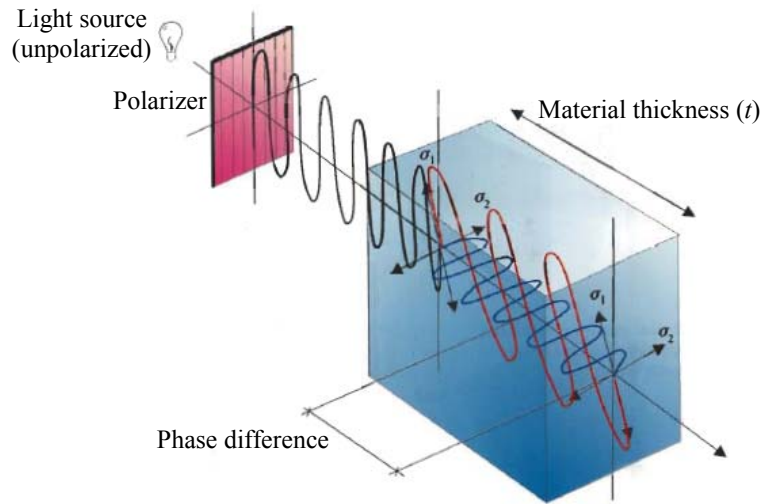


Figure 2-20 Light wave behavior entering and passing through a double refractive material (after McKenzie and Hand, 1999)

$$\delta = N\lambda \quad (2-1)$$

$$|\sigma_1 - \sigma_2| = \frac{\delta}{tC_B} \quad (2-2)$$

- Where
- σ_1 = Major principal stress in the stressed material (in MPa)
 - σ_2 = Minor principal stress in the stressed material (in MPa)
 - t = Material thickness (in mm)
 - C_B = Photoelastic constant (in Brewster; 1 Brewster = 10^{-6} MPa $^{-1}$)
 - δ = Retardation of light wave (nm); $\delta = N\lambda$
 - N = Fringe order
 - λ = Wavelength of white light (nm) (565 nm in glass according to ASTM standards)


The unit “Brewster” for the photoelastic constant (C_B) was initially proposed by Filon in 1912 for recognition of Sir David Brewster who discovered the double refraction of a glass plate under compressive stress. Details of the discovery of photoelastic properties of glass can be found in Brewster (1816). Jessop and Harris (1949) summarized that the photoelastic constant of glass varied between 2 and 4.5 Brewsters. For borosilicate glass (Pyrex[®]), the photoelastic constant is 2.93 (McKenzie and Hand, 1999).

2.6.4 Compensator (tint plate or full wave plate)

A compensator is an optical device that is used conjunction with a polariscope to qualitatively observe photoelastic colors or fringe patterns in photoelastic stressed materials. These colors are used as guidelines for the estimation of retardation values in regions of interest in the stressed specimen. Therefore, the principal stress difference in these regions can be calculated. This research used a full wave plate (Strainoptics RP-100 tint plate) along with a Strainoptics A-100 analyzer (see Figure 3-10 for the Strainoptics A-100 analyzer and RP-100 tint plate).

Mckenzie and Hand (1999) recommended that the tint plate be used for retardation measurement. When the retardation value to be evaluated is small, the tint plate is recommended to be used in conjunction with the polariscope so that difference of colors in photoelatic materials is better distinguishable. The tint plate produces one additional fringe order of retardation in a similar way with the use of a quarter wave plate. When a tint plate is not used, zero retardation begins with black color. When a tint plate is used, zero retardation starts with violet. With the tint plate, color changes are easily observable with changes in applied boundary stress. Figure 2-21 shows

photoelastic fringes with corresponding retardation and principal stress difference in stressed borosilicate glass (Pyrex®).



Colors	Retardation (δ), in nm		Fringe order (N)	$ \sigma_1 - \sigma_2 $	
	no tint plate	with tint plate		MPa	psi
Black	0	565	0	61	8809
Gray	150	450	0.28	48	7016
White-yellow	250	300	0.45	32	4677
Yellow 300	300	250	0.60	27	3898
Orange (dark)	450	100	0.79	11	1559
Red	500	50	0.90	5	780
Violet	565	0	1	0	0
Blue	600	50	1.05	5	780
Blue-green	650	100	1.14	11	1559
Green-yellow	750	220	1.32	24	3430
Yellow 850	850	300	1.50	32	4677
Orange	950	400	1.67	43	6236
Red	1050	480	1.84	52	7484
Violet	1130	565	2	61	8809
Green	1300	735	2.33	79	11459
Green-yellow	1400	835	2.50	90	13019
Pink	1500	935	2.67	101	14578
Violet	1695	1130	3	121	17618
Green	1750	1185	3.10	127	18475

Figure 2-21 Color sequences produced in dark-field circular polariscope, corresponding retardation (δ) values and principal stress difference $|\sigma_1 - \sigma_2|$ of borosilicate glass; using Eq. 2-2 to calculate $|\sigma_1 - \sigma_2|$ by assuming $C_B = 2.93$ Brewsters and $t = 0.125$ in (3.175 mm) (Courtesy: Strainoptics, Inc.)

The author notes that although photoelasticity is an excellent method for experimental stress analysis, the colors in photoelastic stressed materials do not reveal the signs of stress (i.e., tension or compression). The experiences of the experimentalists with use of the tint plate and knowledge of basic mechanics of materials are necessary for the interpretation and analysis of experimental photoelasticity results. This present study

employed photoelasticity with use of glass plates as force sensors for determining horizontal stress in 2D granular assemblies as discussed in Chapters 4 and 5.

CHAPTER III

TESTING MATERIALS AND TEST APPARATUS

This chapter presents an overview of the preparation of testing materials (glass particles), and describes the test apparatus.

3.1 Introduction

This research used 2D granular assemblies of glass particles to simulate an assembly of sand grains. The selected material is borosilicate glass (Pyrex[®]). Glass possesses photoelastic properties, i.e., it is a birefringent materials. Also, borosilicate glass (Pyrex[®]) is inert to chemical reactions. Chemists use it for laboratory glassware.

Besides the glass particles, this research used square (1"x1") glass plates with a central opening (see Figure 4-8) as photoelastic force sensors for determining horizontal stress in 2D granular assemblies.

In this study, colors of light in digital images of the photoelastic stressed glass were separated into their constituent red (*R*), green (*G*) and blue (*B*) components. By comparison to the other two colors, changes in red intensity were found to be the most sensitive to change in applied stress, as discussed further in Chapters 4 and 5. The red intensity (*R*) was therefore used to quantify stress changes during the development,

calibration and application of the photoelastic sensors for determining horizontal stress in 2D granular assemblies.

3.2 Facilities for preparing the glass particles

This section describes the facilities and processes that were used to prepare the glass particles. The facilities listed below are available in the College of Engineering:

- UV light panel and UV light curing adhesive (CHE Department)
- Diamond saw (CHE Department)
- LECO polishing machine and associated holding frame (MSE Department)
- High temperature oven (CHE Department)

UV light panel and UV light curing adhesive

In the preparation of glass particles, Dymax UV light curing adhesive (see Figure 3-1a) was used to glue together glass rods/plates before cutting. The adhesive bonds and hardens quickly within a few minutes by placing it on a UV light panel as shown in Figure 3-1(b).

Diamond saw

The diamond saw, shown in Figure 3-2(a), was used to cut the glass rods and/or the glass plates into the glass particles in the shapes of cylinders and angular prisms. As shown in Figure 3-2(b), during manufacturing of the glass particles, a cutting template was used to ensure that the particles' faces and edges were perfectly perpendicular.

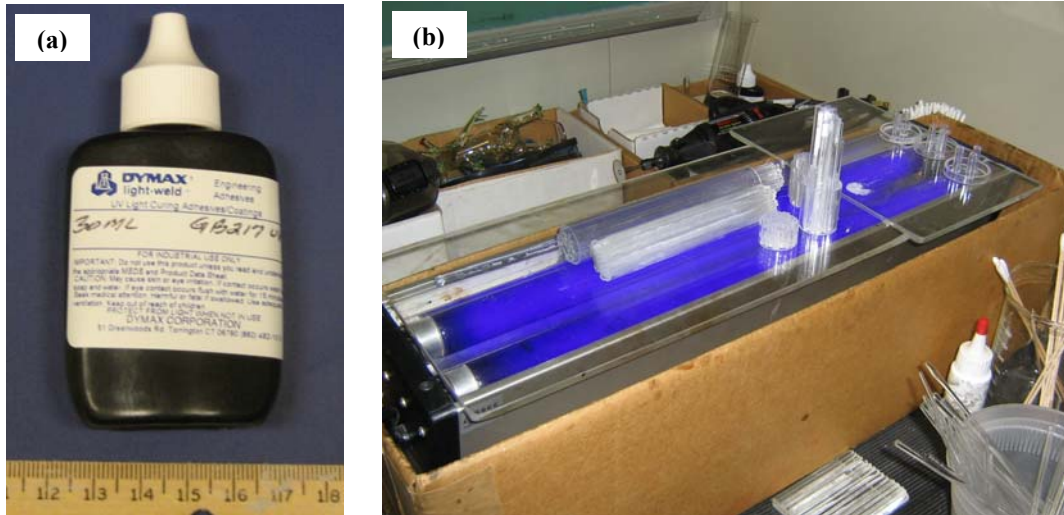


Figure 3-1 (a) Dymax UV curing adhesive and (b) UV light for curing the adhesive

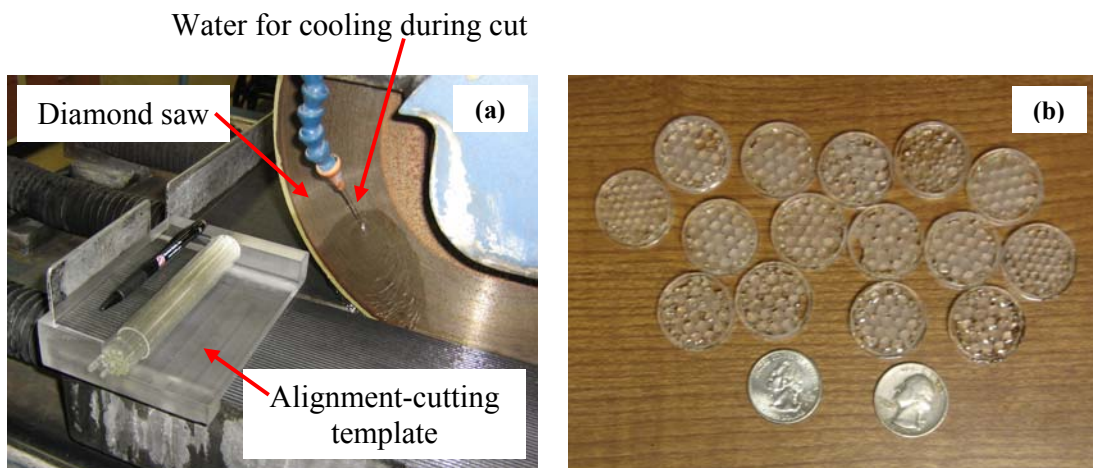


Figure 3-2 (a) Glass rods to be cut using the alignment-cutting template incorporation with the diamond saw (b) glass particles after cutting

LECO polishing machine

A LECO polishing machine is available in the MSE department. The cut particles were assembled into aluminum plate holders as shown in Figure 3-3. The aluminum holders were manufactured to be mounted into the holding frame to facilitate polishing. Figure 3-4 shows the setup of the holding frame mounted to the machine for polishing.

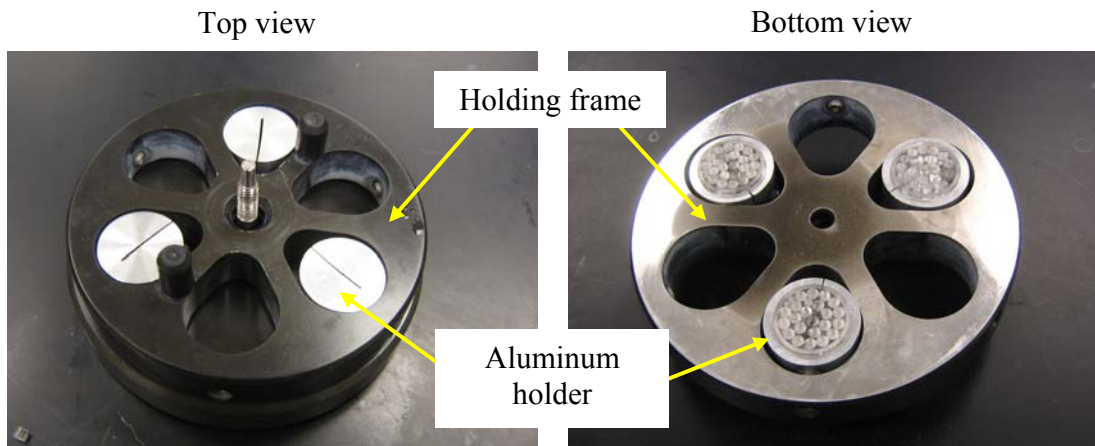


Figure 3-3 Glass particles assembled to a holding frame for polishing

High temperature oven

After cutting and polishing, the glass particles were put into to a high temperature oven (see Figure 3-5). The oven temperature was more than 500 °C. This high temperature is required to burn off the adhesive to disassemble the particles, but it does not damage the glass particles. Finally, residual adhesive on the glass particles was washed away using acetone.

3.3 Glass particles

Figure 3-6 shows the glass particles in the shapes of cylinders and angular prisms. Three types of the glass particles were used in this research as follows.

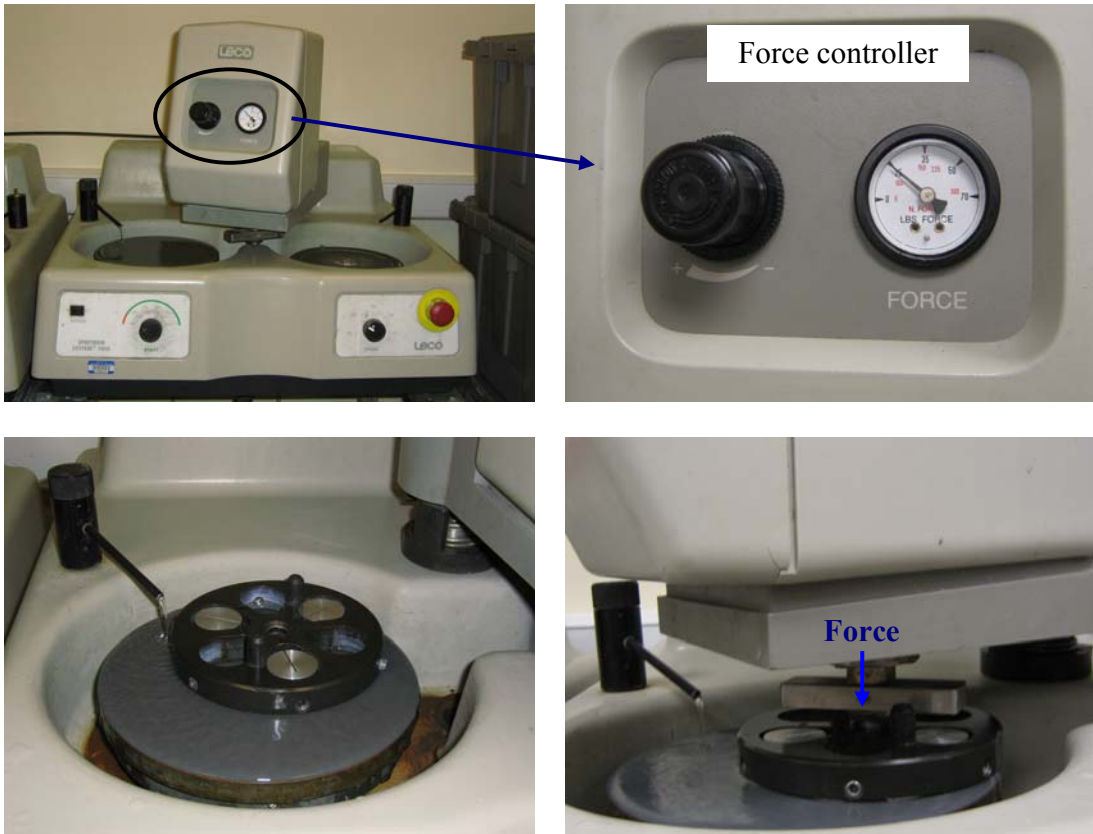


Figure 3-4 LECO polishing machine



Figure 3-5 Oven in the glass laboratory

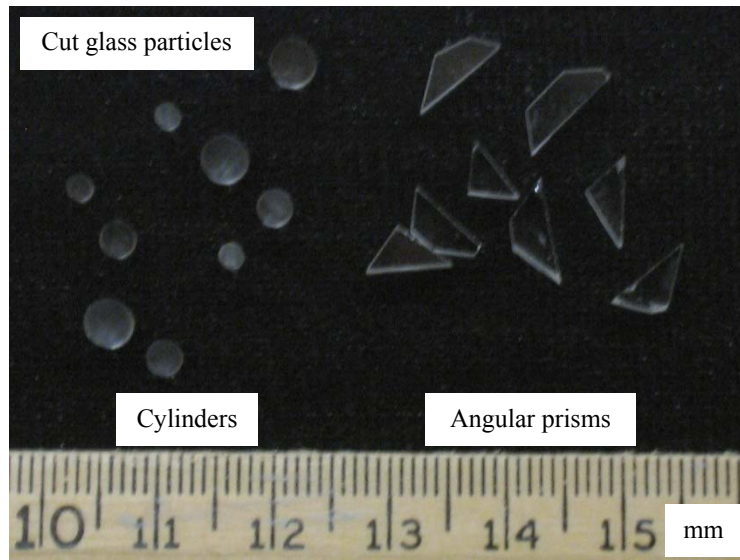


Figure 3-6 Glass particles in the shapes of cylinders and angular prisms

3.3.1 Cylindrical particles with smooth contact surfaces

Cylindrical particles with smooth contact surfaces were prepared by cutting them from commercial glass rods. The glass rods were bundled together using Dymax UV curing adhesive. For cutting, the bundled glass rods were placed on the alignment-cutting template to obtain $\frac{1}{8}$ " thick glass cylindrical particles. The diameters of the glass cylinders were 2 mm, 3 mm, and 4 mm.

3.3.2 Cylindrical particles with rough contact surfaces

To obtain cylindrical particles with rough contact surfaces, glass rods were rubbed with sand papers prior to cutting. After obtaining glass rods with rough surface, the cutting proceeded as described in Section 3.3.1.

3.3.3 Angular prism particles with rough contact surface

A $\frac{1}{8}$ " glass pane was placed on the alignment-cutting template and cut to obtain angular prism glass particles with rough contact surface.

3.4 Test apparatus and hardware components

The setup of the test apparatus for the research project is shown in Figure 3-7. The test apparatus was installed in the Geotechnical Engineering Laboratory (also known as F.E. Richart Soil Dynamics Lab) at the University of Michigan.

3.4.1 Test apparatus

The test apparatus was mounted on a 4-ft long I-Beam (WF6x6x0.23 in). The end of the I-Beam was attached to the wall, and the other end was welded to a vertical steel square tube (4in sq x 0.25in wall tubing). The bottom end of the square tube is placed on the floor. An unslotted strut channel was welded on the top of the beam. The polarized light source was mounted on the wall for illuminating the photoelastic specimens in the test box.

A steel holder was designed to attach with optical hardware components (i.e., Nikon D300 digital camera, Strainoptics A-100 analyzer, and RP-100 tint plate). The steel holder was mounted to the strut channel that was welded on the top of the I-beam. On the strut channel, the steel holder with attached optical hardware components was designed to allow for variable distances between the specimen and optical hardware.

The digital camera was connected to the controlling computer using a USB cable. With this USB interface and the software Nikon Camera Control Pro version 2.0, the

digital camera was controlled from the PC to capture and store photos of the stressed specimens and sensors.

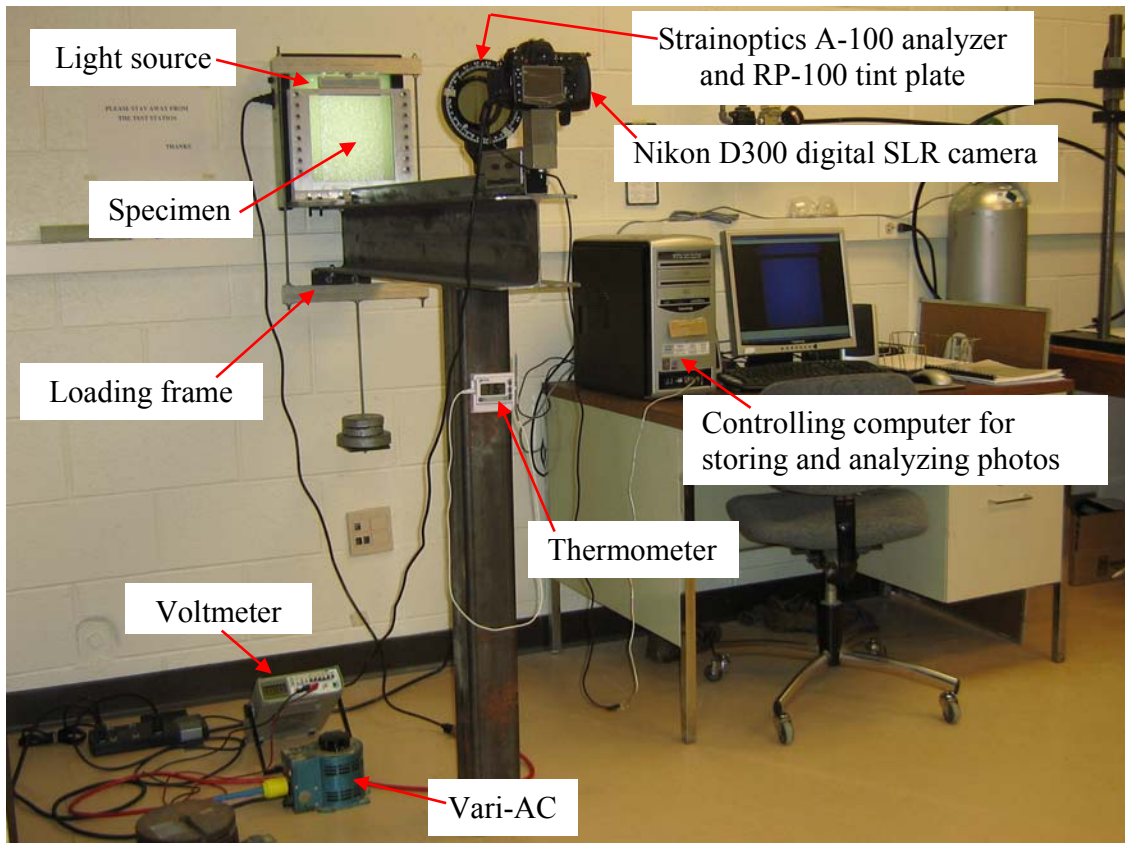


Figure 3-7 Test apparatus used for the research project

3.4.2 Hardware components

This section describes the hardware components in the test apparatus. Figure 3-8 shows the schematic diagram of the photoelastic system for obtaining, recording, and analyzing the photos of specimens. Functions of each component in the apparatus are described in this section. The hardware components in the apparatus are:

- Test box and loading frame
- Light source and set of power supply controllers (UPS, vari-AC and voltmeter)
- Thermometer

- Strainoptics A-100 analyzer
- Strainoptics RP-100 tint plate
- Controlling computer
- Nikon D300 SLR Digital camera

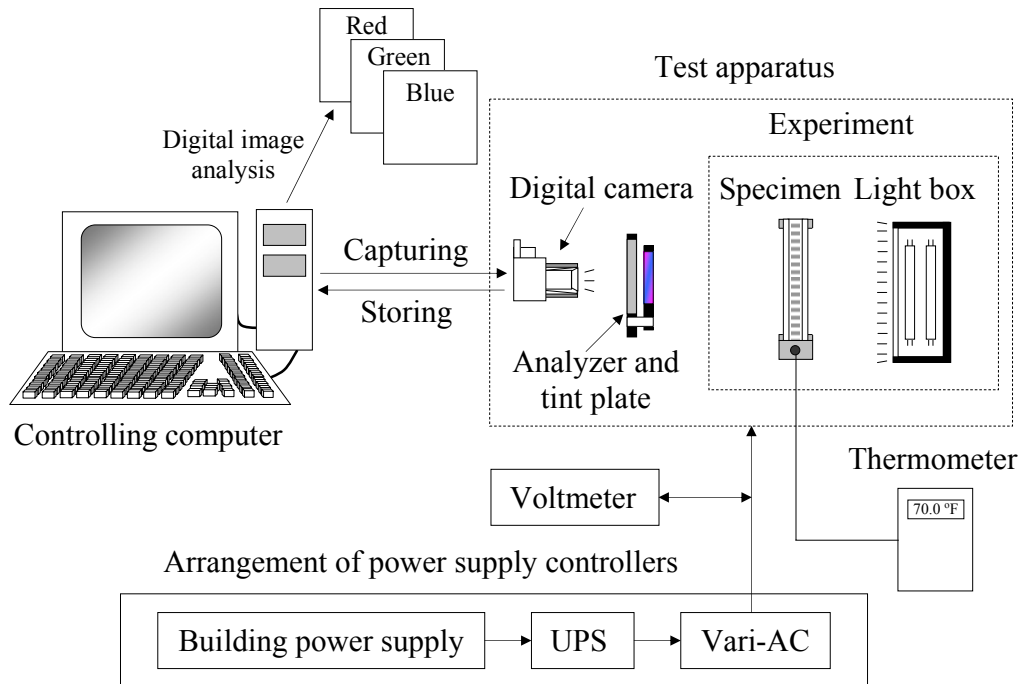


Figure 3-8 Schematic of the photoelasticity system

Test box and loading frame

Figure 3-9 shows the drawing of the test box used in this study. The test box consists of three layers of aluminum plates. Front and rear aluminum plates with 8"x8" viewing window are in the front and the back of the test box.

Between the front and rear aluminum plates is the middle layer of the test box. The middle layer of the test box is the u-shaped aluminum frame. In this middle layer, 2D assemblies of glass particles are placed. The top of the test box is open so that vertical

load can be applied to the 2D granular assemblies. The load frame, made of aluminum, was used to apply vertical loading to the 2D granular assemblies (see Figure 3-7 for the setup of a loaded specimen). To increase the applied vertical loading, weights are added to the bottom of the load frame.

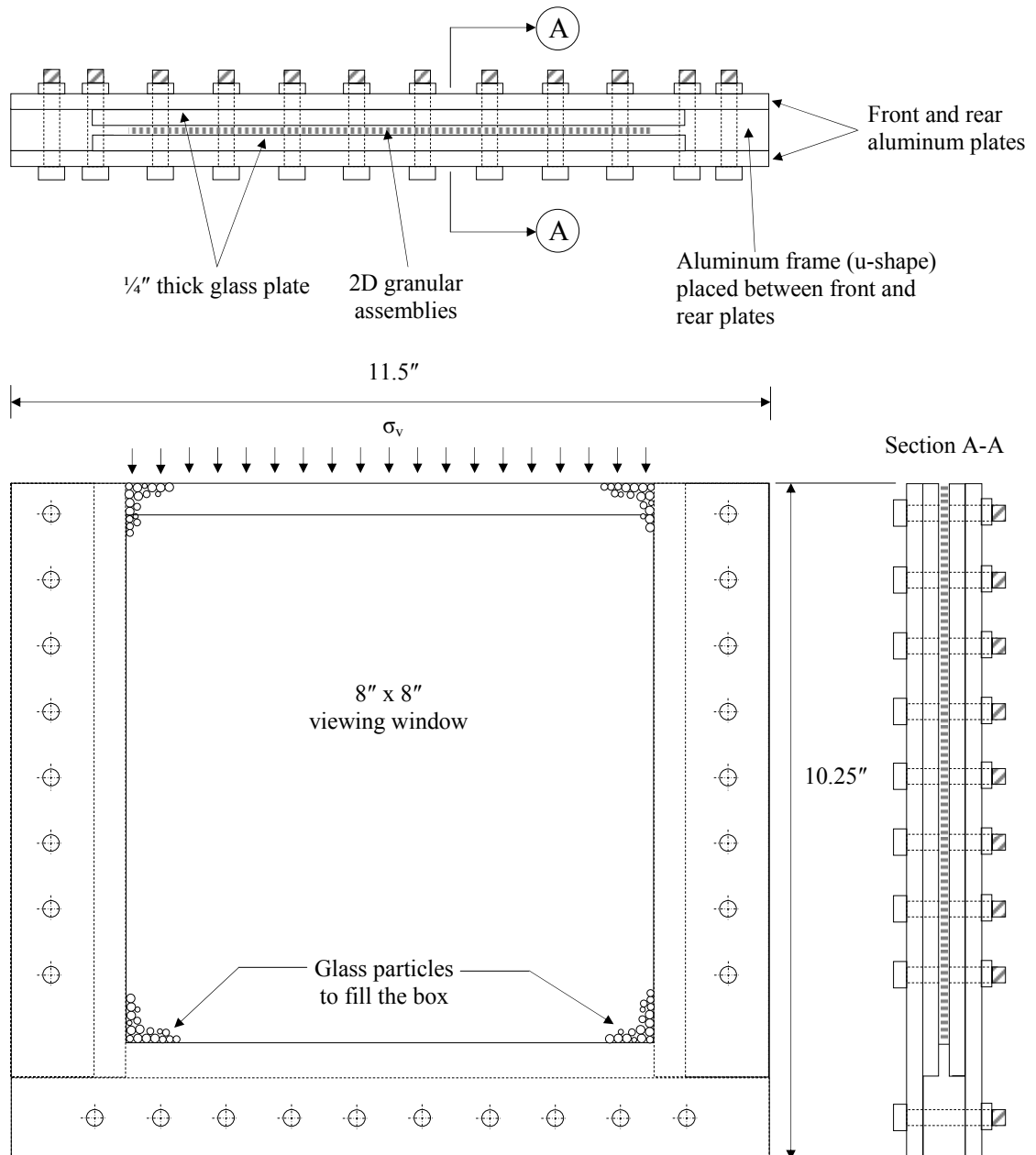


Figure 3-9 Test box

To prevent collapse of the stack of 2D granular assemblies during the tests, two ¼" thick glass plates were placed in front of and behind the granular assembly. The author also realized that light in the surrounding area of the test station influences test results. Therefore, all extraneous lights in the laboratory and at the test station were eliminated during the tests. Light in the laboratory was turned off. Black-painted plates cover extraneous light at the test station. Windows were all blocked to prevent light from entering into the laboratory.

Light source and set of power supply controllers

The light source for this research was purchased from Strainoptics Inc. The light source was placed behind the test specimens. It provides polarized light and uniformly illuminates the specimen through the viewing window of the test box.

Although the light box is designed to be directly plugged into an AC grounded outlet, slight variations in the line voltage from the building power supply were found to influence the light source intensity. Figure 3-10 shows that the red intensity of the light source itself depends on the supplied voltage.

Preliminary results of red intensity values versus temperatures presented in Chapter 4 shows that red intensity value depend significantly on the temperature in the vicinity of the measuring devices (i.e., Nikon D300 digital camera, Strainoptics A-100 analyzer and RP-100 tint plate). However, this study did not focus extensively on the effects of temperature on red intensity values. For long period testing in future research, the author recommends that the temperature in the laboratory, and in the vicinity of the measuring devices, be strictly controlled.

To minimize the effects of the supplied line voltage on red intensity, an uninterruptible power supply (UPS) was used to reduce fluctuation of electrical voltage from the building power supply. A vari-AC (voltage transformer) was plugged to the UPS to adjust the voltage that supplies the test apparatus. A voltmeter was connected between the vari-AC and the test apparatus. The voltmeter measured the voltage supplied to the system. For the study in presented in Chapters 4 and 5 of this dissertation, the supplied voltage was controlled to within a range of 120.15 ± 0.15 volts during the tests.

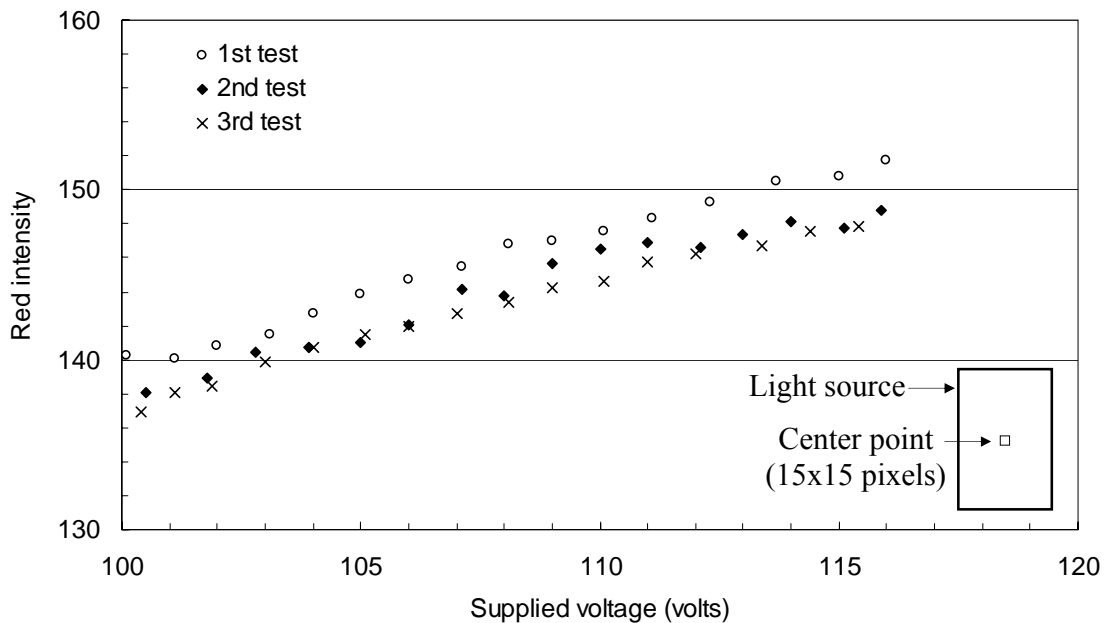


Figure 3-10 Red intensity at the center of the light source versus supplied voltage

Thermometer

An Oregon Scientific THC-138 thermometer was used in this research. The thermometer had a sensor with a 3-ft connection wire. The operating range of the thermometer is -58°F to 158°F . The resolution of the thermometer was 0.2°F .

Strainoptics A-100 analyzer

Figure 3-11 shows the Strainoptics A-100 analyzer. Throughout this research, the directional scale was set at 90°. This orientation of the polarizing axis in the A-100 analyzer is perpendicular to the polarizing axis of the linear polarizer in front of the light source. So, the circular polariscope is in dark-field observations. The dark-field observations have dark background on the light panel, thereby providing the best view for photoelastic observations.

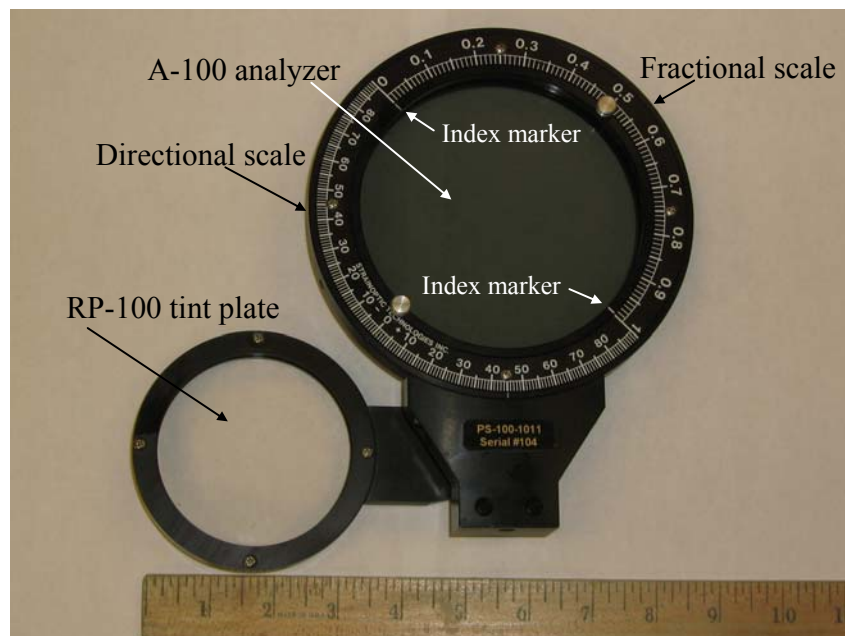


Figure 3-11 Strainoptics A-100 analyzer and RP-100 tint plate

A fractional scale, ranging from 0 to 1, is an analog readout for a fraction of the retardation (δ) of the light wave. The fractional scale provides an estimation of the retardation value, but the final photoelastic analysis and interpretation for stresses still depends largely on the judgement and experience of the photoelastic experimentalist. A rough approximation of stresses at the point of interest is obtained if the stresses are

estimated using the fractional scale. Instructions for the use of the fractional scale can be found in the instruction manual from Strainoptics, Inc. via www.strainoptics.com.

To overcome the lack of precision of the fractional scale, this research used digital image processing for obtaining intensities of light colors, and for analyzing photos of specimens. The digital image processing technique is described in Section 3.5.

Strainoptics RP-100 tint plate

The Strainoptics RP-100 tint plate (or a full wave plate) works in a similar way as a quarter wave plate. It provides additional phase difference (retardation) of one wavelength of the light wave. In other words, when the tint plate is used to view the photoelastic specimens, one additional fringe order is added, and it qualitatively provides a better view of difference in colors in the photoelastic materials. The tint plate should be used especially when the retardation to be evaluated is small in order to better differentiate colors in the photoelastic stressed material.

Controlling computer

The processor of the controlling personal computer (PC) was an Intel Pentium 4 Processor 530 (3.0 GHz, 800MHz FSB, 1MB L2). The controlling PC had 1024 MB DDR dual channel with approximately 200 GB of hard drive storage and 17 inch LCD color flat panel monitor. The software; Nikon Camera Control Pro version 2.0 and Matlab 7.4 (R2007a), were used. Nikon Camera Control Pro version 2.0 controlled the digital camera for capturing photos of specimens and transferred the photos to the PC. Digital image processing in Matlab 7.4 (R2007a) was used to analyze the photos of specimens for color intensities.

Digital camera

A Nikon D300 SLR digital camera was used in this research. The maximum camera resolution is 2848x4288 pixels. The lens was Nikon AF-S 60 mm f/2.8 macro lens. An aperture f/10 was used, and the exposure time (shutter speed) of the camera was set at 0.625 second. Figure 3-12 shows the user interface of the Nikon Camera Control Pro version 2.0 and setting throughout the research project.

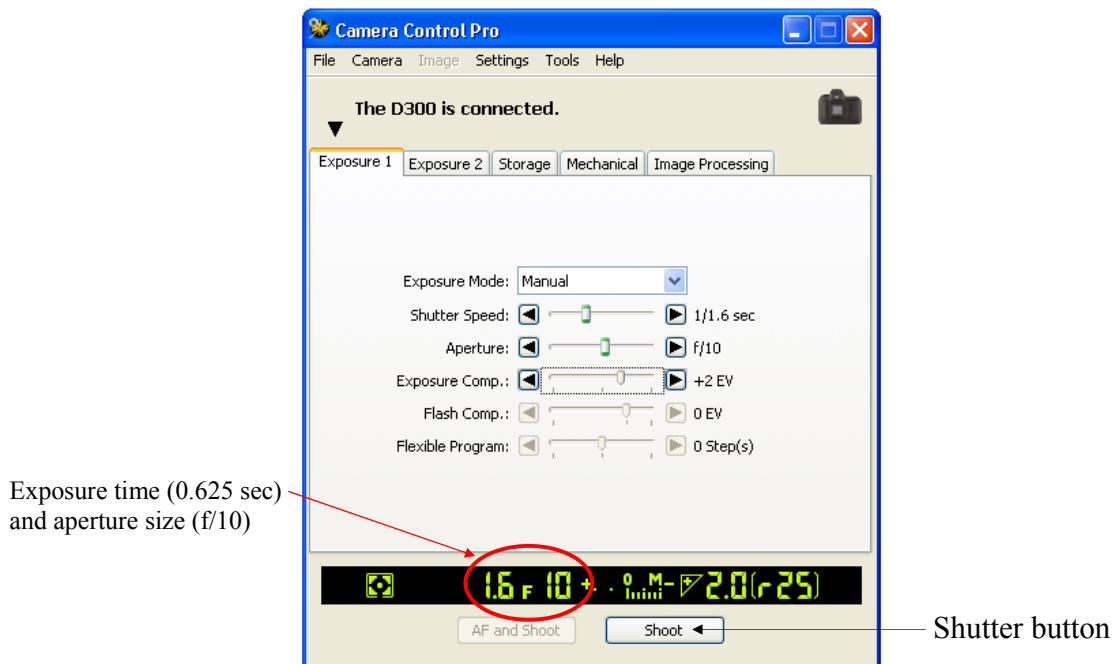


Figure 3-12 User interface of Nikon Camera Control Pro version 2.0

3.5 Digital image processing

With the advent of modern color charged-coupled device (CCD) cameras and digital image processing technology, digital photos with true colors can be easily captured and digitally recorded. The true colors in digital photos consist of three colors on three independent planes: red (*R*), green (*G*) and blue (*B*). Digital image processing

provides the R , G , and B intensities in the regions of interest from photos of the specimens.

Figure 3-13 presents the procedure for obtaining color intensities from digital photos. The digital photos are imported into the image processing tool in Matlab 7.4 (R2007a). Three independent matrices for the R , G and B intensity values are produced. Each element in the matrices represents the intensities of red, green and blue in each pixel of the photos. The intensity values of R , G and B are integers between 0 and 255. This is the maximum and default color resolution of the Nikon D300 SLR digital camera.

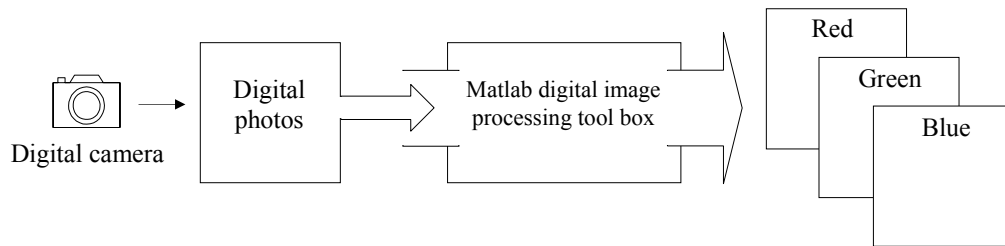


Figure 3-13 Procedure for obtaining three independent matrices of R , G and B intensities

In this study, the color intensities are calibrated versus stresses in the photoelastic stressed materials. To quantify stresses from R , G , and B intensities, calibration curves relating color intensities at key pre-selected points to applied vertical stress are established.

CHAPTER IV

CALIBRATION OF GLASS PLATE PHOTOELASTIC SENSORS

4.1 Introduction

Photoelasticity is a well-known method for measuring stresses in transparent materials by passing polarized light through it. Stresses are most often determined from the analysis of photoelastic fringes. The retardation or phase difference (δ) of light waves is estimated from the photoelastic fringes. The retardation value is used to calculate the in-plane principal stress difference ($\sigma_1 - \sigma_2$) at points of interest in the stressed transparent material.

This chapter presents the calibration of glass plate photoelastic sensors. The relations between applied stress (σ) and R , G , B intensity values are presented in the subsequent sections of this chapter. Based on test results from this preliminary study, the “*relative red intensity* (R_{rel} or $R_o - R_\sigma$)” is introduced as the parameter that would be used to track changes in the applied stress to the glass plates. Calibration charts relating relative red intensity and applied stress are presented in this chapter.

4.2 Experimental setup

The test apparatus and associated hardware were presented previously in Chapter 3 (see Figure 3-7). During the tests, all lights in the laboratory were turned off to ensure that illumination came only from the polarized light source used in this study.

It was realized that the lights and the digital camera are very important components for photoelastic experiments. Image sensors (i.e., digital imager or CCD) in the camera body is sensitive to the amount of light that strikes it. Therefore, the same aperture size (f/10) and exposure time or shutter speed (0.625 sec) were set throughout the project.

It was also realized that excess light from the polarized light source itself could cause variations in color intensities captured in the images. The term “excess lights” means the extraneous light may be captured by the camera when taking photos of the photoelastic specimens as shown in Figure 4-1. Therefore, all possible light reflections and surrounding lights from the light source were eliminated during the test. The elimination of the surrounding lights was achieved as shown in Figure 4-1. In addition, Figure 4-2 shows a thin flat black aluminum plate used in conjunction with photoelasticity test apparatus. The thin black plate has pin holes in locations corresponding to the regions of interest in which stresses were to be measured. This additionally reduced variations in light color intensity during the tests.

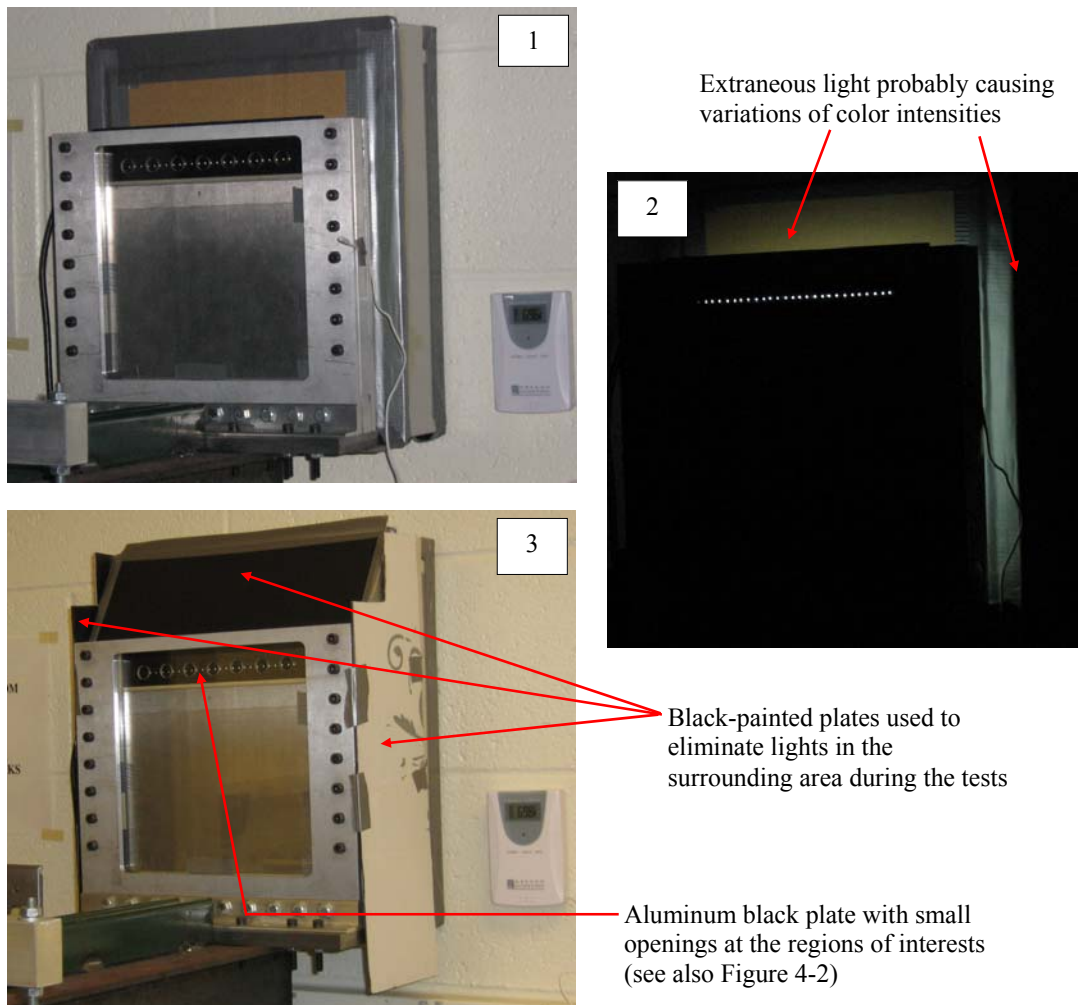


Figure 4-1 Test setup with light eliminated at the surrounding area of the test station

4.3 Results and discussions

4.3.1 Color intensities in a 6 mm x 6 mm stressed glass plate

In the earliest tests, uniaxial loads were applied to a 6 mm x 6 mm glass plate. The plate thickness was 3.175 mm ($\frac{1}{8}$ "). This glass plate thickness is the same as the thickness of 2D granular assemblies and the thickness of glass plate sensors.

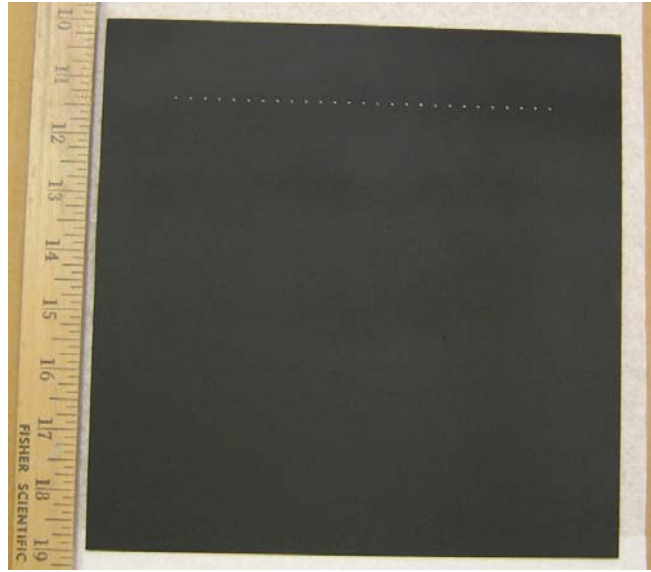


Figure 4-2 Thin black aluminum plate with small openings at the regions of interests

Figure 4-3 shows the test setup with the 6 mm x 6 mm glass plate. In this background study, the vertical stress was gradually increased from 0 to 875 psi. After applying each vertical stress increment, digital photos of the stressed glass plate were taken. Digital photos of the stressed glass were imported into a digital image processing program in Matlab 7.4 (R2007a) to obtain R , G , B intensities. As shown in Figure 4-3, a 1 mm x 1 mm central zone of the stressed glass was monitored for the average R , G , B intensity values.

Plots of R , G and B intensities versus applied vertical stress are shown in Figure 4-4. Figure 4-4 shows that the red (R) and green (G) intensity values change with changes in applied vertical stress, but the blue (B) intensity remains constant with changes in the applied vertical stress.

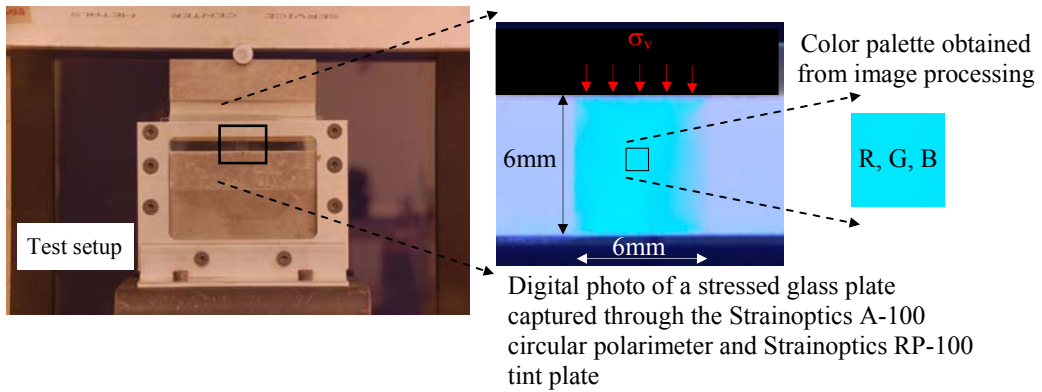


Figure 4-3 Test setup with the 6 mm x 6 mm glass plate

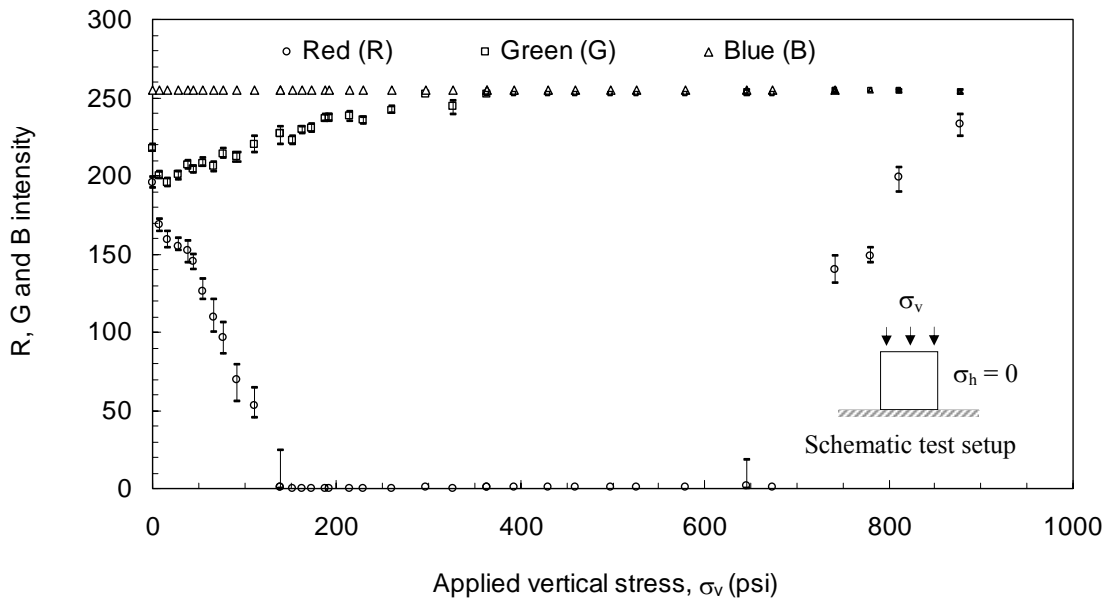


Figure 4-4 Applied vertical stress versus R , G , B intensity values from the central zone (1 mm x 1 mm) of 6 mm x 6 mm glass plate.

For vertical stress increasing from 0 to 140 psi, the red intensity decreases while green intensity increases. For increasing vertical stress beyond 140 and upto 400 psi, the red intensity is constant while green intensity continues to increase. For changes in the applied vertical stress between 360 and 740 psi, there is no detection of changes in R , G and B intensities. For applied vertical stress from 740 psi to 875 psi, the red intensity

increases, but the intensities of the other two colors (i.e., green and blue) do not change. Figure 4-5 shows the applied vertical stress with corresponding *R*, *G*, and *B* intensities obtained from the digital image processing in Matlab 7.4 (R2007a).

For this research, the range of expected applied stresses (to the top of the sensors) was approximately between 0 and 40 psi. Figure 4-4 shows that in this stress range from 0 to 40 psi, *R*-intensity drops rapidly, *G*-intensity gradually increases, but the *B*-intensity remains constant.

Figure 4-4 suggests that *R*- and *G*- intensities can be used to track changes in applied vertical stress on the glass plates. However, for the same increment of applied stress, the decrease in *R*-intensity is much larger than the increase in *G*-intensity. In other words, red intensity is more sensitive to changes in the applied stresses between 0 and 40 psi as compared to green and blue intensities. Therefore, change in *R*-intensity is the parameter used to track changes in stress in the photoelastic sensors as discussed further in Sections 4.3.2 and 4.3.3.

4.3.2 Calibration of the glass plate photoelastic sensors

This section discusses test results from the calibration of glass plate photoelastic sensors. Every glass plate sensor has a central hole as shown in Figure 4-6. The dimensions of the glass plate sensors were 1" x 1". The plate thickness was $\frac{1}{8}$ ". The diameter of the hole was 0.5". After calibration, the glass plates from this section were used as force sensors for determining horizontal stress in the 2D granular assemblies.

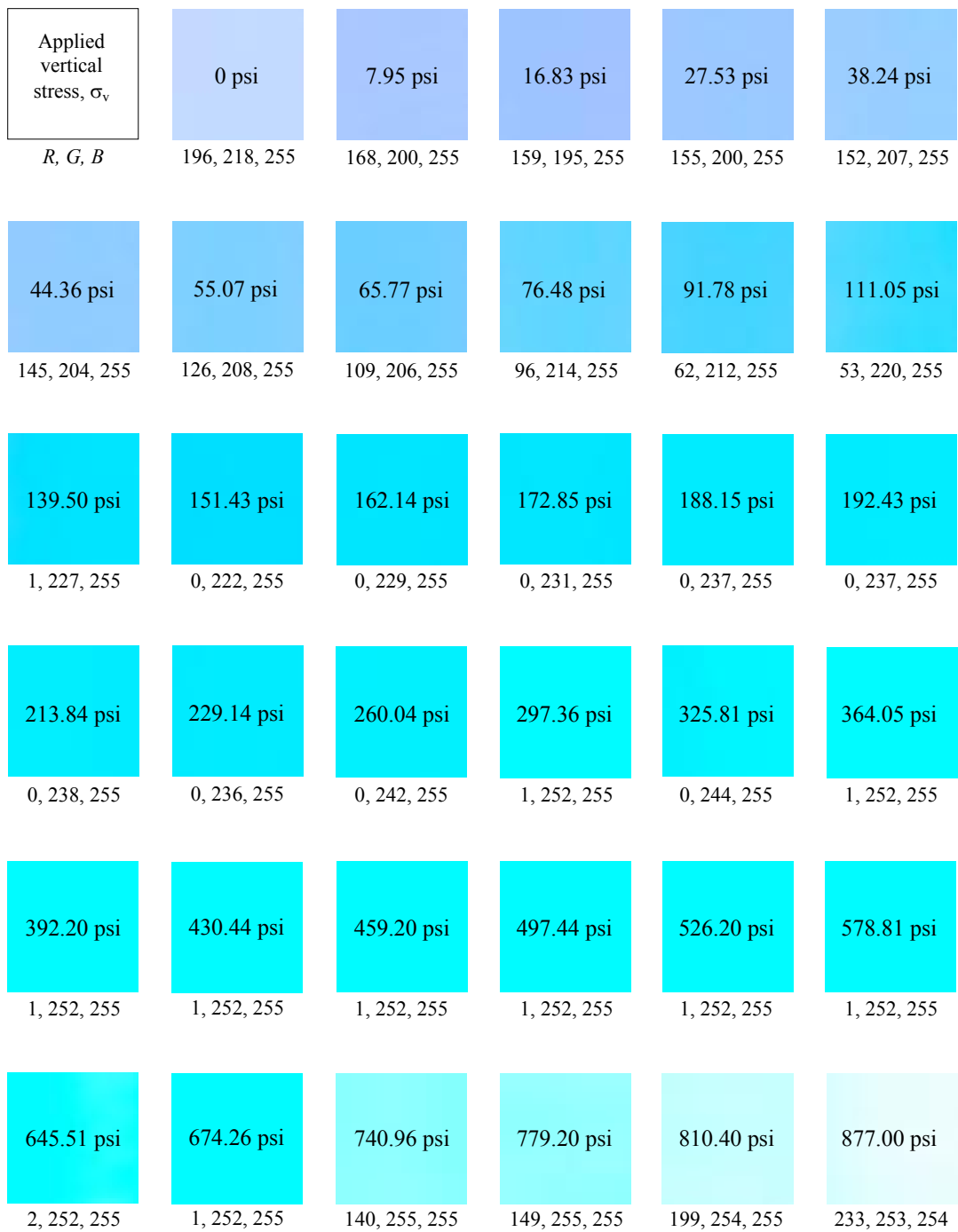


Figure 4-5 Applied vertical stress and corresponding *R*, *G* and *B* intensities from the central zone (1 mm x 1 mm) of 6 mm x 6 mm glass plate

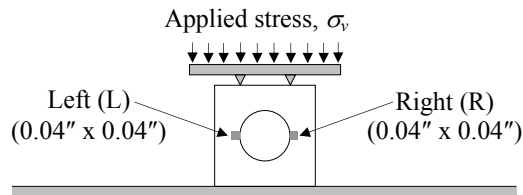


Figure 4-6 Glass plate sensors and schematic test setup for the calibration

The central hole in the glass plate sensors was made to induce stress concentrations around the perimeter of the hole. This increases the resolution of stress changes through changes in the red intensity value. In other words, strains around the central hole are higher than they would be in a glass plate with no hole.

From the theory of elasticity, the stress concentration at the two critical points on the perimeter of the hole in the stressed glass is 3.0. An aluminum bridge with two sharp edges was attached on the top of the glass plates. The two edges of the aluminum bridge were directly above the left and right sides of the central hole (i.e., points L and R). Points L and R are the regions where the red intensities were monitored to track changes in the applied vertical stress. The bridge focused greater loads to the L and R points, and thus enhanced the resolution of stress through greater induced change in the red intensity values.

In the preliminary study discussed in Chapter 3, it was found that variations in supplied electrical voltage and temperature influenced the red intensity value. To minimize these effects, the supplied voltage and the laboratory temperature were controlled during the tests for developing the calibration charts. The supplied voltage was controlled within 120.15 ± 0.15 volts. The laboratory temperature was controlled in a range of 72.0 ± 0.5 °F.

In developing the calibration curves, individual glass plate sensors were vertically loaded using the load frame (see Figure 3-7). A similar test setup for the calibration of the glass plate sensors is also shown in Figure 4-3. The average red intensity from 13 x 13 pixel regions ($0.04'' \times 0.04''$) at points L and R shown in Figure 4-7 were computed.

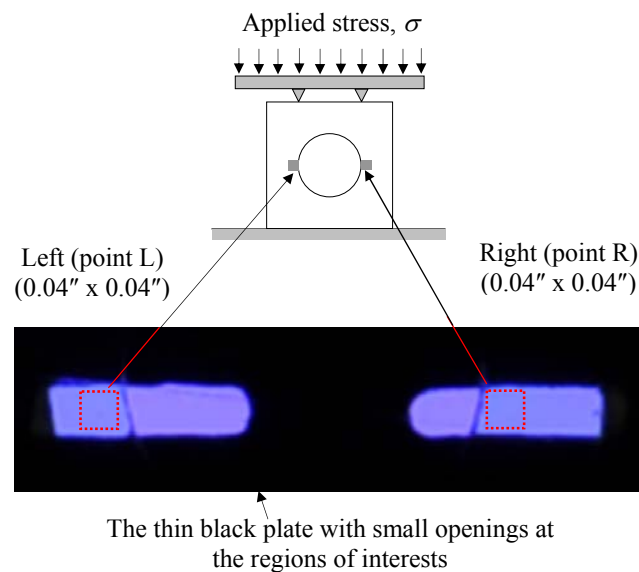


Figure 4-7 Example of an image from calibration tests

4.3.3 Calibration charts

Ten glass plate sensors were calibrated. The ten sensors were labeled S1, S2, ..., S10. After developing the calibration charts, the sensors were attached to the sidewalls of

the test box as shown in Figure 4-8. These sensors were used for determining the horizontal stress in the 2D granular assemblies as discussed in Chapter 5.

The calibration charts related the applied stress (σ) to *relative red intensity* (R_{rel}). In this study, Relative red intensity (R_{rel}) is defined as the difference between the red intensity of stress-free glass (R_o) and the red intensity of stressed glass (R_σ) at the same location. The relative red intensity is expressed by Eq. (4-1).

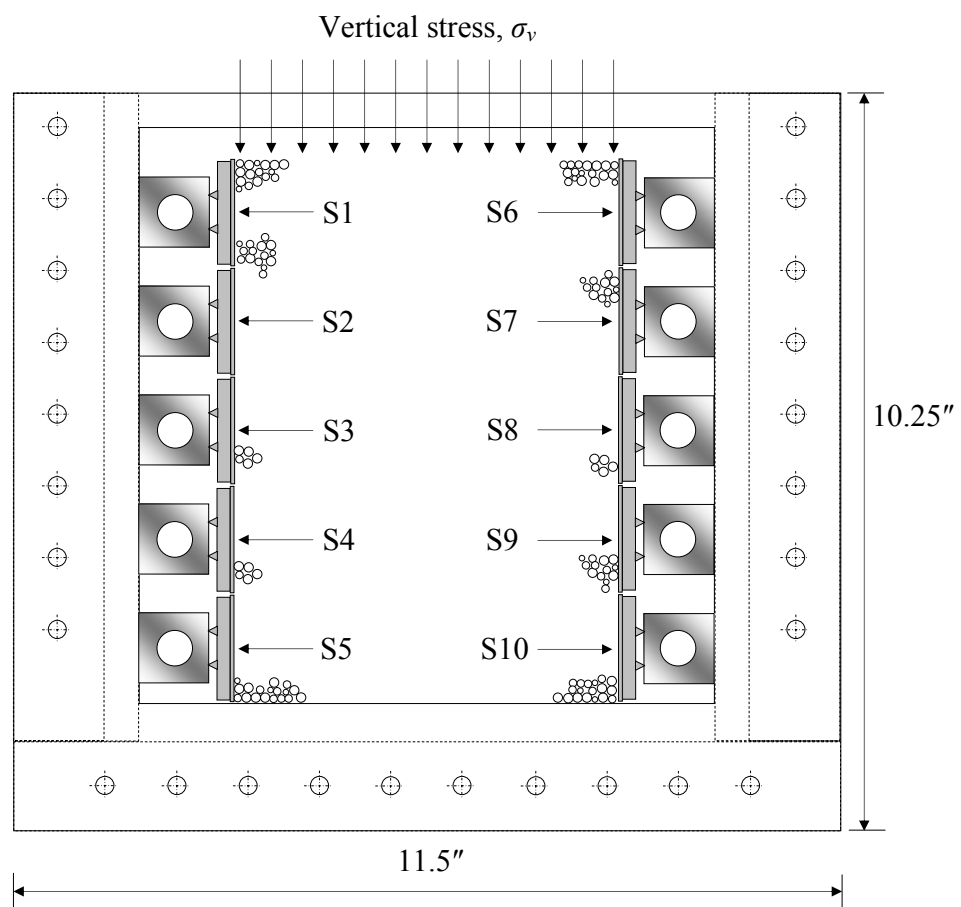


Figure 4-8 Test box attached with the glass plate sensors at the sidewalls

In the preparation of the calibration charts, values of the applied stress were normalized by atmospheric pressure ($P_a = 14.69$ psi) to obtain the dimensionless applied

stress (σ/P_a). The calibration charts (i.e., R_{rel} versus σ/P_a) for sensors S1 and S2 are shown in Figure 4-9 and Figure 4-10, respectively. The remaining charts for sensors S3 to S10 are included in Appendix A.

As may be observed in Figures 4-9 and 4-10, the relationships between R_{rel} and σ/P_a can be written in the form of quadratic equations. The general form of the equations for the calibration charts is expressed by Eq. (4-2). Conversely, the applied stress can be obtained using Eq. (4-3) when the relative red intensity is known. In Chapter 5, Eq. (4-3) will be used to convert the values of relative red intensity to horizontal stress in the 2D granular assemblies. Table 4-1 summarizes the empirical coefficients a and b for sensors S1 to S10. Graphical results with the equations corresponding to the calibration charts can be found in Appendix A.

$$R_{rel} = R_o - R_\sigma \quad (4-1)$$

$$R_{rel} = a\left(\frac{\sigma}{P_a}\right)^2 + b\left(\frac{\sigma}{P_a}\right) \quad (4-2)$$

$$\sigma = \frac{P_a}{2a} \left[-b + \sqrt{b^2 + 4aR_{rel}} \right] \quad (4-3)$$

- where
- R_{rel} = Relative red intensity (dimensionless)
 - R_o = Red intensity of stress-free glass plate (dimensionless)
 - R_σ = Red intensity of stressed glass (dimensionless)
 - a, b = Empirical coefficients in the calibration equations
 - σ = Stress applied to the top of the glass plate sensors
 - P_a = Atmospheric pressure in the same unit as applied stress, σ
 - σ/P_a = Dimensionless applied stress

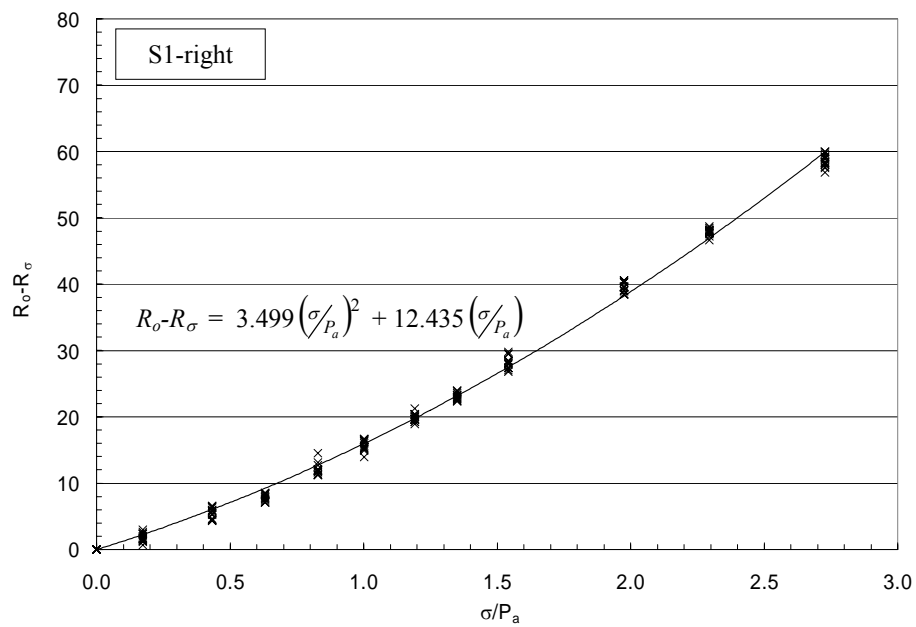
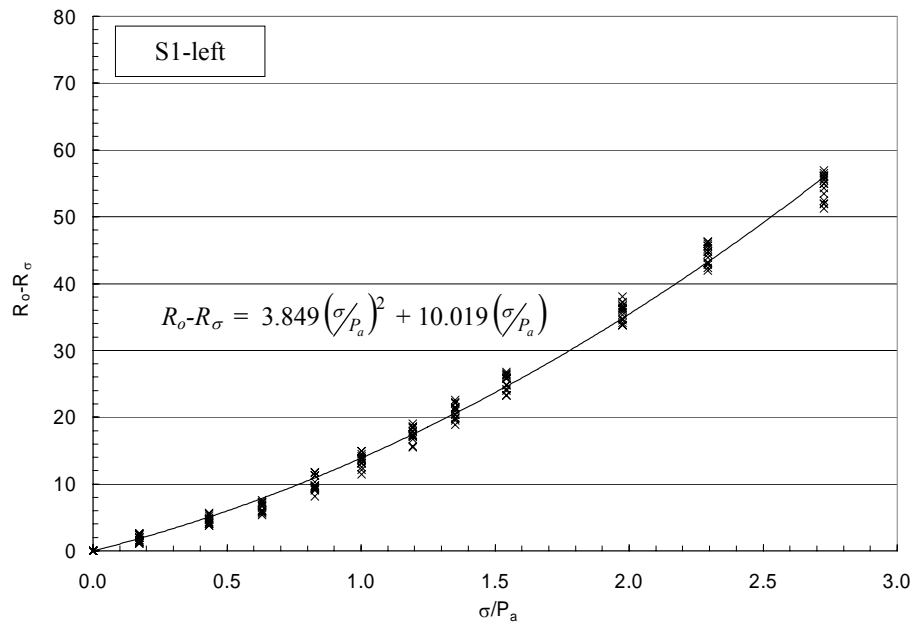
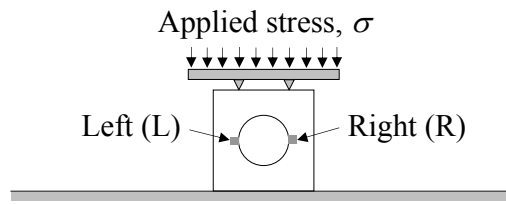


Figure 4-9 Calibration charts for sensor S1 at points L (top) and R (bottom)

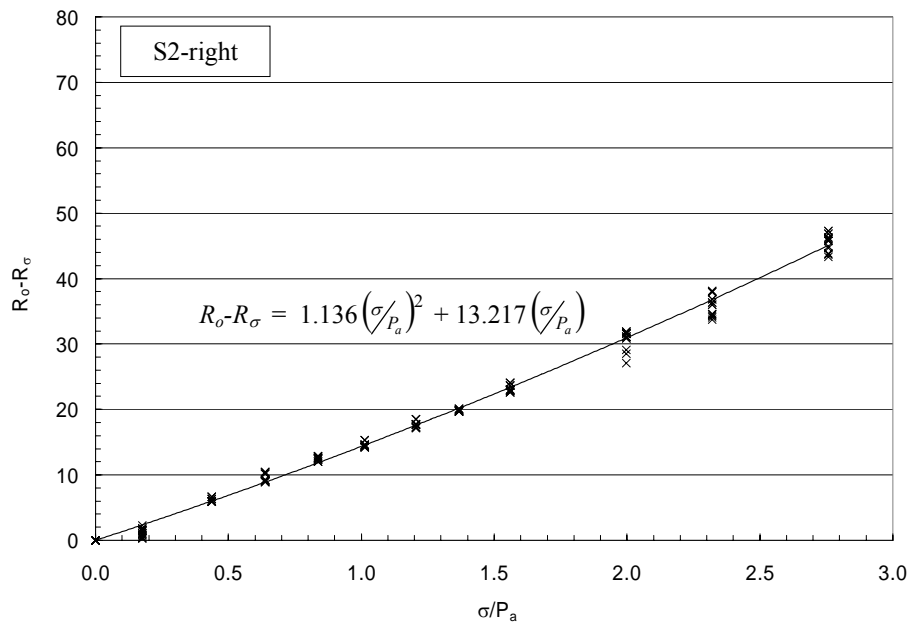
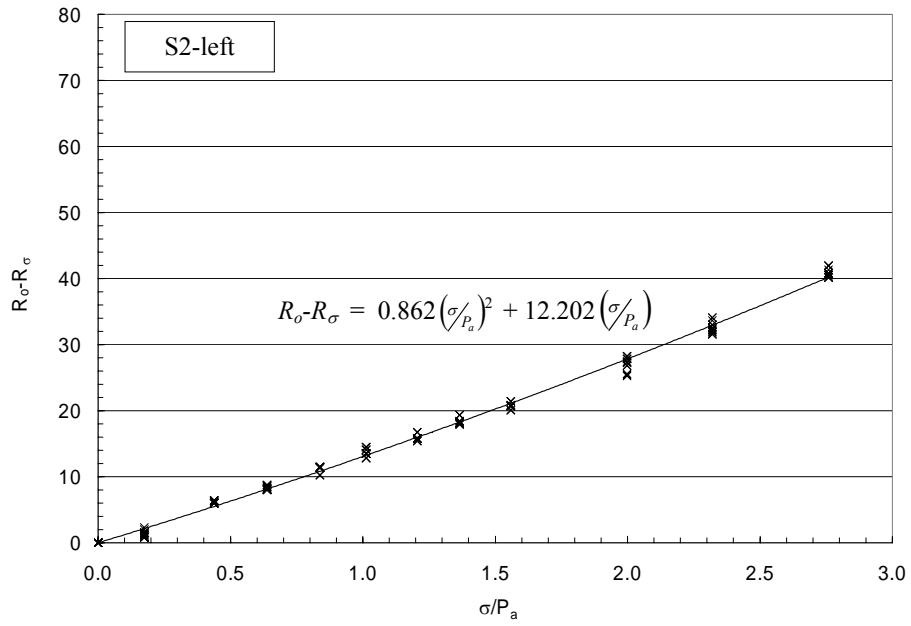
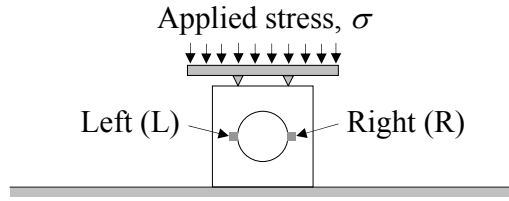


Figure 4-10 Calibration charts for sensor S2 at points L (top) and R (bottom)

Table 4-1 Empirical coefficients a and b for calibrations for sensors S1 to S10

Sensor #	Left			Right		
	a	b	r^2	a	b	r^2
S1	3.849	10.019	0.994	3.449	12.435	0.997
S2	0.862	12.202	0.996	1.136	13.217	0.995
S3	2.248	4.340	0.992	1.916	3.552	0.990
S4	1.927	4.563	0.975	2.856	6.006	0.991
S5	3.280	11.045	0.995	3.994	13.642	0.990
S6	1.292	20.862	0.995	2.039	15.420	0.990
S7	2.162	8.993	0.994	1.087	13.420	0.971
S8	2.027	20.900	0.988	0	23.359	0.975
S9	0.879	19.342	0.992	1.931	22.652	0.992
S10	2.125	15.306	0.998	1.663	15.380	0.995

4.4 Assessment of temperature effects on red intensity values

During the tests, temperature was controlled using a heater. Figure 4-11 shows the setup for the study of temperature effects on red intensity values. The specimen from Test #5-12 was used for this study. Pilot Tests #T1 and #T2 were performed.

Red intensity values and temperatures at the time of the measurement from sensors S3 and S8 are presented and discussed in this section. Similar results for the study of temperature effects were also observed at the other sensors. The remaining plots of red intensity and temperature versus time of measurement are included in Appendix A.

4.4.1 Discussion of results from Test #T1

In Test #T1, temperatures in the laboratory, inside the test box (i.e., temperature of the specimen), and in the vicinity of the devices (i.e., camera, Strainoptics A-100 analyzer and RP-100 tint plate) were recorded when the red intensity of the sensors were

measured. Figure 4-12 shows red intensity and temperature versus time of measurement for Test #T1.

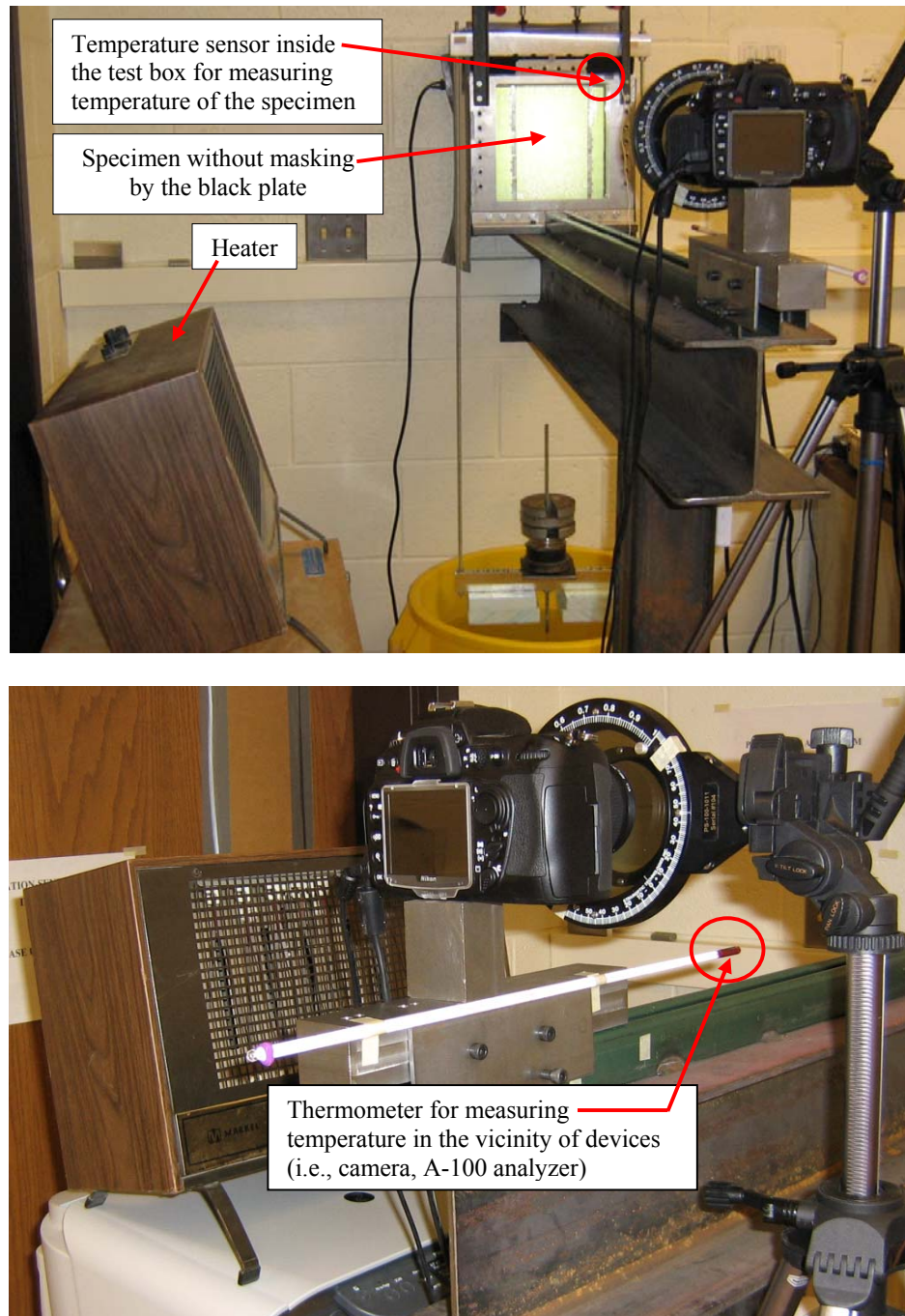


Figure 4-11 Test setup for assessment of temperature effects on red intensity values for pilot Tests #T1 and #T2

After 240 minutes, a heater was turned on to increase the temperature at the test station. Two thermometers measured temperatures during the test. The first thermometer measured the temperature in the vicinity of devices, and the other measured the temperature of the specimen inside the test box. Temperature versus time of measurement is shown in Figure 4-12(a). It shows that temperature inside the test box did not change when the temperature in the vicinity of the measuring devices increased, (i.e., the temperature inside the test box went up only 0.2 °F, from 80.4 °F to 80.6 °F). At this moment, Figure 4-12(b) and (c) show that the red intensity in the sensors increases with increasing temperatures in the vicinity of the devices. This observation demonstrates that temperature in the vicinity of the devices is the primary cause of the variation in red intensity.

4.4.2 Discussion of results from Test #T2

A similar test setup to that shown in Figure 4-11 was used for Test #T2. In Test #T2, temperature at the test station was controlled using the heater. Temperatures inside the test box and in the vicinity of the devices were recorded and are plotted in Figure 4-13(a).

Figure 4-13(a) shows that while the heater was adjusted to the desired temperatures of the devices, the temperature inside the test box went up and finally stabilized at a constant temperature of 77.5 °C, similar to Test #T1. The stabilization of the temperature inside the test box was observed after 2 hours. This observation confirms that red intensity values fluctuated due to changes of temperature in the vicinity of the devices, as is surmised from the results shown in Figure 4-13(b) and (c).

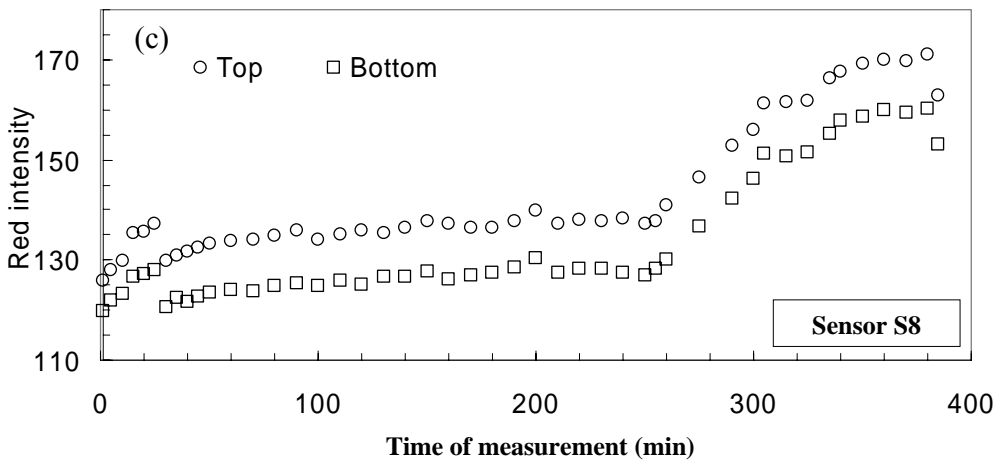
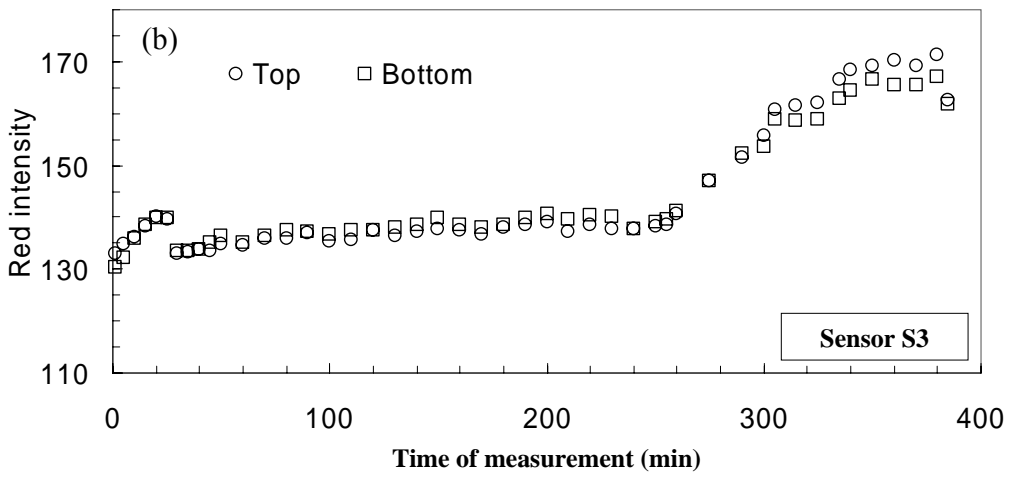
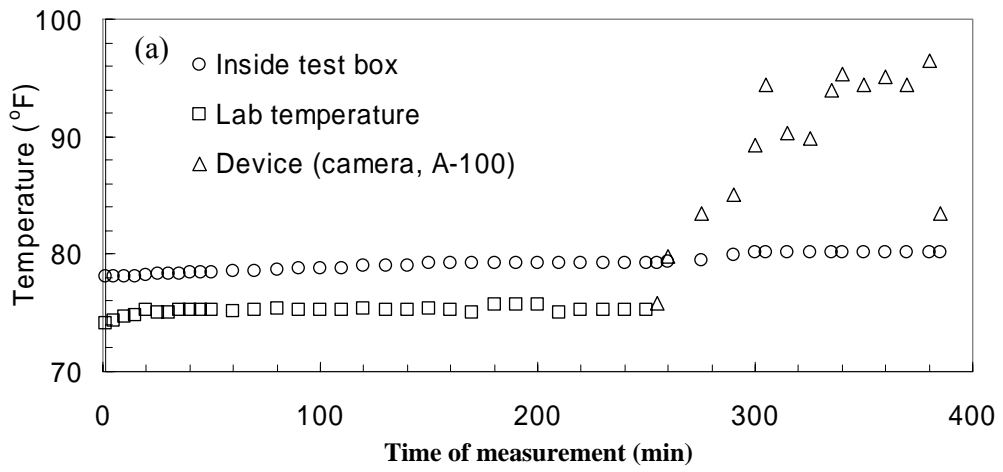


Figure 4-12 Red intensity and temperatures versus time at the measurements from sensors S3 and S8 from Test #T1

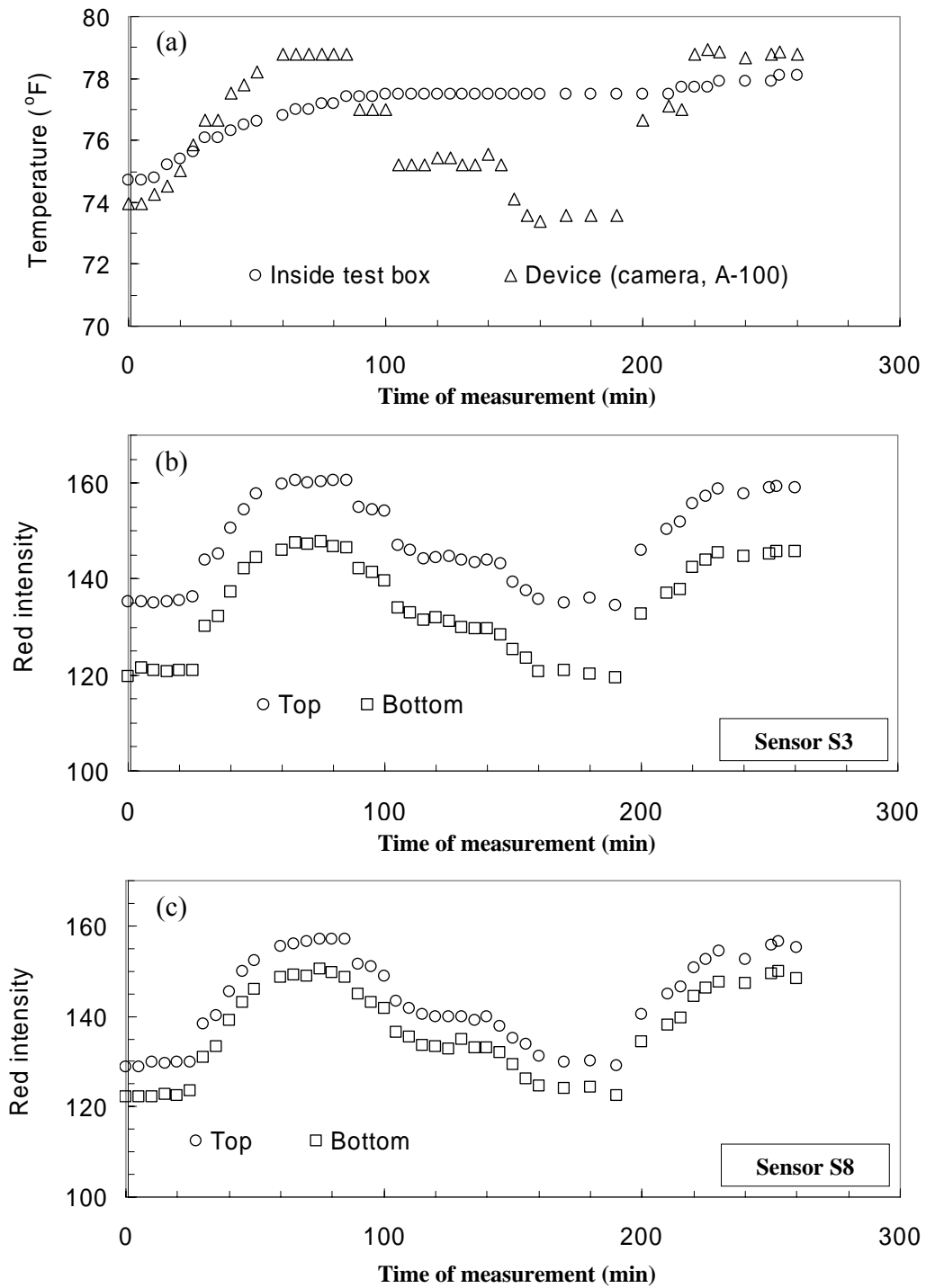


Figure 4-13 Red intensity and temperatures versus time at the measurements from sensors S3 and S8 from Test #T2

In summary, fluctuations of temperature in the vicinity of the devices cause variation of red intensity readings. Results also showed that the values of red intensity did not return to the same values after the temperature in the vicinity of the devices was returned to the previous value. Further studies are necessary to understand the effects of temperature on red intensity values. The results presented in this dissertation are only from two pilot tests which may serve as a guide for future research.

4.5 Concluding remarks

4.5.1 Extraneous light in the vicinity of the test station needs to be eliminated during the tests to reduce noise in the color intensity values.

4.5.2 This research used a thin black plate with small openings to eliminate excess light on the specimens. These small openings are located at points corresponding to the regions of interest where the colors in the stressed glass were to be observed.

4.5.3 For increasing applied stress (σ) from 0 to 139 psi, changes in red intensity were selected to track changes in stress. The *relative red intensity* ($R_{rel} = R_{\sigma} - R_{\sigma}$) is proposed as a parameter that can be used to monitor changes in the applied stress.

4.5.4 A quadratic equation fits the calibration data well. The correlation coefficients (r^2) of the calibration charts are greater than 0.975 indicating a good fit and a strong correlation between R_{rel} and σ/P_a . The relationships between R_{rel} and σ/P_a for the glass plate sensors are expressed by Eqs. (4-1), (4-2) and (4-3). The empirical coefficients a and b are summarized in Table 4-1.

4.5.5 Two pilot tests were performed to assess the effects of temperature on red intensity values. Results showed that red intensity increased with the temperature in the vicinity of the measuring devices (i.e., Nikon D300 digital camera, Strainoptics A-100

analyzer and RP-100 tint plate). Temperature inside the test box did not change with changes in the temperature in the vicinity of the devices. The temperature in the test box was insulated by the viewing window glass plate.

CHAPTER V

**APPLICATION OF PHOTOELASTICITY
FOR MEASURING HORIZONTAL STRESS
IN 2-DIMENSIONAL GRANULAR ASSEMBLIES**

5.1 Introduction

This chapter presents the use of photoelasticity for determining horizontal effective stress in 2D granular assemblies under zero lateral strain (K_o) conditions. The glass plate sensors discussed in Chapter 4 were attached to both sides of the test box for determining horizontal stress. The glass plate sensors were employed to determine the horizontal stress for the two following cases:

- (1) during loading and unloading
- (2) as a function of time in specimens under sustained vertical loading

Previous methods for measuring the horizontal stress of soils under K_o conditions can be found in Dyvik (1985), Thomann (1990), Thomann and Hryciw (1990), Mesri and Hayat (1993), Hryciw and Thomann (1993) and Mesri and Vardhanabhuti (2007).

Dyvik et al. (1985) built an oedometer having a fluid-filled chamber placed around the ring. The chamber was connected to a pressure transducer that measures the pressure of the fluid. During vertical loading or unloading of specimens in the oedometer,

the fluid pressure was equivalent to the horizontal stress in the specimens. Because the fluid was incompressible, the lateral zero strain or K_o conditions were approximately maintained during the tests. The purpose of that study was to measure the coefficient of horizontal stress at rest (K_o) of Norwegian clays. A similar technique for measuring lateral stress of soils using silicon oil around the perimeter of an oedometer was reported by Mesri and Hayat (1993) and Mesri and Vardhanabhuti (2007).

Thomann (1990) measured the horizontal stress of sands under K_o conditions. The experiments were performed in an oedometer having a movable piston at the mid-height of the oedometer wall. The piston was connected to a threaded rod. The threaded rod was connected to a load cell to measure the horizontal stress of the specimen in the oedometer. To maintain K_o conditions, the threaded rod pushed the piston and therefore the the soils back to zero lateral displacement position during the tests. Detailed descriptions of the device can be found in Thomann (1990).

5.2 Experimental setup

Figure 5-1 shows the test box. The ten calibrated glass plate sensors (from Chapter 4) were attached to both sides of the test box. Sensors S1, S2, S3, S4 and S5 were on the left side, and sensors S6, S7, S8, S9 and S10 were on the right side.

The largest 2D granular assembly that would fit in the test box is 7.5" x 5.0". For smaller specimen dimensions, an aluminum plate (i.e., spacer) could be placed in the test box. In this study, the width of the specimens was kept at 5.0", but the height of the specimens was varied.

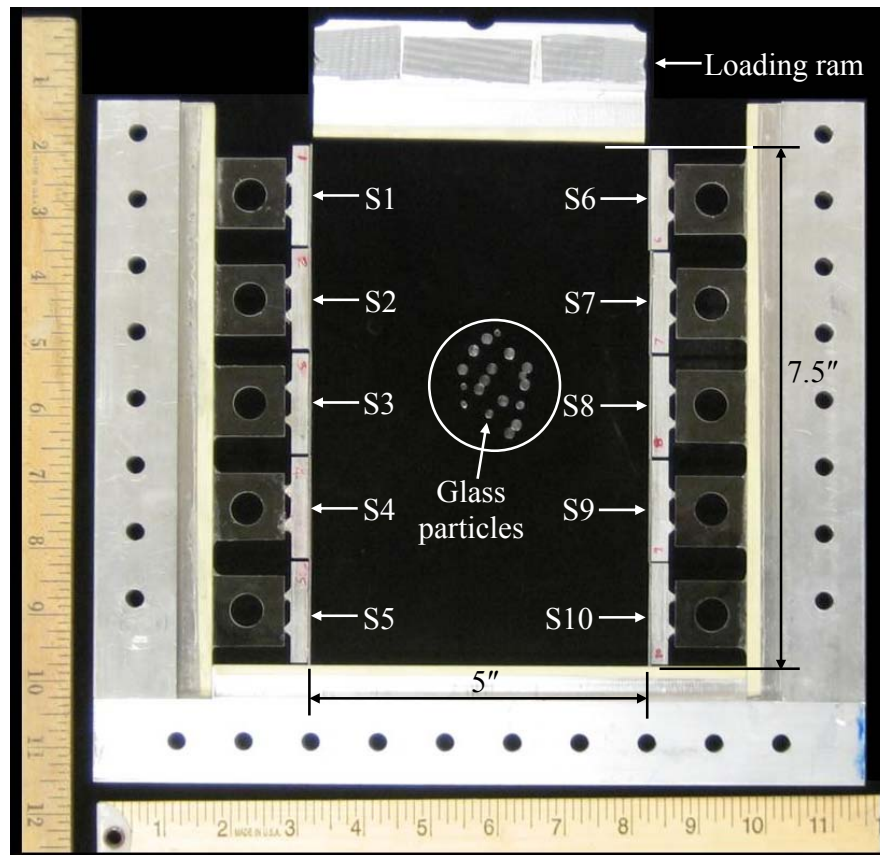


Figure 5-1 Test box with the calibrated glass plate sensors at the sidewalls

Specimens of 2D granular assemblies were assembled manually. Figure 5-2 shows a typical test setup. In addition to the feature in the calibration, the calibrated sensors were now attached at both sides of the test box were for determining horizontal stress of the granular assemblies. Two dial gauges on the top of the specimen were also used to measure surface settlement at the left and right sides of the specimens. Figure 5-3 shows 1.5" x 5.0" specimens with 550 cylindrical particles and 300 angular prism particles.

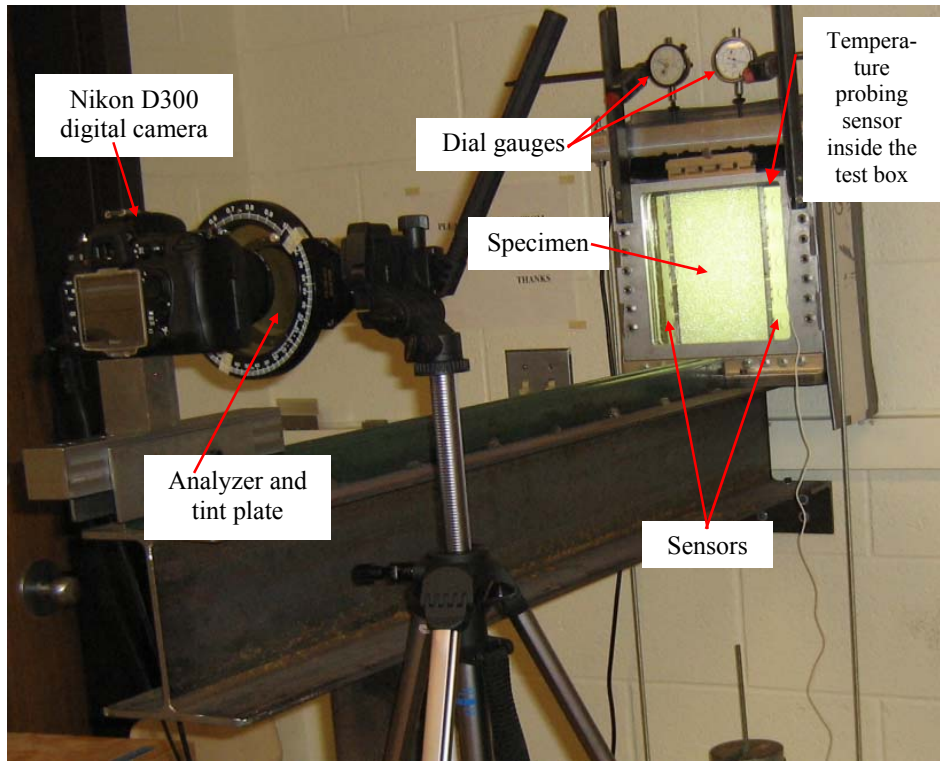


Figure 5-2 Typical setup for experiments in this chapter

5.3 Results and discussions

5.3.1 Stiffness of granular assemblies and possibility of particle seating and sliding in 2D granular assemblies

Deformations of 2D granular assemblies consist of elastic compression of the glass individual particles and volume contraction (i.e., reduction in void ratio) of the particle assembly. The compressibility of glass particles is small by comparison to the volume contraction of the particle assembly. The observation of volume contraction is attributed to seating and sliding of particles in the particle assembly. The particle motions was manifested by surface settlements during loading as well as under sustained loading (i.e., during aging). Grain crushing was not observed even at the maximum applied vertical stress of 40.9 psi. After particle seating and/or sliding, there would be volume

contractions of the loaded granular assemblies. The settlement at specimen surface could signify motion of particles in the assembly at which shearing stress reduced at the particle contacts containing high shearing stress. In other words, the particles come into a more stable contact with reduced shearing stress at the contact, improved micro-interlocking and possibly increased frictional resistance.

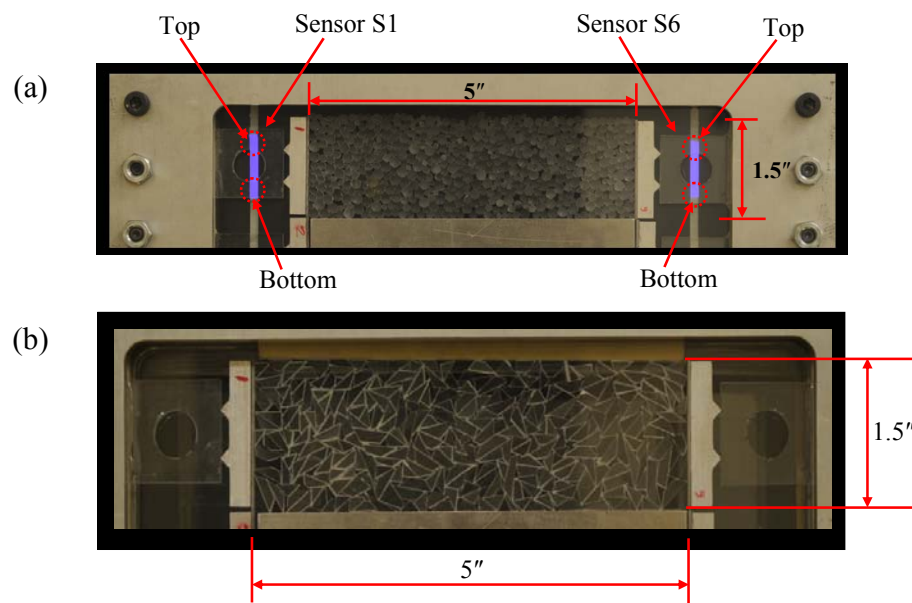


Figure 5-3 1.5" x 5.0" specimens: (a) 550 cylinders and (b) 300 angular prisms

Hardin (1987) proposed a model for one-dimensional strain in normally consolidated cohesionless soils as shown in Figure 5-4. Point *a* to *b* in Figure 5-4 shows a constant value of dimensionless stiffness coefficient for 1D strain (S_{1Dmax}), which describes the constrained stiffness for 1D strain in cohesionless soils in the region prior to grain crushing. Eq. (5-1) expresses the 1D strain model proposed by Hardin (1987) for constant S_{1D} in normally consolidated cohesionless soils. This present research employed this model to quantify stiffness of 2D granular assemblies.

$$\frac{1}{e} = \frac{1}{e_o} + \frac{1}{S_{1D}} \left(\frac{\sigma_v}{P_a} \right)^p \quad (5-1)$$

- where e_o = Initial void ratio
 e = Void ratio
 S_{1D} = Dimensionless stiffness coefficient for 1D strain
 p = exponent on the term σ_v/P_a ; p depends on geometry of glass particles and dimensionality (2D versus 3D) of specimens

Hardin proposed that p in Eq. (5-1) is equal to 0.5 for normally consolidated sands. The values of p in this study were different. The different values of p for normally consolidated sands ($p = 0.5$) than for 2D granular assemblies in this study are probably attributed to the geometry of the particles and the dimensionality (2D versus 3D) of the granular assemblies. The value of p observed for each test was determined based on the highest correlation coefficient (r^2) that fits the linear relationship well for each set of $1/e$ vs $(\sigma_v/P_a)^p$ data.

Figures 5-5 to 5-6 show plots of applied vertical stress versus surface settlement for an assembly of 300 angular prism particles (1.5"x5.0") and an assembly of 1810 cylindrical particles (4.5"x5.0"), respectively. Figure 5-7 shows the Hardin's 1D strain model with variations of p and r^2 for the specimens with 300 angular prisms and 1810 cylinders. Figure 5-7(a) and Figure 5-7(c) show that a linear relationship with a selected value of p could fit $1/e$ vs $(\sigma_v/P_a)^p$ data. According to the definition by Hardin (1987), the 1D plot shown in Figure 5-7 did not show the signature of grain crushing. The value of

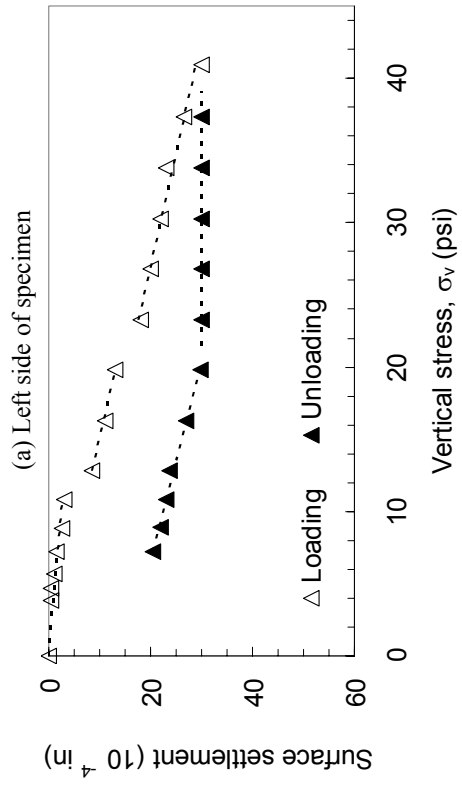
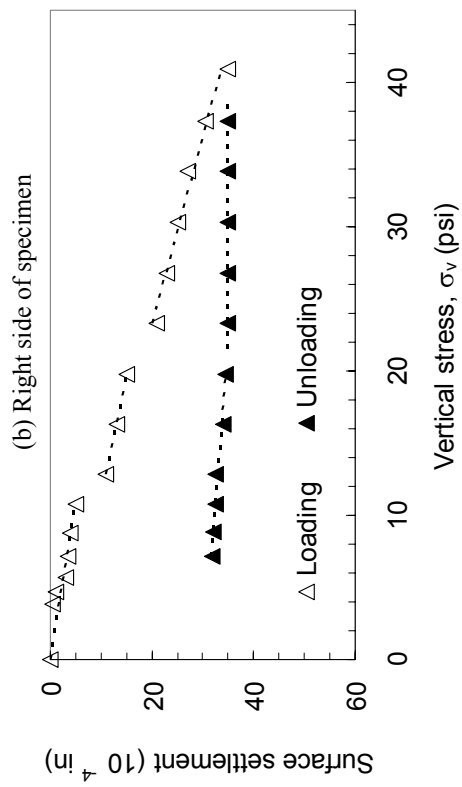


Figure 5-5 Surface settlement at left and right sides of a 1.5"x5.0" specimen with 300 angular prisms during loading and unloading

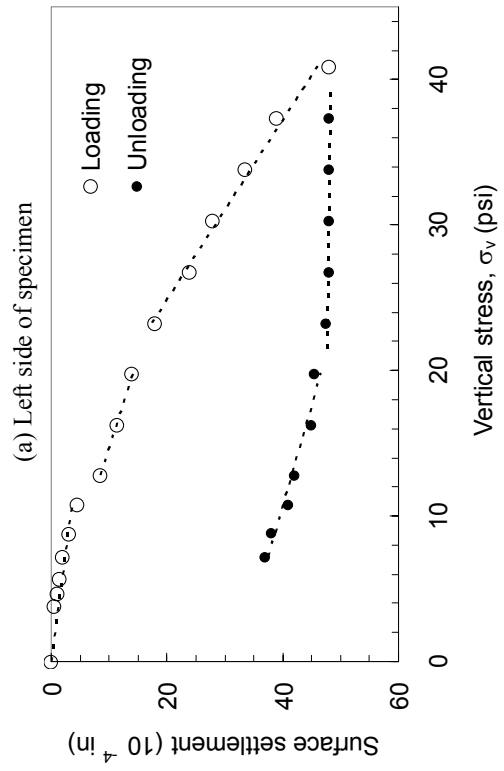
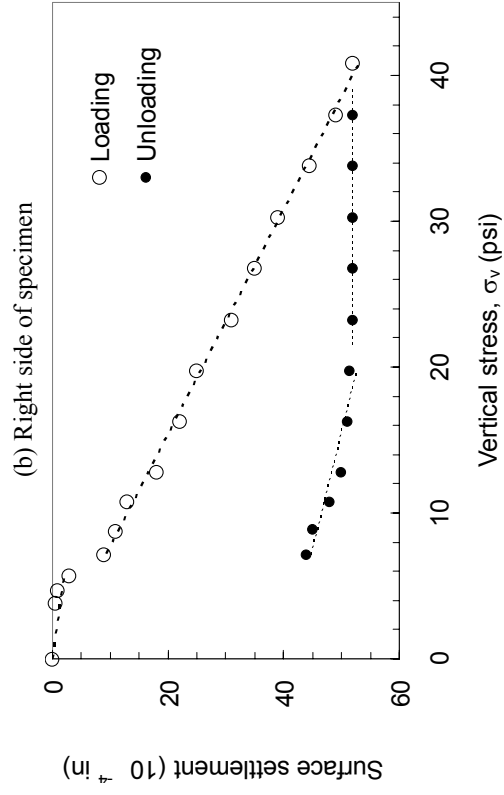


Figure 5-6 Surface settlement at left and right sides of a 4.5"x5.0" specimen with 1810 smooth cylinders during loading and unloading

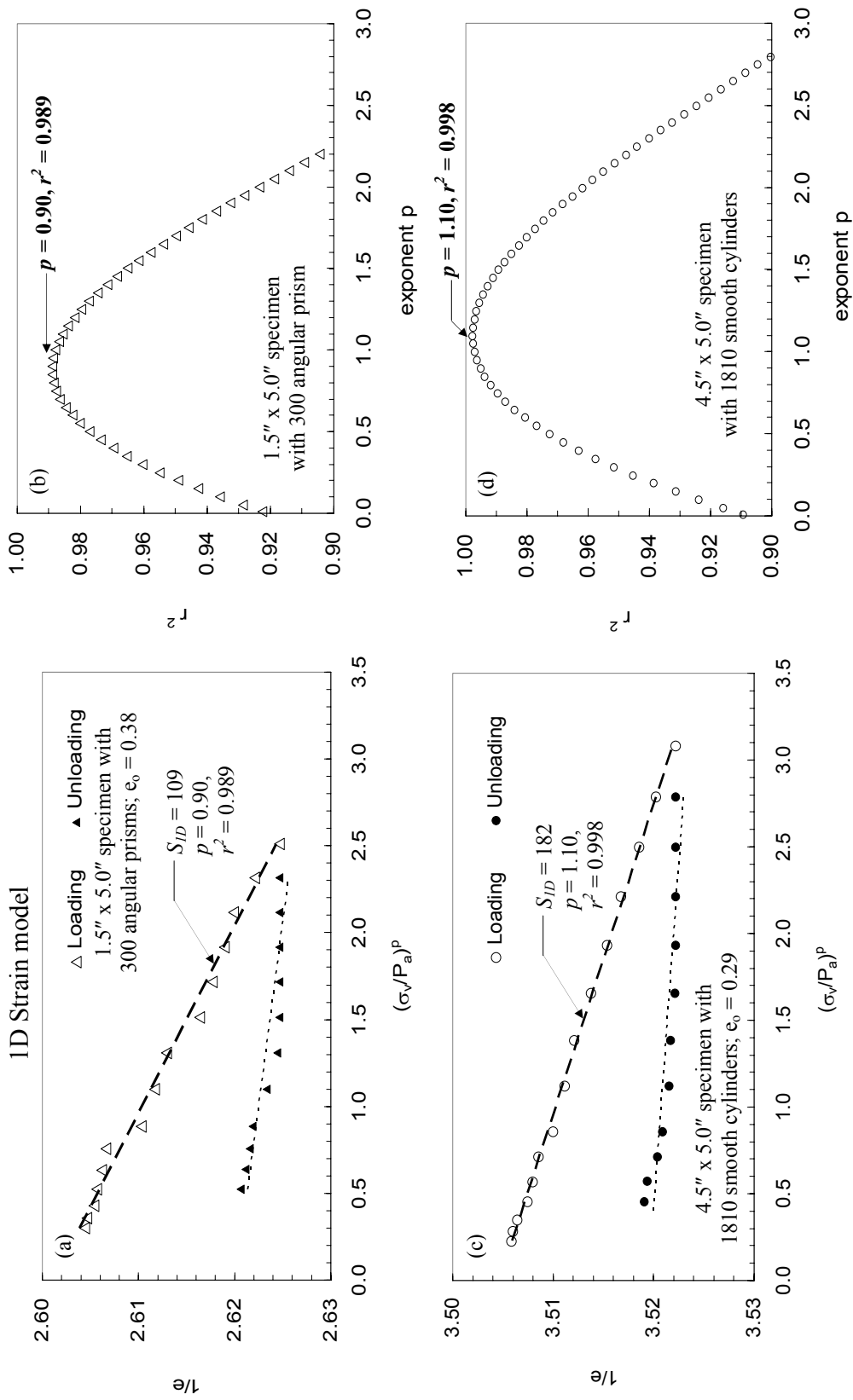


Figure 5-7 1D strain model with variations of p and r^2 for 1.5" x 5.0" specimen (300 angular prism particles) and 4.5" x 5.0" specimen (1810 smooth cylindrical particles)

In Figure 5-7(a), the linear relationship does not fit the data very well. This could possibly be attributed to some effects, e.g., vibrations caused by rapidly placing the loads to the top of specimen which in turn resulted in unbalanced loading, uncontrolled vibrations from people walking close by the test station and/or slamming of the laboratory door, etc. In other words, uncontrolled/unintended vibrations during the tests may ultimately result in large variations in the results. In some cases, Thomann and Hryciw (1992) showed that even small vibrations could cause a significant loss in strength and stiffness of sands.

Combined with results from tests discussed later in this chapter, the values of p ranges between 0.80 and 1.25. The author hypothesizes that variations for the values of p depends on the geometry of glass particles and/or the dimensionality (2D versus 3D) of the granular assemblies. However, this study did not focus on the study of these variations. Further study may be required to acquire a better understanding of the exponent p for 2D granular assemblies.

Figure 5-8 shows a series of photos from the test performed on a 1.5" x 5.0" specimen with 550 cylinders. The left side of each photo is the wall of the test box. In this series of photos, loss and re-formation of contacts was observed. Sliding of particles was also noticed. The following paragraph describes movements of select particles labeled #1 to #8 as shown in Figure 5-8(c).

From Figure 5-8(a) to 5-8(b), a loss of contact between particles #1 and #3 was seen. Downward movements of particles #3 and #4 were clearly observable, but the contact between particles #2 and #4 was not lost. Loss and formation of contacts were also found at other places in the specimen. Particles #5 and #6 moved towards each other

and came into contact. Particle #7 moved towards the wall and finally made a contact with the sidewall while particle #8 lost contact with the wall.

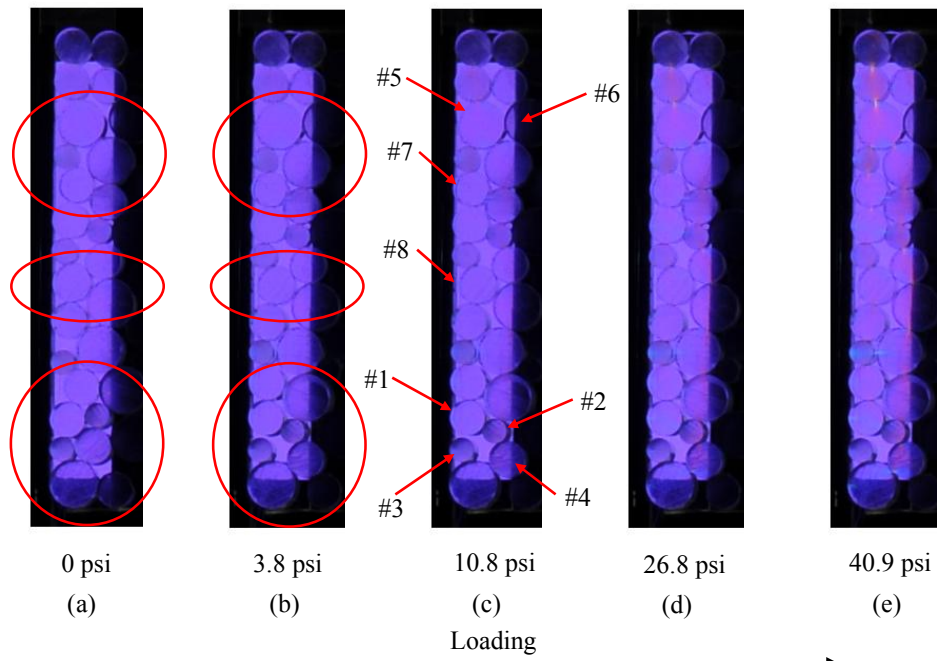


Figure 5-8 Particle sliding and appearance of load chains (photos from Test #5-2) in a specimen with 550 cylindrical particles

The photos in Figure 5-8 also show that load chains were observed through photoelasticity by the naked eye when the applied vertical stress reached 10.8 psi (Figure 5-8c). Contact stresses became higher as stress was further increased to 26.8 psi and 40.9 psi. This was confirmed by increases in color intensities of load chains as shown in Figure 5-8(d) and (e).

During aging in sands, a decrease in high shearing stress at grain contacts as a result of particle seating could occur, particularly at low confining pressure where contacts are most likely to be found. At high confining pressure, particles in the assembly

had already come into better contact with each other. Therefore, individual particles tend to slide and/or roll at high confining pressure.

5.3.2 Coefficient of lateral earth pressure at rest (K_o)

The coefficient of lateral earth pressure defines the stress state of soils under zero lateral strain or " K_o " conditions. It is defined by the ratio of the horizontal to vertical effective stress as expressed by Eq. (5.2), noting that for dry soils, effective stresses are equal to total stresses.

$$K_o = \frac{\sigma'_h}{\sigma'_v} \quad (5-2)$$

where K_o = Coefficient of lateral earth pressure at rest

σ'_h = Horizontal effective stress

σ'_v = Vertical effective stress

K_o can be determined by either *in situ* or laboratory testing. For *in situ* testing, K_o can be determined using pressuremeters (PMT), or the flat plate dilatometer (DMT) while in the laboratory, K_o can be obtained by specialized oedometer testing. Previous laboratory testings for measuring K_o were discussed in Chapter 2 (Dyvik et al., 1985; Thomann, 1990; Thomann and Hryciw, 1990; Mesri and Hayat, 1993 and Mesri and Vardhanabhuti, 2007). This study presents a newly proposed applications using photoelasticity with the use of calibrated glass plate sensors for determining σ_h in 2D granular assemblies, and for estimating K_o of the specimens.

Table 5-1 summarizes the initial conditions of test specimens for the study of horizontal stress coefficient at rest (K_o). Figure 5-9 and 5-10 show plots of horizontal versus vertical stress during loading and unloading from Tests #5-1 and #5-2. In these

tests, the dimensions of the specimens were 1.5" x 5.0", and the horizontal stresses of the specimens were determined using sensors S1 and S6 on the left and right sides of the specimens, respectively.

Table 5-1 Initial conditions of test specimens for the study of K_o values

Test #	Particles in the specimen		# of particles	Initial void ratio, e_o	Dimensions of specimens (in)		Sensors for horizontal stress measurements	
	Contact surface	Particle shapes			Height	Width	Left	Right
5-1	Smooth	Cylinder	550	-	1.5	5.0	S1	S6
5-2	Smooth	Cylinder	550	-	1.5	5.0	S1	S6
5-3	Smooth	Cylinder	550	0.24	1.5	5.0	S1	S6
5-4	Smooth	Cylinder	550	0.24	1.5	5.0	S1	S6
5-5	Rough	Angular prism	300	0.38	1.5	5.0	S1	S6
5-6	Rough	Angular prism	300	0.38	1.5	5.0	S1	S6
5-7	Smooth	Cylinder	1810	0.29	4.5	5.0	S1,S2,S3	S6,S7,S8

Figure 5-11 shows plots of vertical versus horizontal stresses of the specimen during loading and unloading from Test #5-7. The dimensions of the specimen from Test #5-7 were 4.5" x 5.0". Horizontal stresses for Test #5-7 were measured using sensors S1, S2, S3 on the left side, and sensors S6, S7, S8 on the right side. In Figure 5-11, results from sensors S2 and S7 are shown. The remaining test results for K_o values from other tests are in Appendix B.

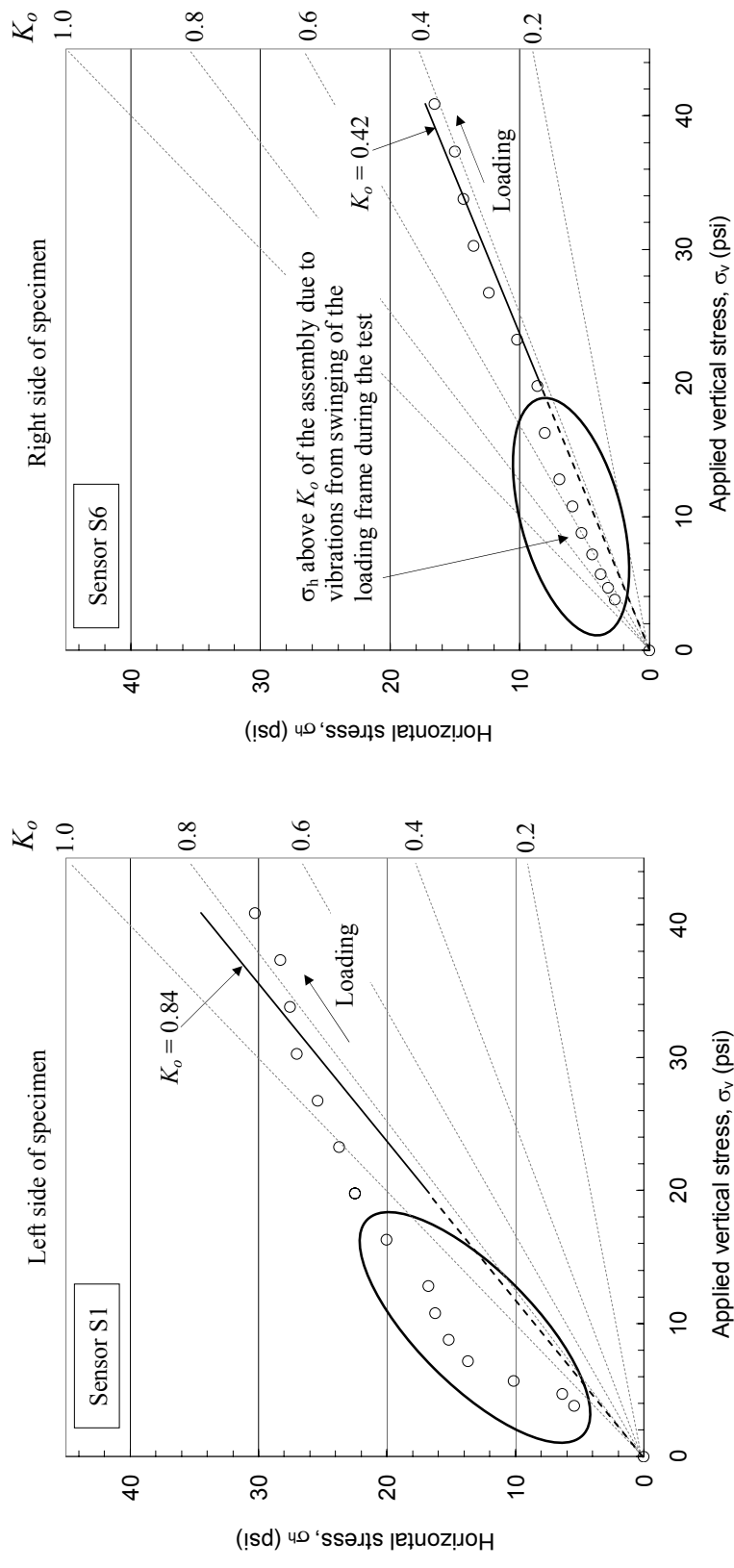


Figure 5-9 Horizontal versus vertical stress on loading and unloading from sensors S1 and S6 from Test #5-1

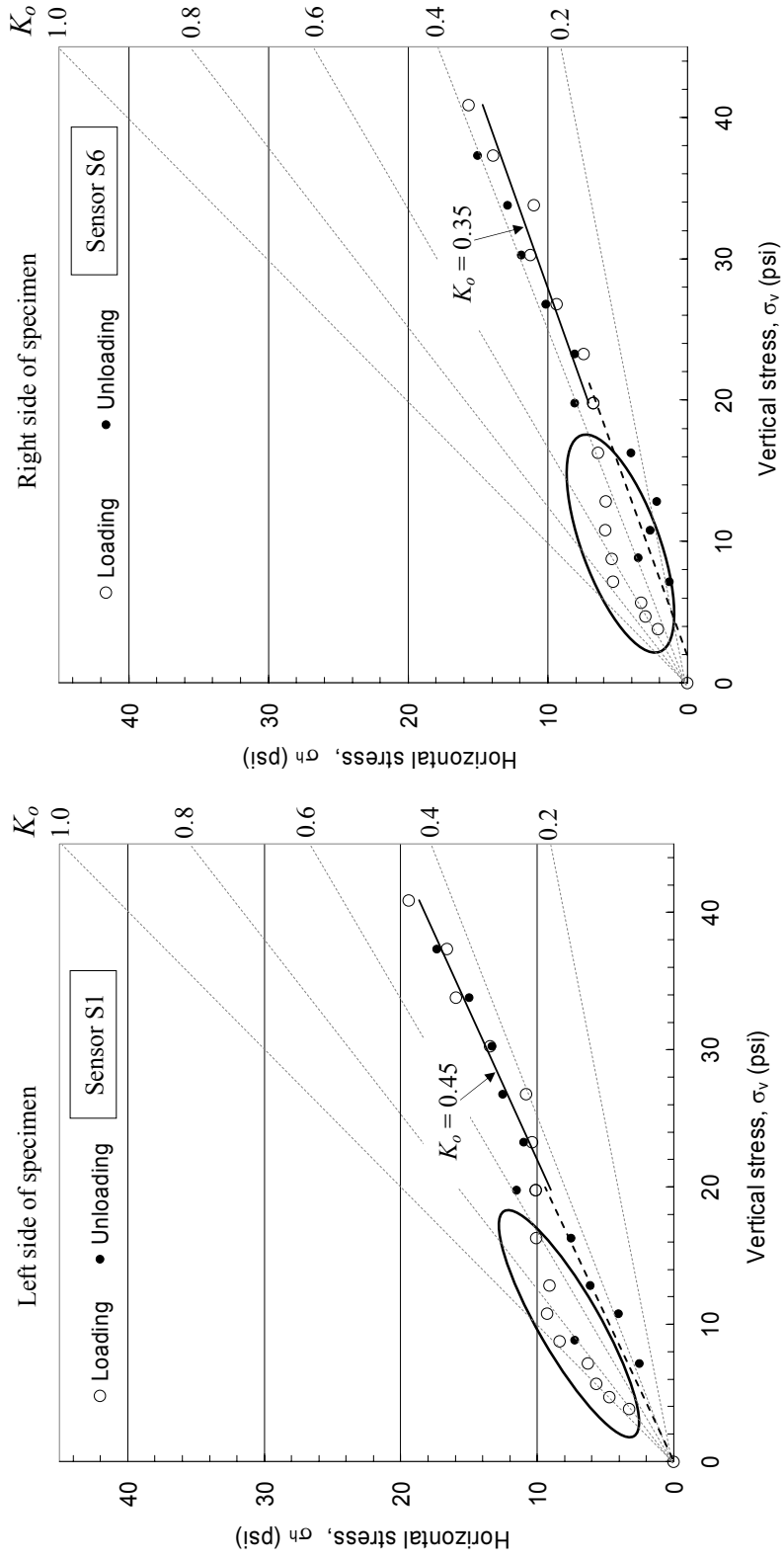


Figure 5-10 Horizontal versus vertical stress on loading and unloading from sensors S1 and S6 from Test #5-2

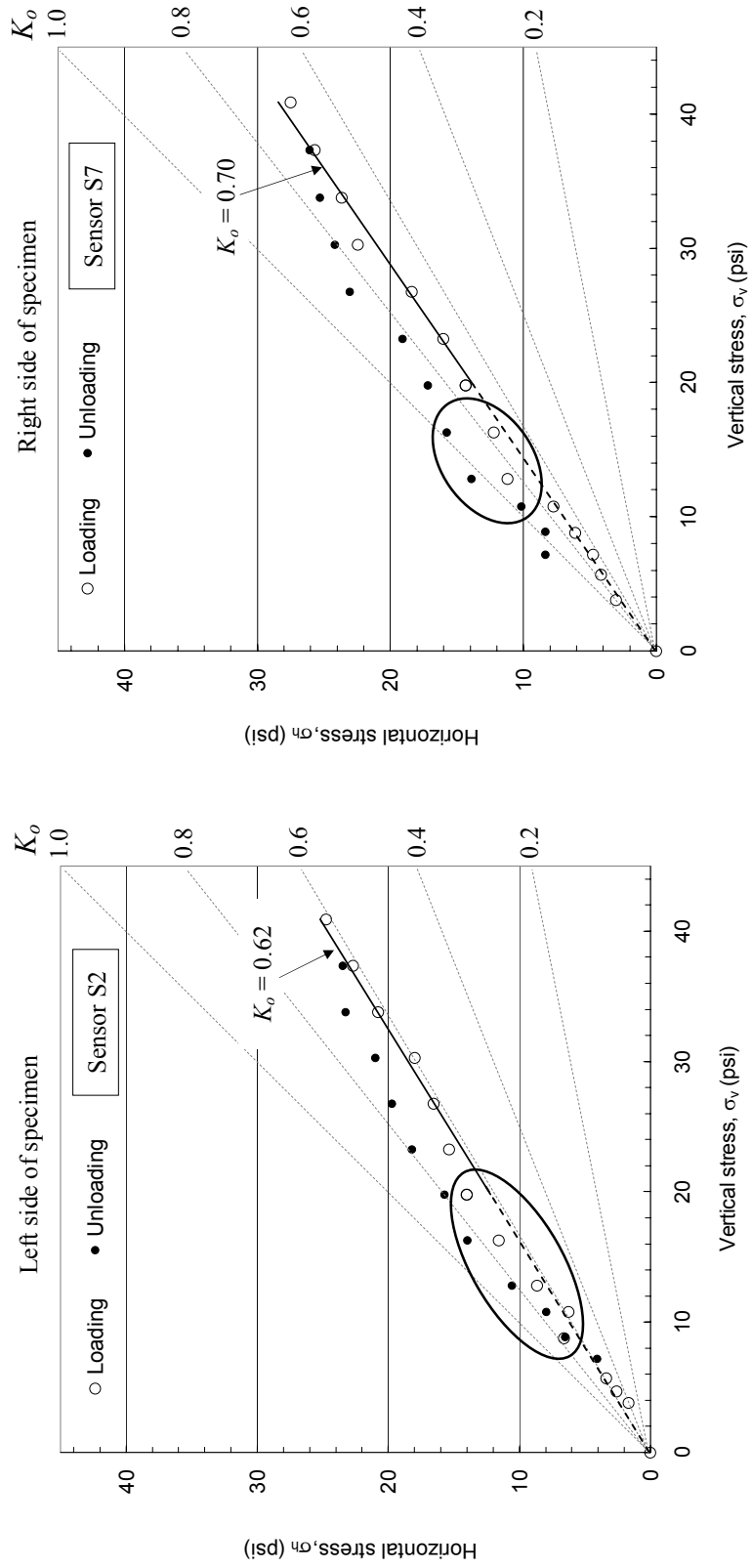


Figure 5-11 Horizontal versus vertical stress on loading and unloading from sensors S2 and S7 from Test #5-7

To obtain the value of K_o , the data from each test was fitted to a linear model. The y-intercept was forced at zero and only the data at the vertical stress higher than 20 psi were included in the linear fitting. Figures 5-9 to 5-11 show that for the applied vertical stress lower than 20 psi, the values of horizontal stress fall far above the line representing K_o . In this study, K_o of the 2D granular assemblies ranged between 0.30 and 0.84. Large variations of K_o values were attributed to unbalanced loading during the tests, which in turn may have been due to rapid loading of the specimen.

It was observed that when the applied vertical stress was lower than 20 psi, high values of horizontal stress could be attributed to a crooked position of the loading frame during the tests. Vibrations (or swinging) of the load frame may have resulted in high horizontal stress compared to what it should be. These high values of horizontal stress could also be due to small vibrations around the test station.

When the vertical stress was increased, the load frame came into better contact with the top of the specimen. Thus, the system became more stable and motionless. The effects of vibrations from the swinging of the loading frame were thus minimized. Therefore, horizontal stress obtained from readings of relative red intensity yielded reasonable K_o values when the applied vertical stress was greater than 20 psi.

5.3.3 Time-dependent horizontal stress in 2D granular assemblies

For decades, there has been evidence of time-dependent increases in strength and stiffness in recently disturbed/deposited sands. In geotechnical engineering, this improvement has been known as *aging of sands*. However, the investigations into the time-dependent mechanisms in granular assemblies have been inconclusive, sometimes raising more questions than resolving (Terzaghi, 1934; Mesri et al, 1990; Schmertmann,

1991; Charlie et al, 1992; Barton, 1993; Bowman and Soga, 2003; Baxter and Mitchell, 2004; Bowman and Soga, 2005; Mitchell, 2008; Green et al., 2008, etc.).

Previous researchers discussed macro-interlocking of sand particles and micro-interlocking of grain asperities as being mechanisms of aging in sands (Mesri et al, 1990; Barton, 1993), while others suggested that particle rearrangements or grain readjustment with redistribution of stresses at particle contacts in granular assemblies are mechanisms of time-dependent changes (Terzaghi, 1934; Mesri et al, 1990; Schmertmann, 1991). These mechanical aging processes ultimately cause changes in horizontal or confining stress of granular assemblies. This research concludes with a series of time-dependent surface settlement tests to study the aging process. Table 5-2 summarizes the initial conditions of specimens in the tests.

5.3.3.1 Preliminary study

In Chapter 2, it was hypothesized that mechanical aging causes time-dependent changes in horizontal stress of 2D granular assemblies. In this study, time-dependent changes in horizontal stress were monitored through the changes in relative red intensity in photoelastic glass plate sensors.

In the early stage of the aging study, pilot tests with small specimen dimensions were performed (Tests #5-8 to #5-11). Preliminary results from Tests #5-8 to #5-11 are discussed in this section. The results from these preliminary Tests #5-8 to #5-11 lead to a test program using much larger test specimens (Tests #5-12 to #5-16).

The specimen in Test #5-8 was aged immediately after completion of Test #5-1 using a vertical stress of 40.9 psi. During aging, the values of relative red intensity and

thus horizontal stress were monitored by sensors S1 and S6 and recorded at various times. The results are shown in Figure 5-12.

Table 5-2 Initial conditions of specimens for time-dependent surface settlement tests

Test #	Particles in the specimens		# of particles	Initial void ratio, e_o	Sustained vertical stress (psi)	Dimensions of specimens (in)		Sensors for horizontal stress measurements	
	Contact surface	Particle shape				Height	Width	Left	Right
5-8	Smooth	Cylinder	550	-	40.9	1.5	5.0	S1	S6
5-9	Smooth	Cylinder	550	-	12.8	1.5	5.0	S1	S6
5-10	Smooth	Cylinder	1810	0.29	23.3	4.5	5.0	S1,S2,S3	S6,S7,S8
5-11	Smooth	Cylinder	2725	0.26	40.9	7.5	5.0	S1,S2,S3, S4,S5	S6,S7,S8, S9,S10
5-12	Smooth	Cylinder	2725	0.26	23.3	7.5	5.0	S1,S2,S3, S4,S5	S6,S7,S8, S9,S10
5-13	Rough	Angular prisms	1390	0.38	40.9	7.5	5.0	S1,S2,S3, S4,S5	S6,S7,S8, S9,S10
5-14	Rough	Angular prisms	1390	0.38	23.3	7.5	5.0	S1,S2,S3, S4,S5	S6,S7,S8, S9,S10
5-15	Rough	Cylinder	2370	0.29	40.9	7.5	5.0	S1,S2,S3, S4,S5	S6,S7,S8, S9,S10
5-16	Rough	Cylinder	2370	0.28	23.3	7.5	5.0	S1,S2,S3, S4,S5	S6,S7,S8, S9,S10

Figure 5-12 shows an obvious time-dependent increase in horizontal stress only on the left side of the specimen. Based on data from the left side, one would believe that aging effects in granular assemblies cause the increase in horizontal stress. However, data from the right side are inconclusive.

In Figure 5-9, results from Test #5-1 previously showed that K_o was 0.84 and 0.42, on the left and right sides of the specimen, respectively. The value of K_o on the left side was two times larger than that on the right side. Therefore, the conclusions for this observation would still be inconclusive as the value of K_o on the left and right sided of the specimen varied greatly. It is possible that an unbalanced bias loading favoring the left side of the specimen could be the cause of the discrepancy.

Figure 5-13 shows plots of relative red intensity and horizontal stress versus time for a 1.5" x 5.0" specimen (Test #5-9). The specimen contained 550 smooth cylinders. In this test, the specimen was aged under a constant vertical stress of 12.8 psi for 4 days. Increases in horizontal stress were not observed, probably because the applied vertical stress was relatively low. Therefore, the degree of particle rearrangement was likely relatively small.

Figure 5-14 presents horizontal stress versus time with the corresponding surface settlement for a 4.5" x 5.0" specimen (Test #5-10). The specimen consisted of 1810 smooth cylinders and was aged under a constant vertical stress of 23.3 psi. Time-dependent increases in horizontal stress were monitored using sensors S1, S2 and S3 on the left side and sensors S6, S7 and S8 on the right side. The surface settlement indicates that the particles in the granular assembly specimen moved or rearranged under K_o conditions. Additional results for Test #5-10 are shown in Appendix C.

Time-dependent increases in horizontal stress were observed on the left side of the specimen by sensor S3. For the test results from sensors S1 and S2, increases in horizontal stress were observed after one day of the test (i.e., 1440 minutes after the test began).

On the right side of the specimen, time-dependent increases in horizontal stress were observed by sensors S6, S7 and S8. The increases in horizontal stress began to occur after 100 minutes.

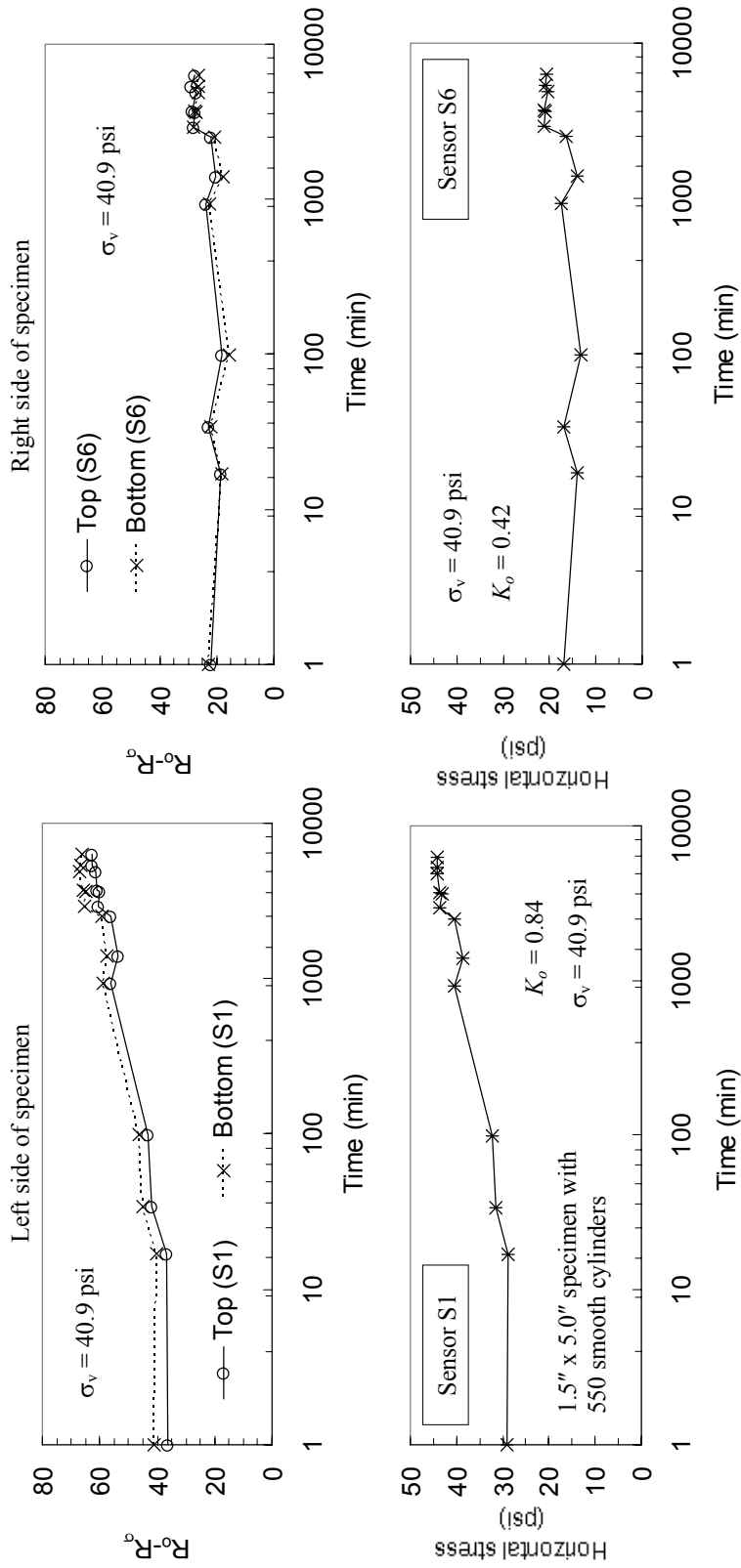


Figure 5-12 Relative red intensity and horizontal stress versus time versus for Test #5-8

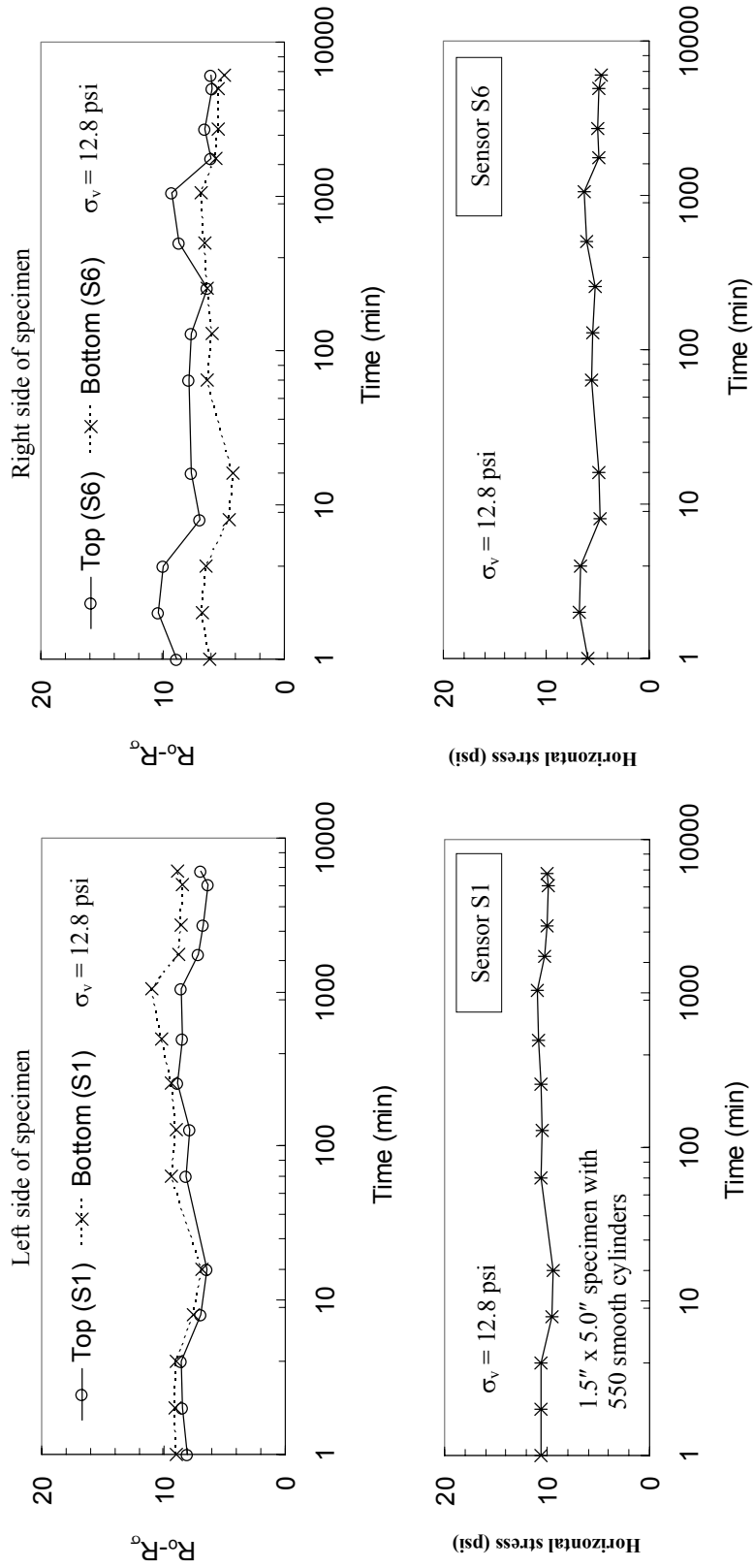


Figure 5-13 Horizontal stress and surface settlement versus time for Test #5-9

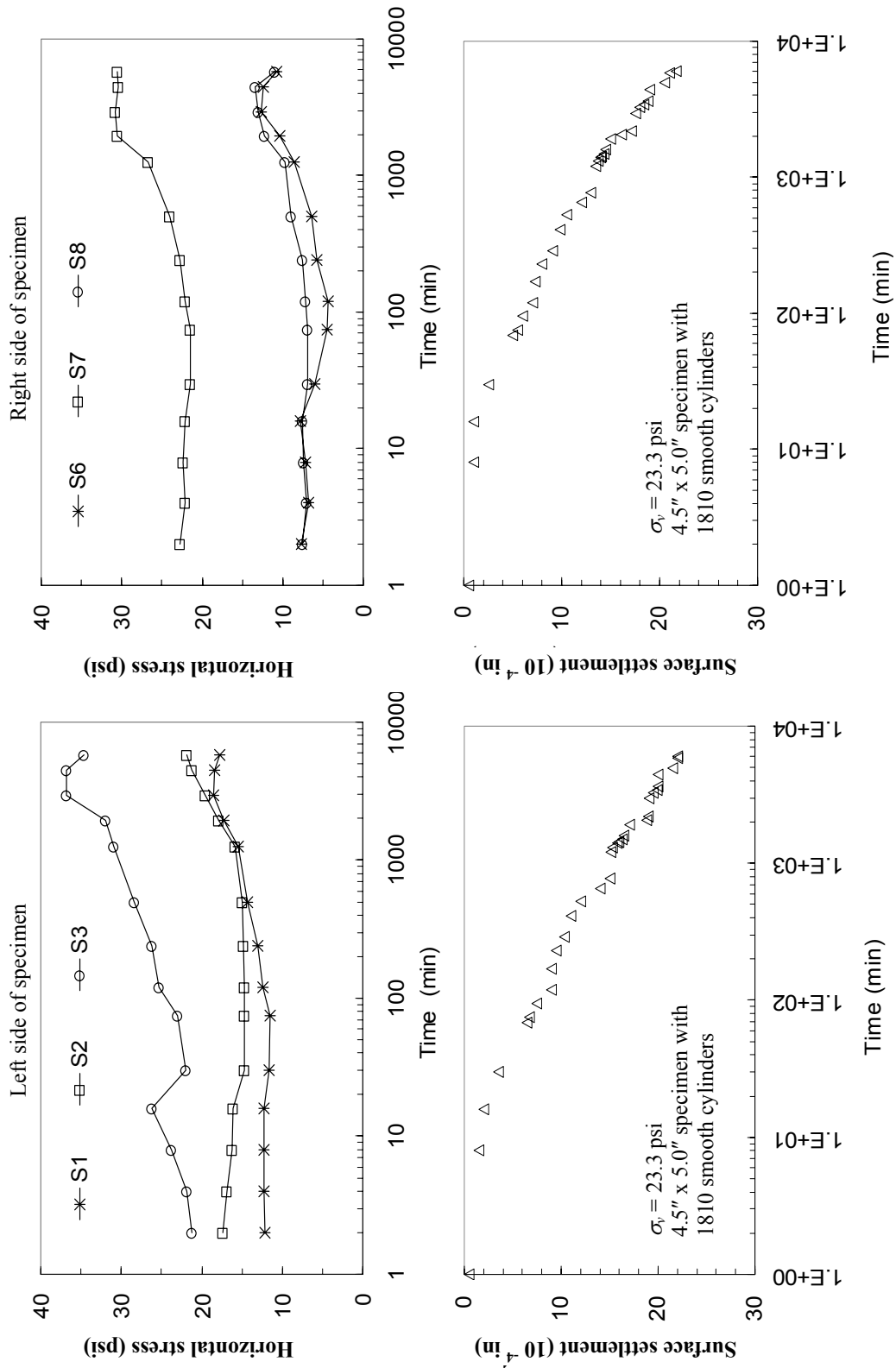


Figure 5-14 Horizontal stress and surface settlement versus time for Test #5-10

The results from Test #5-9 appear to show that time-dependent surface settlement are linked to increases in horizontal stress with time. Creep tests for parametric evaluation (Tests #5-11 to #5-16) are presented and discussed in Section 5.3.3.2.

Figures 5-15 and 5-16 show changes in horizontal stress ($\Delta\sigma_h$) as a function of surface settlement (Δ_y) for Tests #5-10 and #5-13. Similar results for other tests are shown in Appendix C. Changes in the horizontal stress as a function of surface settlement may be expressed by Eq. (5-1):

$$\Delta\sigma_h(\Delta_y) = \sigma_h(\Delta_y) - \sigma_h(0) \quad (5-1)$$

where $\Delta\sigma_h(\Delta_y)$ = Change in horizontal stress corresponding to a surface settlement of Δ_y

$\sigma_h(\Delta_y)$ = Horizontal stress corresponding to a surface settlement of Δ_y

$\sigma_h(0)$ = Horizontal stress corresponding to a zero surface settlement (i.e., at $t = 0$)

In Figures 5-15 and 5-16, the changes in horizontal stress from all of the sensors in each test are plotted. As hypothesized, results show that horizontal stress increases as surface settlement increases. Increases in horizontal stress are obviously observed when the settlement increased from 0 to 15×10^{-4} in. For surface settlement greater than 15×10^{-4} , changes in horizontal stress seem to be limited to a maximum value up to 12 psi in Figure 5-16. On the left side of the specimen, data points from Test #5-13 as shown are very scattered probably due to environmental effects e.g., temperature. The effects of temperature on red intensity values will be presented and discussed in Section 5.4.

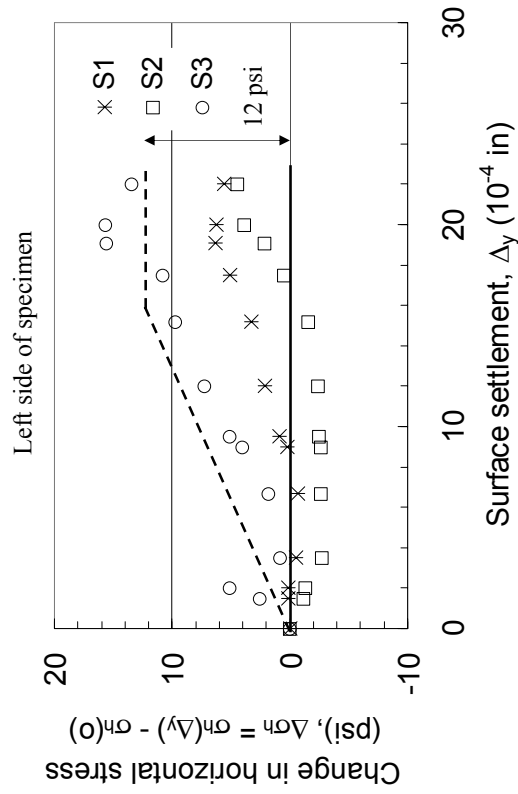
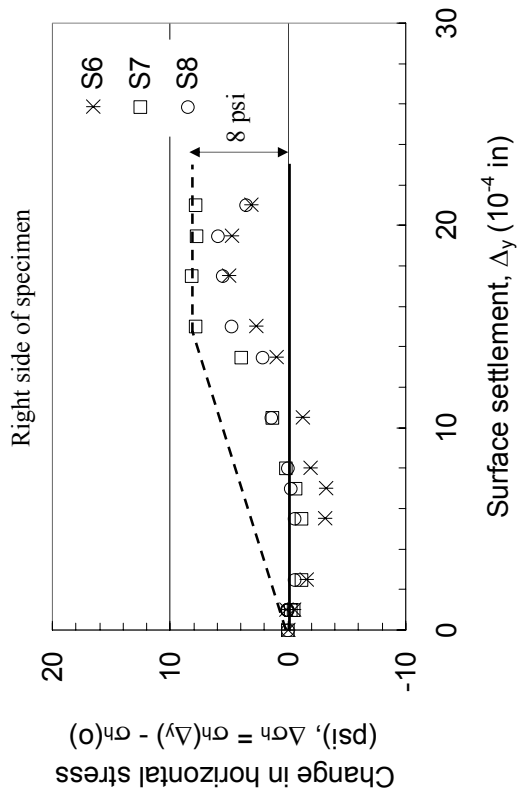


Figure 5-15 Changes in horizontal stress versus surface settlement for Test #5-10

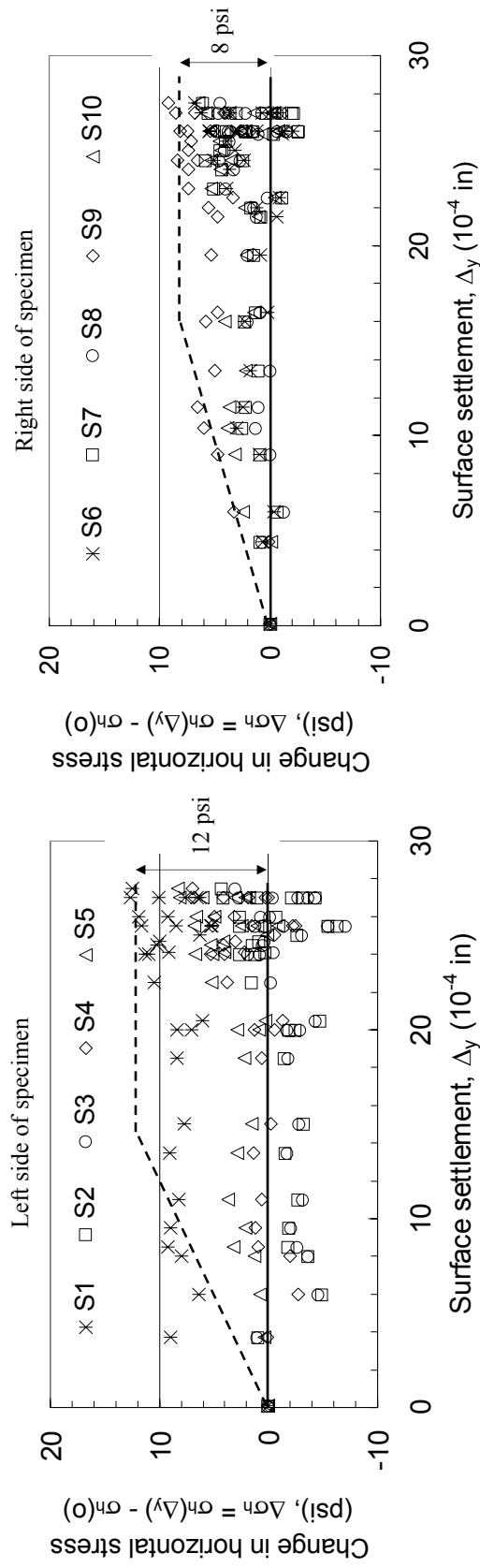


Figure 5-16 Changes in horizontal stress versus surface settlement for Test #5-13

5.3.3.2 Parametric study of time-dependent surface settlement tests

This section discusses the results from time-dependent surface settlement tests for parametric evaluation. The specimens underwent compression under K_o conditions under constant sustained vertical stress continuously for 7 to 10 days. The effects of constant vertical stress, particle shape and particle surface roughness are discussed in the following sections:

(1) Discussion on results of specimens under constant vertical stress

To study the effects of the magnitude of the vertical stress on time-dependent surface settlement, tests were performed at two levels of constant vertical stress ($\sigma_v = 23.3$ psi and 40.9 psi). Figures 5-17 to 5-18 present surface settlement versus time for the two different vertical stresses. The particles for test results shown in Figure 5-17 were for smooth cylinders while the particles for the test results in Figure 5-18 were angular prisms.

Figure 5-17 shows that the assembly of cylinders under 40.9 psi vertical stress compressed about twice as much as under 23.3 psi vertical stress. But, as may be observed in Figure 5-18 the assembly of angular prisms compressed about four times as much at 40.9 psi vertical stress than that under 23.3 psi vertical stress. This observation indicates that the compressibility of the cylinder assembly was larger than that of the angular prism assembly. The effects of particle shapes on compressibility are discussed in the following section.

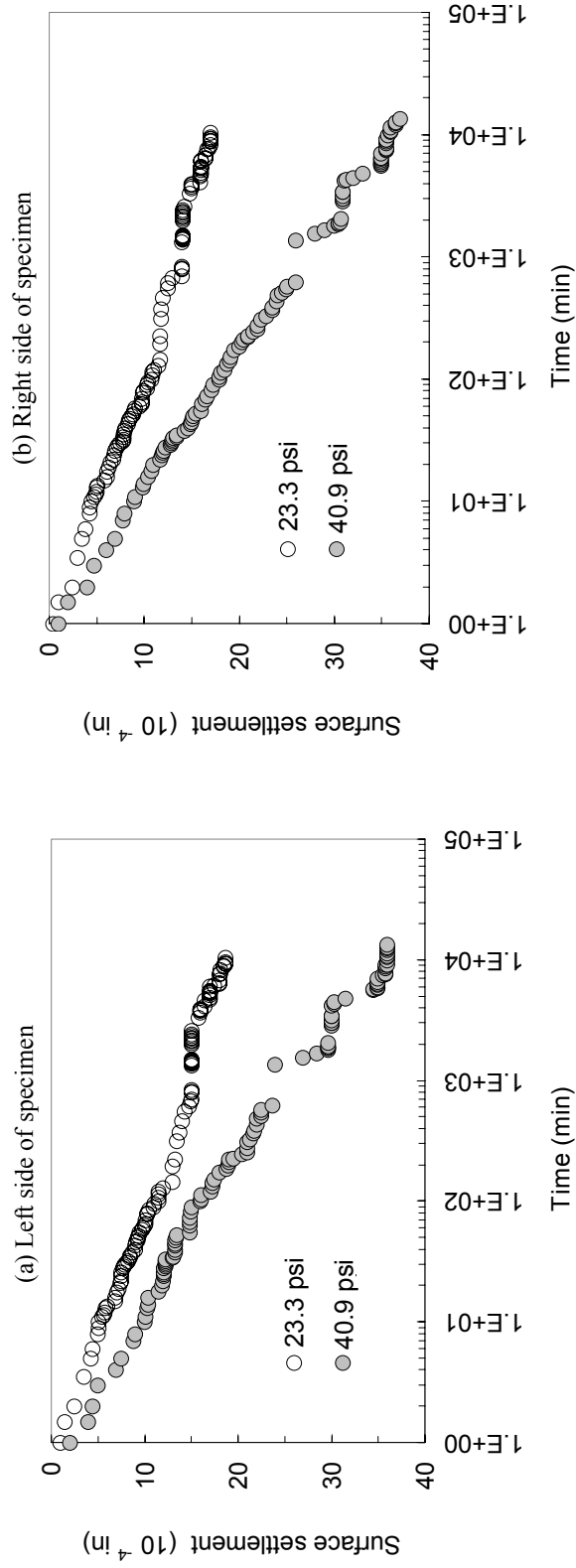


Figure 5-17 Surface settlements versus time for 7.5" x 5.0" specimens with smooth cylinders under two different vertical stresses

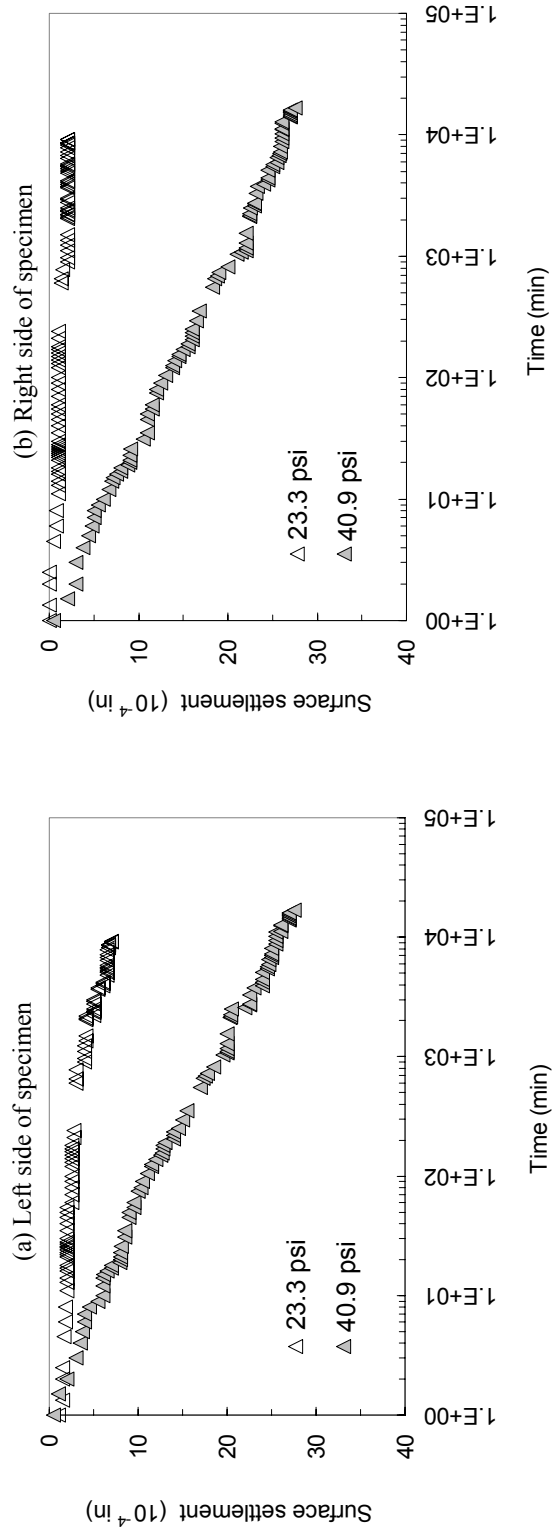


Figure 5-18 Surface settlements versus time for 7.5" x 5.0" specimens with angular prisms under two different vertical stresses

The test results indicate that time-dependent processes in granular assemblies depend on the levels of vertical stress. Regardless of particle shape specimens under high vertical stress (40.9 psi) show more surface settlement than at low vertical stress (23.3 psi). Under higher vertical stress, particles are subjected to larger intergranular driving force on individual particles compared to particles in specimens under low vertical stress. Therefore, compression of the particle assembly requires less time under high vertical stress.

(2) Discussion of particle shape effects

Surface settlement due to loading

This section discusses the effects of particle shape. Surface settlements versus applied vertical stress for assemblies of smooth cylinders and angular prisms during loading are shown in Figure 5-19. Based on visual observations, very little immediate settlement for the assembly of angular prisms was observed on the left side of the specimen (Figure 5-19a) during loading. This implies that particle sliding did not appear in the assembly of angular prisms because individual angular prisms were stacked in stable positions.

Friction on the contact surfaces of angular prisms prohibited large sliding of particles in the assemblies. In addition, the arrangement of angular prisms in the assembly made particle motions kinematically unfavorable. Therefore, motions of particles in the assembly of angular prisms are apparently lower than the motions of particles in the assembly of cylinders. This contributes to stiffness of assembly of angular prisms higher than that of assembly of cylinders.

Figure 5-20 shows Hardin's 1D strain model for the assemblies of smooth cylinders and angular prisms using average surface settlements from Figure 5-19. The initial void ratios were 0.26 and 0.38 for the assemblies of cylinders and angular prisms, respectively. Although angular prism particles seem to be packed efficiently in the assembly, the initial void ratio in the assembly of angular prisms is higher than that for the assembly of smooth cylinders because small cylindrical particles could be placed in the skeletal voids of larger particles in the assembly. Based on visual observations (without using photoelasticity), many cylindrical particles in the assembly appeared under the arches of particles, and the particles were not in contacts with adjacent particles.

S_{1D} was 95 for the assembly of cylinders and 278 for the assembly of angular prisms. Despite the higher void ratio ($e_o = 0.38$) of the angular prism assembly, the stiffness of the angular prism assembly was higher than that of the cylinder assembly. The lower compressibility (i.e., higher stiffness) for the assembly of angular prisms could also be attributed to the arrangement of particles in the specimens as discussed above (i.e., unfavorable motions of angular prisms are due to the arrangement of the particles in the particle assembly). The material stiffness of angular prisms and cylinders is identical. Thus, under the same contact stress applied to assemblies of cylinders and angular prisms, elastic compression is not likely to be a major contributing factor in the overall difference in contractions of the assemblies.

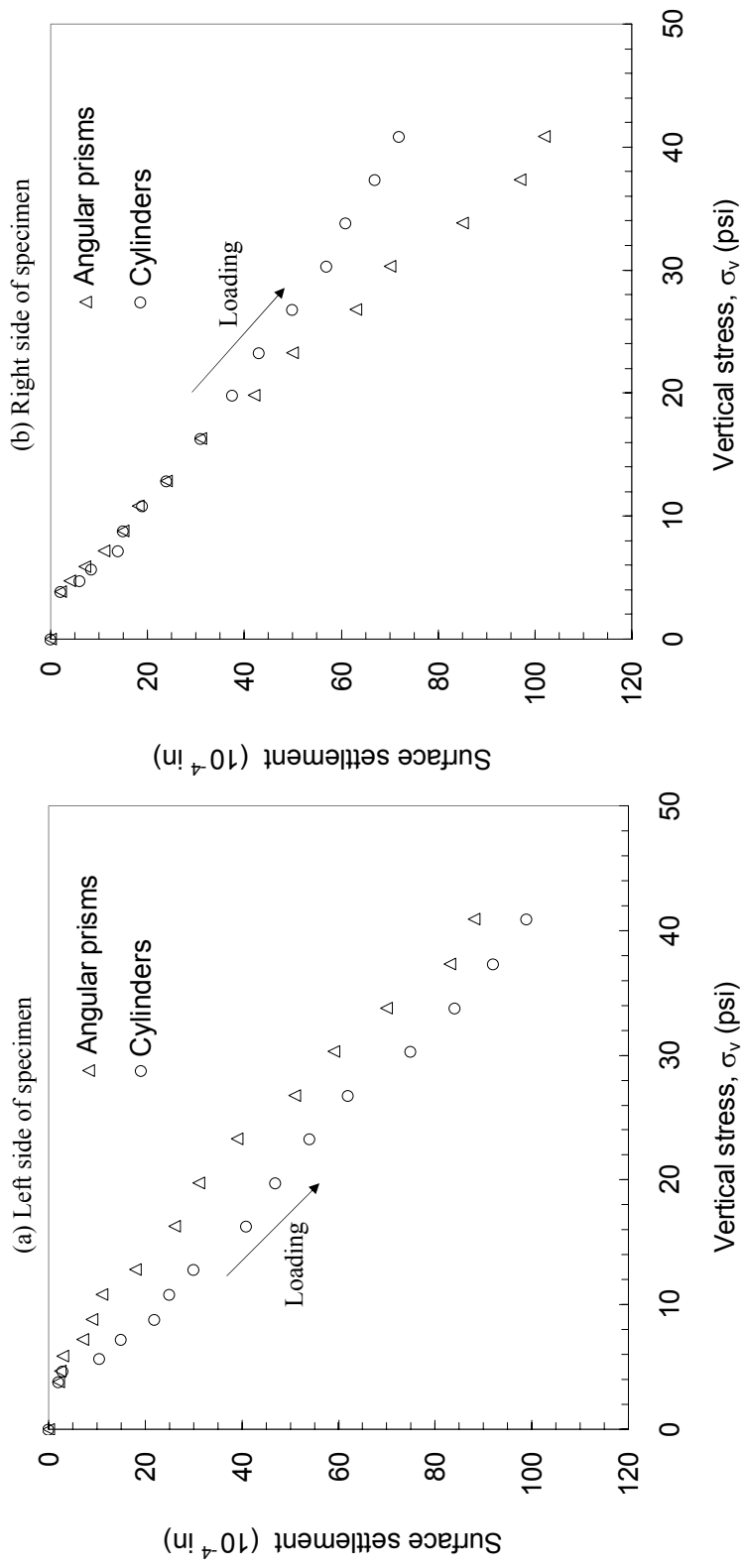


Figure 5-19 Surface settlements of 7.5" x 5.0" specimens with cylinders and angular prisms during loading

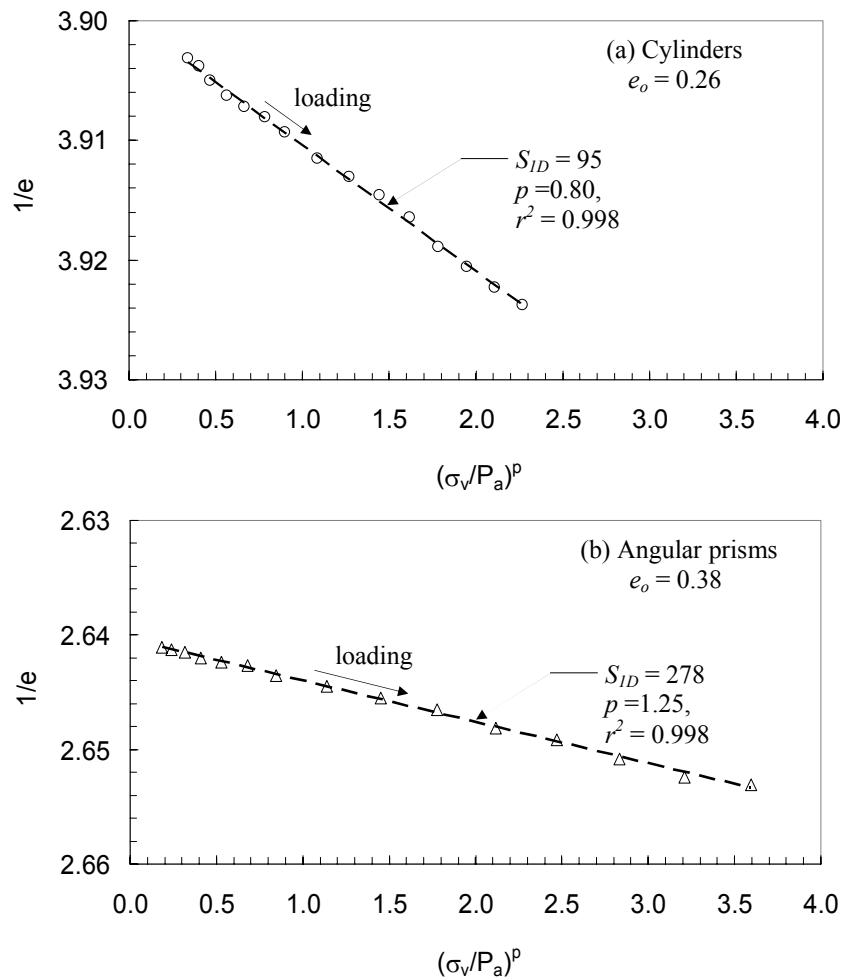


Figure 5-20 Hardin's 1D strain model for 7.5" x 5.0" specimens with (a) cylinders and (b) angular prisms

Surface settlement during incremental loading, sustained loading and unloading

This section presents surface settlement for the assemblies of cylinders and angular prisms during incremental loading, under sustained loading, and during subsequent unloading. The results of surface settlement was fitted to the Hardin's 1D strain model as discussed in the previous section. This section focuses on the discussion of the surface settlement during sustained loading and subsequent unloading.

To study the effects of particle shape, assemblies of cylinders and angular prisms were used. Figures 5-21 and 5-22 show surface settlements versus applied vertical stress during incremental loading, under sustained loading and during subsequent unloading. The time-dependent surface settlements under constant vertical stresses of 23.28 psi and 40.90 psi from Figures 5-21 and 5-22 are plotted with time and are shown in Figures 5-23 and 5-24, respectively.

Under sustained loading, surface settlement for the assembly of angular prisms was much smaller than that for the assembly of cylinders. It takes much longer for time-dependent surface settlement to occur in the angular prism assembly. During unloading, the specimens rebounded, but the slope of the surface settlement to the vertical stress was less than that during loading. This indicates permanent skeletal compression occurred in the assembly. In other words, the 2D granular assemblies did not behave elastically.

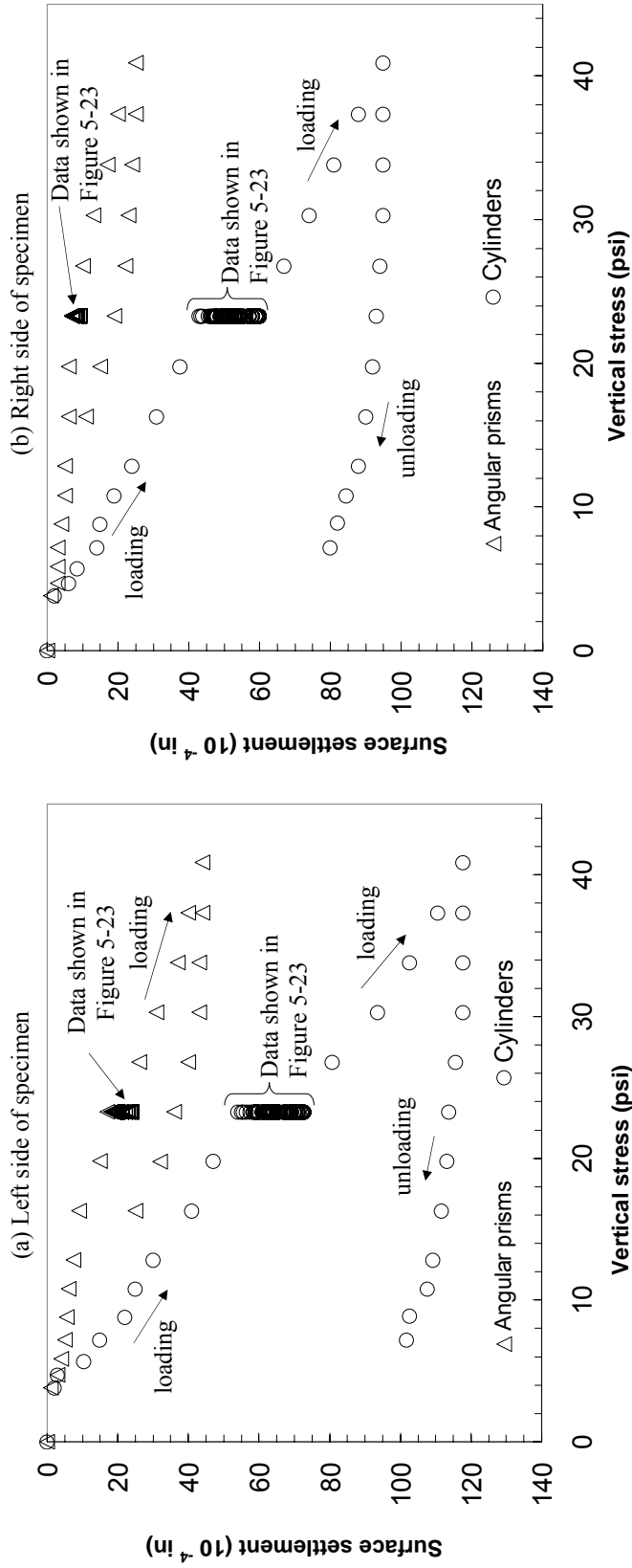


Figure 5-21 Surface settlement of 7.5" x 5.0" specimens with cylinders and angular prisms during incremental loading, under sustained vertical stress of 23.3 psi and during unloading (time-dependent surface settlement plots also shown in Figure 5-23)

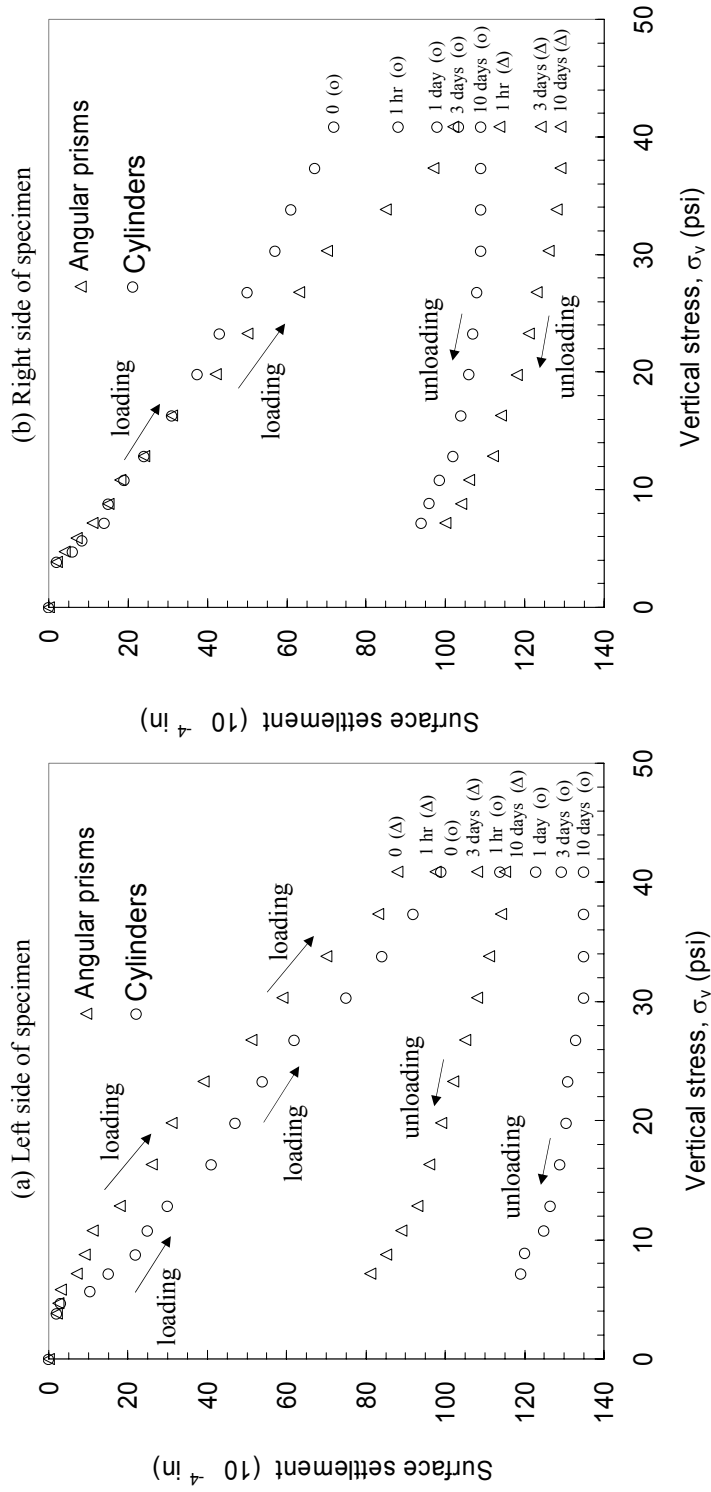


Figure 5-22 Surface settlement of 7.5" x 5.0" specimens with cylinders and angular prisms during incremental loading, under sustained vertical stress of 40.9 psi and during unloading (time-dependent surface settlement plots also shown in Figure 5-24)

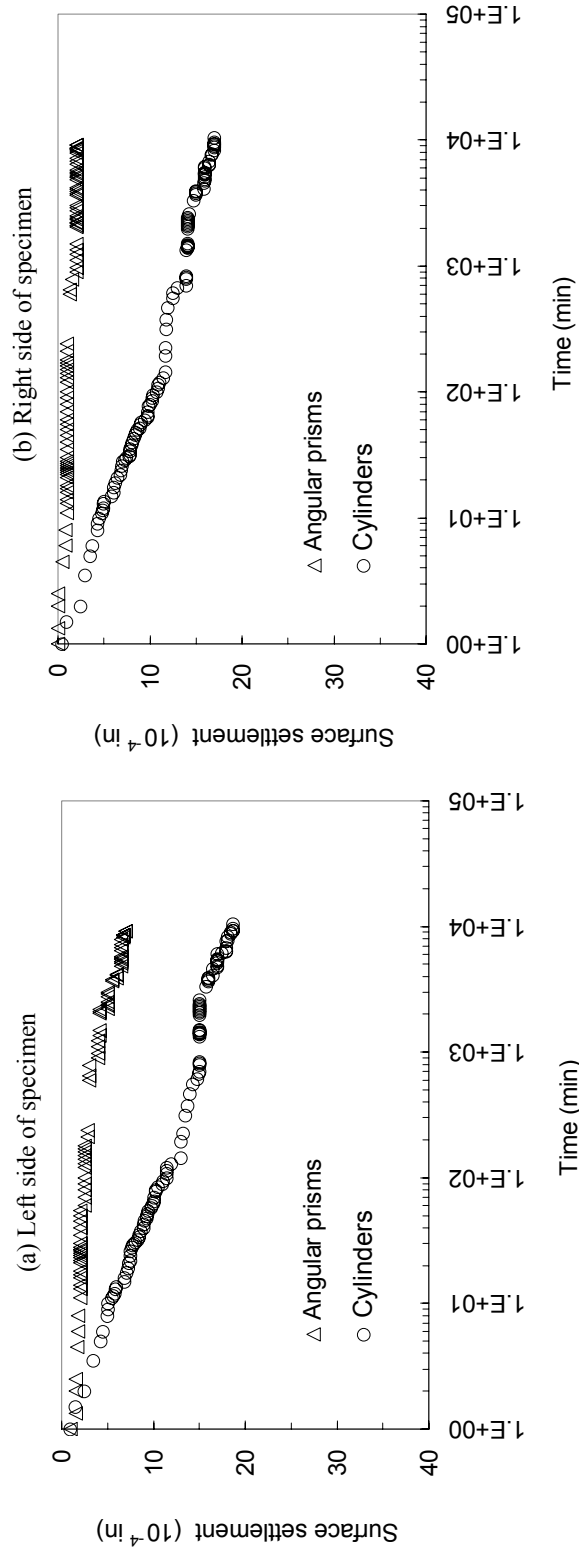


Figure 5-23 Surface settlement versus time for 7.5" x 5.0" specimens with cylinders and angular prisms under a constant vertical stress of 23.3 psi

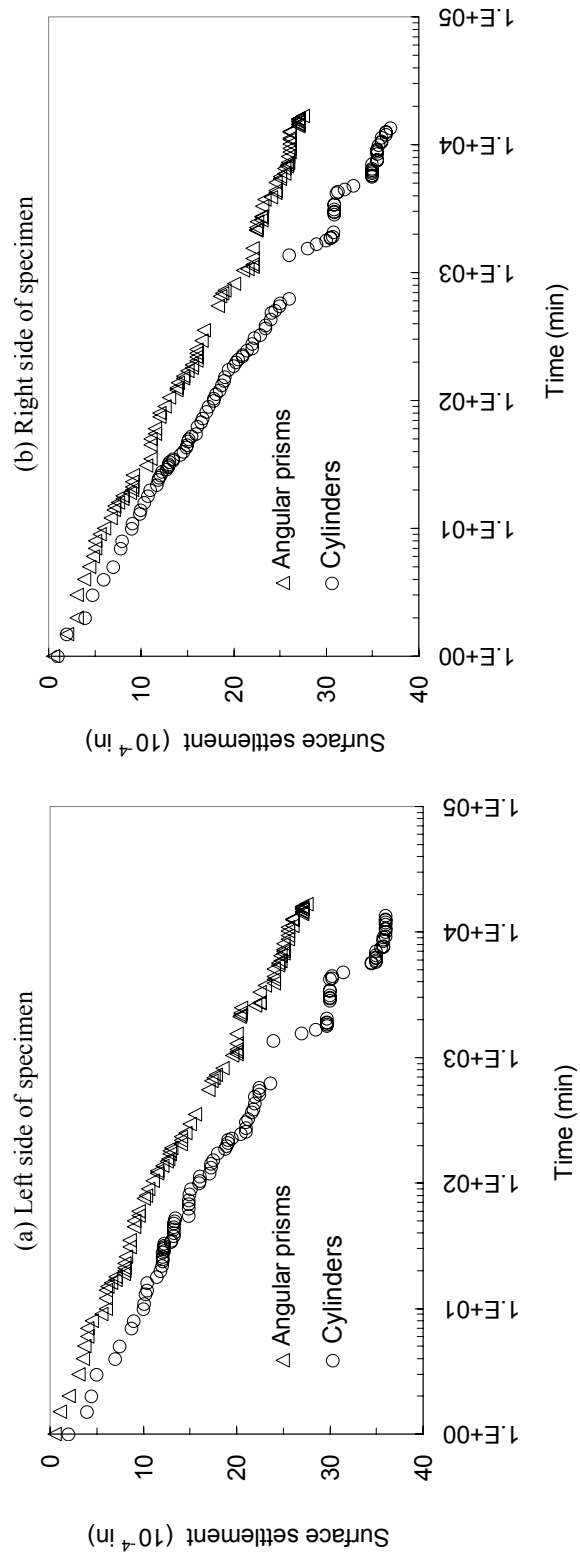


Figure 5-24 Surface settlement versus time for 7.5" x 5.0" specimens with cylinders and angular prisms under a constant vertical stress of 40.9 psi

(3) Discussion of particle surface roughness effects

Surface settlement due to loading

Surface settlement versus applied vertical stress for the assemblies of smooth and rough cylinders during loading are presented in Figure 5-25.

During loading, Figure 5-25 shows, on the left side, the surface settlement for the assembly of rough cylinders lower than that for the assembly of smooth cylinders. On the right side, the surface settlements of rough and smooth cylinders were similar.

On average, the assembly of rough cylinders showed less surface settlement than the assembly of smooth cylinders. This is attributed to greater friction at the contact surfaces of rough cylinders. The frictional surfaces of rough cylinders inhibited particle motions during loading.

Surface settlement during incremental loading, sustained loading and unloading

Figures 5-26 and 5-27 show surface settlement of specimens with smooth and rough cylinders versus applied vertical stress during incremental loading, under sustained loading, and during subsequent unloading. Time-dependent surface settlements under constant vertical stresses of 23.3 psi and 40.9 psi from Figures 5-26 and 5-27 are plotted with time shown in Figures 5-28 and 5-29, respectively.

Figures 5-26 and 5-27 confirm that the 2D granular assemblies do not behave elastically. During loading, volume contraction and elastic compression of particles resulted in settlement. Upon unloading, the small rebound of the specimen surface was probably due to elastic expansion of the particles.

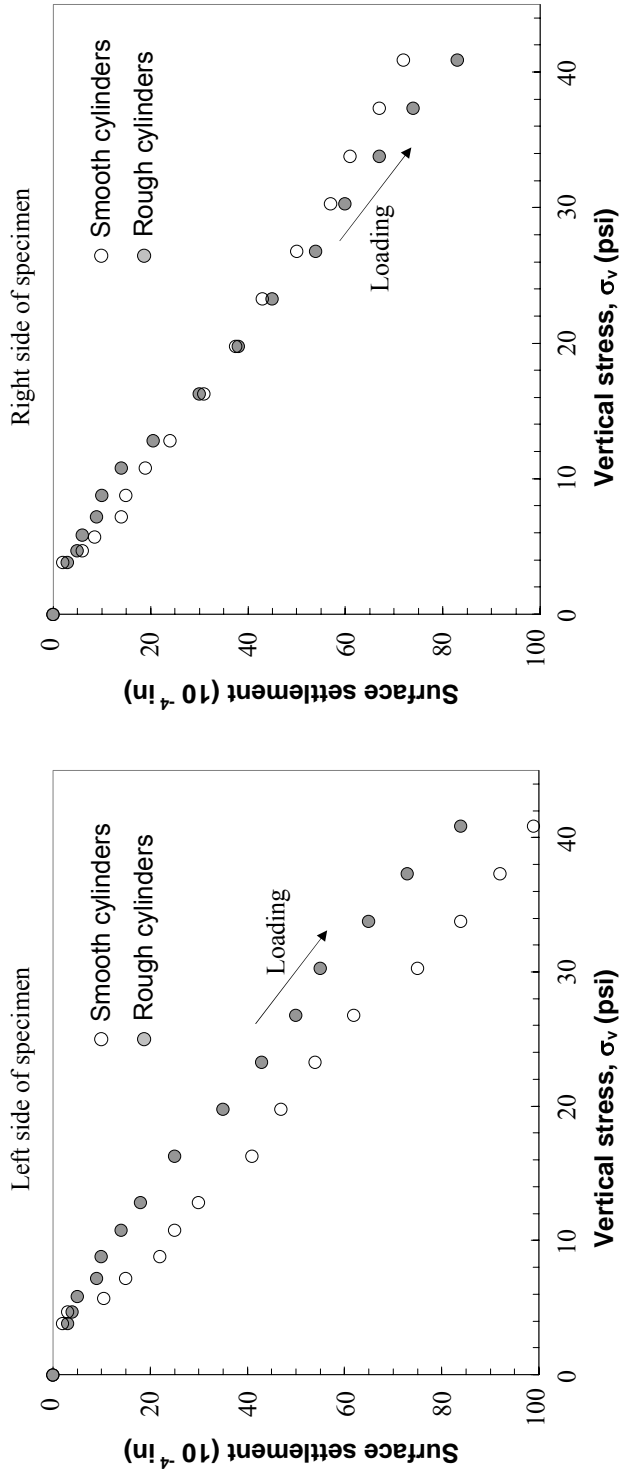


Figure 5-25 Surface settlement of 7.5" x 5.0" specimens with smooth and rough cylinders during loading

Figures 5-28 and 5-29 show surface settlement versus time for the assemblies of smooth and rough cylinders at constant vertical stresses of 23.3 psi and 40.9 psi, respectively. Time-dependent surface settlement occurs at a slower rate in an assembly of rough cylinders than in an assembly of smooth cylinders. During unloading, the specimen surfaces rebounded. The assemblies of smooth and rough cylinders upon unloading behave similarly. Permanent vertical deformation was also observed.

Figure 5-28 shows that at ages between 0 and 300 minutes, surface settlements for the assemblies of smooth and rough cylinder were similar. For age greater than 300 minutes, the assembly of rough cylinders continued to settle until about 1000 minutes. After 1000 minutes (about 1 day), additional surface settlement of the rough cylinder assembly was only 2×10^{-4} in., while the surface of the smooth cylinder assembly seemingly continued to settle.

Figure 5-29 shows that time-dependent surface settlement for the rough cylinder assembly was smaller than the settlement of the smooth cylinder assembly. As previously discussed, this could be attributed to friction from particle surface roughness. In the long term, further improvement of micro-interlocking of particle asperities could be developing with time via rolling and sliding of particles in the assembly. The micro-interlocking, formed with time, may enhance strength and stiffness in granular assemblies with time (Terzaghi, 1934; Mesri et al., 1990, Thomann, 1990, Schmertmann, 1987; Schmertmann, 1991; Barton, 1993; Bowman and Soga, 2003; Mitchell, 2008).

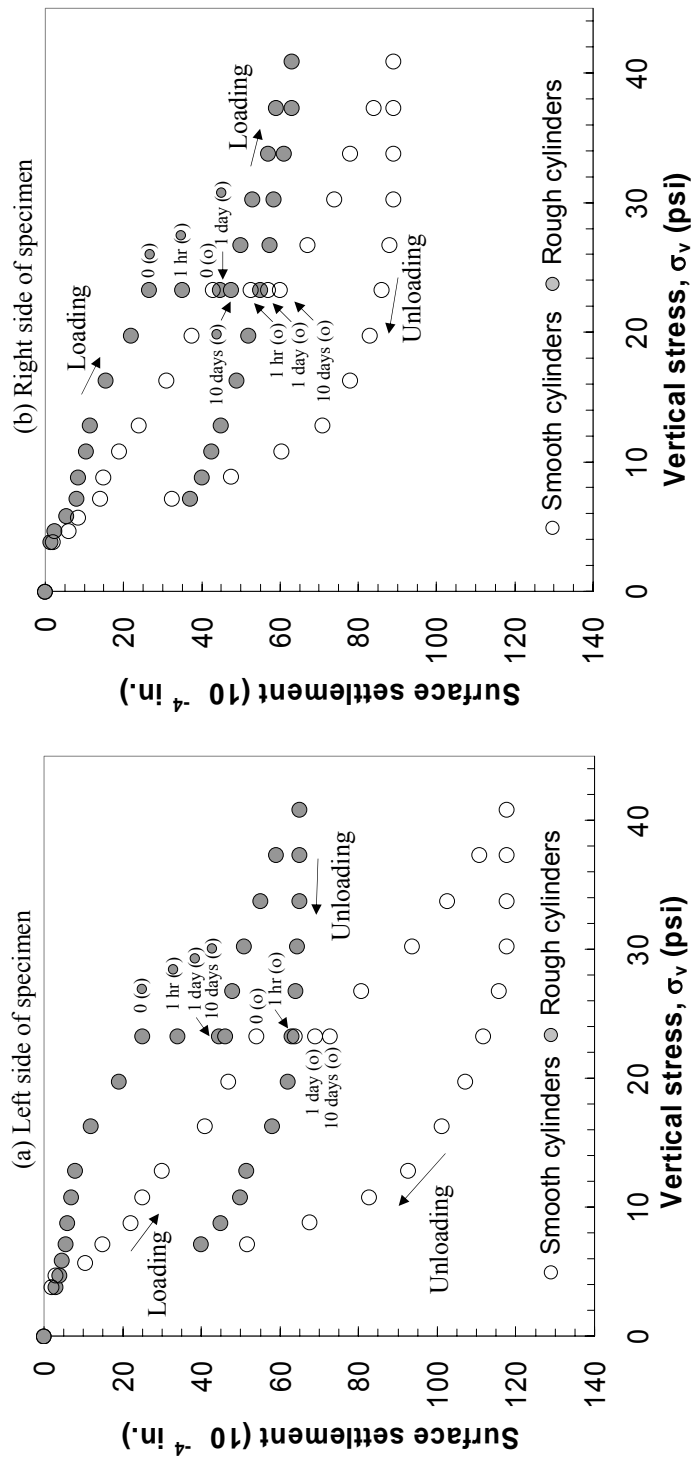


Figure 5-26 Surface settlements of 7.5" x 5.0" specimens with smooth and rough cylinders during incremental loading, under sustained vertical stress of 23.3 psi and during unloading (time-dependent surface settlement plots also shown in Figure 5-28)

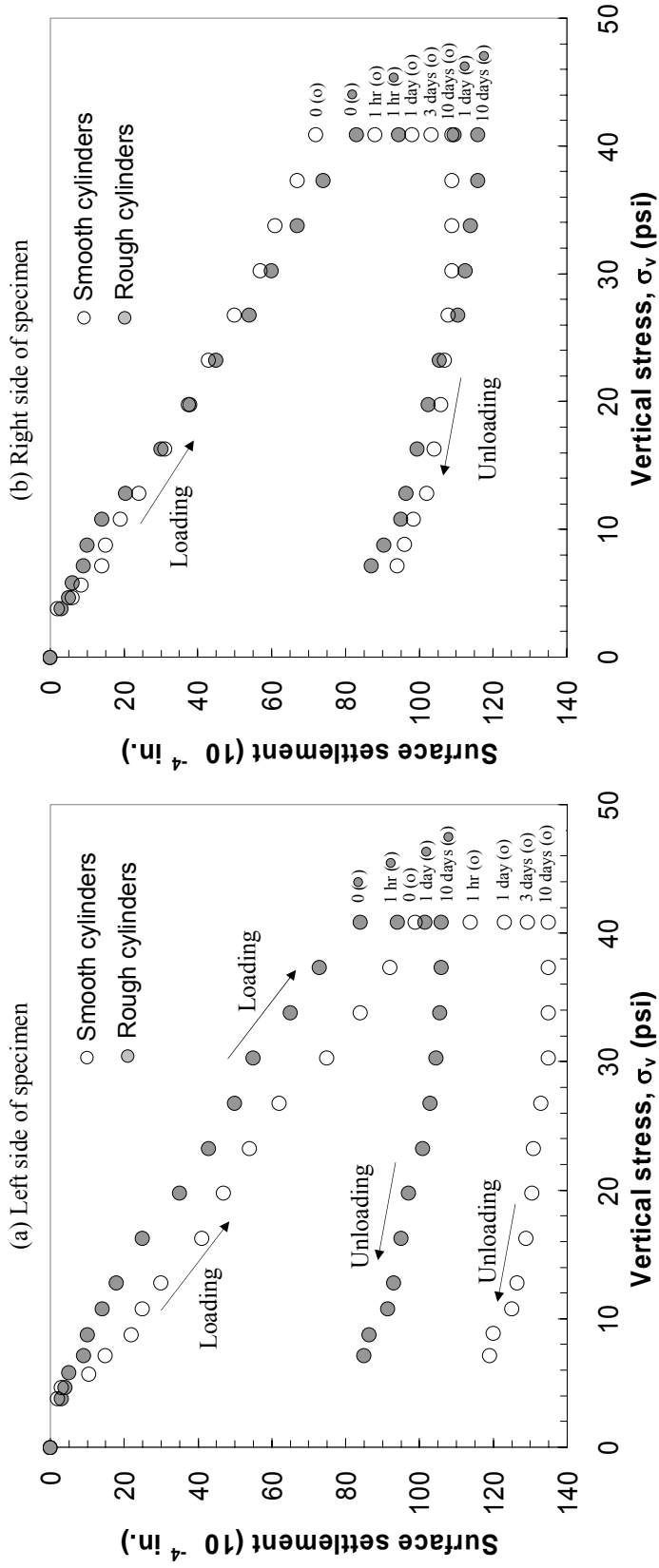
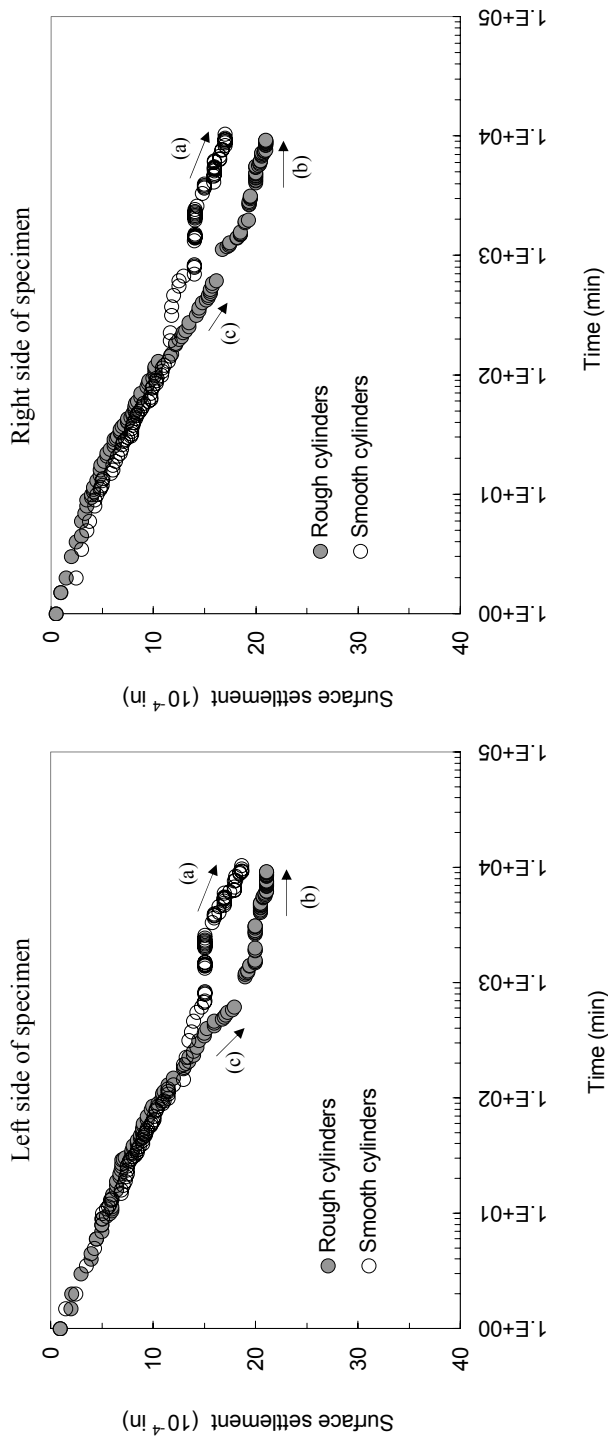


Figure 5-27 Surface settlements of 7.5" x 5.0" specimens with smooth and rough cylinders during incremental loading and under sustained vertical stress of 40.9 psi and during unloading (time-dependent surface settlement plots also shown in Figure 5-29)



- (a) Continuation of settlement for smooth cylinder assembly (while rough cylinder assembly stop to settle) after 10,000 minutes (1 week)
- (b) Rough cylinder assembly stop settling before 10,000 minutes
- (c) Settlement of rough cylinder assembly probably due to vibrations during the test

Figure 5-28 Surface settlements versus time for 7.5" x 5.0" specimens with smooth and rough cylinders under a constant vertical stress of 23.3 psi

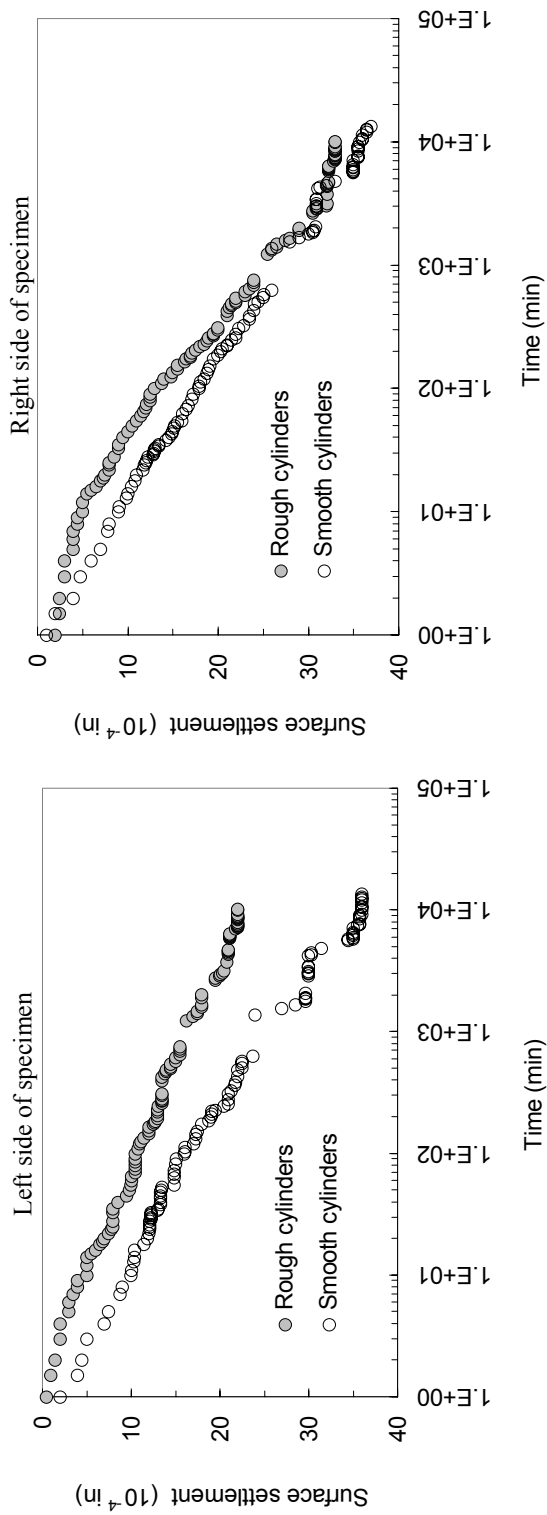


Figure 5-29 Surface settlement versus time for 7.5" x 5.0" specimens with smooth and rough cylinders under a constant vertical stress of 40.9 psi

In the hypothesis of the formation of micro-interlocking, Barton (1993) states “More effective interlocking creates a jigsaw effect and becomes a true cohesion in that shear of grains is necessary to permit the development of a complete shear surface.” For long term, micro-interlocking of grain asperities at particle contacts may be affected by chemical bonding, and becomes intergranular welding at a molecular scale (Dapples, 1972).

5.3.3.3 Analysis of Bowman’s hypothesis

This section presents the formation of force chains in granular assemblies during loading, and discusses the possibility of the force chain buckling in aged specimens as hypothesized by Bowman and Soga (2003).

Discussion of experimental results

Photos from Test #5-12 are presented herein. The photos show force chains during loading and during aging. In Test #5-12, the specimen was aged at 23.28 psi vertical stress for 7 days, during which time photos of the force chains in the specimen were captured. The specimen included 2725 smooth cylinders. After obtaining the photos of the specimen from Test #5-12, three regions in the specimen each with dimensions of 5.50" x 0.75" were selected to observe and study the formation of force chains during loading and to monitor time-dependent changes in shapes of the force chains. Figure 5-30 shows the three selected regions. Red lines were manually drawn over the force chains to better illustrate the force chains upon loading and at various times during aging.

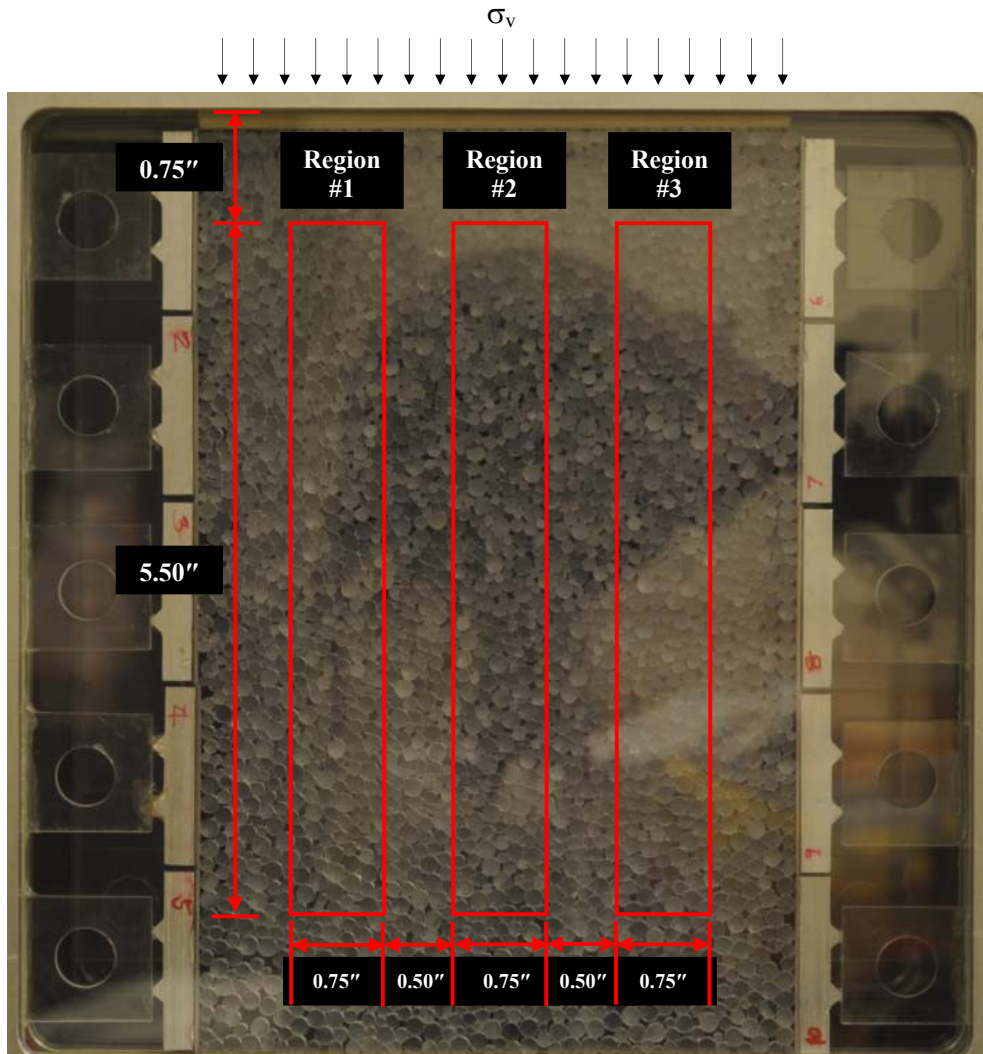


Figure 5-30 Selected regions for observing force chains in the specimen during loading and during aging

Figure 5-31 shows the formation of force chains in region #1 of the specimen during loading. Similar photos of force chains in regions #2 and #3 are included in Appendix D. The force chains are formed upon initial loading and parallel the direction of major principal stress. This observation is similar to Figure 2-11 in Chapter 2 (Oda et al, 1985; Kuhn and Mitchell, 1993; Kuhn, 1999). In Figure 2-11, Oda et al. (1985) schematically proposes that voids elongate, and the shape of the voids becomes parallel

to the direction of major principal stress. Figure 5-31 also shows that when the vertical stress increases, the number of distinguishable force chains increases. The length over which they are discernable also increases. This also demonstrates that the vertical stress applied at the specimen surface transfers into the force chains. When the vertical loading increases, this not only forms good contacts of particles, but also increases in stresses transferred into/through the force chains as visually observed by increases in color intensities in the particles in the force chains as previously discussed in Section 5.3.1 (see also Figure 5-8 for increases in color intensity of particles in force columns due to loading). The new loads applied at the specimen surface were mostly carried by pre-existing force chains.

Figure 5-32 shows force chains versus time in region #1 under a constant vertical stress of 23.28 psi. It shows that the shapes of the force chains change with time. During aging, particles rearrange to reduce shearing (frictional) stress at individual particle contacts (Terzaghi, 1934; Schmertmann, 1991). At the beginning (i.e., no age), the force chains were somewhat bent (due to previous loading from 0 psi to 23.3 psi). With time under constant the vertical loading at 23.3 psi, the vertical force chains further bend laterally, and arching of particles may locally be formed in the granular assemblies with time. After the 5th day of the test, further changes in the shapes of force chains were not visually observed. Also, further surface settlement after the 5th day was relatively small. Future tests using a larger specimen with more particles are recommended to gain a better understanding (into the formation of particle arches during loading and during aging), and to examine (and possibly validate) Bowman's hypothesized aging mechanism. Discussion of Bowman's hypothesis is included in the following section.

Discussion of hypothesized aging mechanism

According to Radjai et al. (1998) and Bowman and Soga (2003), strong force networks appear to be the (vertical) chains (assuming that σ_1 is in the vertical direction) through which forces are transmitted while weak force networks support the force chains laterally. Particles in the weak force network carry less loads than the particles in the vertical force chains. Particles in the weak networks tend to rearrange themselves. Finally, the weak networks would move away from the chains, resulting in the formation of self-supporting networks (i.e., arches of particles). However, this study did not show experimental evidence of the force chain buckling. Larger specimens may be needed to confirm this hypothesis of the formation of the particle arching networks during aging. As discussed in the previous section, experimental results show the possibility for the formation of self-supporting (arching) network with time. However, this study showed results different from Bowman's hypothesized mechanism of buckling of force chains with time due to disappearance of lateral support from nearby weak force networks. This study only suggests that Bowman's mechanism may occur as shown by changes in the shape of the force chains. A conceptual buckling of the force chains (as shown in Figure 2-13 by Bowman and Soga, 2003) may be better observed locally when a larger specimen is used for testing.

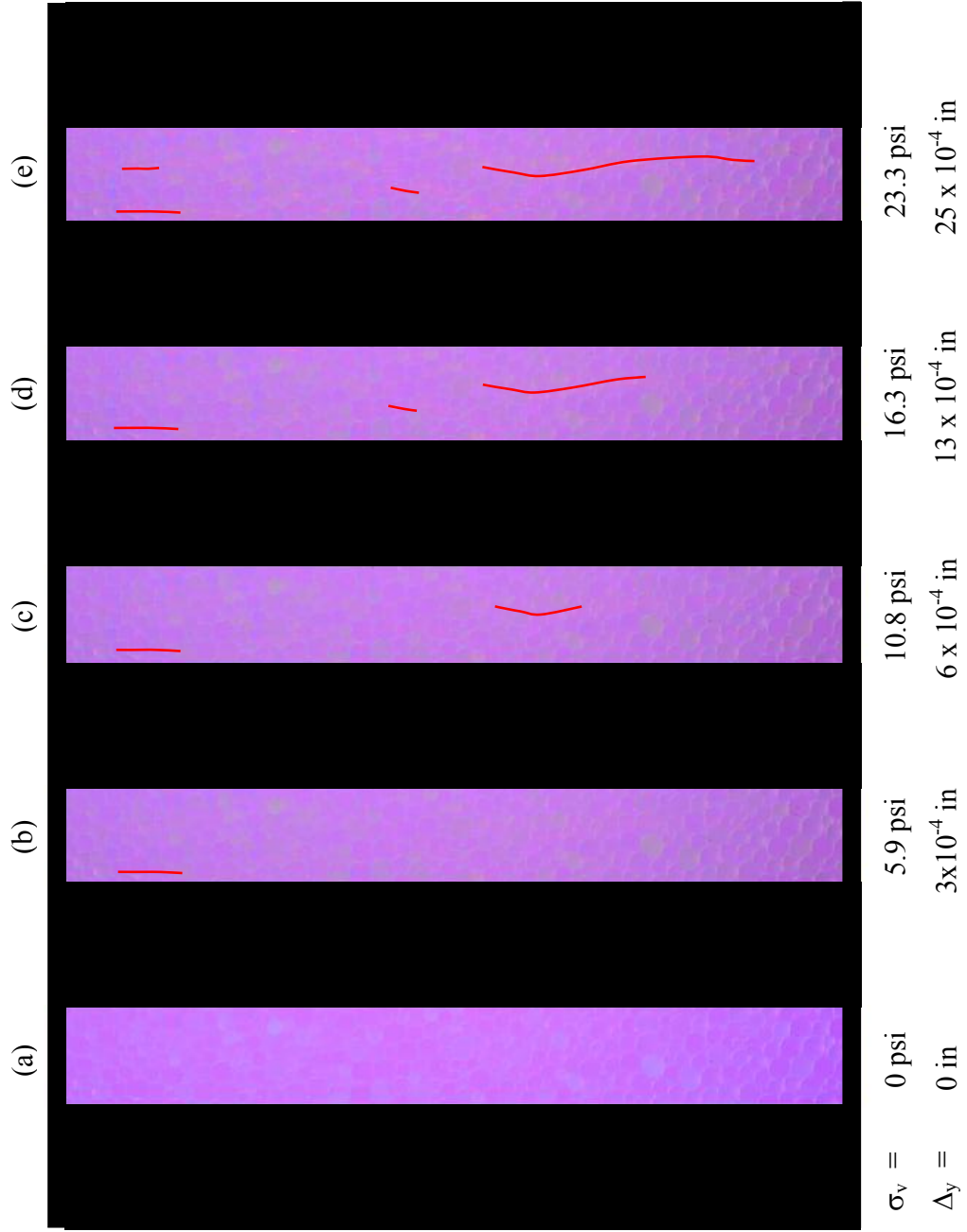


Figure 5-31 Formations of force chains in the direction of major principal (vertical) stress in region #1 during loading from 0 psi to 23.3 psi (see Figure 5-30 for the location of region #1)

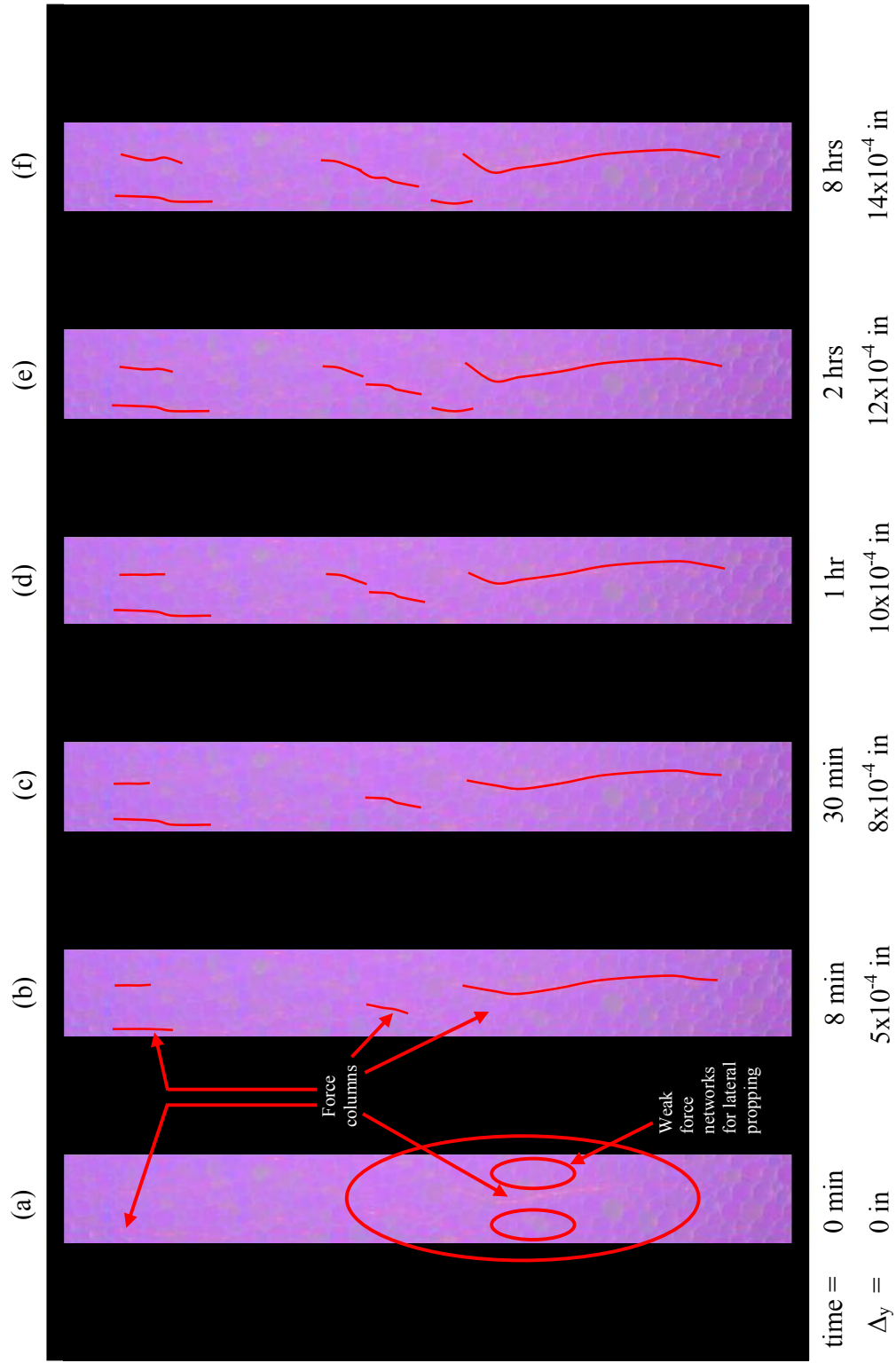


Figure 5-32 Force chains versus time in the region #1 under a constant vertical stress of 23.3 psi (see Figure 5-30 for the location of region #1)

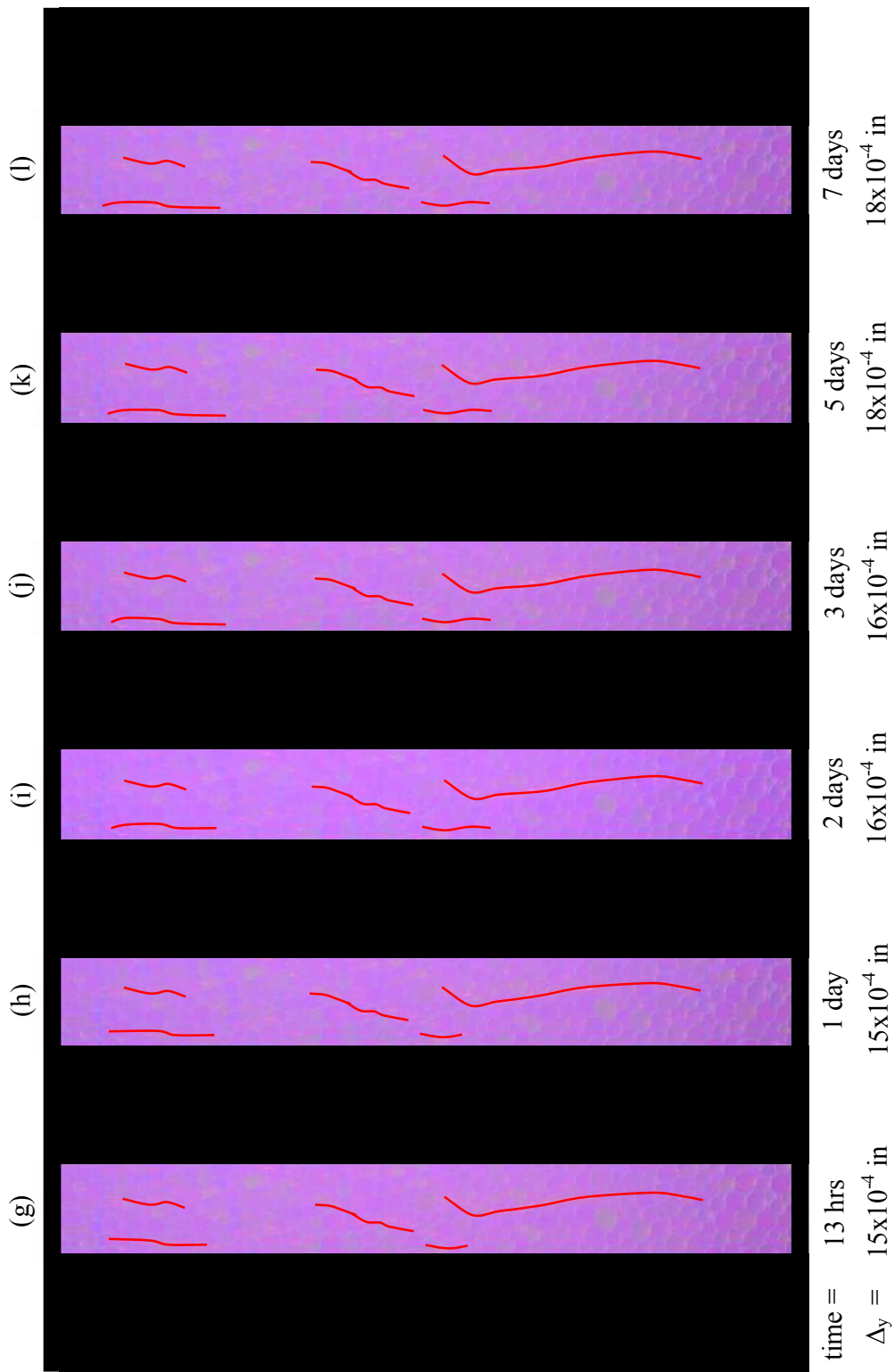


Figure 5-32 (cont.) Force chains versus time in region #1 under a constant vertical stress of 23.3 psi (see Figure 5-30 for the location of region #1)

It is believed that the force chains would be bent further during aging. In the end, this process may create arches of particles that are self-supporting networks. During this process, loads may be transferred laterally, thereby resulting in an increase in horizontal stress. For future study, changes in the shape of force chains would be better observed using a larger specimen with more particles and loaded for a longer period of time.

This study also revealed that mechanical aging due to particle rearrangement should occur with time. Particle rearrangement involves particle sliding and rotation (Kuhn and Mitchell, 1993; Kuhn, 1999; Bowman, 2002; Bowman and Soga, 2003). In this study, it was manifested by time-dependent surface settlement of 2D granular assemblies. During aging, particles rearrange into more stable positions in which they possess reduced shearing (frictional) stress at particle contacts (Terzaghi, 1934; Mesri, 1990; Schmertmann, 1987; Schmertmann, 1991).

When unloading, results showed that permanent vertical deformation occurred. Rebounding at the specimen surface should likely come from elastic expansion of the glass particles in the granular assemblies. This indicates inelastic behavior of the 2D granular assemblies. During aging, there is a permanent settlement. The combination of vertical strains and a condition of global constraint against lateral expansion (K_0 condition) while local lateral strains do occur results in a reorientation of interparticle force resultants to a more horizontal direction, thereby increasing horizontal stress. Upon unloading, the particles remain interlocked and thus, the developed horizontal stress are not relieved.

CHAPTER VI

CONCLUSIONS AND RECOMMENDATIONS

6.1 Conclusions

A test apparatus has been developed for particulate micromechanics research using photoelasticity. Photoelasticity is a well-known method for measuring stresses in solid translucent materials. Most commonly, stresses are determined from developed photoelastic fringes. The in-plane principal stress difference can be estimated using the phase difference or retardation (δ) of light waves that pass through the stressed photoelastic materials.

In this study, digital image processing for intensities of light color (*RGB*) was employed to analyze photos of stressed specimens of glass particles. The assemblies of glass particles were used to simulate sand grains. Shapes of the glass particles included cylinders and angular prisms. This study used three sets of the glass particles:

- (a) Cylindrical particles with smooth contact surfaces,
- (b) Cylindrical particles with rough contact surfaces, and
- (c) Angular prism particles with rough contact surfaces.

Hardin's dimensionless stiffness coefficient for 1D strain (S_{1D}) was used to quantify the stiffness of the 2D granular assemblies. The value of p in the term $(\sigma_v/p_a)^p$ for 1D strain model was found to depend on the geometry of the glass particles and is believed to also depend on the dimensionality (2D versus 3D) of the particle assembly. In this study, the value of p ranged between 0.80 and 1.25 for the 2D materials tested whereas Hardin (1987) proposed $p = 0.5$ for real normally consolidated sands.

Glass plates having a central hole were manufactured for use as force sensors for determination of horizontal stress and estimation of K_o in the 2D granular assemblies. Prior to testing, the glass plate sensors were calibrated. Calibration charts showing relative red intensity ($R_o - R_\sigma$) versus dimensionless applied stress (σ_v/p_a) were developed for ten such sensors. A quadratic equation fits the calibration lines very well. The correlation coefficients (r^2) were greater than 0.975, indicating a strong relationship between $R_o - R_\sigma$ and σ_v/p_a .

The calibrated glass plate sensors were attached to the side of the test box. These glass plate photoelastic sensors were employed for determining horizontal stress of the 2D granular assemblies during loading-unloading, and for monitoring horizontal stress of the specimens at various times under sustained vertical loading.

The horizontal stresses in the assembly of glass particles were determined through the relative red intensity at two pre-selected points on each of the glass plate sensors. The system was successful at determining horizontal stress in 2D granular assemblies, and for estimating K_o . In this study, K_o in the 2D granular assemblies ranged between 0.30 and 0.89. Table 6-1 summarizes the values of K_o determined for Test #5-1 to Test #5-7. Variations in the values of K_o were attributed to unbalanced loading, which in turn may

have been due to the loading rate. The glass plate sensors and an associated relative red intensity with calibration curves may be adapted for other scientific uses and engineering applications.

Table 6-1 Summary of K_o values

Test #	Depth of specimens (in)		K_o	
	from	to	Left	Right
5-1	0	1.5	0.84	0.42
5-2	0	1.5	0.45	0.35
5-3	0	1.5	0.69	0.50
5-4	0	1.5	0.51	0.40
5-5	0	1.5	0.63	0.51
5-6	0	1.5	0.38	0.38
5-7	0	1.5	0.55	0.47
5-7	1.5	3.0	0.62	0.70
5-7	3.0	4.5	0.89	0.30

Based on the test results from this study, mechanical aging due to particle rearrangement is proposed to be a viable mechanism for aging in granular assemblies. In this study, time-dependent surface settlement were observed to be likely due to rearrangement of particles. This ultimately resulted in time-dependent increases in the horizontal stress in the granular assemblies which were restrained against global lateral expansion while the assemblies strained vertically.

Particle seating likely results in reductions of shearing stresses at the particle contacts containing shearing stress higher than frictional resistance. Afterward, new contacts with reduced shearing stresses probably develop, thereby reducing the degree of particle rearrangement with time. After particle seating, the stable contacts with increased

frictional resistance and improved micro-interlocking contribute to an increase in stiffness and strength of the particulate assembly.

Particle seating should occur particularly at small contacts that exists primarily at low confining pressure. The particle seating could involve some shearing off of grain asperities, after which the particles may rapidly move into improved seating with larger contact areas. At high confining pressures, better contacts of particles with increased micro-interlocking may already have formed. Contacts of particles under high confining pressure would result in particles sliding and/or rolling.

Time-dependent surface settlement was observed to depend on the magnitude of the applied vertical stress, particle shape, and particle surface roughness.

- Stress is transferred from the specimen surface through force chains paralleling the major principal stress. Individual particles in the granular assemblies rearrange/move due to intergranular (shearing) forces imposed on the particles. Therefore, time-dependent surface settlement and particle rearrangement occur more rapidly at higher vertical stresses.
- Assemblies of cylindrical particles showed more surface settlement than those of angular prism particles under the same applied stress. By visual observation, individual angular prism particles in the assembly were placed efficiently on adjacent particles. Face-to-face contacts of angular prisms resulted in larger contact areas than the contact areas of cylinders under the same compressive stress. The arrangement of angular prisms makes particle motion kinematically unfavorable compared to assemblies of cylinders. Unlike cylinders, the angular prisms could not roll.

- Surface settlement for assemblies of smooth cylinders was higher than those for assemblies of rough cylinders. Friction from particle surface roughness may delay particle arrangement from occurring in the assemblies of rough cylinders. But, micro-interlocking of surface roughness may be developed with time and it may increase strength and stiffness of granular assemblies.

Extensions and new formation of force chains were observed during loading. This observation indicates more loads, from the specimen surface, transferred into/through the force chains via particle contacts. Results from this study partially support the aging mechanisms proposed by Bowman and Soga (2003). Bowman's hypothesis is supported by the observed time-dependent changes in the patterns of force chains. However, force chain buckling (as shown in Figure 2-13) as hypothesized by Bowman and Soga (2003) was not fully confirmed in this study. In this study, the force chains were observed to bend with time. This may ultimately result in the formation of the arches of particles through which forces are transferred laterally. Therefore, this process would result in an increase of horizontal stress. Larger specimens are recommended for better observation of time-dependent changes in patterns of force columns, and for examining Bowman's hypothesized aging mechanisms which may finally explain the time-dependent improvement of strength and stiffness, possibly due to increases in horizontal stress in granular assemblies.

6.2 Recommendations for future research

6.2.1 Other applications for the use of relative red intensity in stressed photoelastic materials and the developed glass plate sensors are recommended as follows:

- To measure horizontal stress of specimens with 3D granular assemblies, such as the assemblies of sand particles, crushed glass, glass beads, etc.
- To estimate other coefficients of lateral earth pressure, i.e., K_a and K_p , of granular assemblies.
- To study the effects of overconsolidation on the values of coefficients of lateral earth pressure (K_o , K_a and K_p).

6.2.2 Study of stresses at particle contacts for 2D and 3D granular assemblies are recommended for future study.

6.2.3 Larger dimensions of test specimens are recommended for studying the patterns of force chains, and for testing Bowman's hypothesized mechanisms of time-dependent buckling of the force chain columns.

6.2.4 In this study, the location of the light source during calibration of the glass plate sensors was different from the location when the sensors were used for the measurements of horizontal stress of the granular assemblies. And, the sensors were not recalibrated in their final locations. Consequently, it had been questioned whether the calibration charts of individual sensors could always be employed for estimating the horizontal stress of 2D granular assemblies. Therefore, further development of the system and test apparatus' glass plate sensors is recommended to address this issue.

6.2.6 Further studies are needed to investigate the temperature effects on red intensity values in the photoelastic sensors. Calibrations between temperature and red intensity values should be prepared.

6.2.7 Temperature in the laboratory and in the vicinity of optically measuring devices (i.e., camera, polariscope and tint plate) should be constant, particularly for long duration tests.

6.2.8 Digital cameras and/or microscopes with high resolution in terms of the number of pixels and intensities of colors, would be needed for further studies at the microscopic levels of individual glass particles in the assemblies (e.g., the study of stresses at particle contacts and the study of self-deformation of individual stressed particles).

APPENDICES

APPENDIX A

CALIBRATION CHARTS FOR SENSORS S3 TO S10 AND TEST RESULTS FROM CHAPTER 4

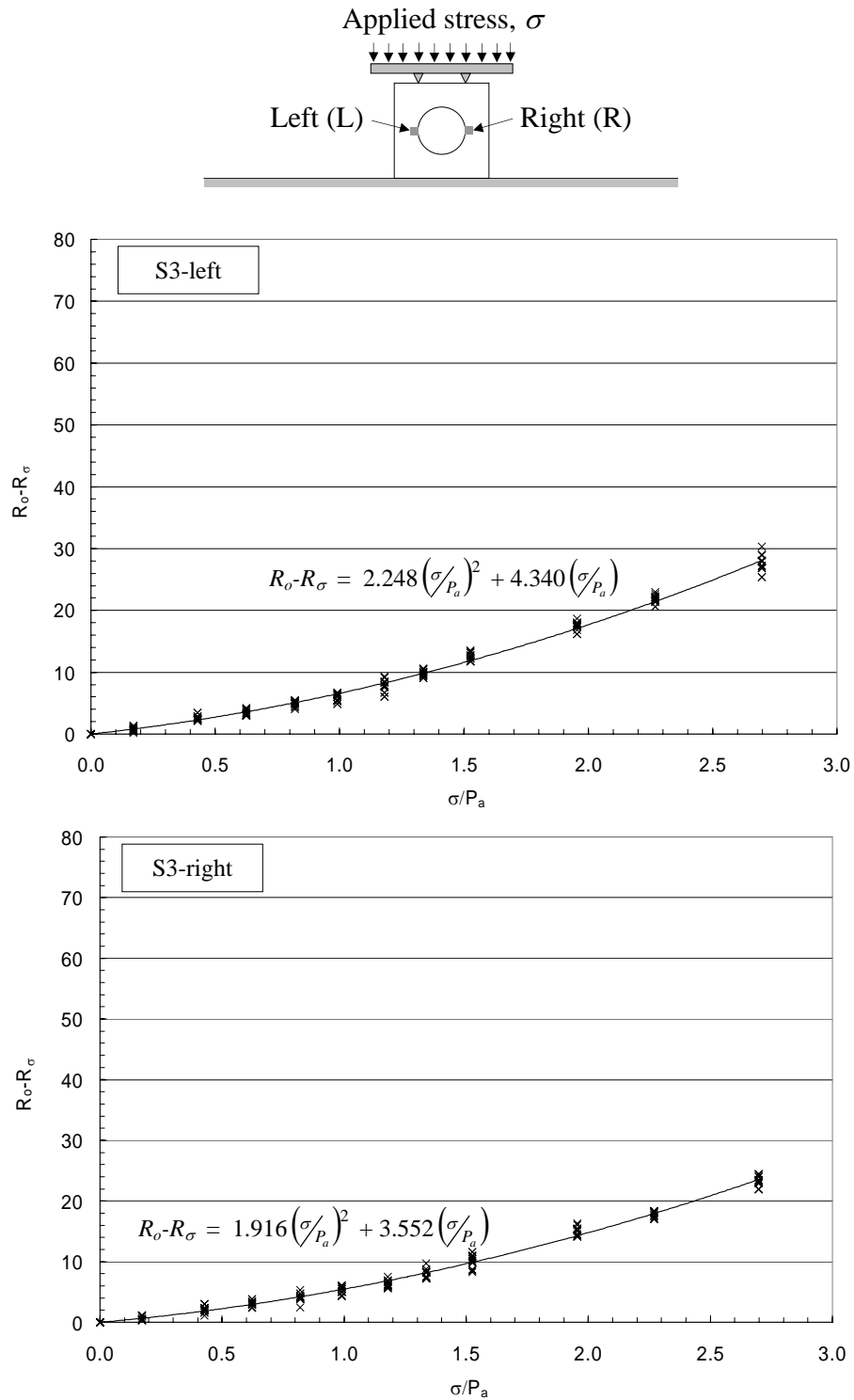


Figure A-1 Calibration charts for sensor S3 at points L (top) and R (bottom)

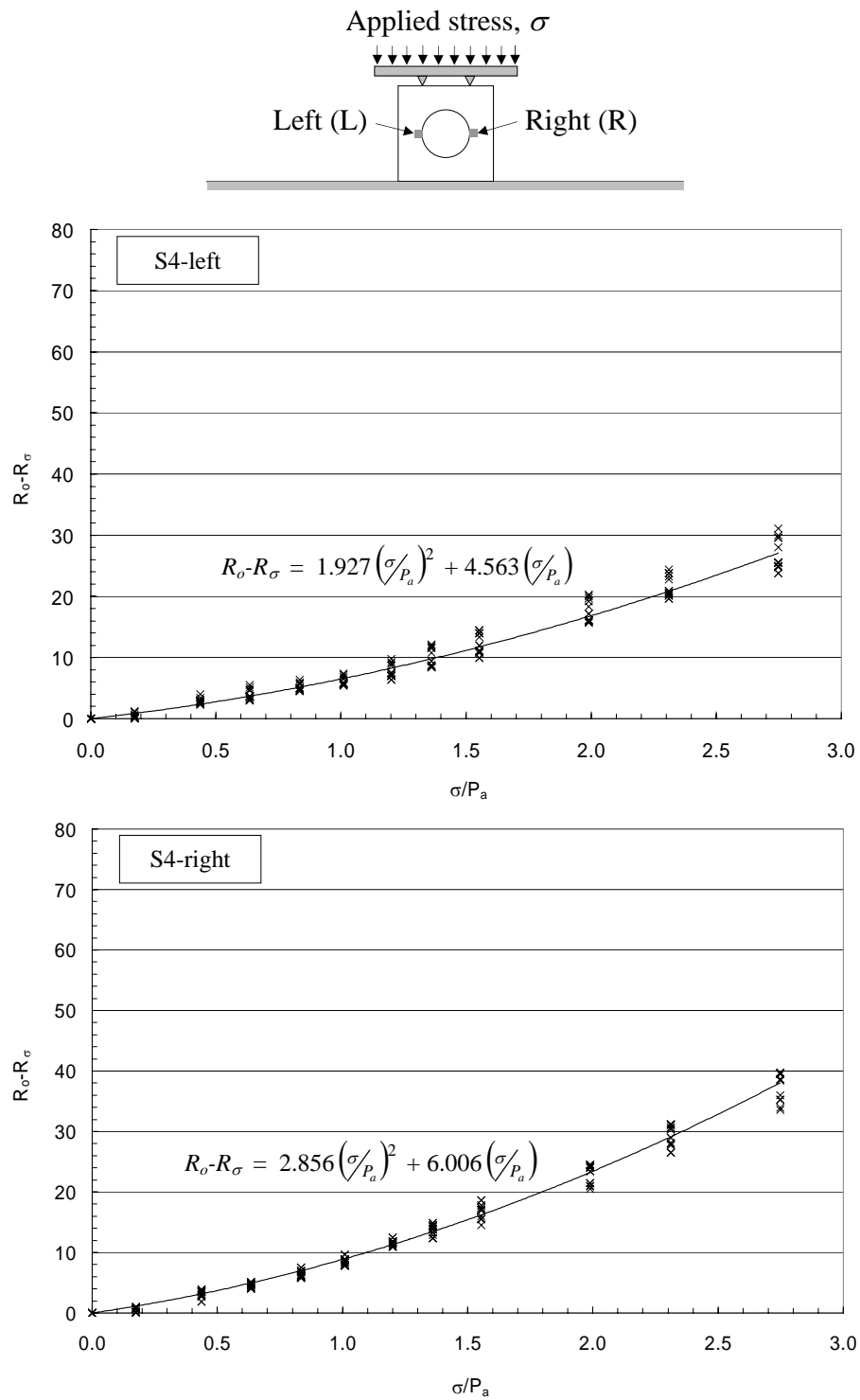


Figure A-2 Calibration charts for sensor S4 at points L (top) and R (bottom)

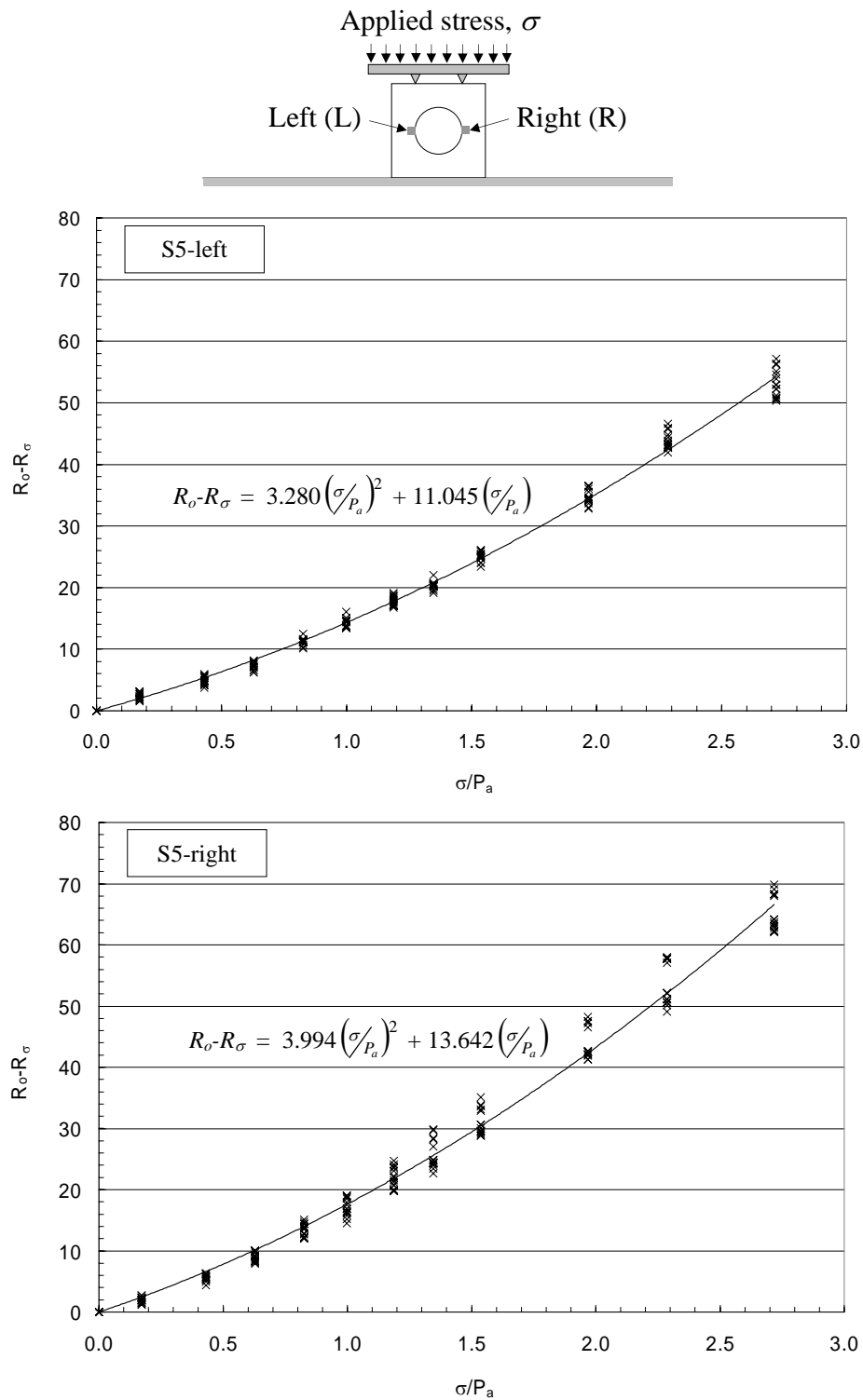


Figure A-3 Calibration charts for sensor S5 at points L (top) and R (bottom)

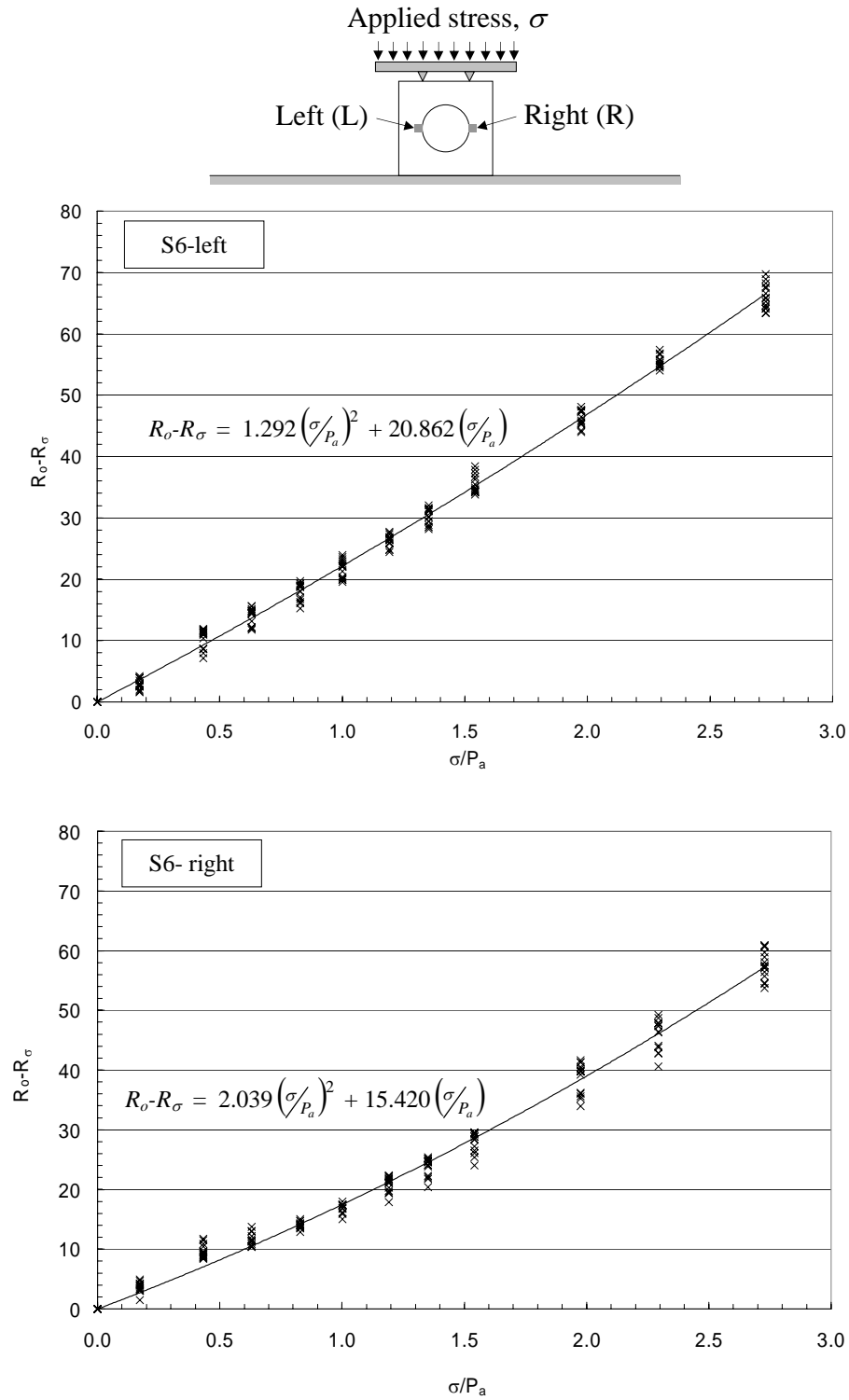


Figure A-4 Calibration charts for sensor S6 at points L (top) and R (bottom)

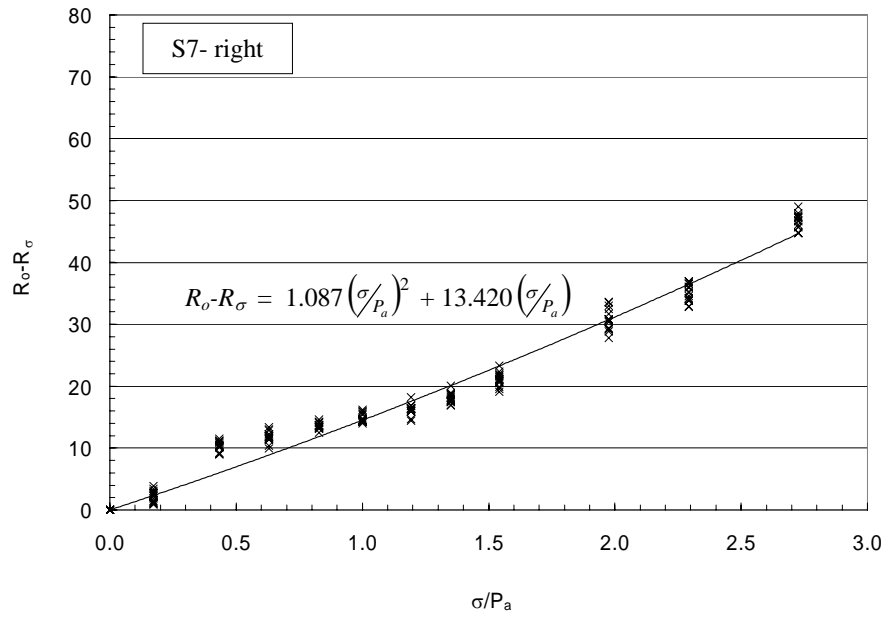
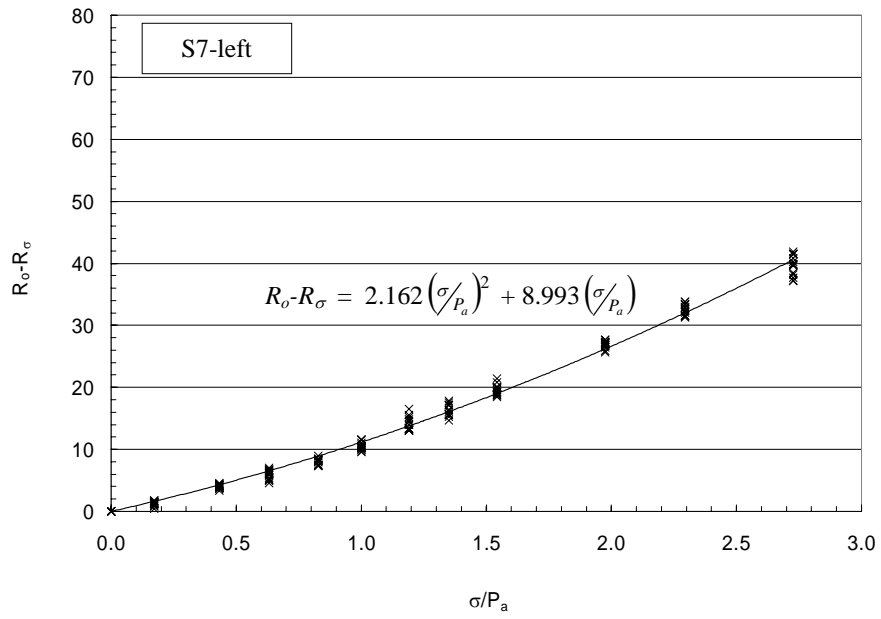
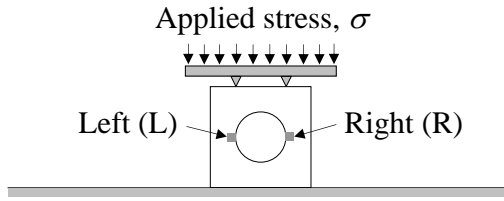


Figure A-5 Calibration charts for sensor S7 at points L (top) and R (bottom)

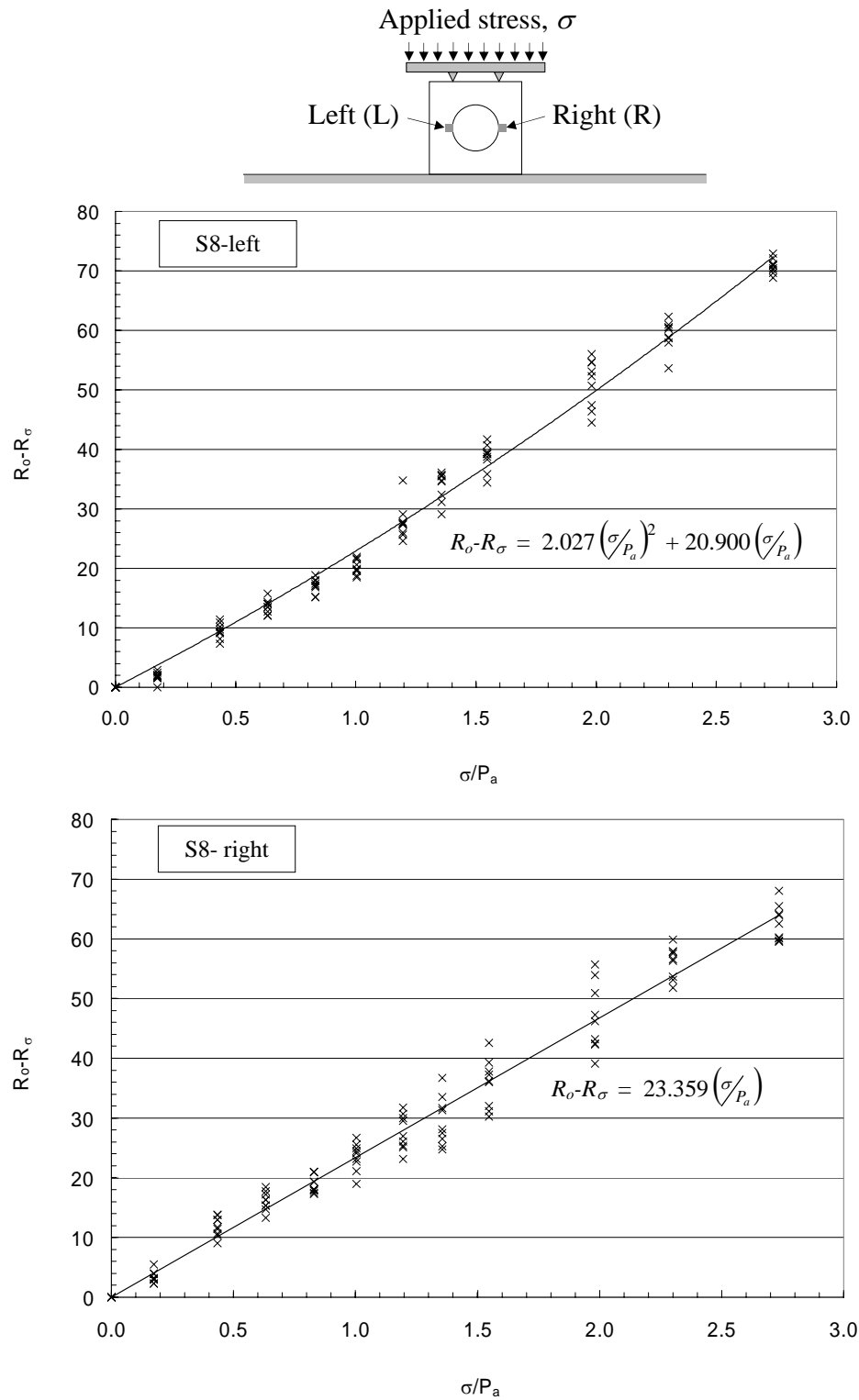


Figure A-6 Calibration charts for sensor S8 at points L (top) and R (bottom)

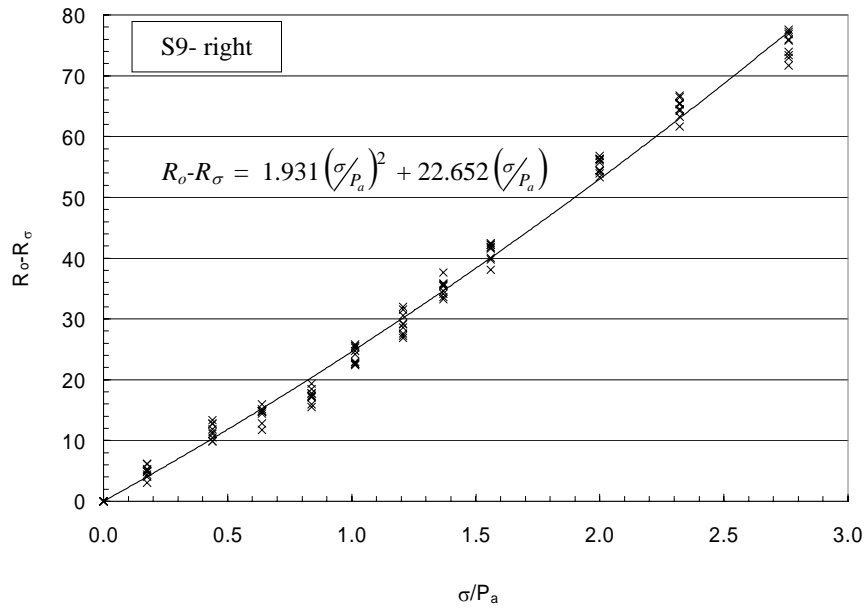
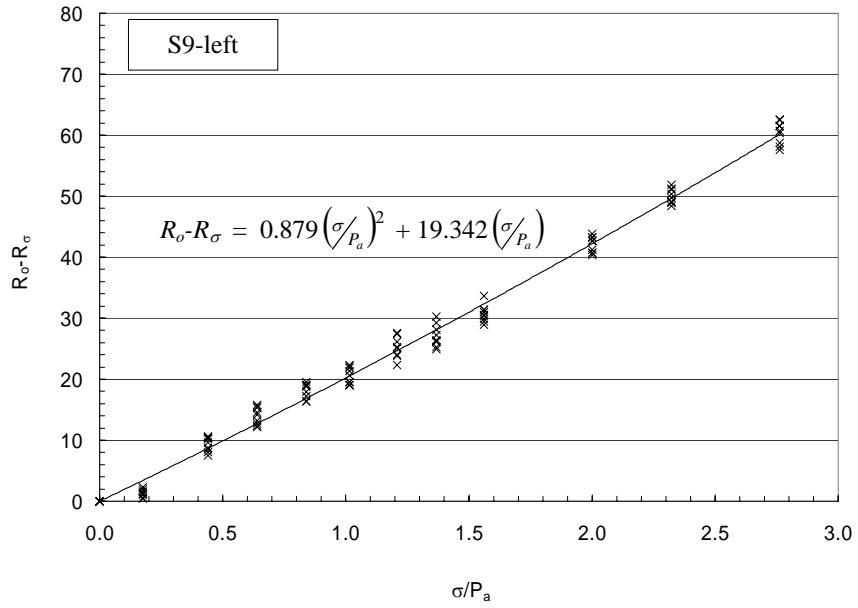
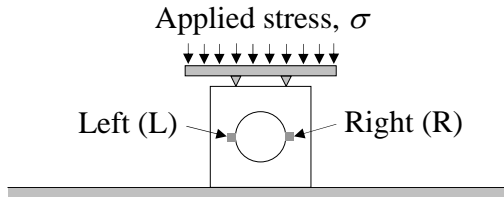


Figure A-7 Calibration charts for sensor S9 at points L (top) and R (bottom)

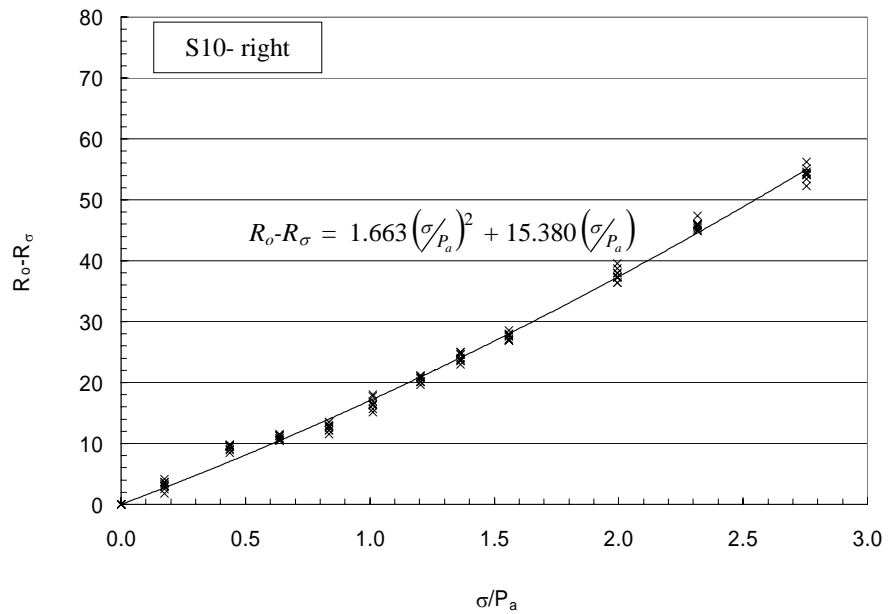
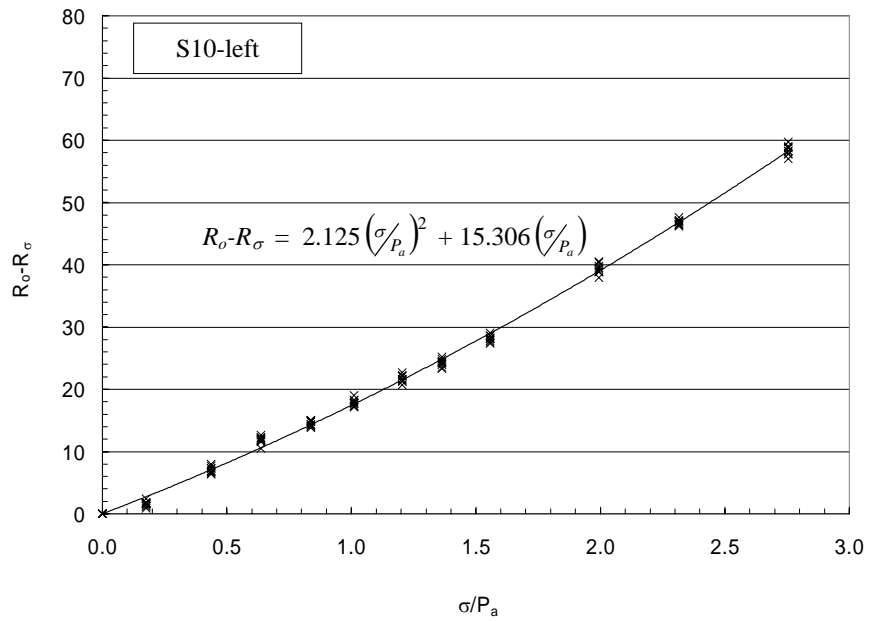
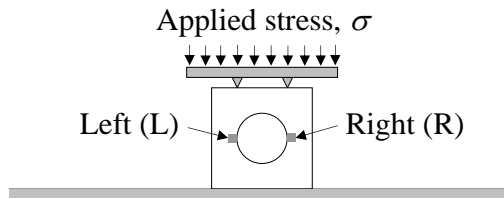


Figure A-8 Calibration charts for sensor S10 at points L (top) and R (bottom)

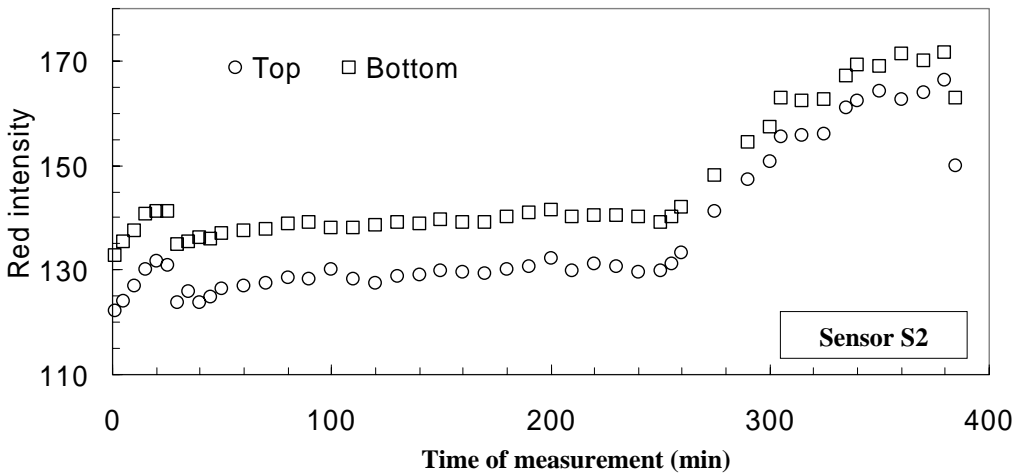
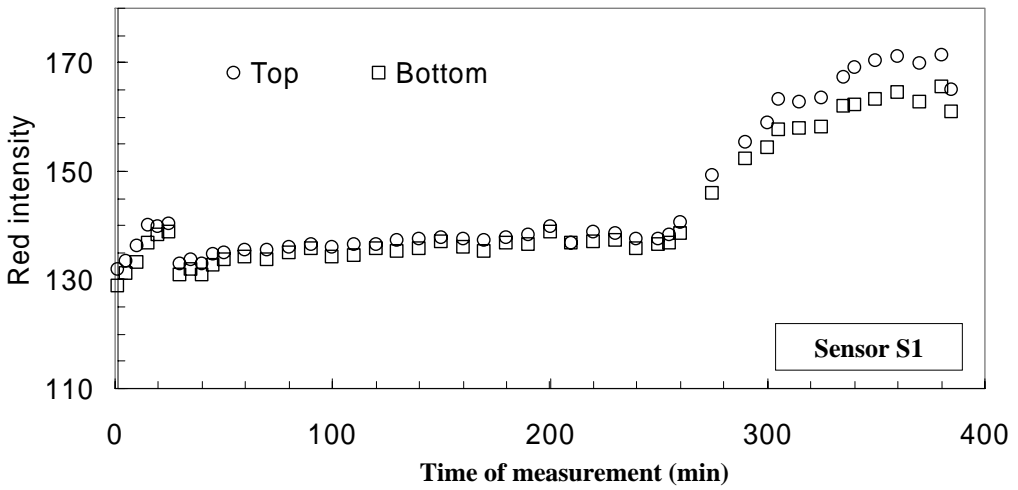
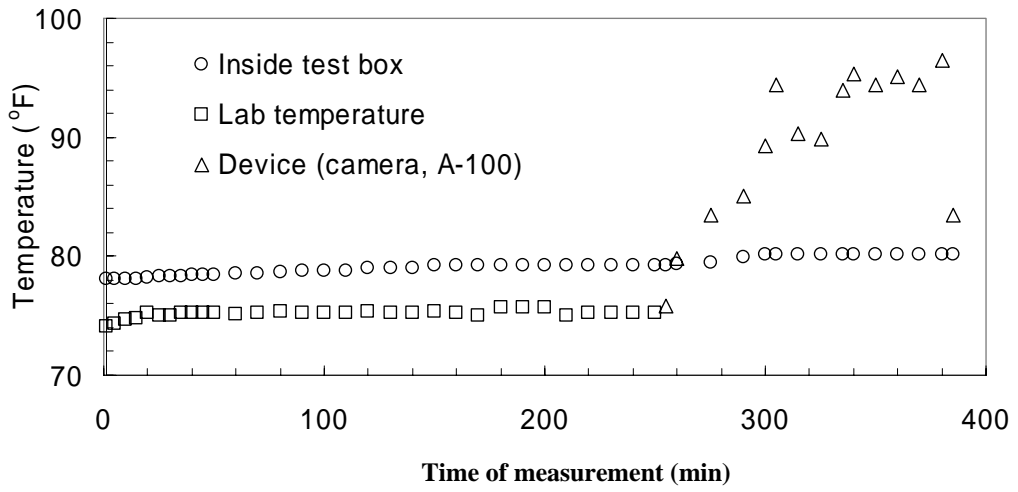


Figure A-9 Red intensity and temperatures versus time at the measurements from sensors S1 and S2 from Test #T1

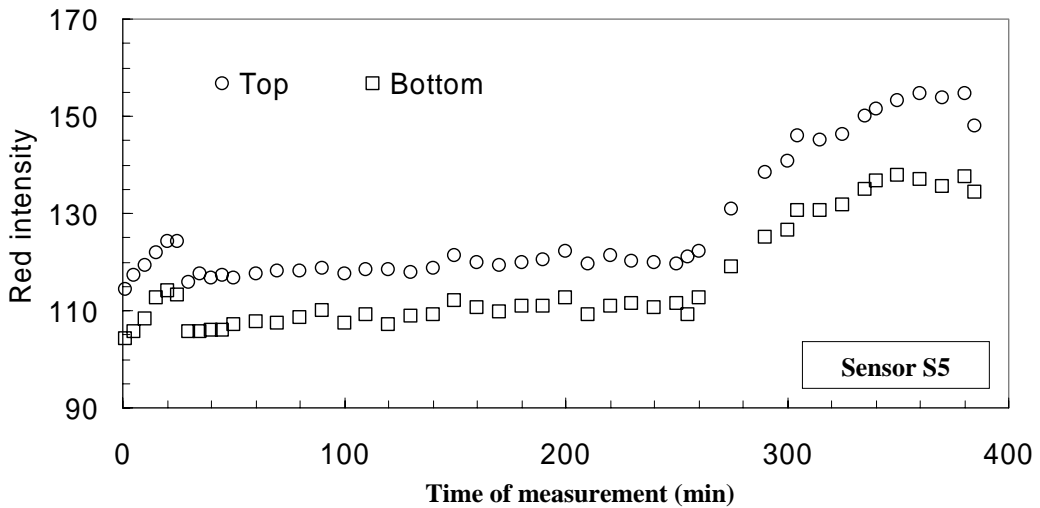
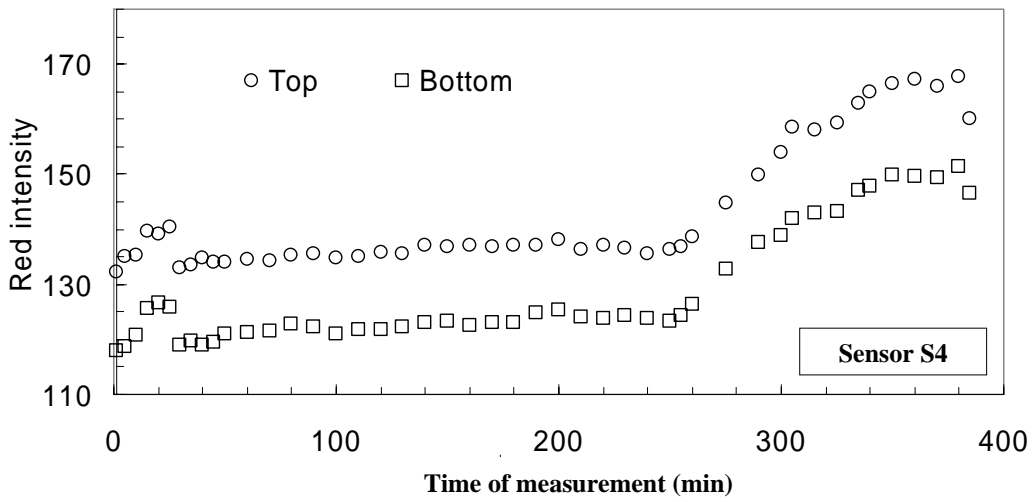
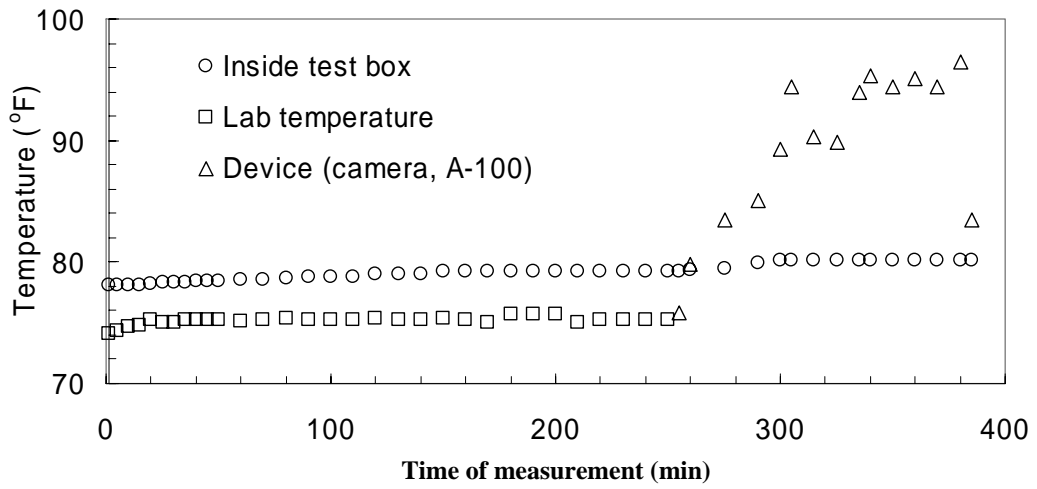


Figure A-10 Red intensity and temperatures versus time at the measurements from sensors S4 and S5 from Test #T1

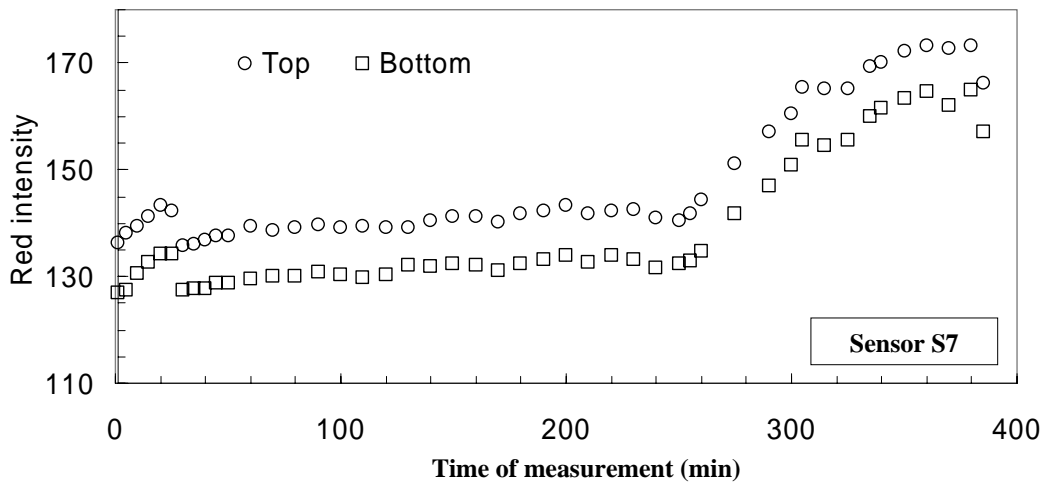
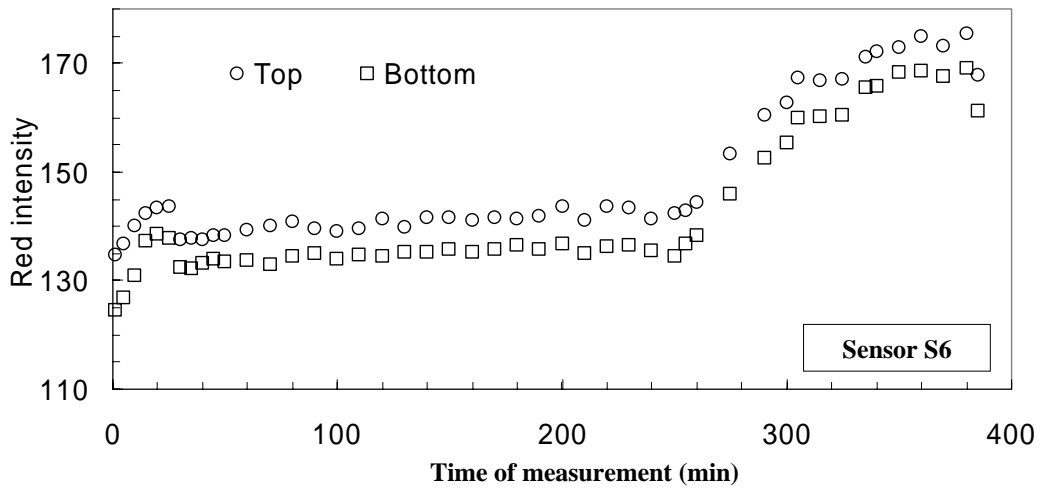
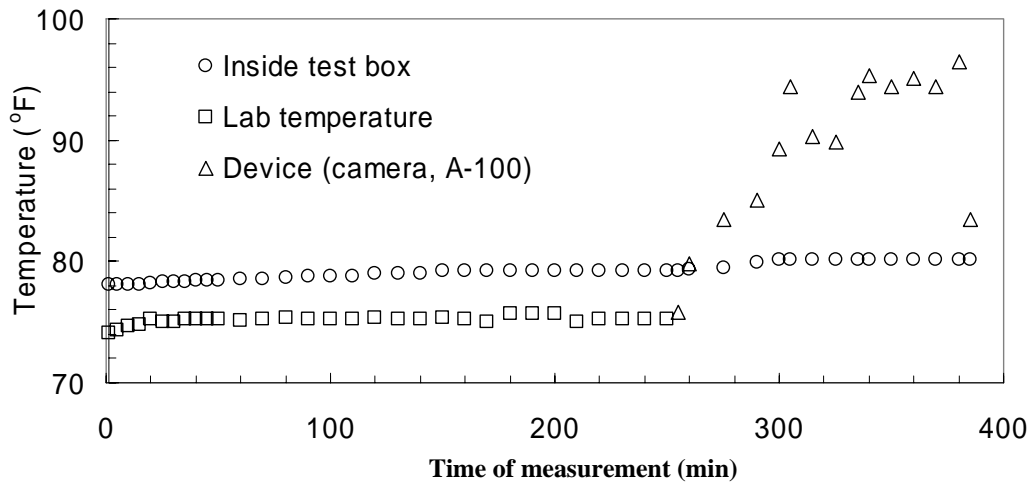


Figure A-11 Red intensity and temperatures versus time at the measurements from sensors S6 and S7 from Test #T1

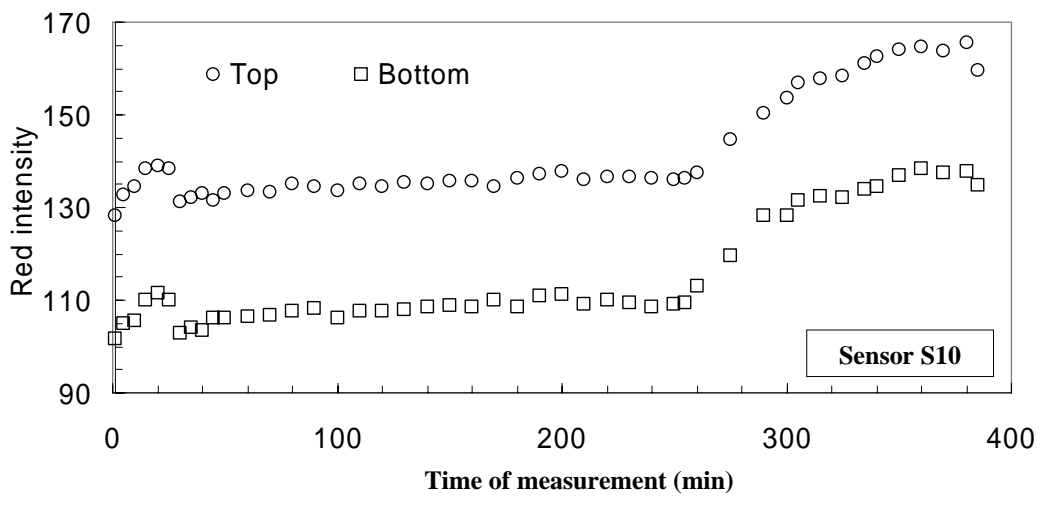
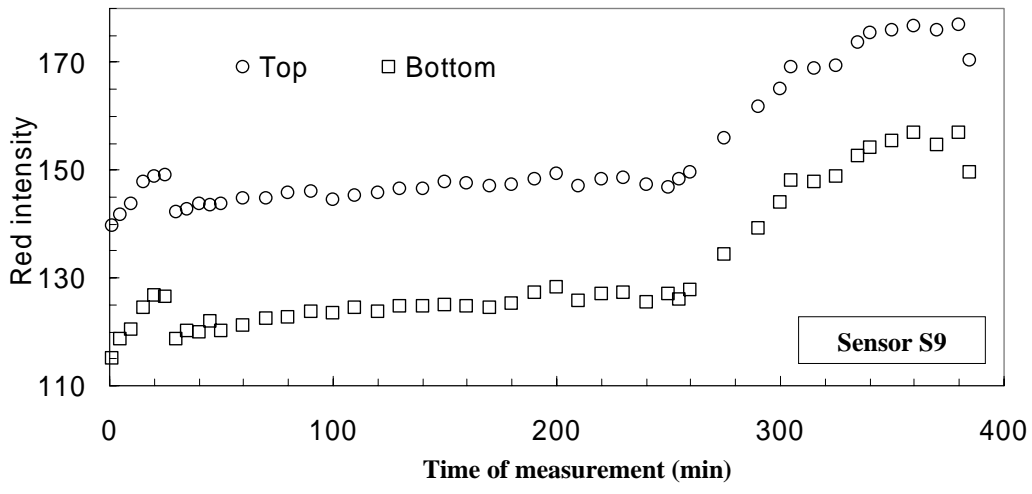
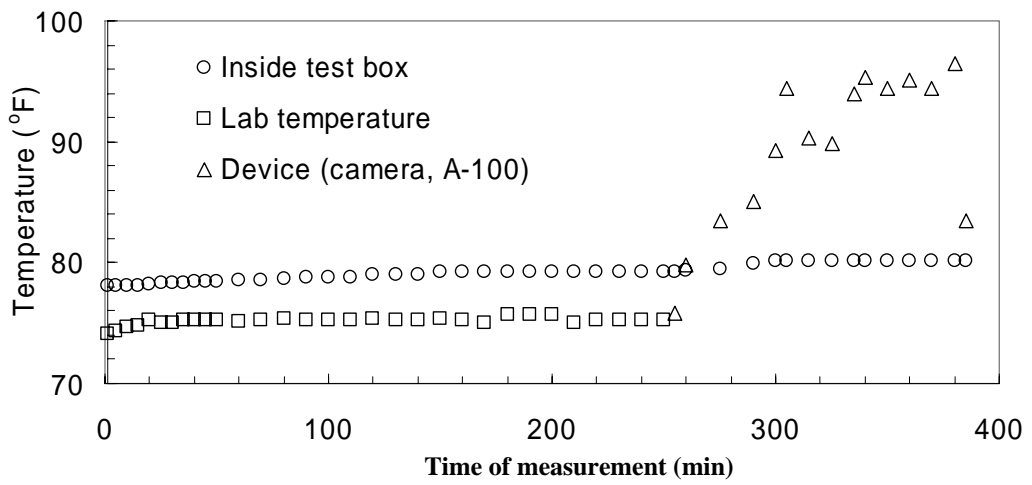


Figure A-12 Red intensity and temperatures versus time at the measurements from sensors S9 and S10 from Test #T1

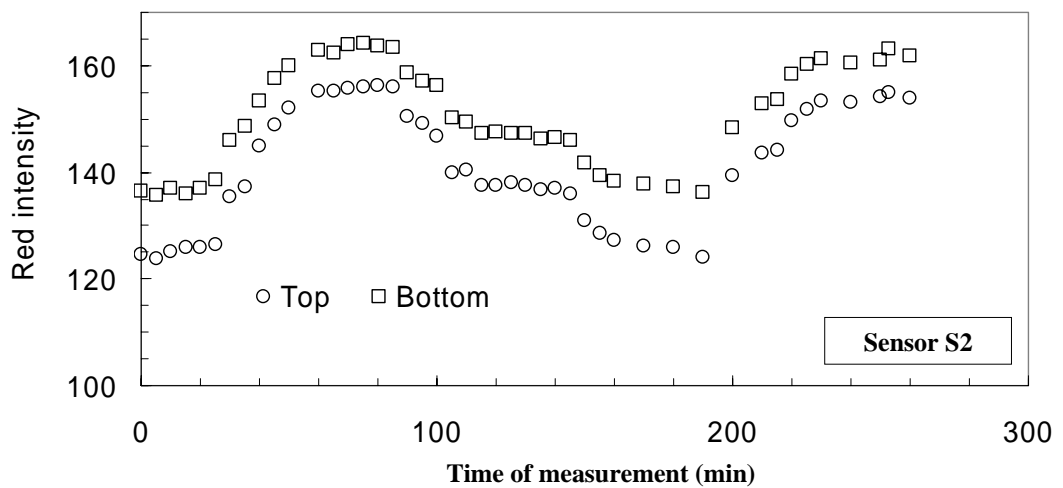
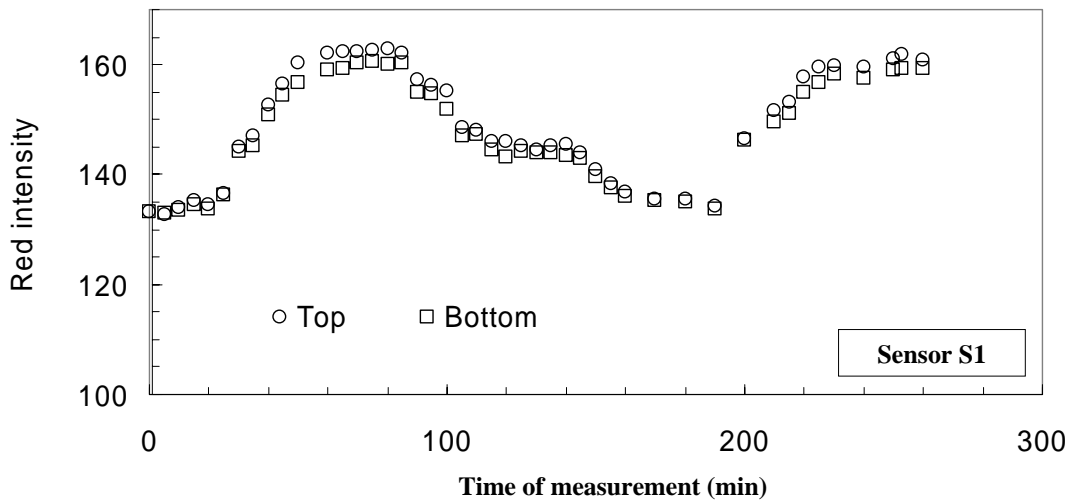
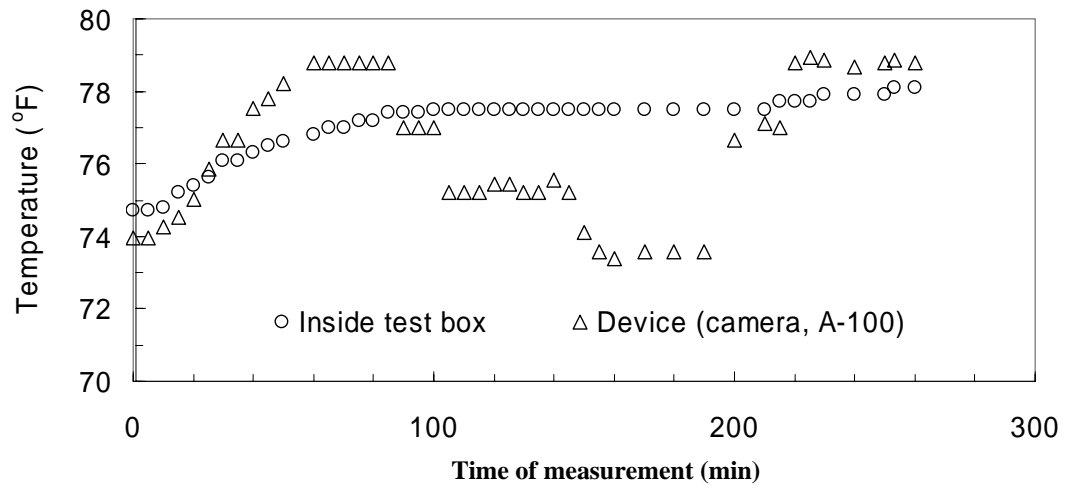


Figure A-13 Red intensity and temperatures versus time at the measurements from sensors S1 and S2 from Test #T2

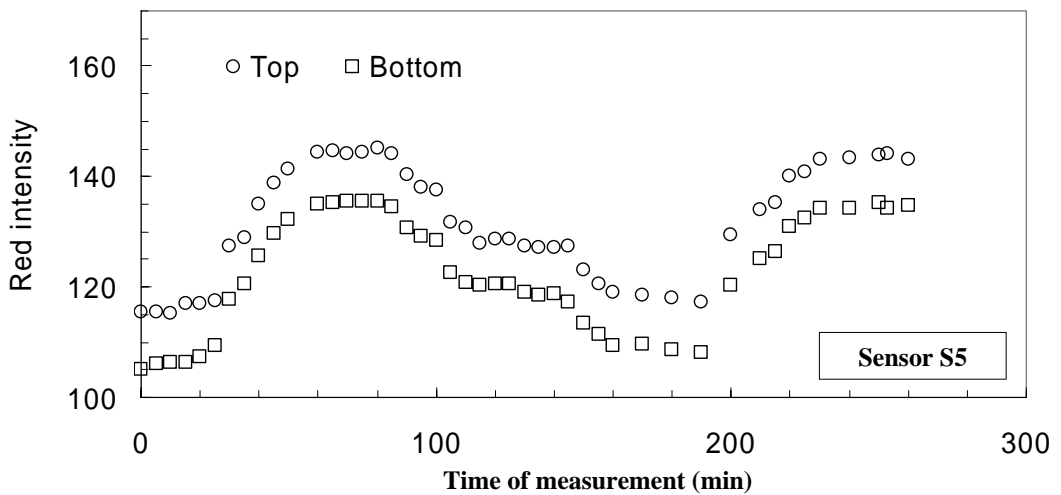
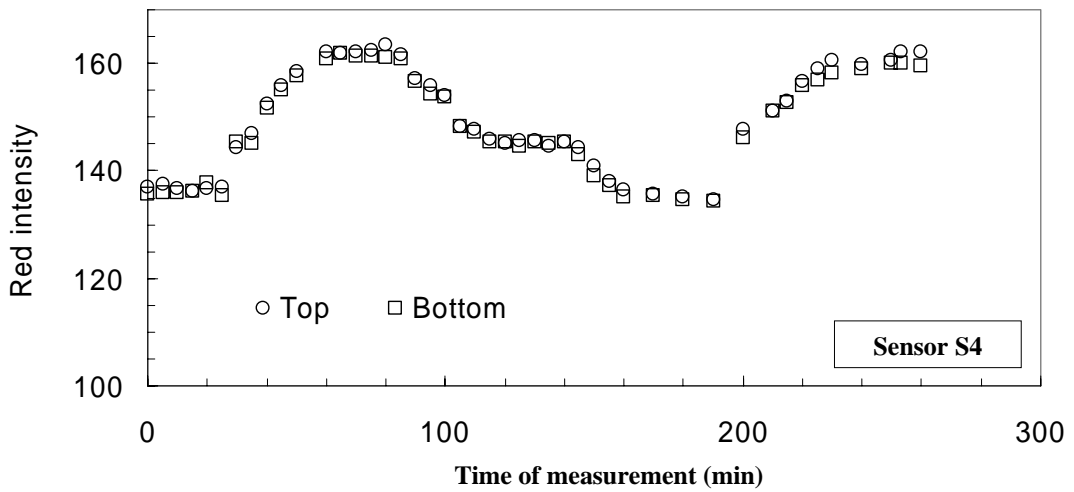
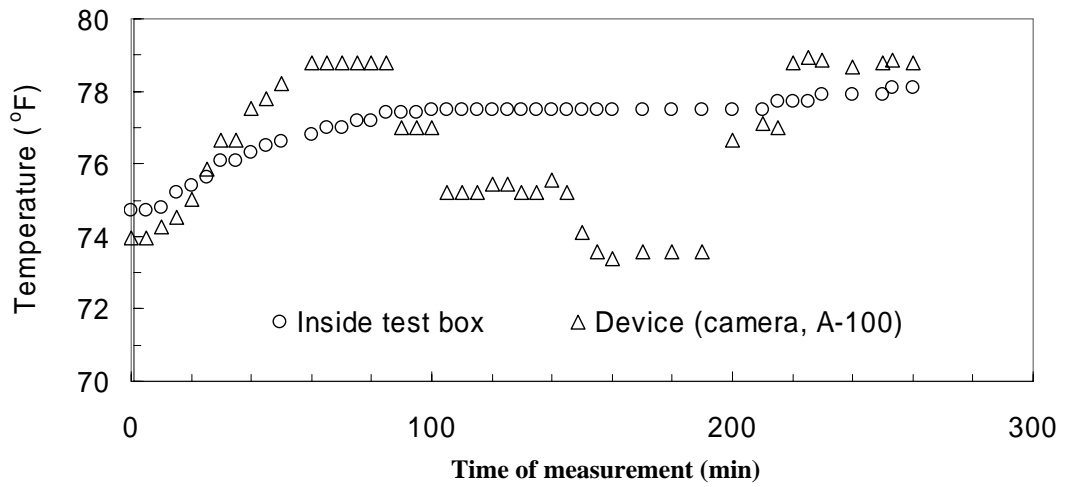


Figure A-14 Red intensity and temperatures versus time at the measurements from sensors S4 and S5 from Test #T2

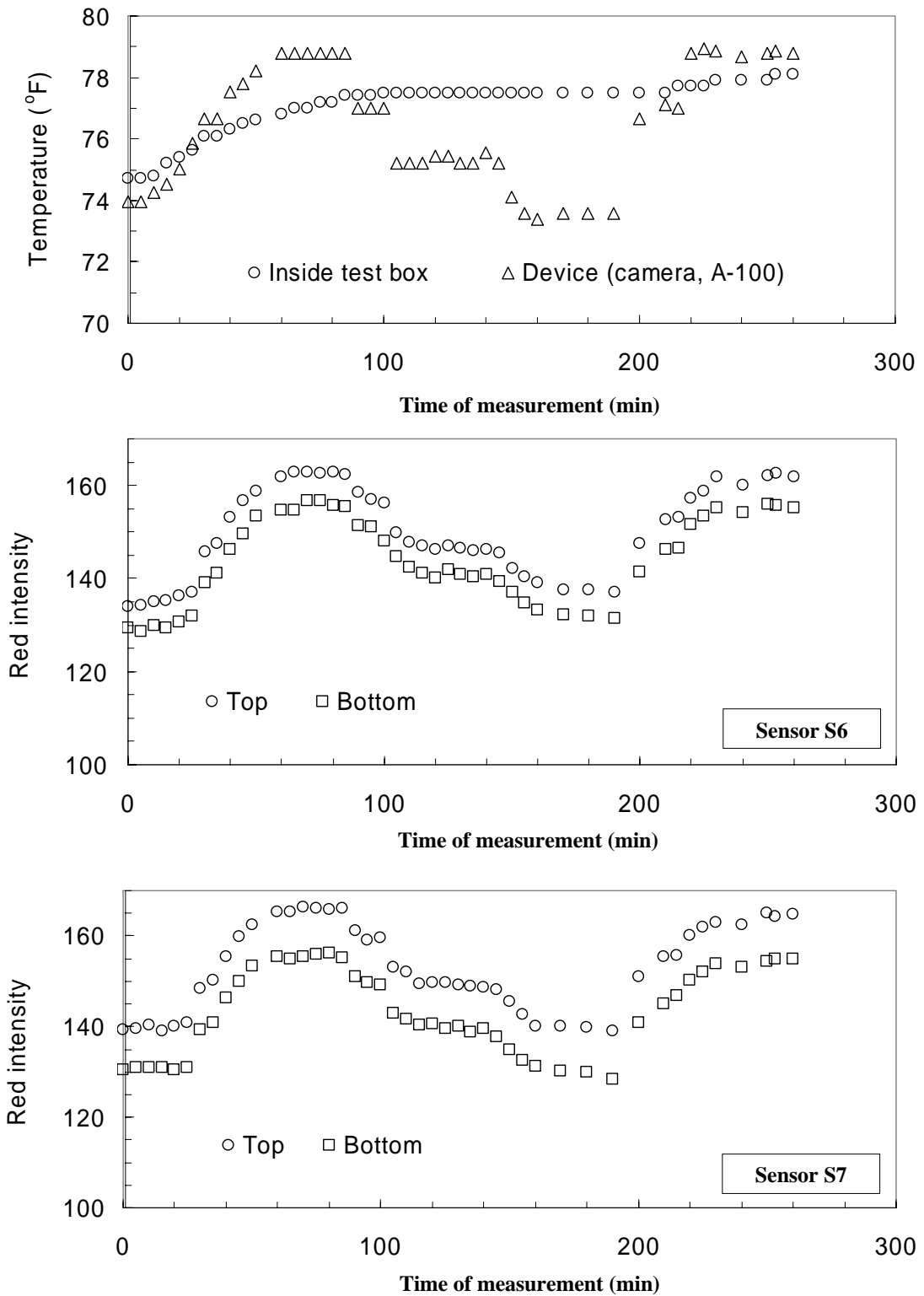


Figure A-15 Red intensity and temperatures versus time at the measurements from sensors S6 and S7 from Test #T2

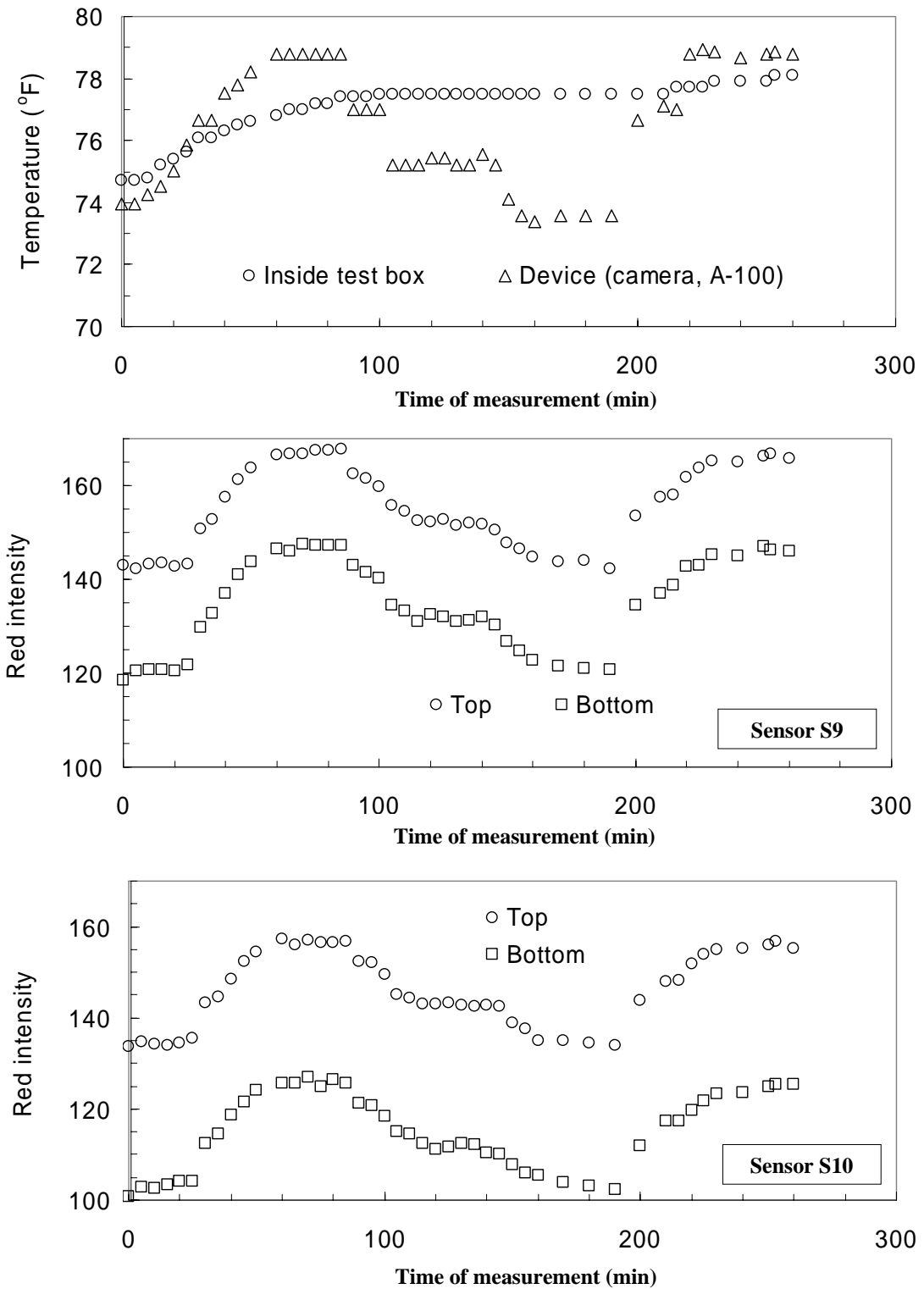


Figure A-16 Red intensity and temperatures versus time at the measurements from sensors S9 and S10 from Test #T2

APPENDIX B

COEFFICIENT OF

LATERAL EARTH PRESSURE AT REST (K_o)

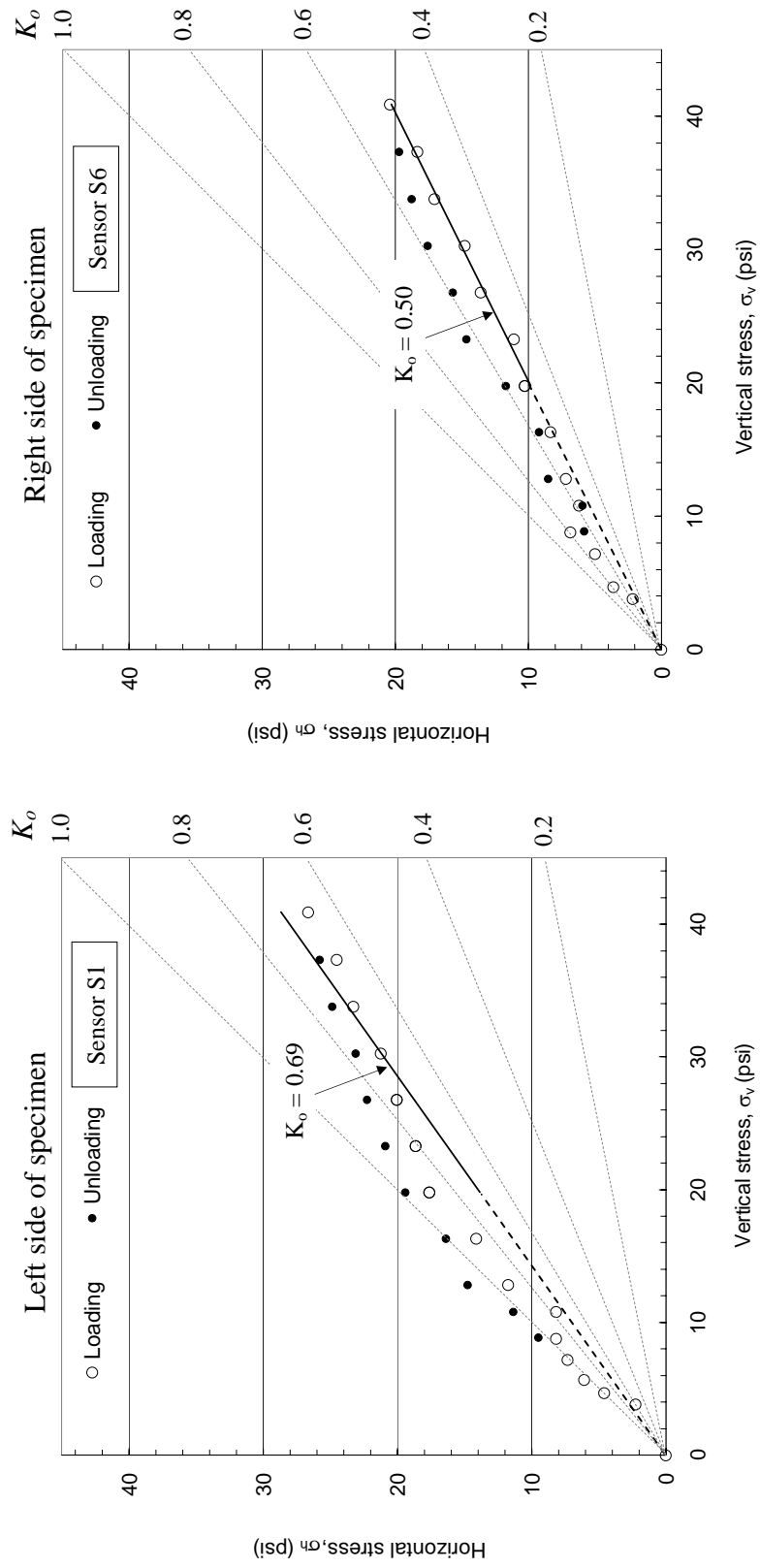


Figure B-1 Horizontal versus vertical stress on loading and unloading from sensors S1 and S6 in Test# 5-3

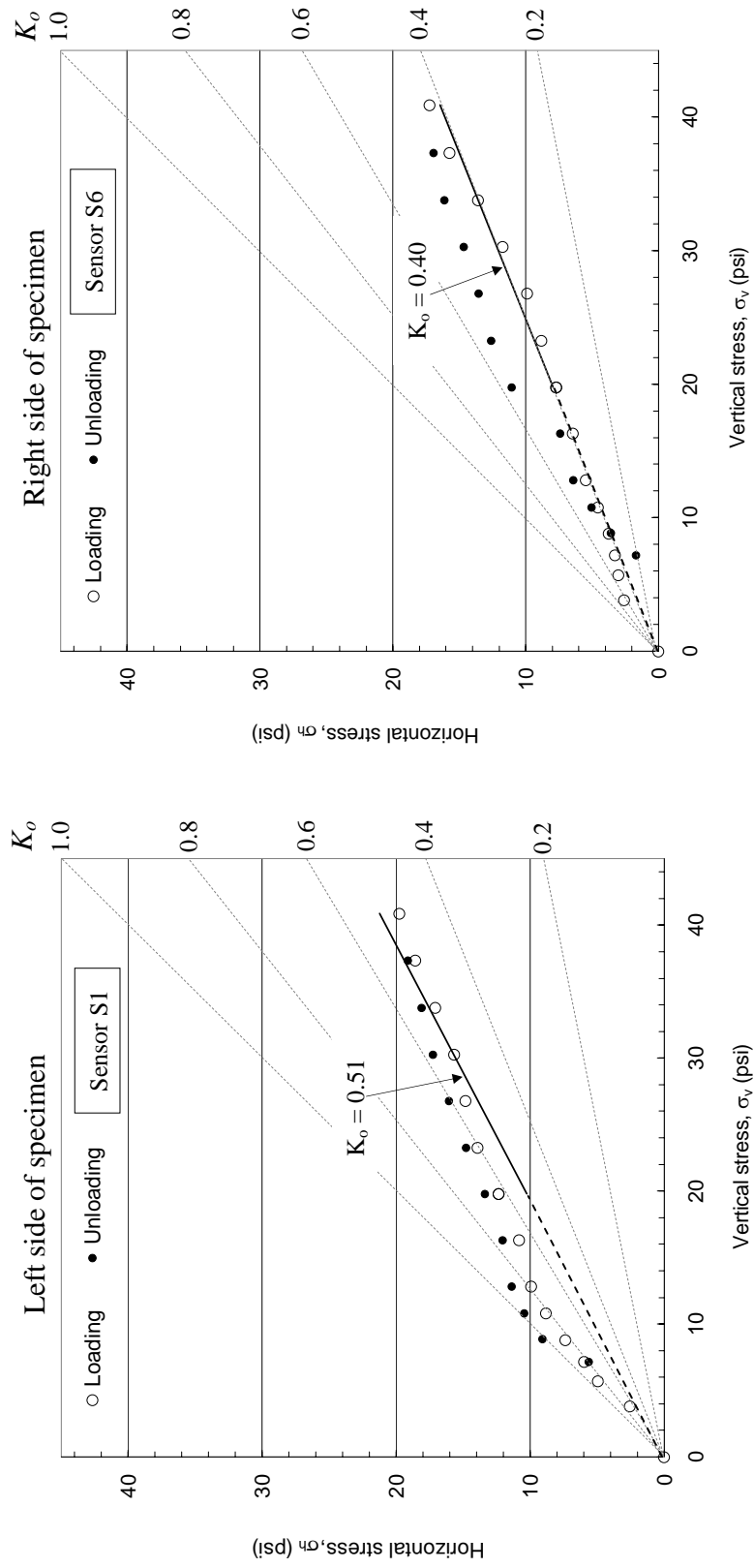


Figure B-2 Horizontal versus vertical stress on loading and unloading from sensors S1 and S6 in Test# 5-4

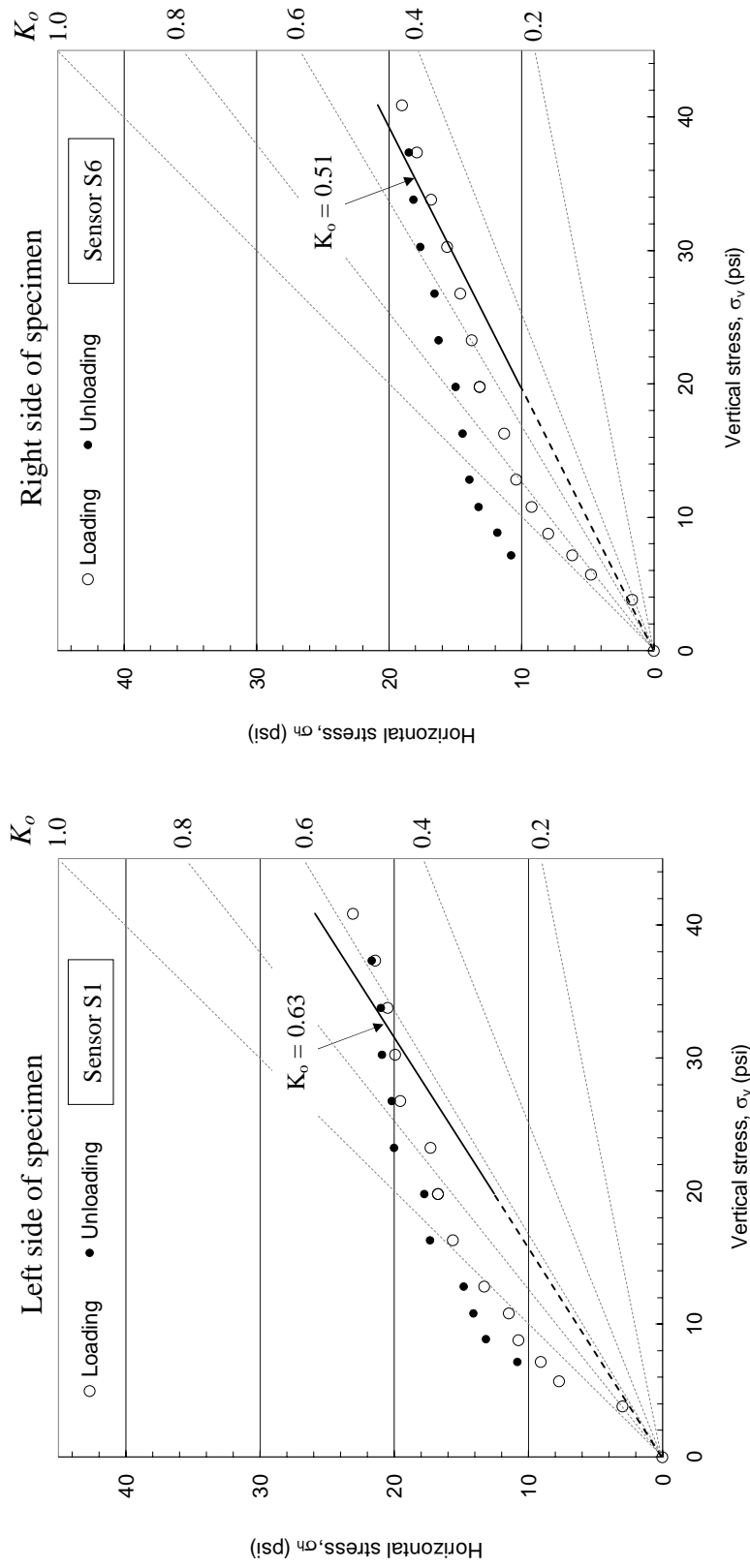


Figure B-3 Horizontal versus vertical stress on loading and unloading from sensors S1 and S6 in Test# 5-5

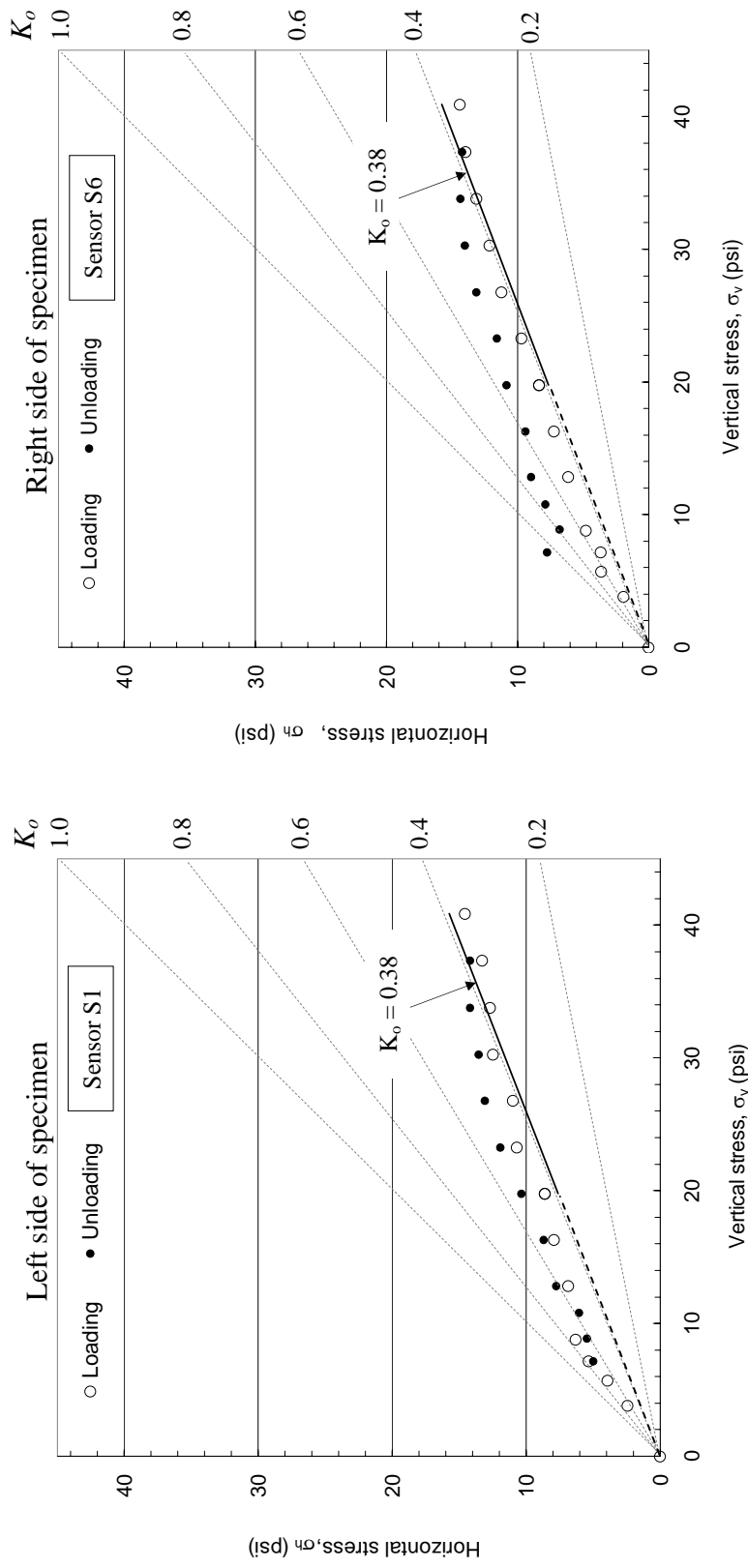


Figure B-4 Horizontal versus vertical stress on loading and unloading from sensors S1 and S6 in Test# 5-6

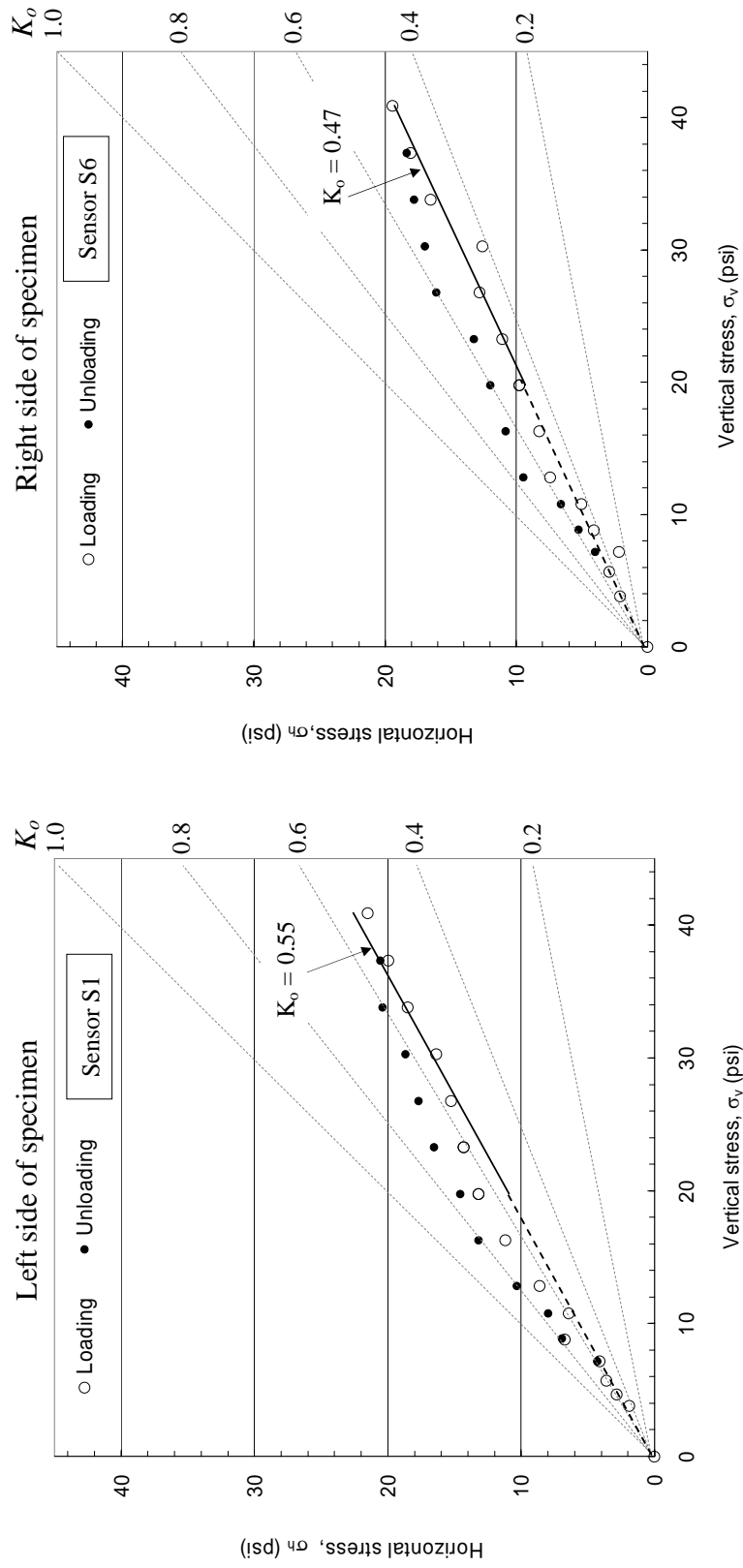


Figure B-5 Horizontal versus vertical stress on loading and unloading from sensors S1 and S6 in Test# 5-7

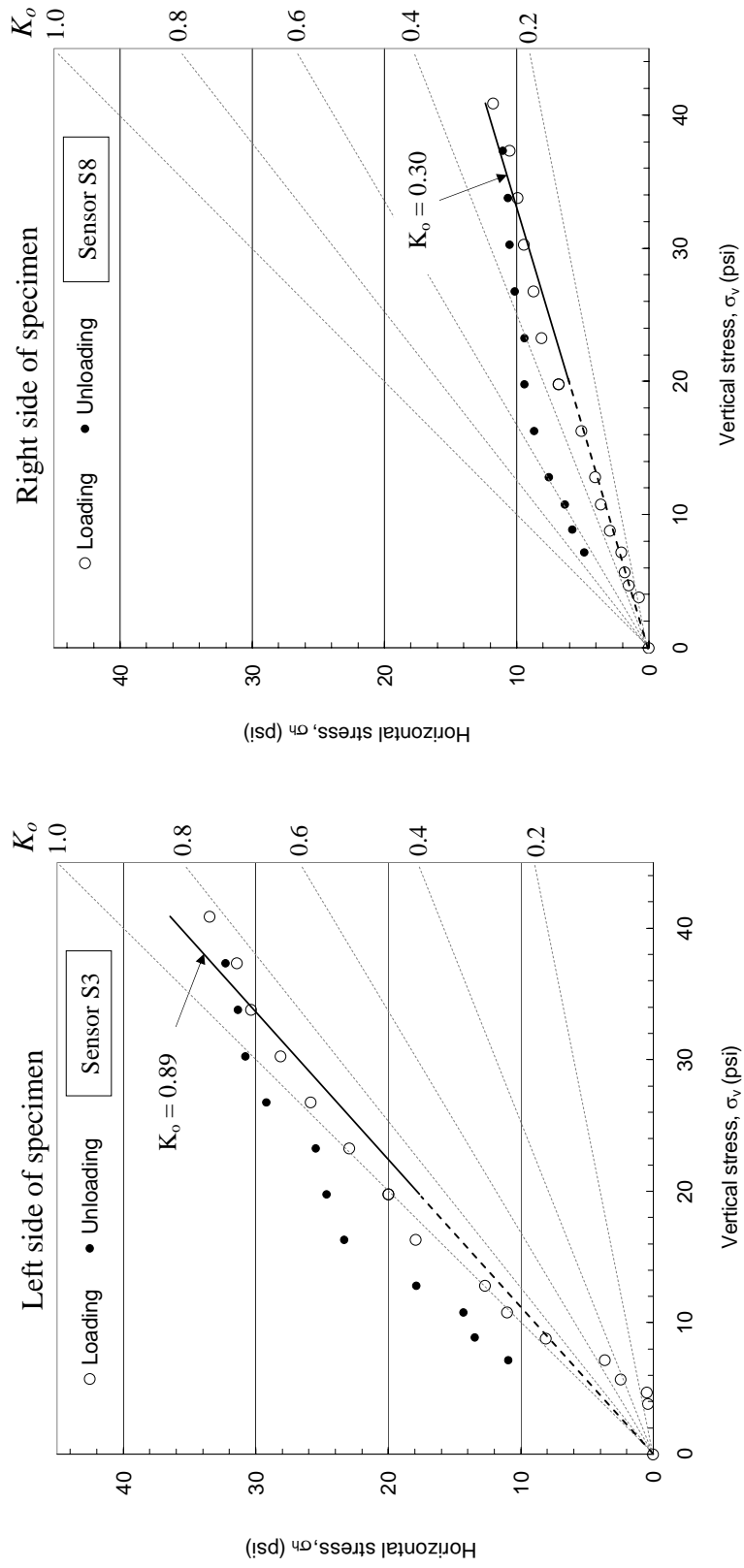


Figure B-6 Horizontal versus vertical stress on loading and unloading from sensors S3 and S8 in Test# 5-7

APPENDIX C

TEST RESULTS FROM CHAPTER 5
(RED INTENSITY, HORIZONTAL STRESS
AND SURFACE SETTLEMENT VERSUS TIME)

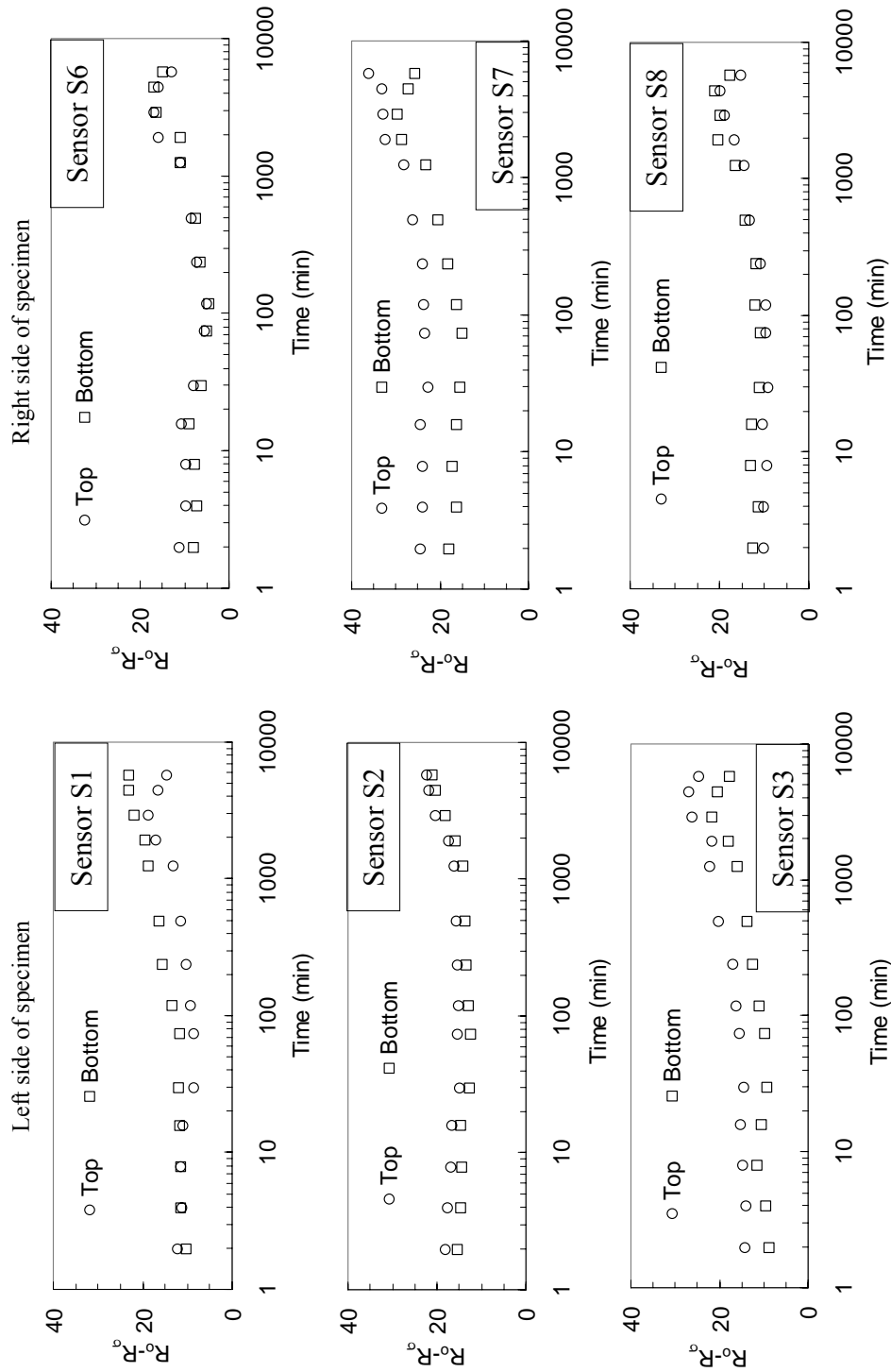


Figure C-1 Relative red intensity versus time from S1, S2, S3 (left) and S6, S7, S8 (right) for Test #5-10

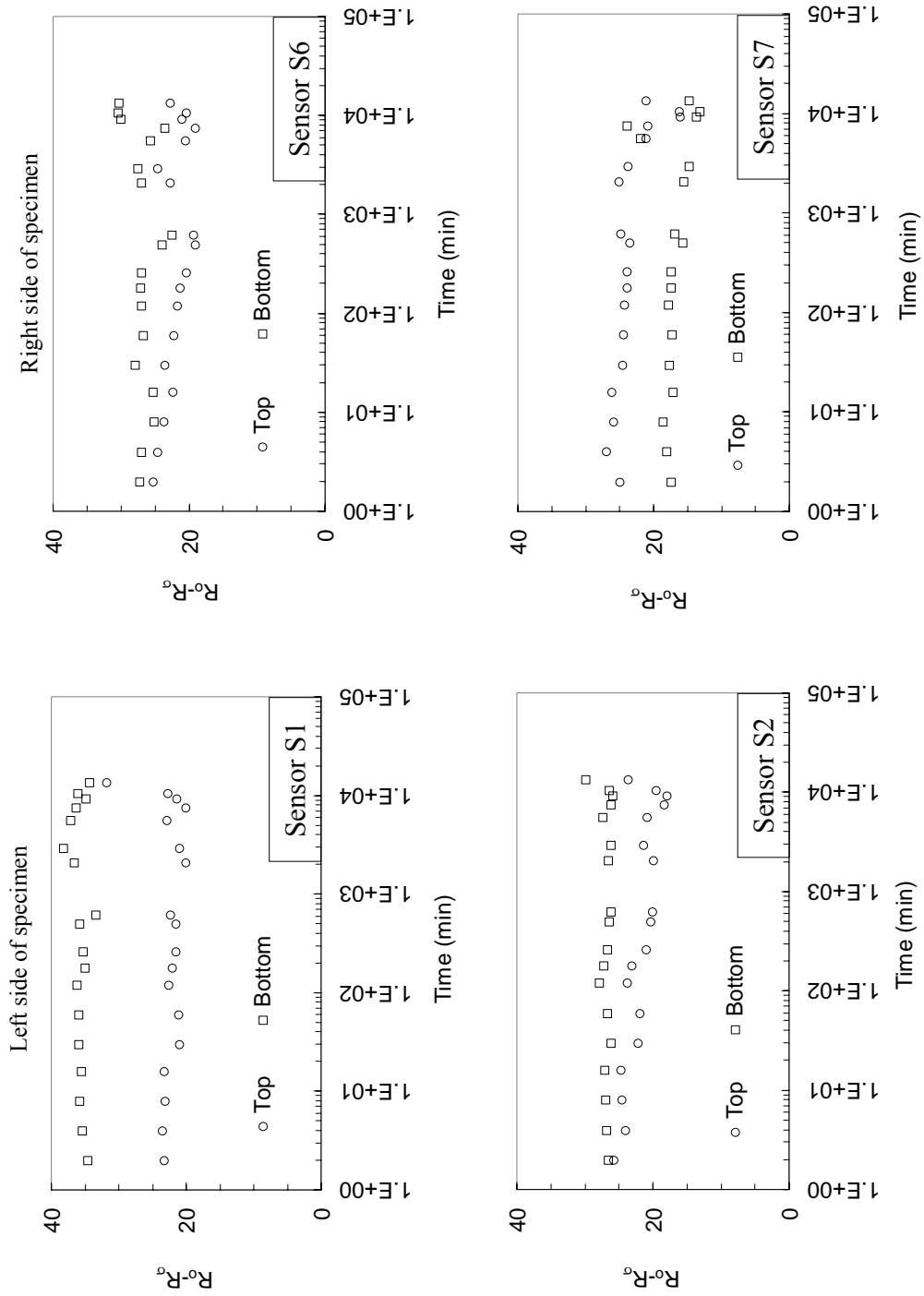


Figure C-2 Relative red intensity versus time from sensors S1, S2 (left) and S6, S7 (right) for Test #5-11

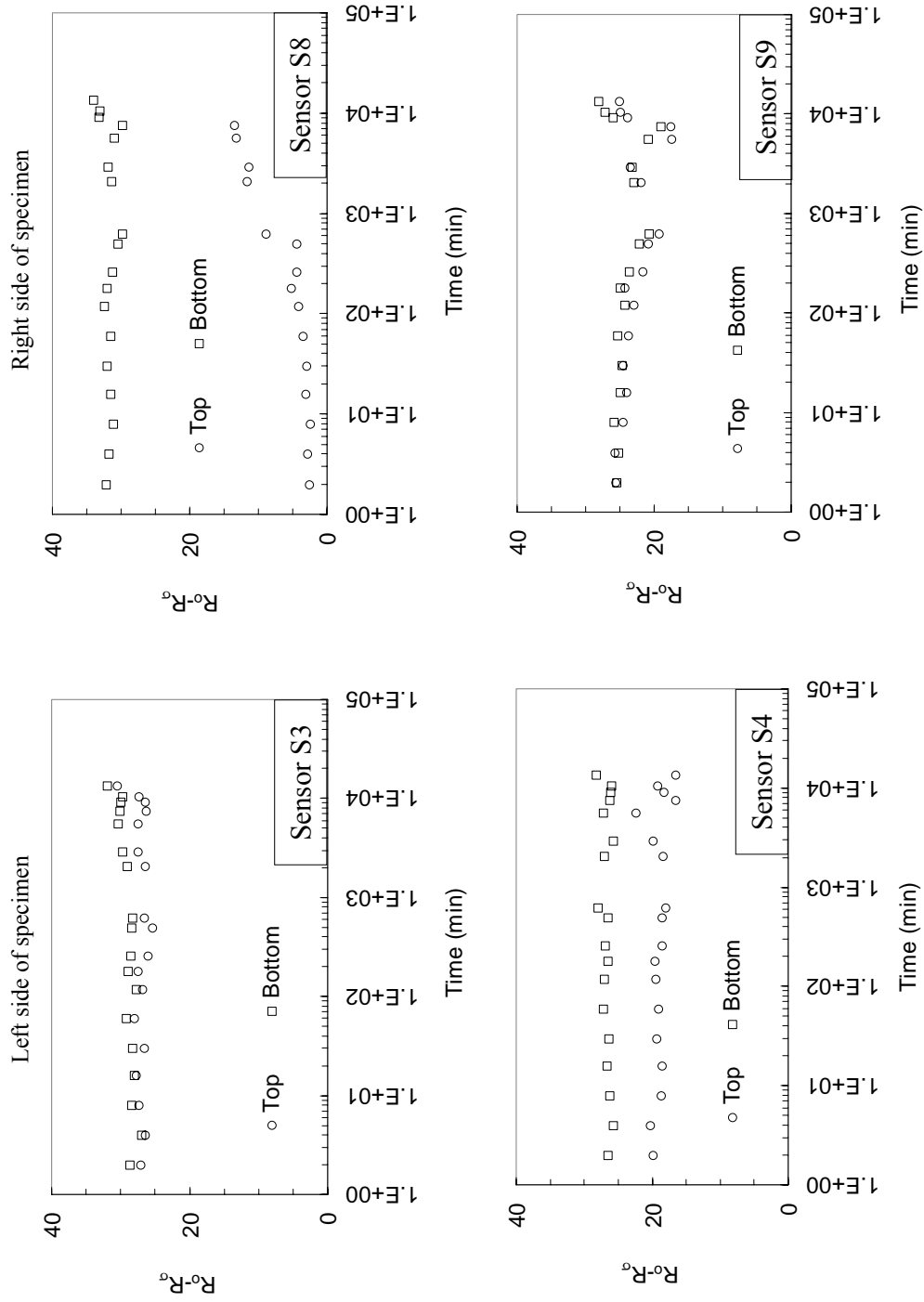


Figure C-3 Relative red intensity versus time from sensors S3, S4 (left) and S8, S9 (right) for Test #5-11

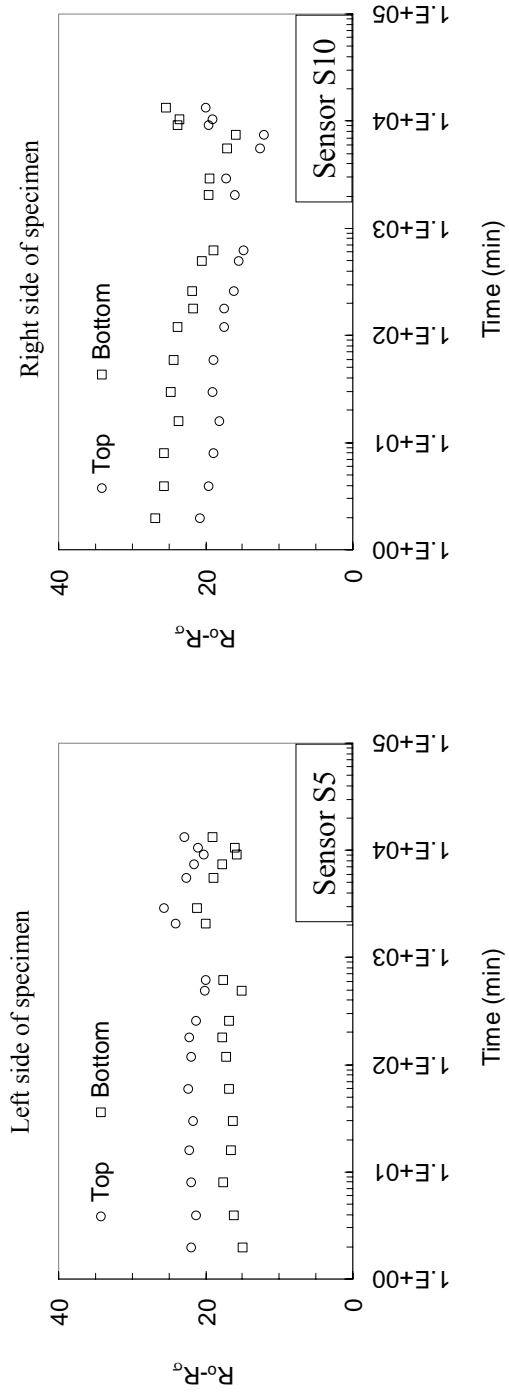


Figure C-4 Relative red intensity versus time from sensors S5 (left) and S10 (right) for Test #5-11

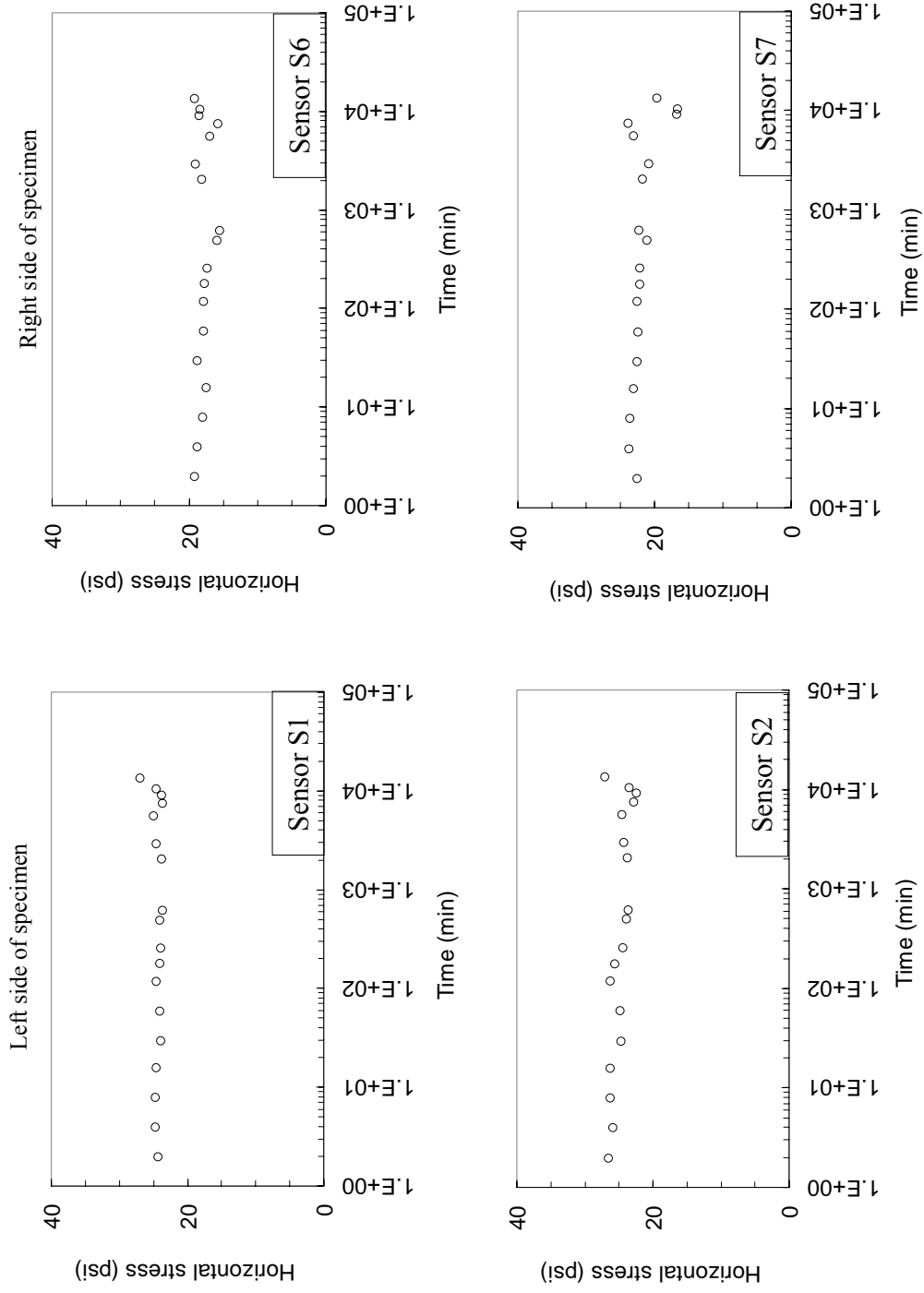


Figure C-5 Horizontal stress versus time from sensors S1, S2 (left) and S6, S7 (right) for test #5-1-1

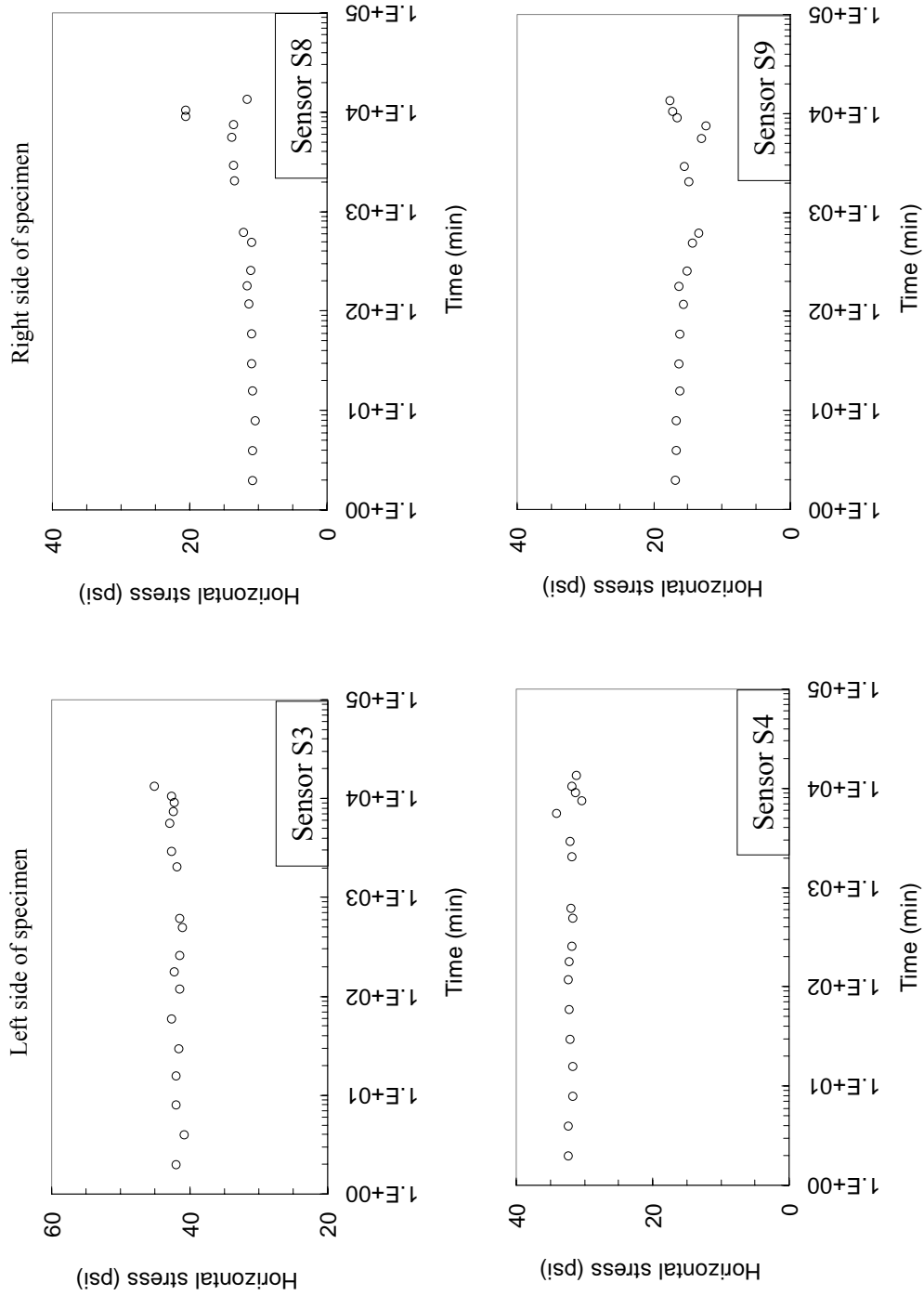


Figure C-6 Horizontal stress versus time from sensors S3, S4 (left) and S8, S9 (right) for Test #5-11

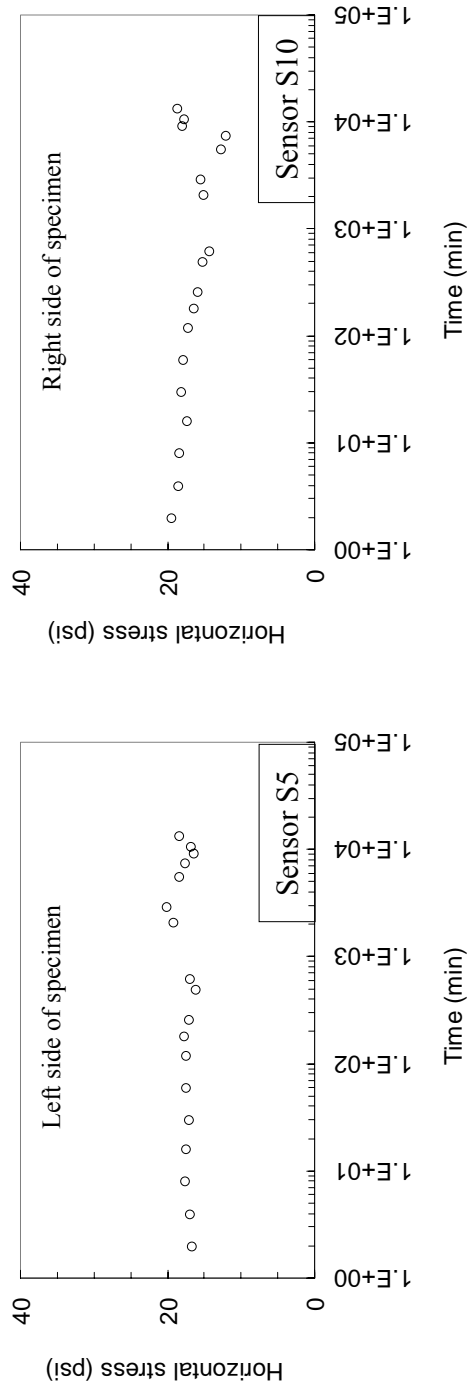


Figure C-7 Horizontal stress versus time from sensors S5 (left) and S10 (right) for Test #5-11

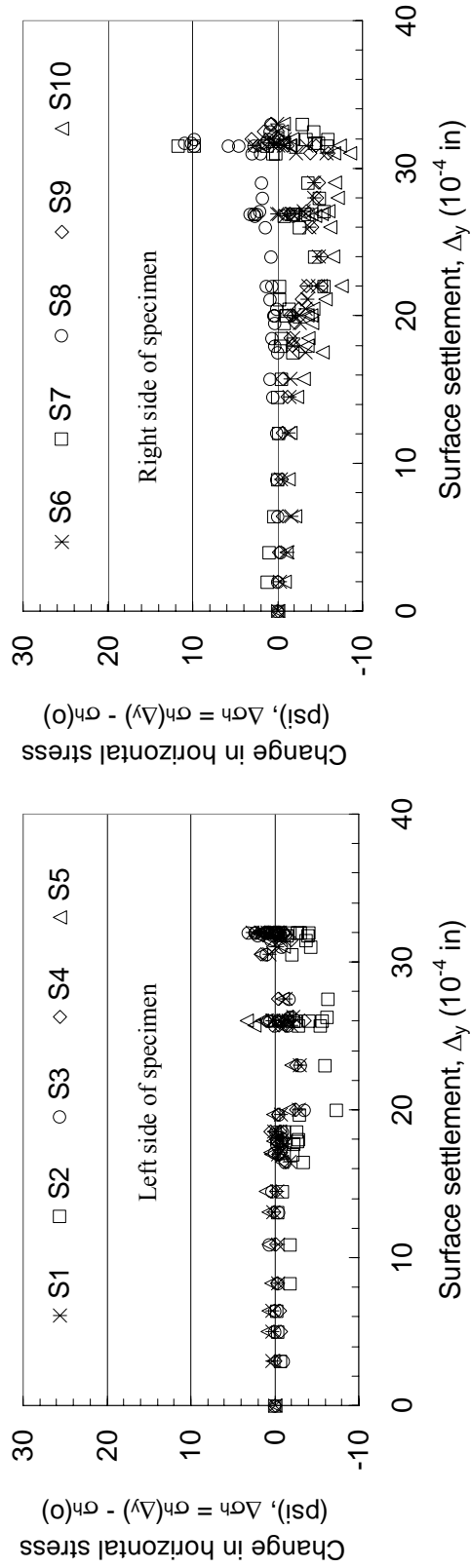


Figure C-8 Changes in horizontal stress versus surface settlement for Test #5-11

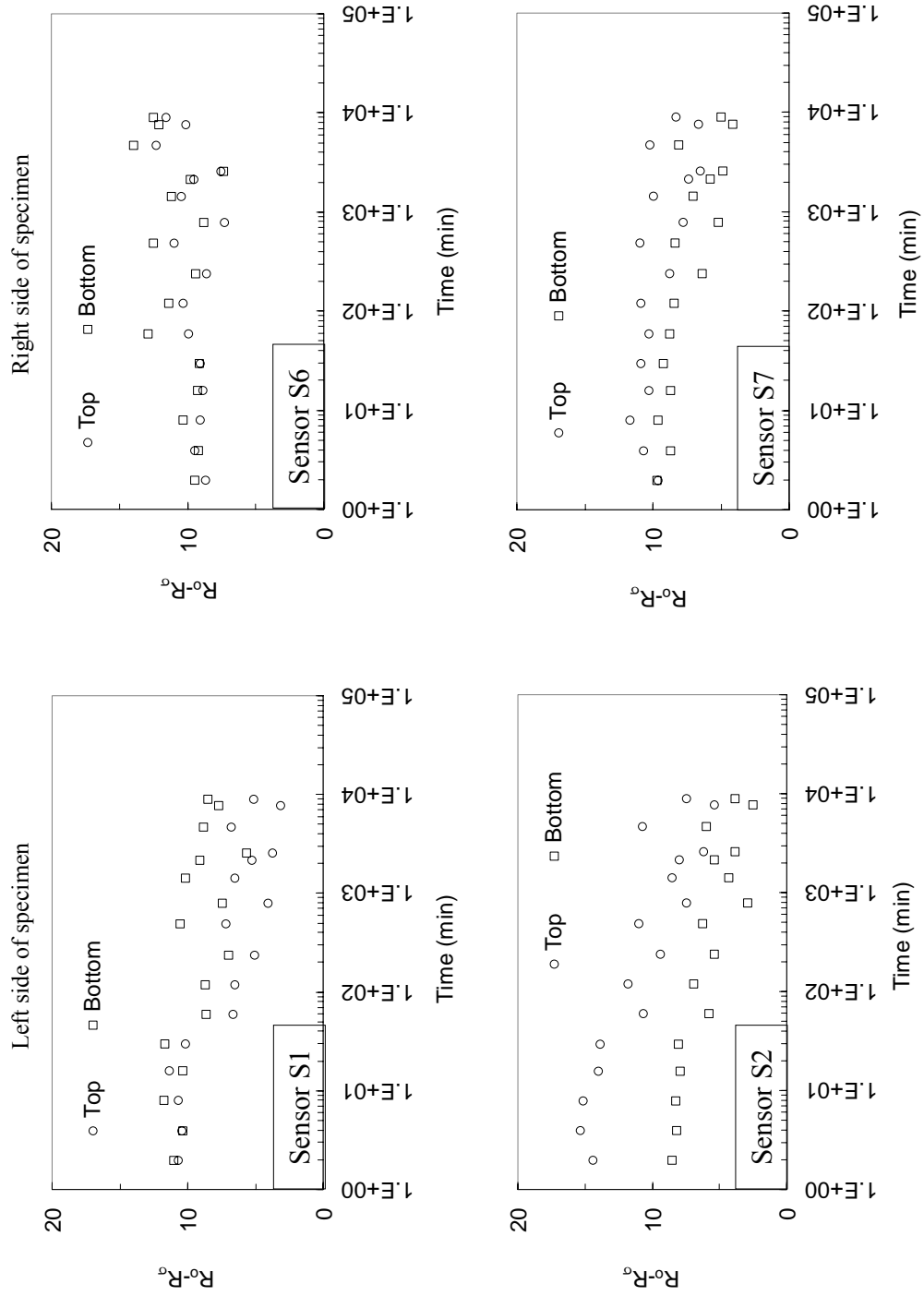


Figure C-9 Relative red intensity versus time from sensors S1, S2 (left) and S6, S7 (right) for Test #5-12

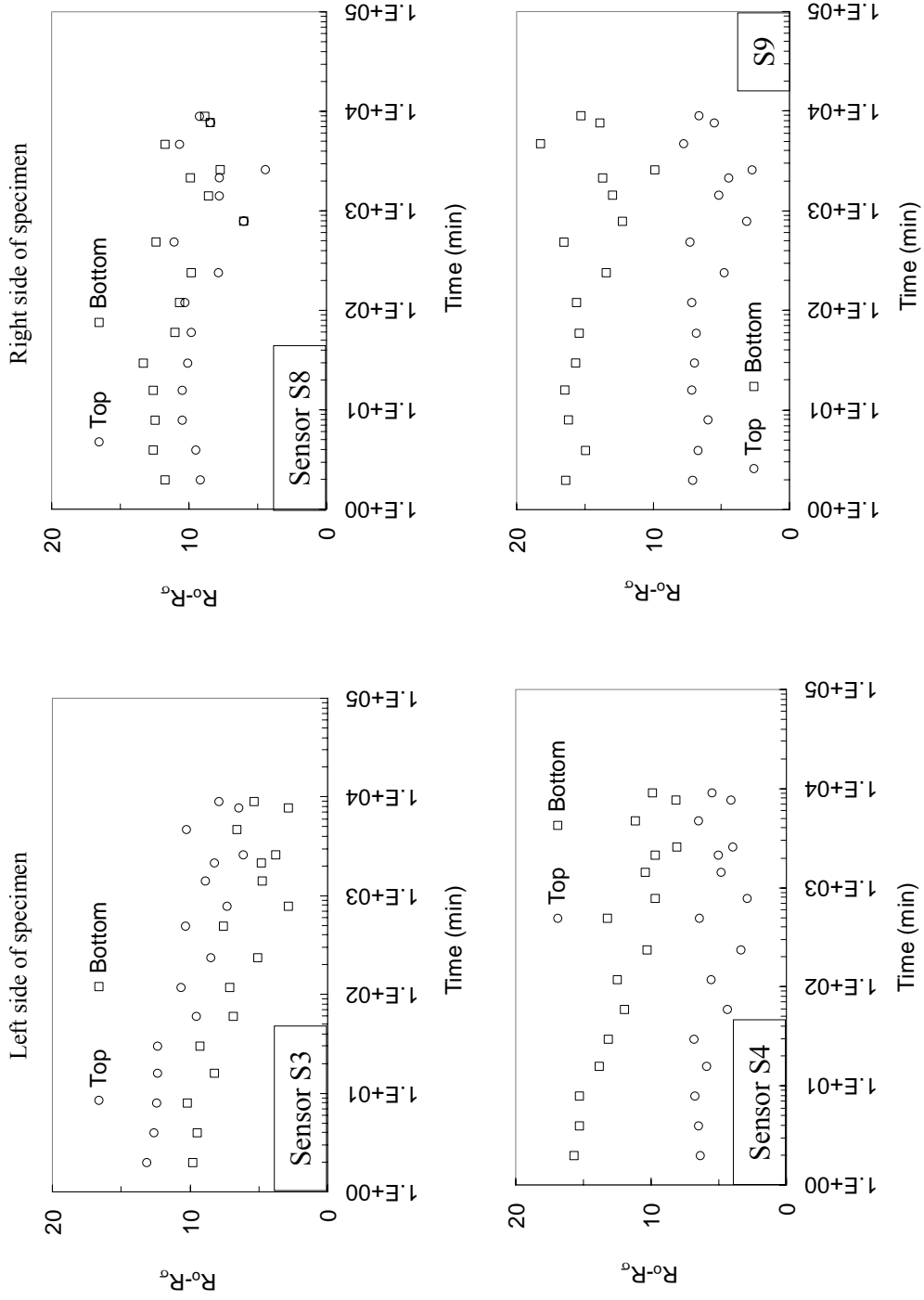


Figure C-10 Relative red intensity versus time from sensors S3, S4 (left) and S8, S9 (right) for Test #5-12

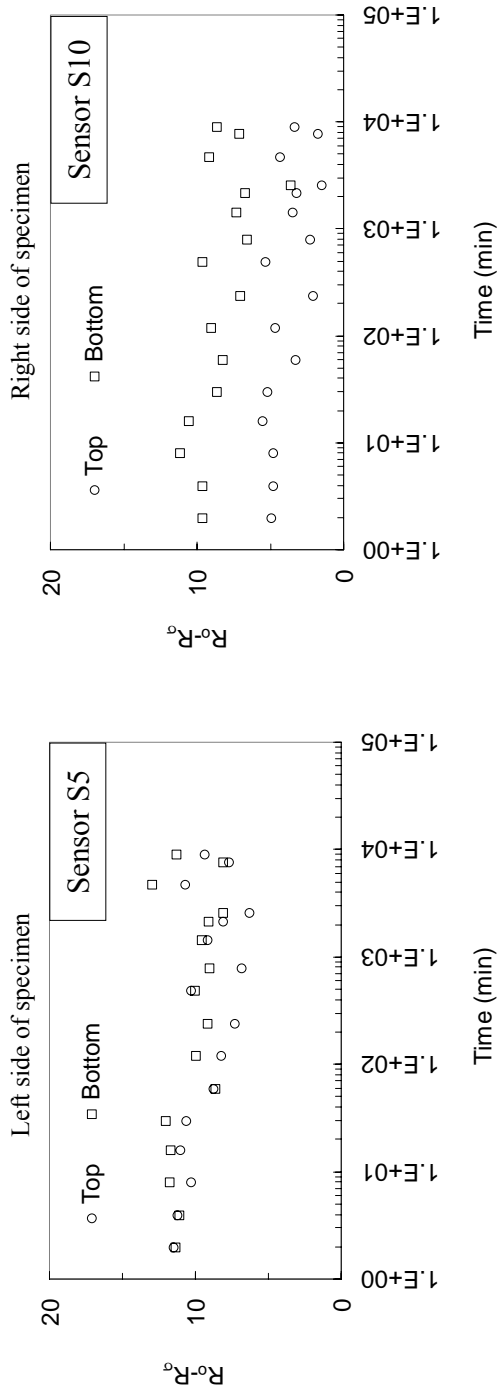


Figure C-11 Relative red intensity versus time from sensors S5 (left) and S10 (right) from test #5-12

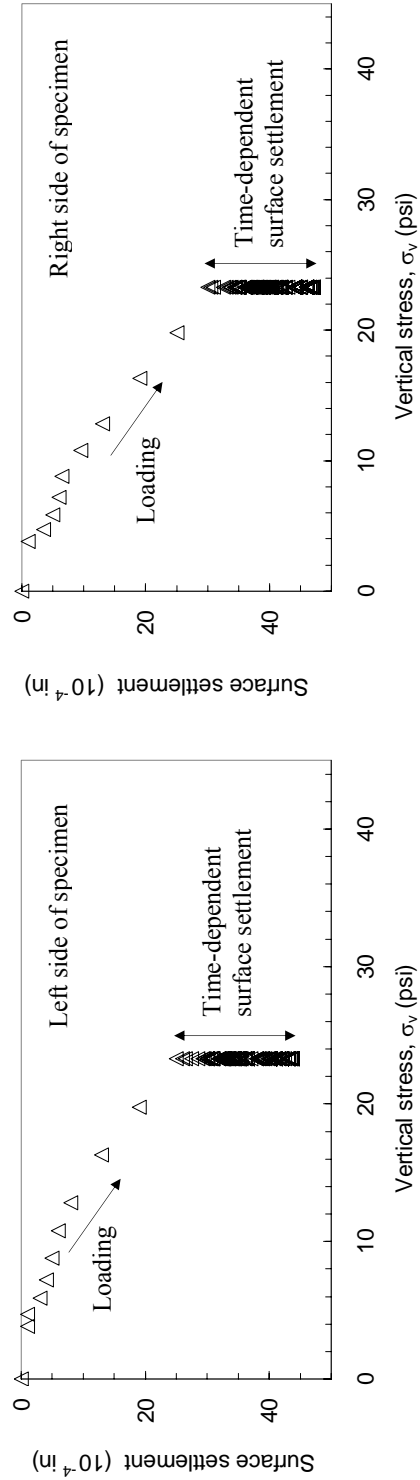


Figure C-12 Surface settlement of specimens during loading and under a constant vertical stress of 23.3 psi for 10 days for Test #5-12

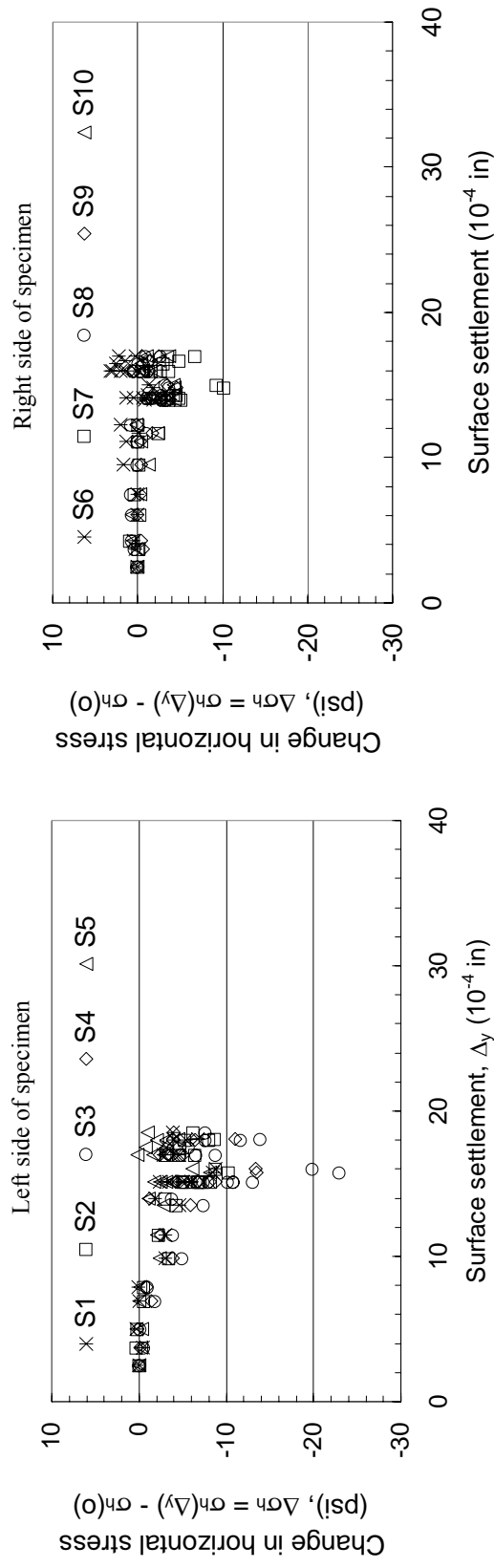


Figure C-13 Changes in horizontal stress versus surface settlement for Test #5-12 (black plate with pin hole was not used during the test)

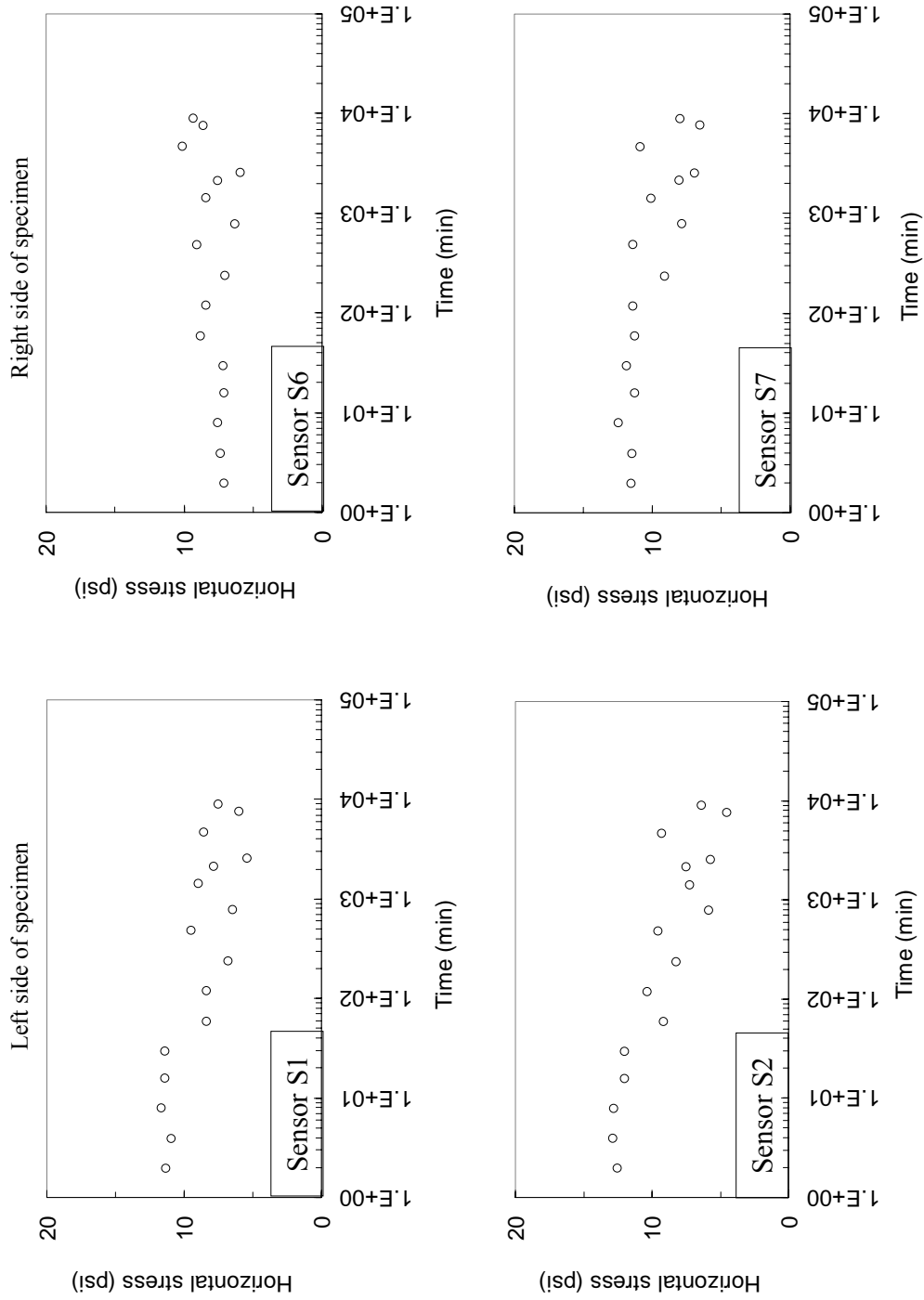


Figure C-14 Horizontal stress versus time from sensors S1, S2 (left) and S6, S7 (right) for Test #5-12

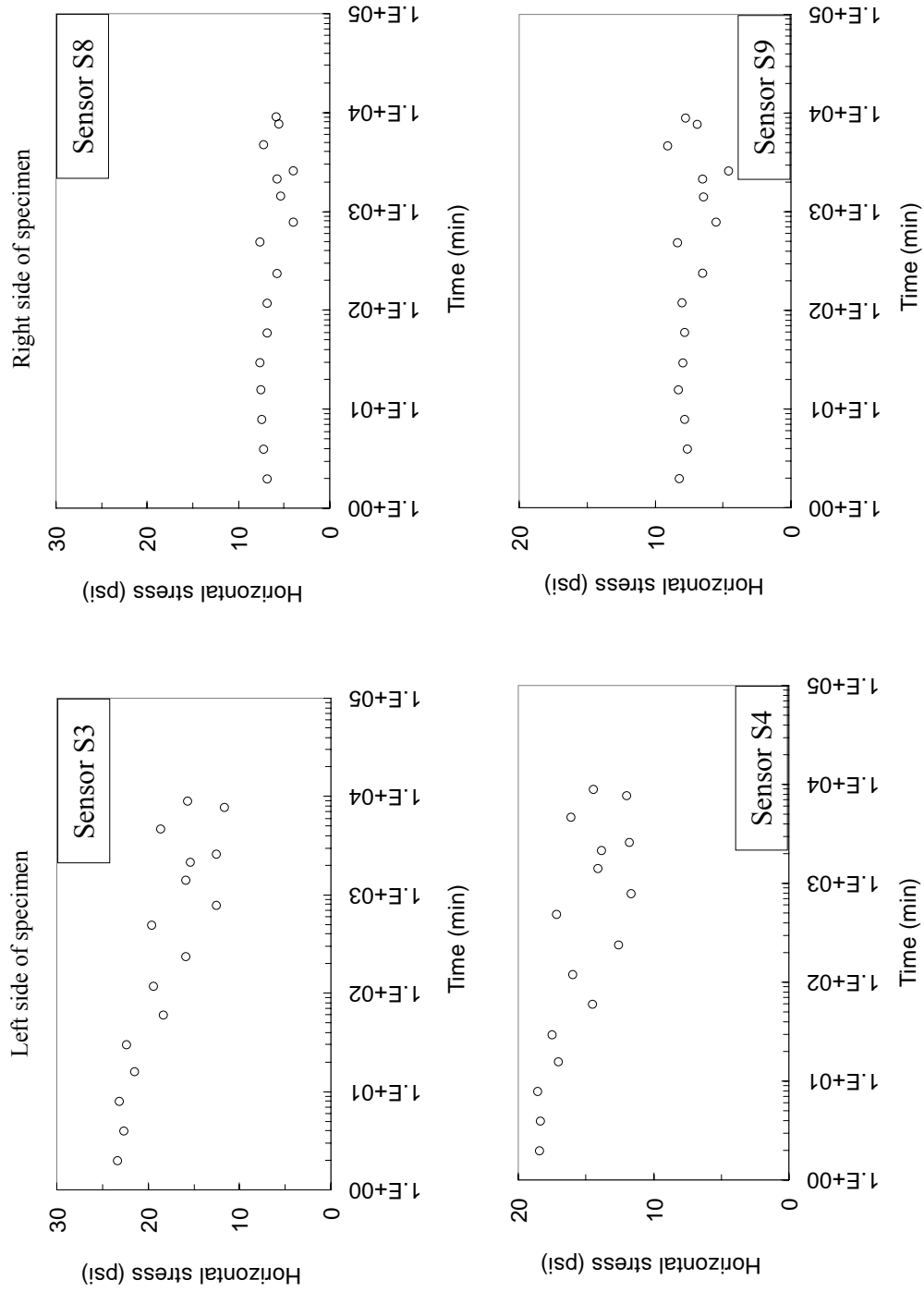


Figure C-15 Horizontal stress versus time from sensors S3, S4 (left) and S8, S9 (right) for Test #5-12

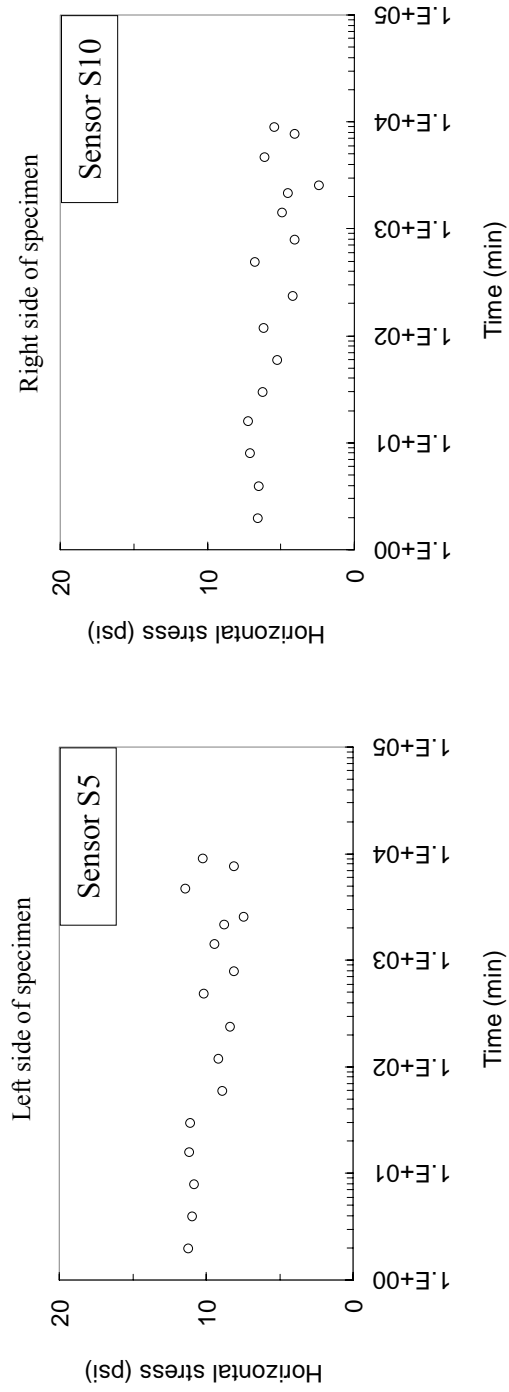


Figure C-16 Horizontal stress versus time from sensors S5 (left) and S10 (right) for Test #5-12

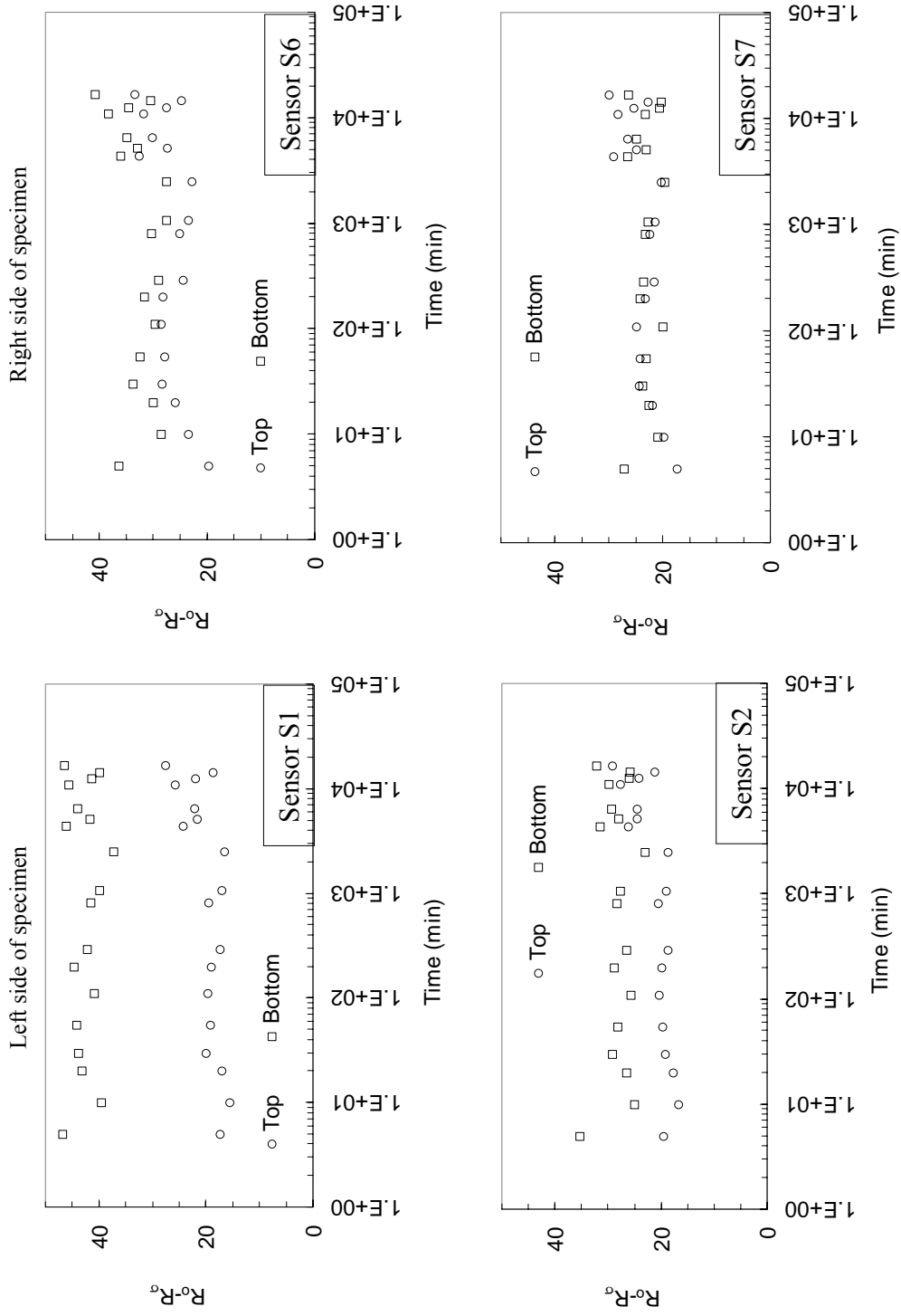


Figure C-17 Relative red intensity versus time from sensors S1, S2 (left) and S6, S7 (right) for Test #5-13

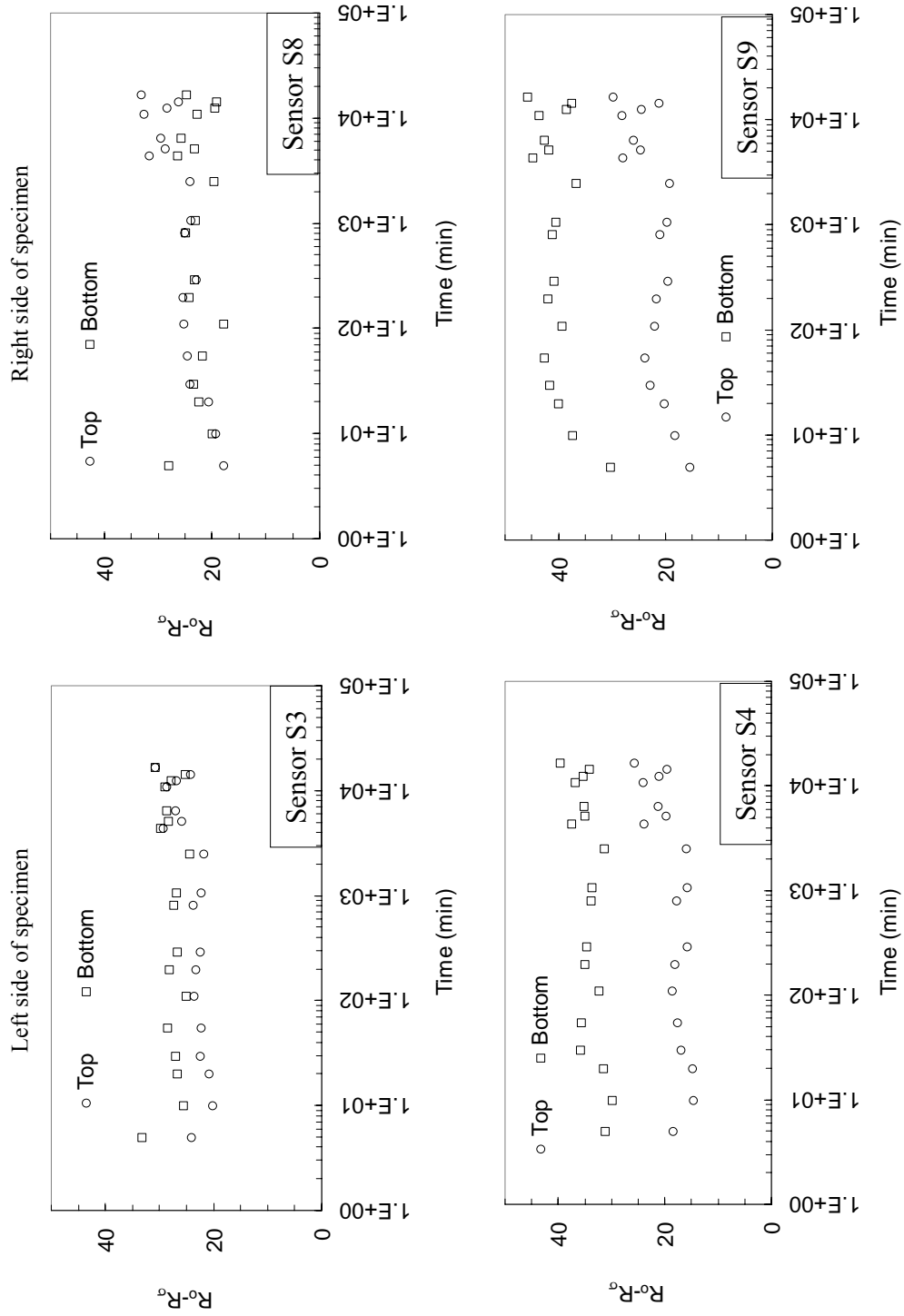


Figure C-18 Relative red intensity versus time from sensors S3, S4 (left) and S8, S9 (right) for Test #5-13

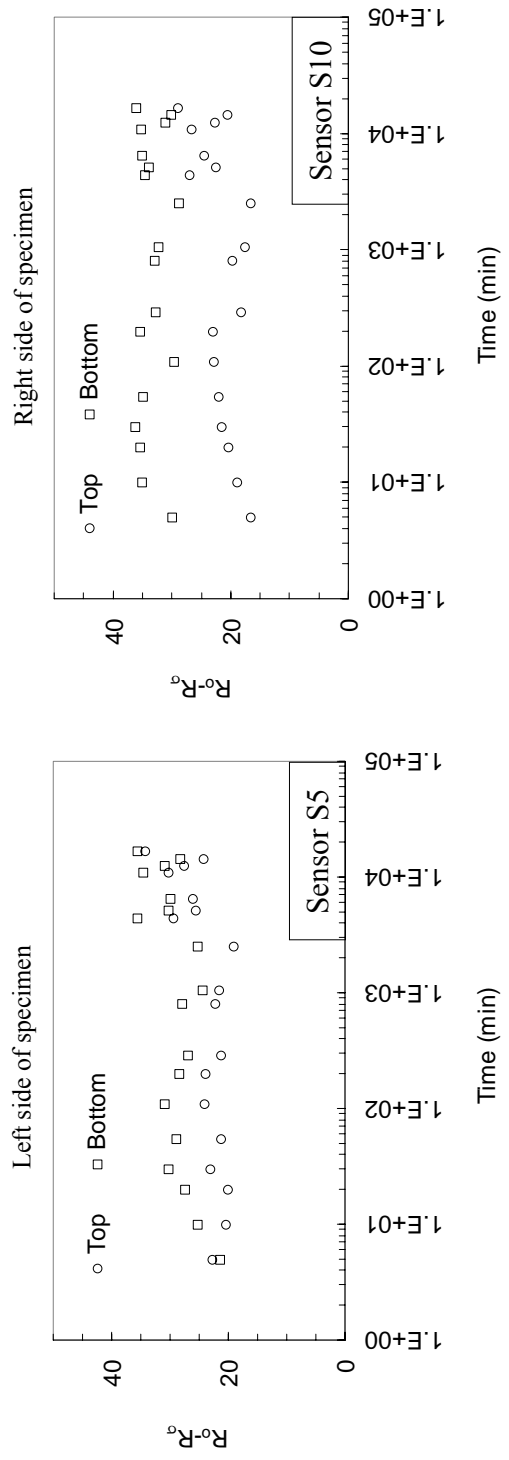


Figure C-19 Relative red intensity versus time from sensors S5 (left) and S10 (right) for Test #5-13

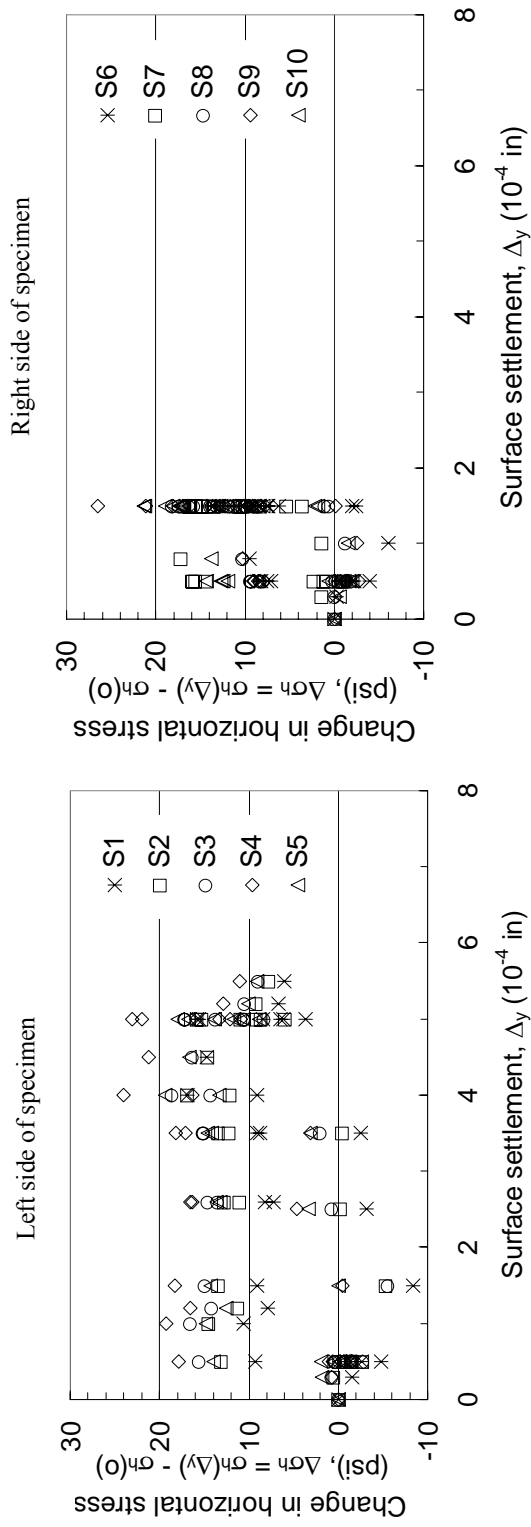


Figure C-20 Changes in horizontal stress versus surface settlement for Test #5-13

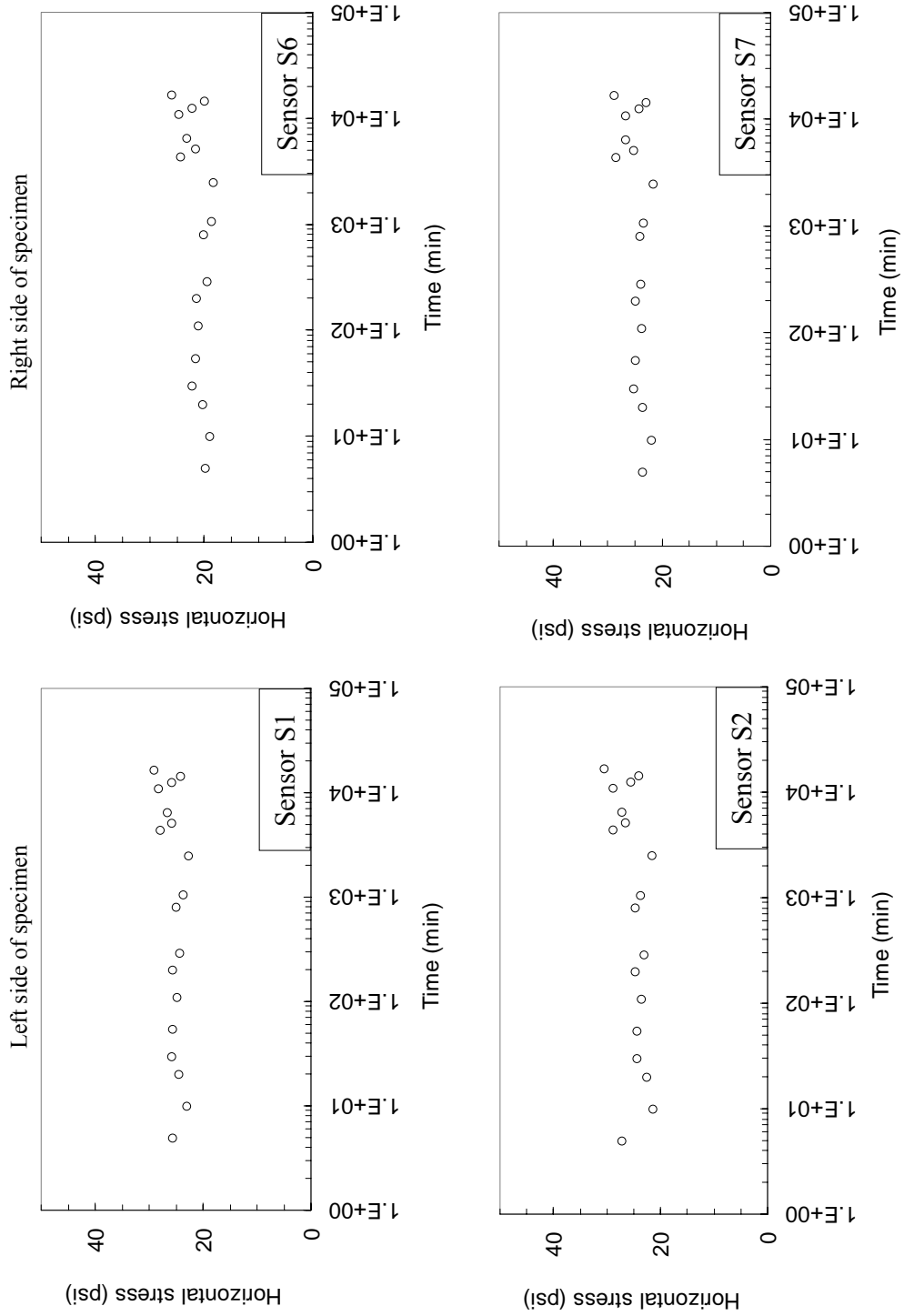


Figure C-21 Horizontal stress versus time from sensors S1, S2 (left) and S6, S7 (right) for Test #5-13

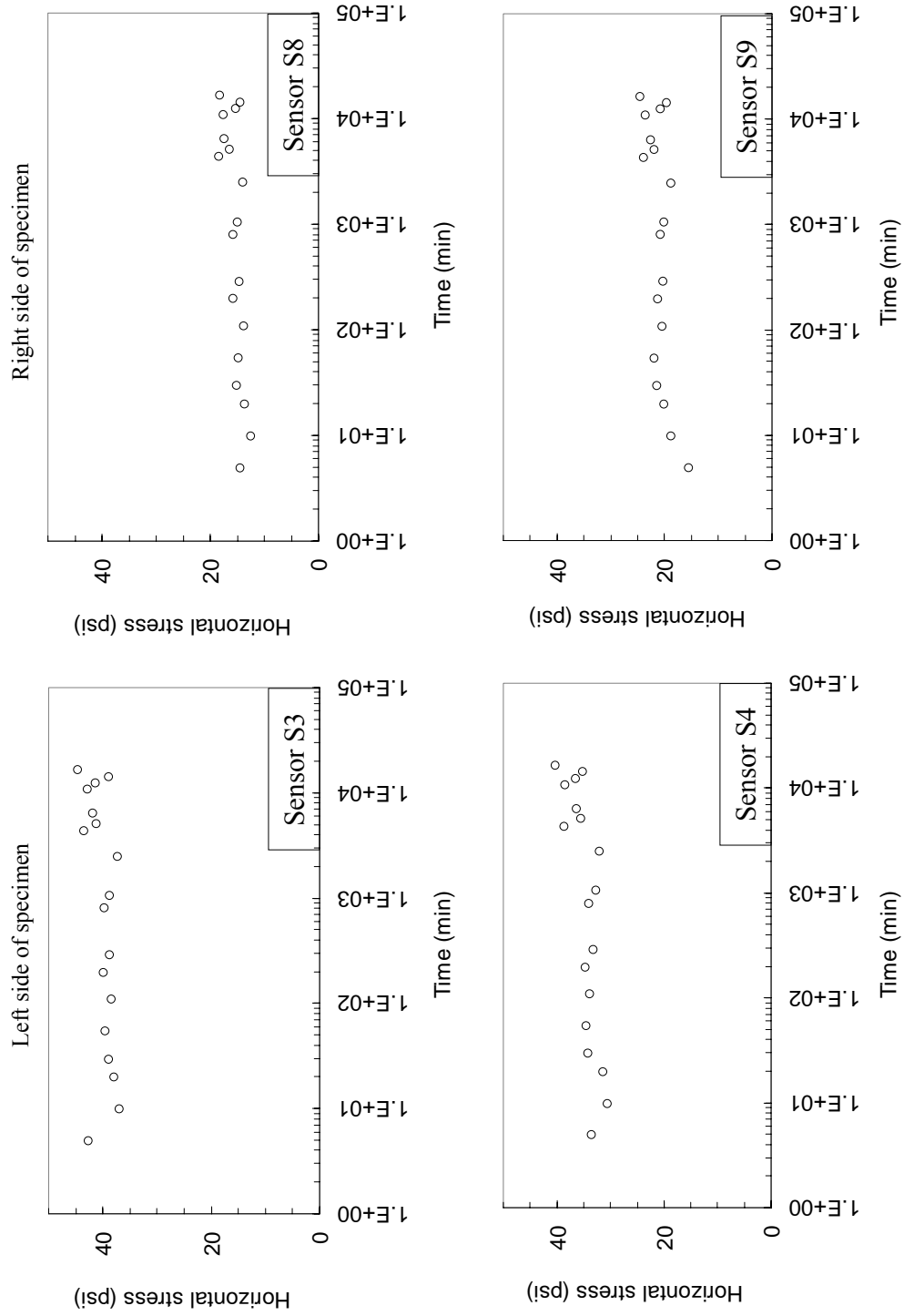


Figure C-22 Horizontal stress versus time from sensors S3, S4 (left) and S8, S9 (right) for Test #5-13

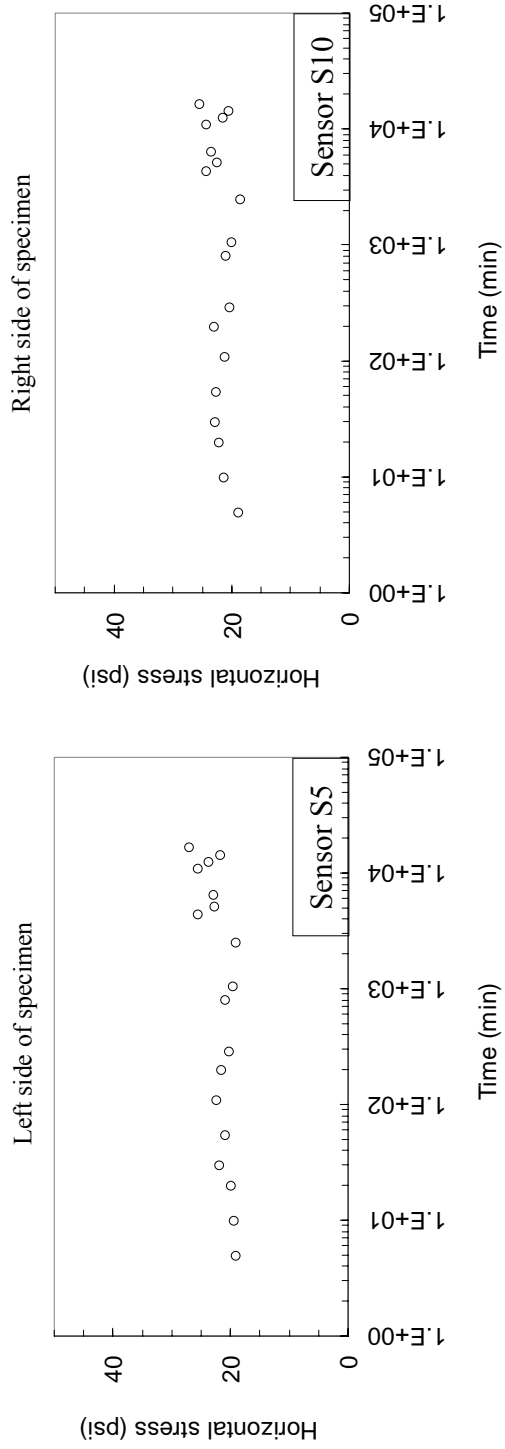


Figure C-23 Horizontal stress versus time from sensors S5 (left) and S10 (right) for Test #5-13

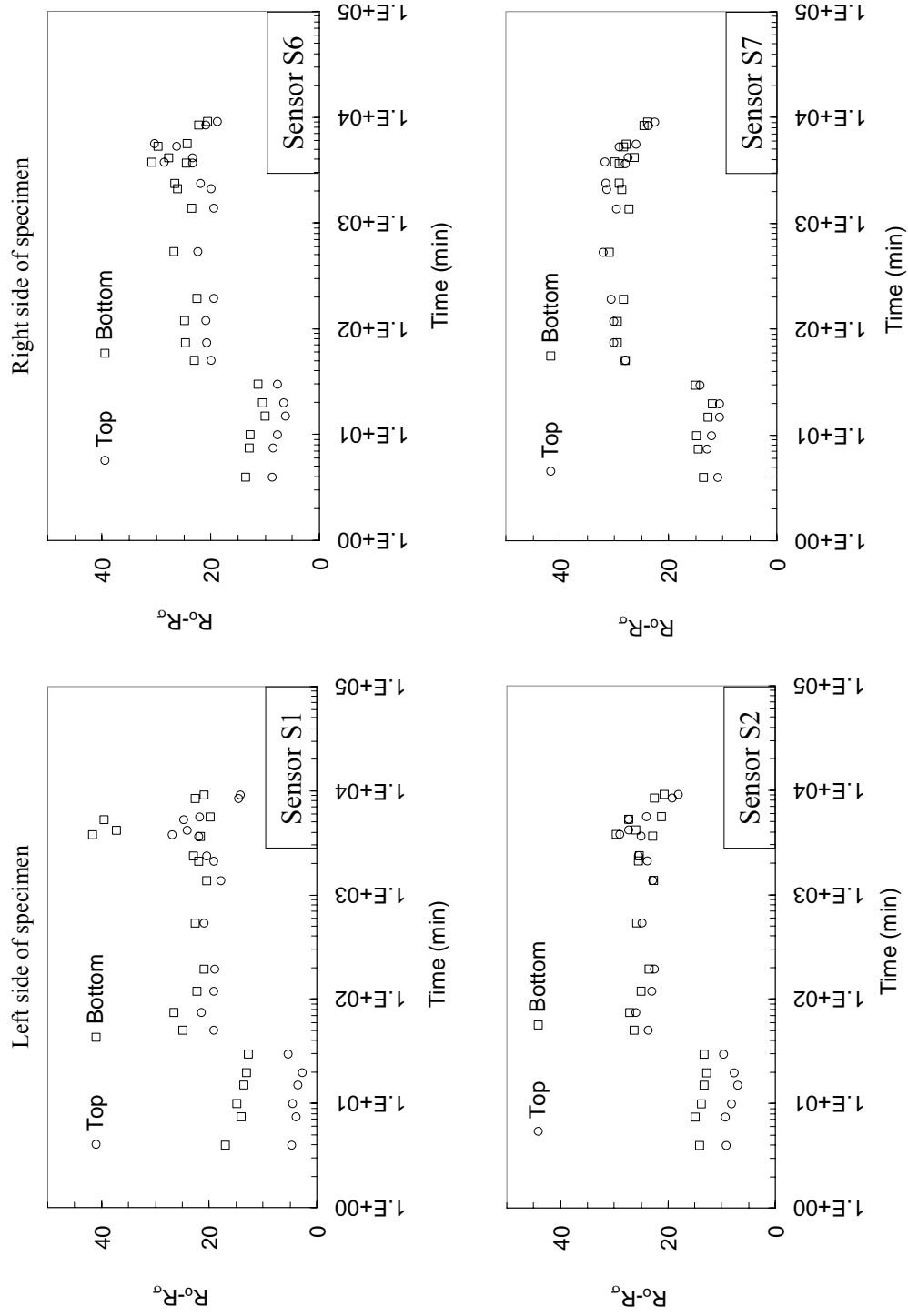


Figure C-24 Relative red intensity versus time from sensors S1, S2 (left) and S6, S7 (right) for Test #5-14

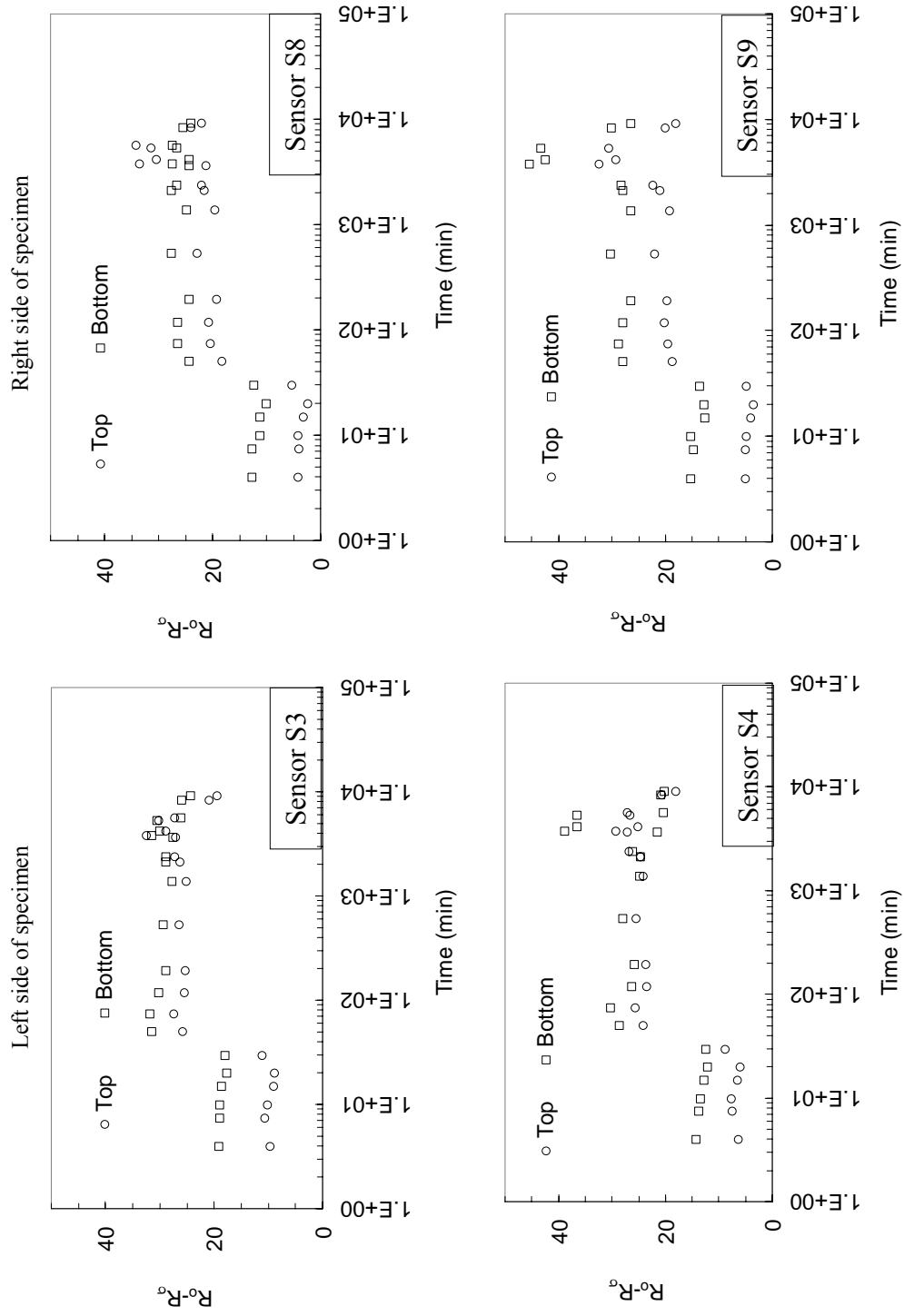


Figure C-25 Relative red intensity versus time from sensors S3, S4 (left) and S8, S9 (right) for Test #5-14

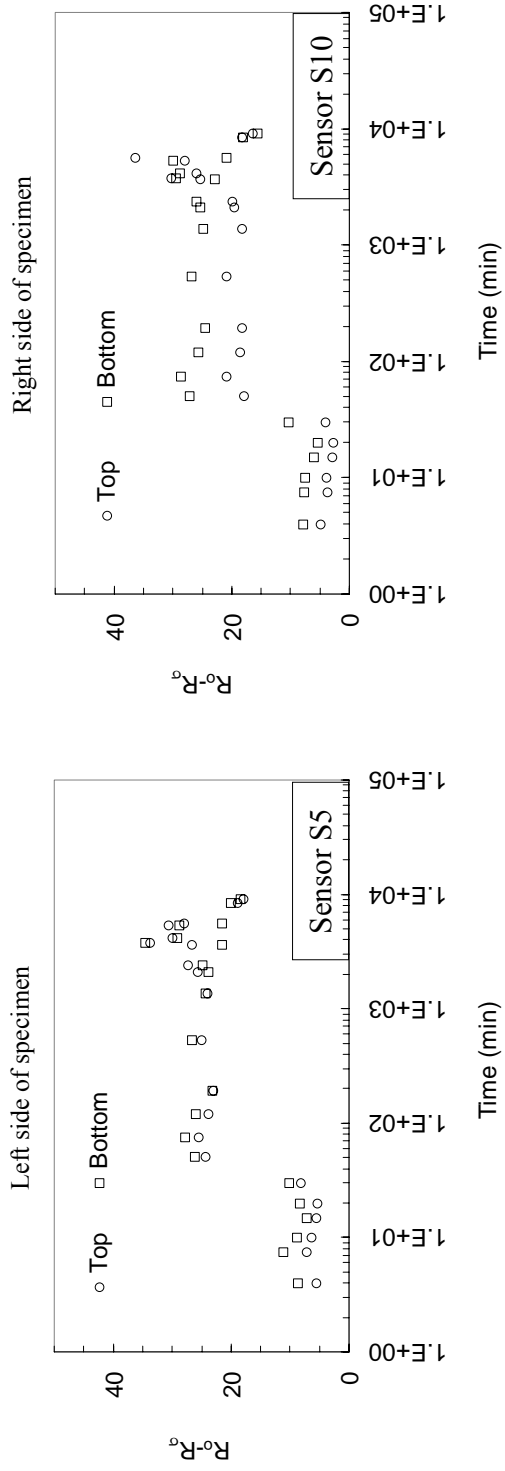


Figure C-26 Relative red intensity versus time from sensors S5 (left) and S10 (right) for Test #5-14

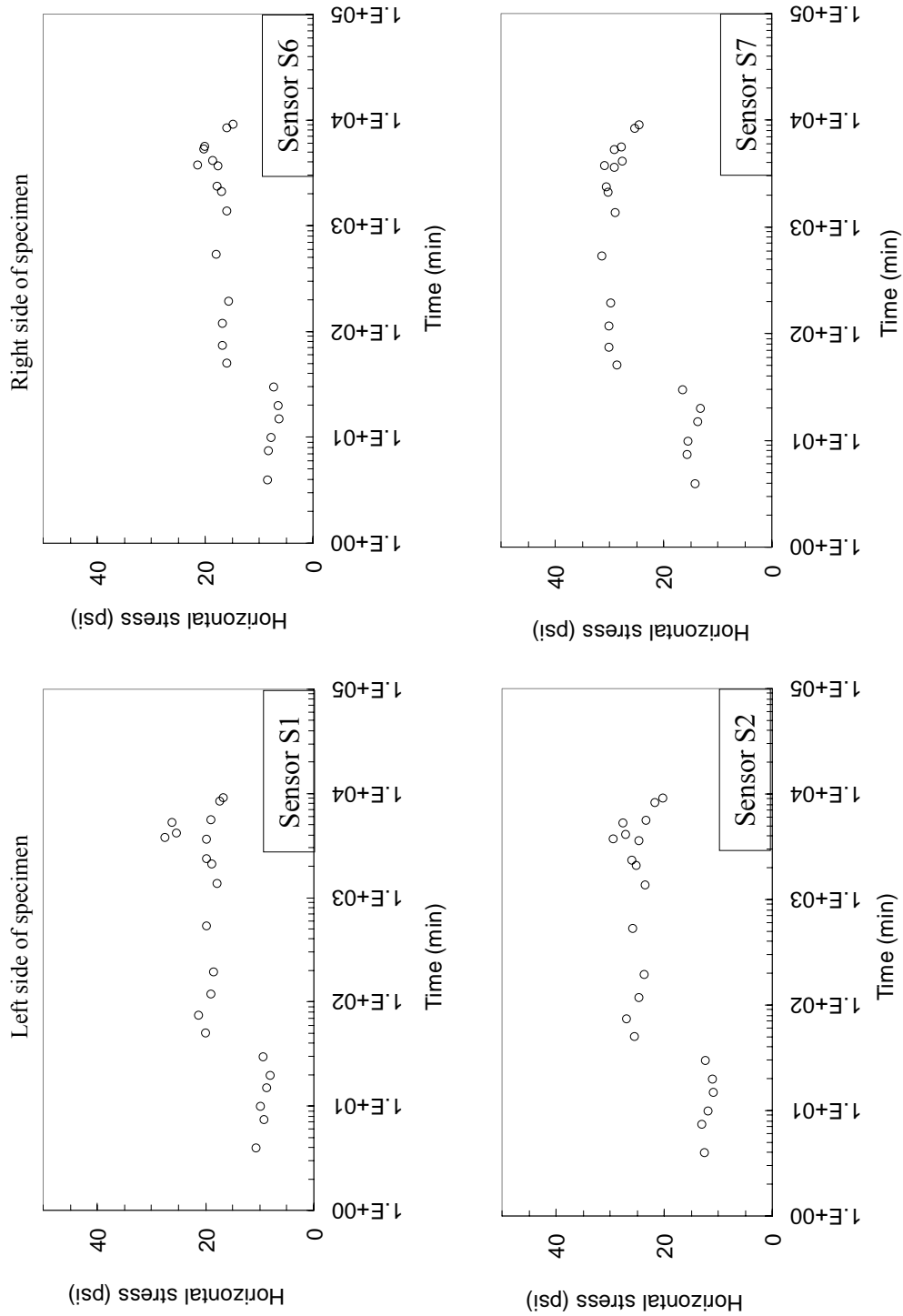


Figure C-27 Horizontal stress versus time from sensors S1, S2 (left) and S6, S7 (right) for Test #5-14

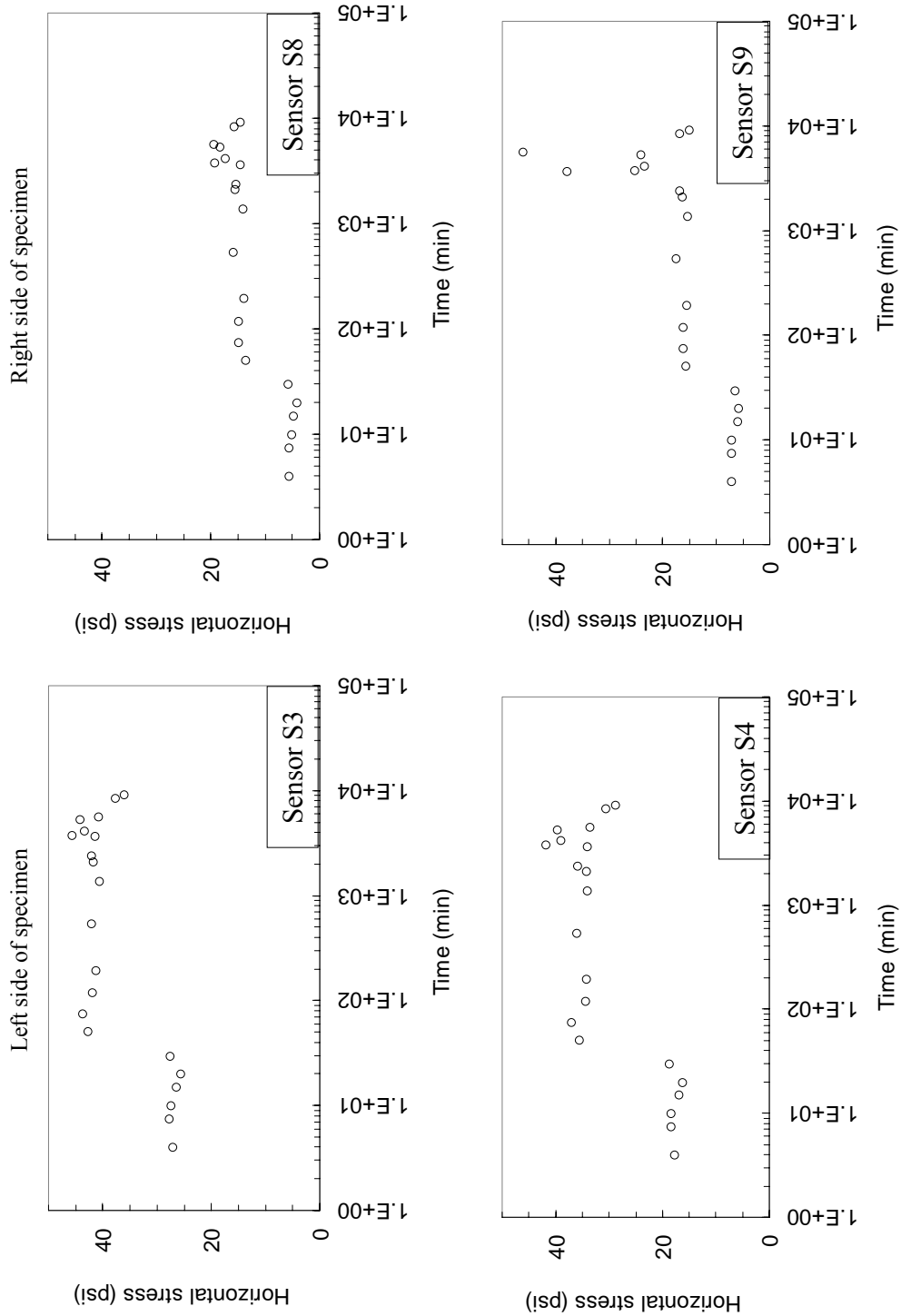


Figure C-28 Horizontal stress versus time from sensors S3, S4 (left) and S8, S9 (right) for Test #5-14

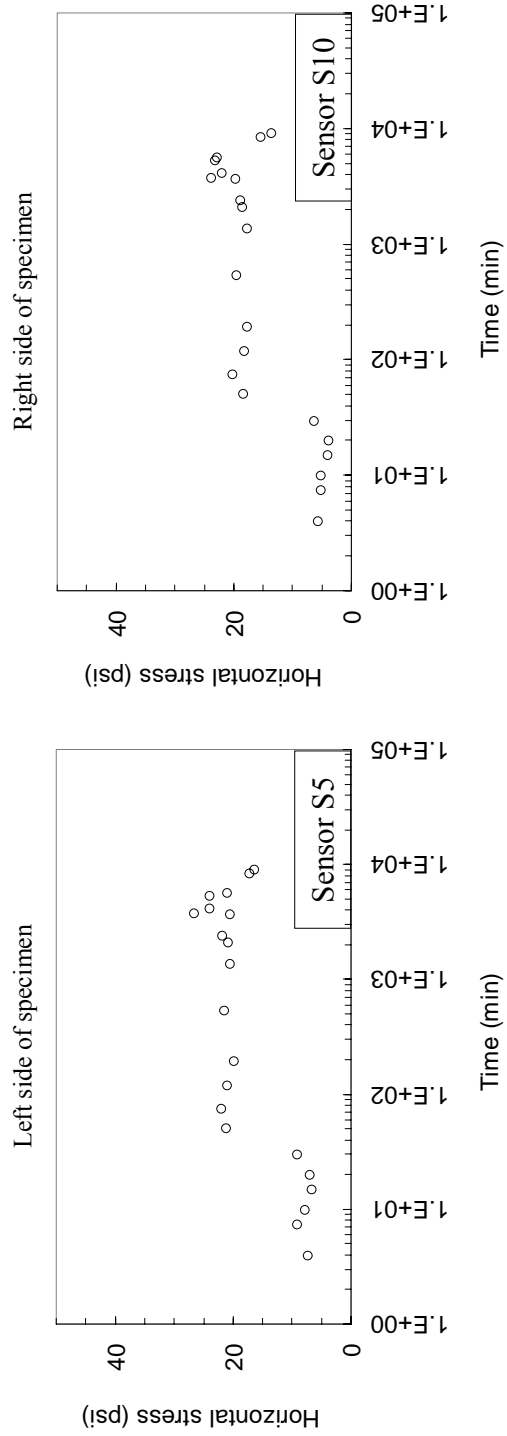


Figure C-29 Horizontal stress versus time from sensors S5 (left) and S10 (right) for Test #5-14

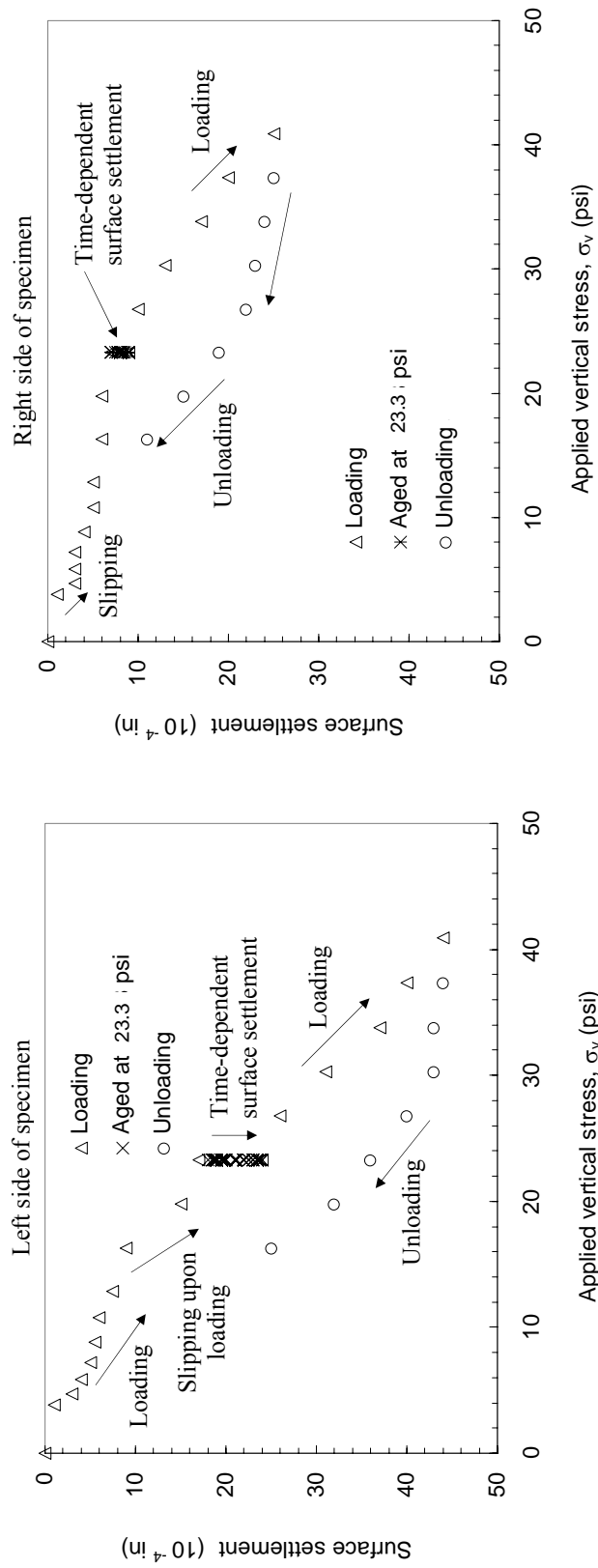


Figure C-30 Surface settlement of specimens during loading, under sustained vertical stress of 23.3 psi for 7 days and during subsequent unloading for Test #5-14

Left side of specimen

Right side of specimen

Test results of red intensity for Test #5-15 are not reported after this point due to unexpected flooding into the lab. At that time, vibrations from the operations for resolving the flooding might cause movement of the setup of the measuring devices, shaking of the light intensity, etc.

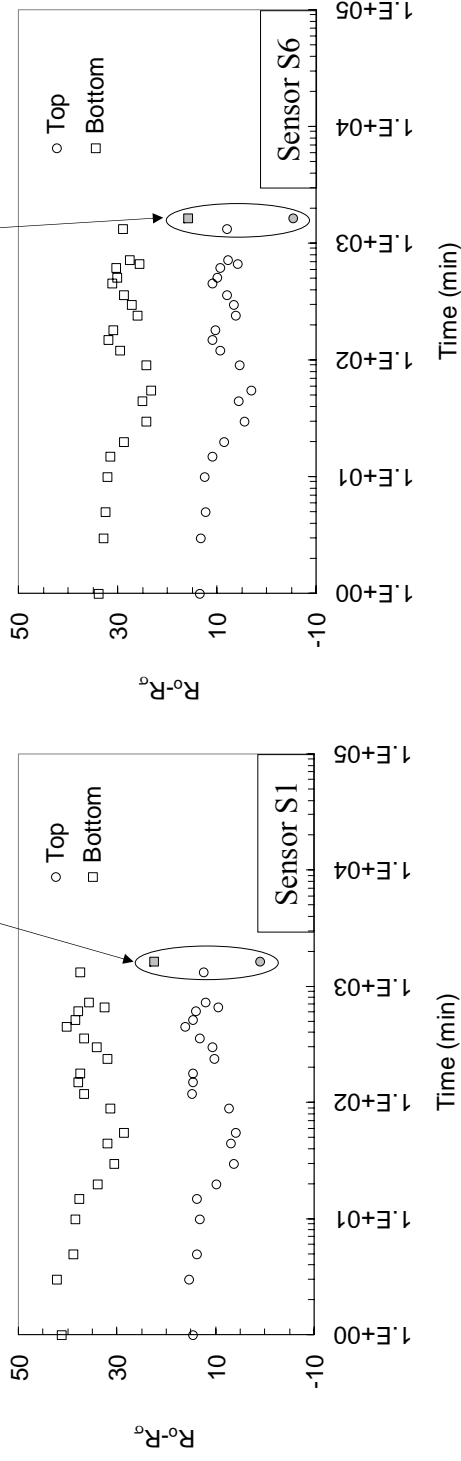


Figure C-31 Relative red intensity versus time from sensors S1 (left) and S6 (right) for Test #5-15

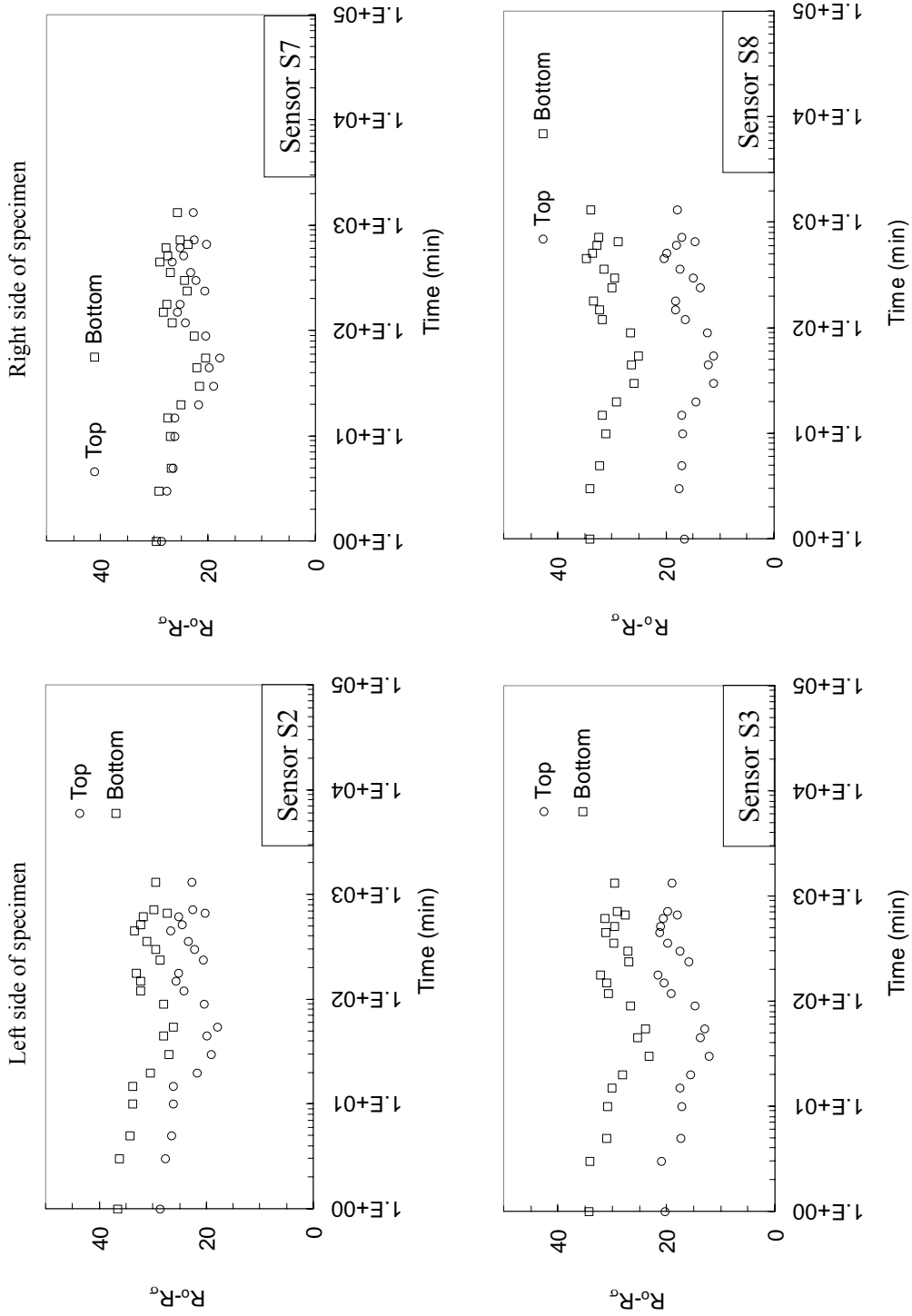


Figure C-32 Relative red intensity versus time from sensors S2, S3 (left) and S7, S8 (right) for Test #5-15

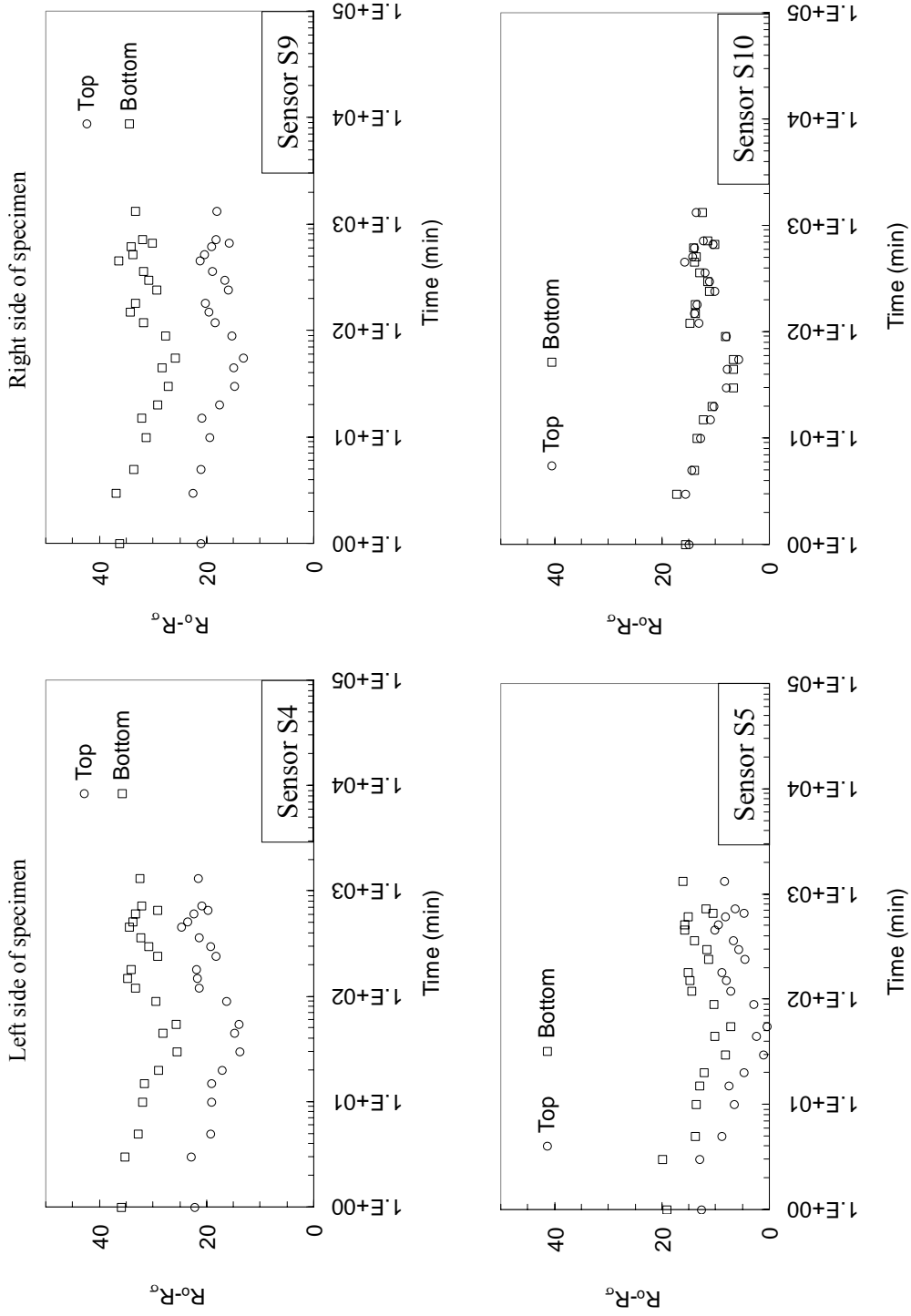


Figure C-33 Relative red intensity versus time from sensors S4, S5 (left) and S9, S10 (right) for Test #5-15

Left side of specimen

Right side of specimen

Test results of red intensity for Test #5-15 are not reported after this point due to unexpected flooding into the lab. At that time, vibrations from the operations for resolving the flooding might cause movement of the setup of the measuring devices, shaking of the light intensity, etc.

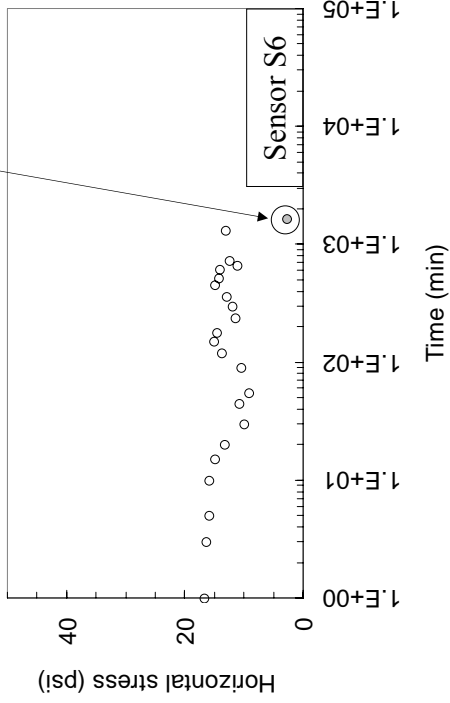
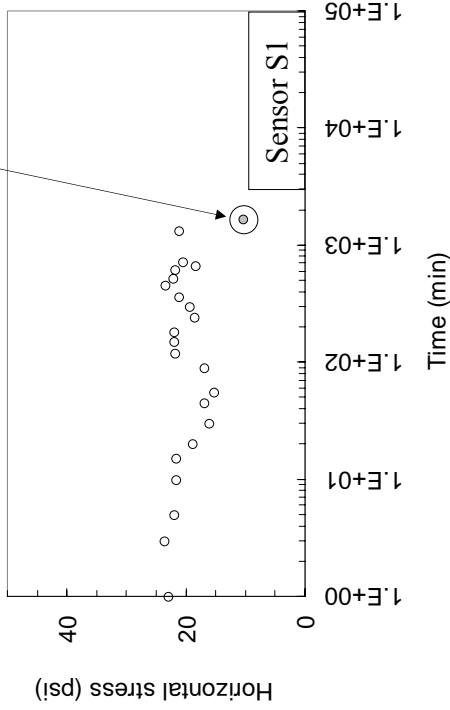


Figure C-34 Horizontal stress versus time from sensors S1 (left) and S6 (right) for Test #5-15

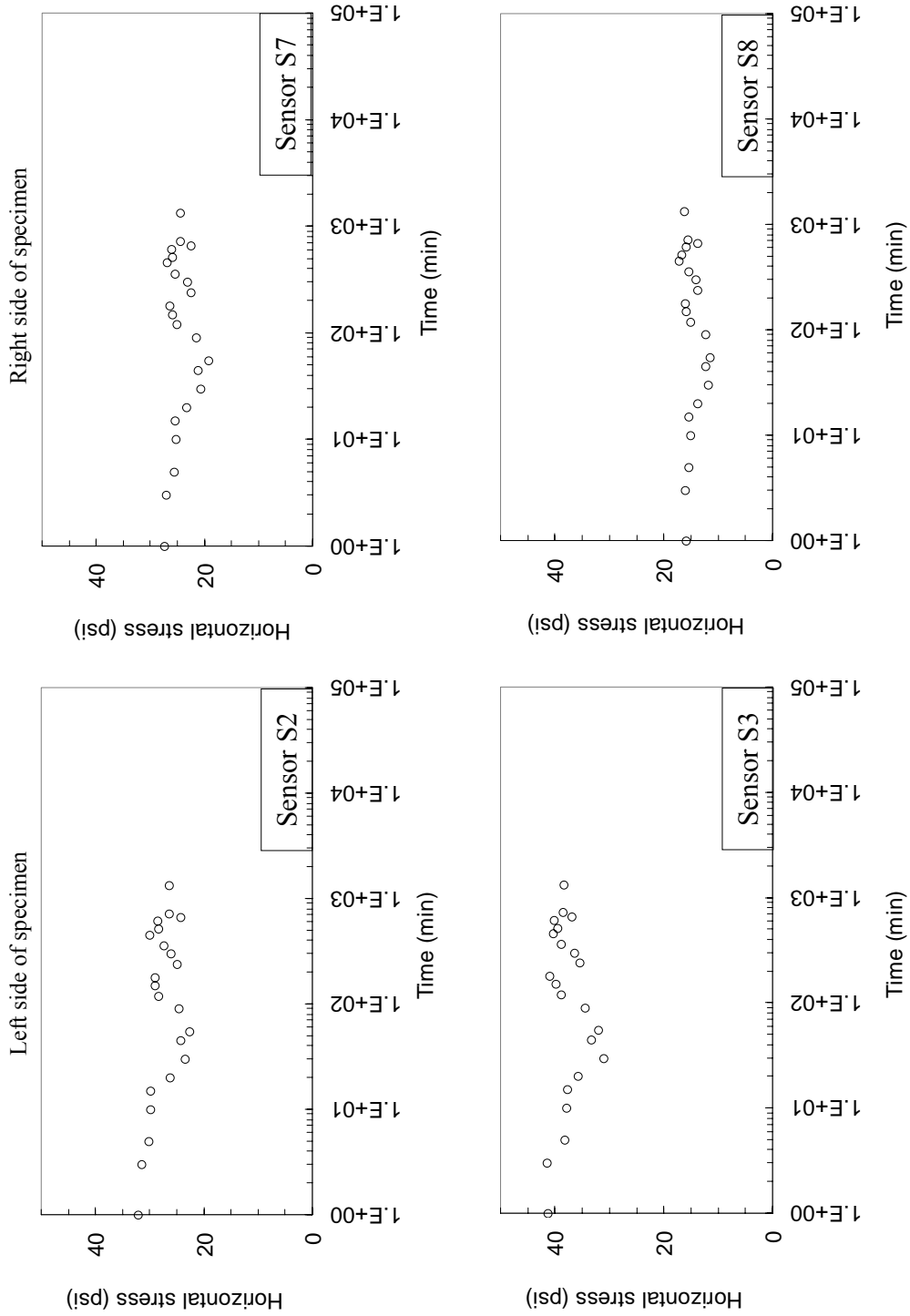


Figure C-35 Horizontal stress versus time from sensors S2, S3 (left) and S7, S8 (right) for Test #5-15

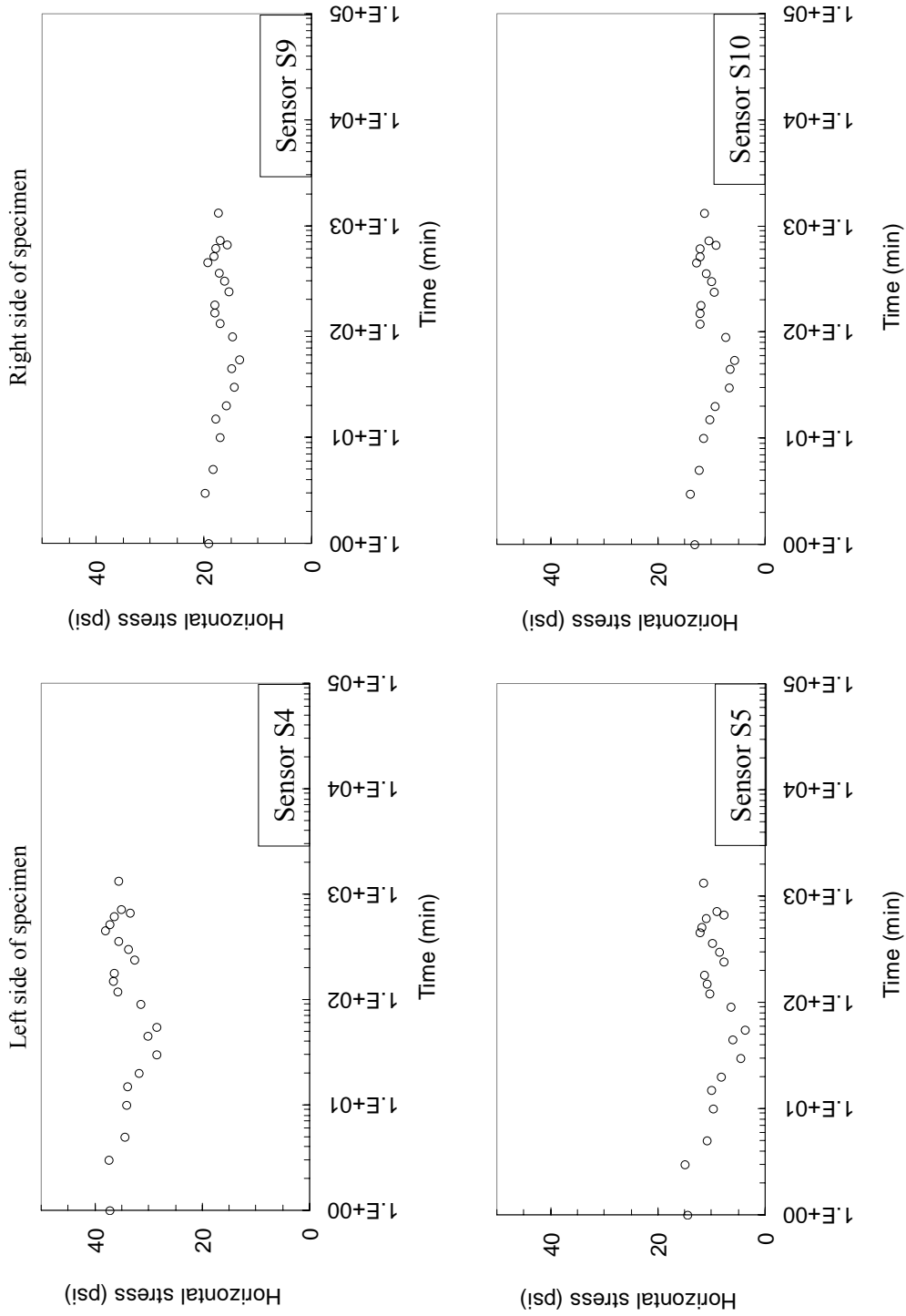


Figure C-36 Horizontal stress versus time from sensors S4, S5 (left) and S9, S10 (right) for Test #5-15

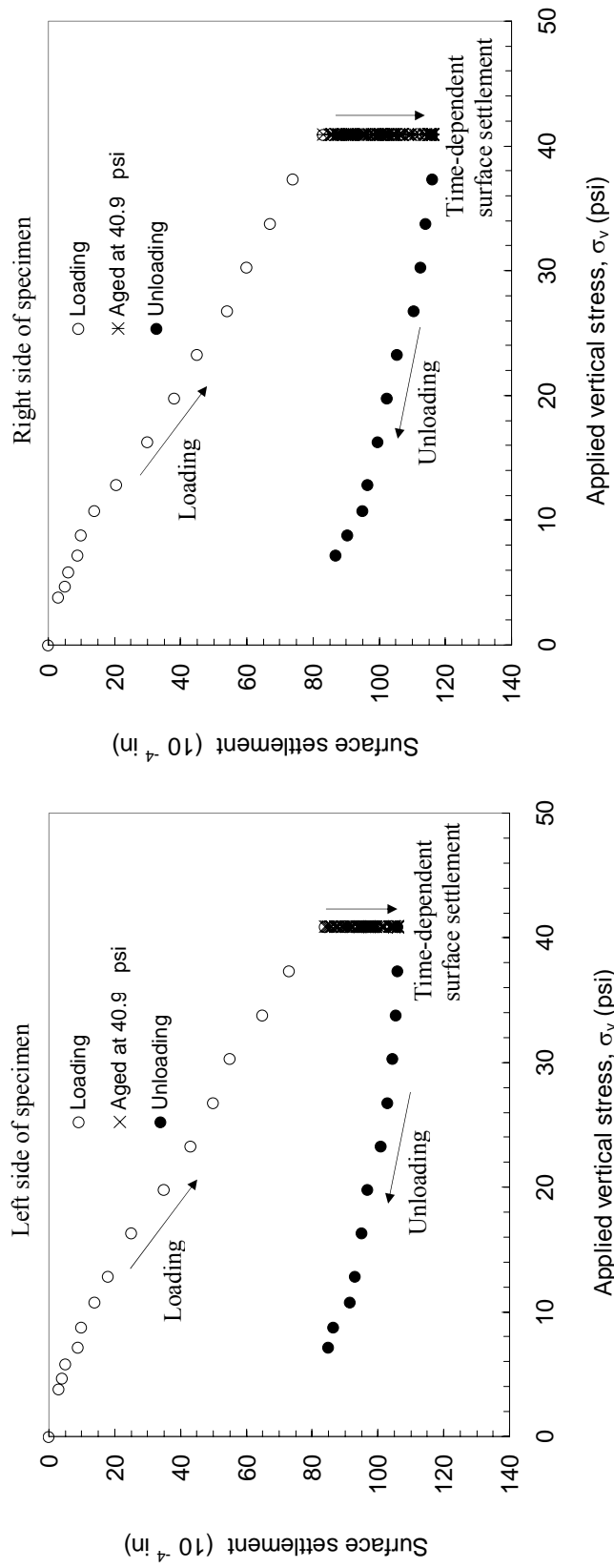


Figure C-37 Surface settlement due to loading, under sustained vertical stress of 40.9 psi vertical stress for 7 days and during subsequent unloading for Test #5-15

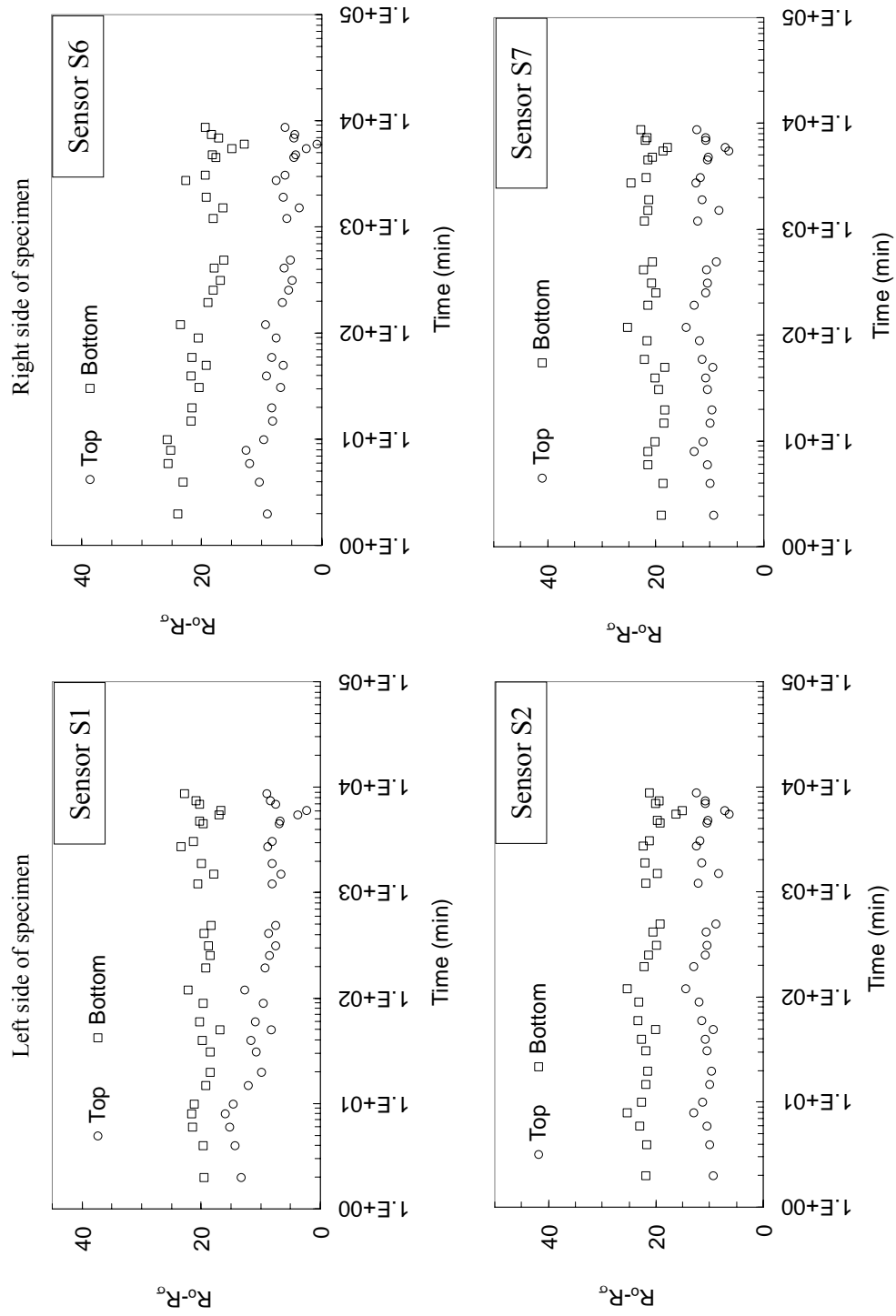


Figure C-38 Relative red intensity versus time from sensors S1, S2 (left) and S6, S7 (right) for Test #5-16

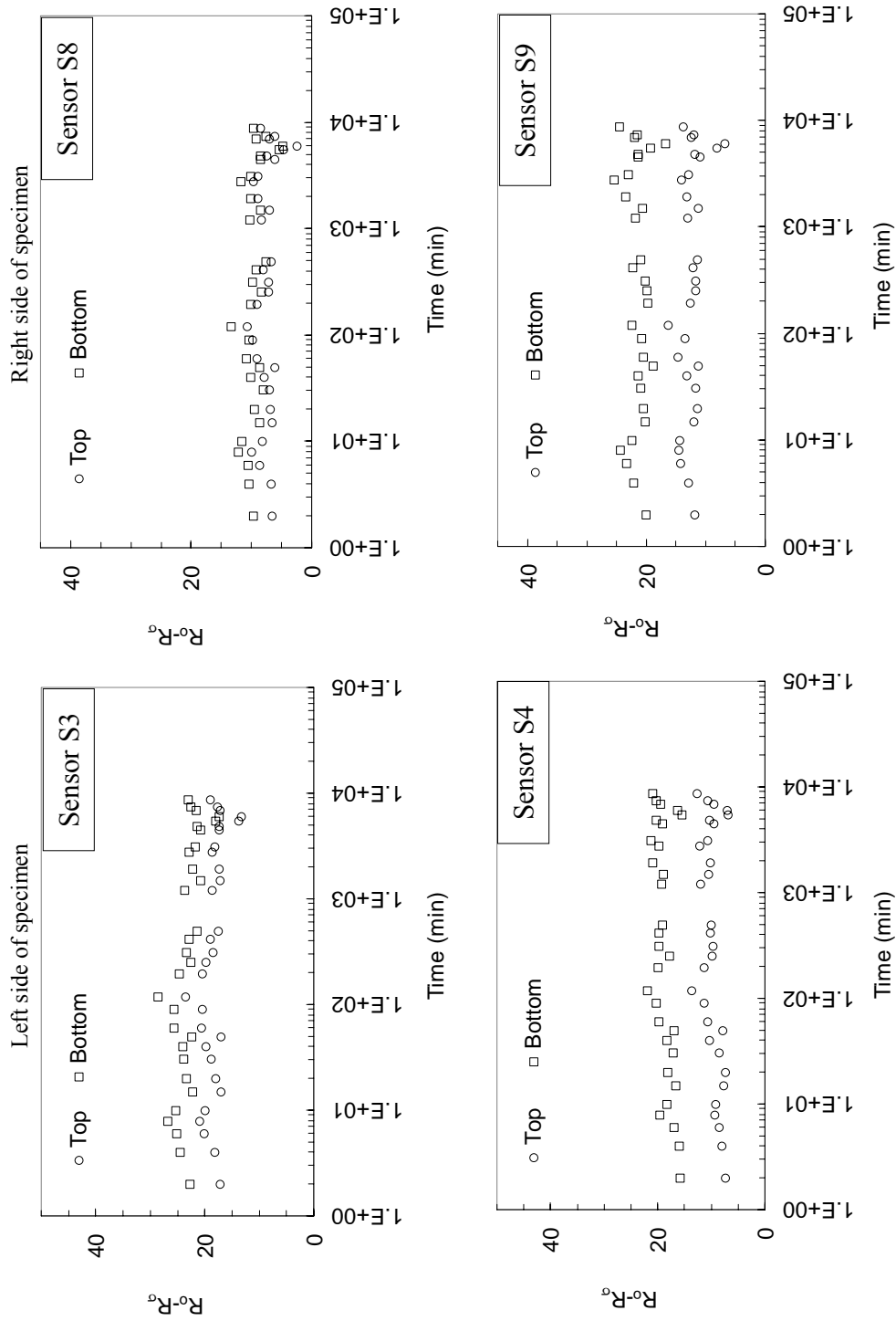


Figure C-39 Relative red intensity versus time from sensors S3, S4 (left) and S8, S9 (right) for Test #5-16

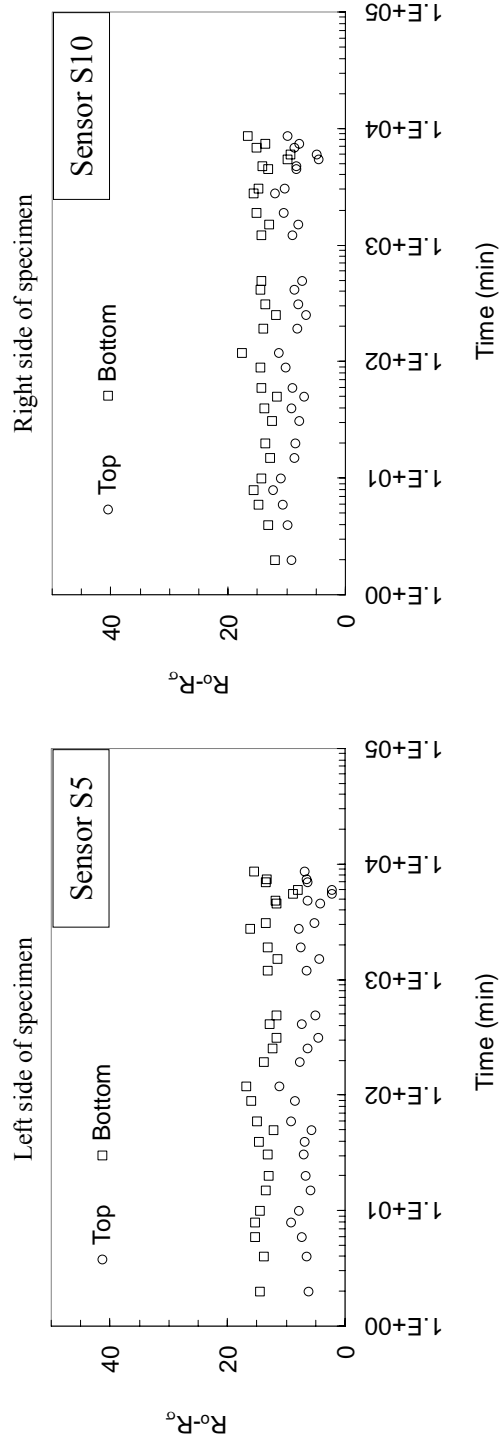


Figure C-40 Relative red intensity versus time from sensors S5 (left) and S10 (right) for Test #5-16

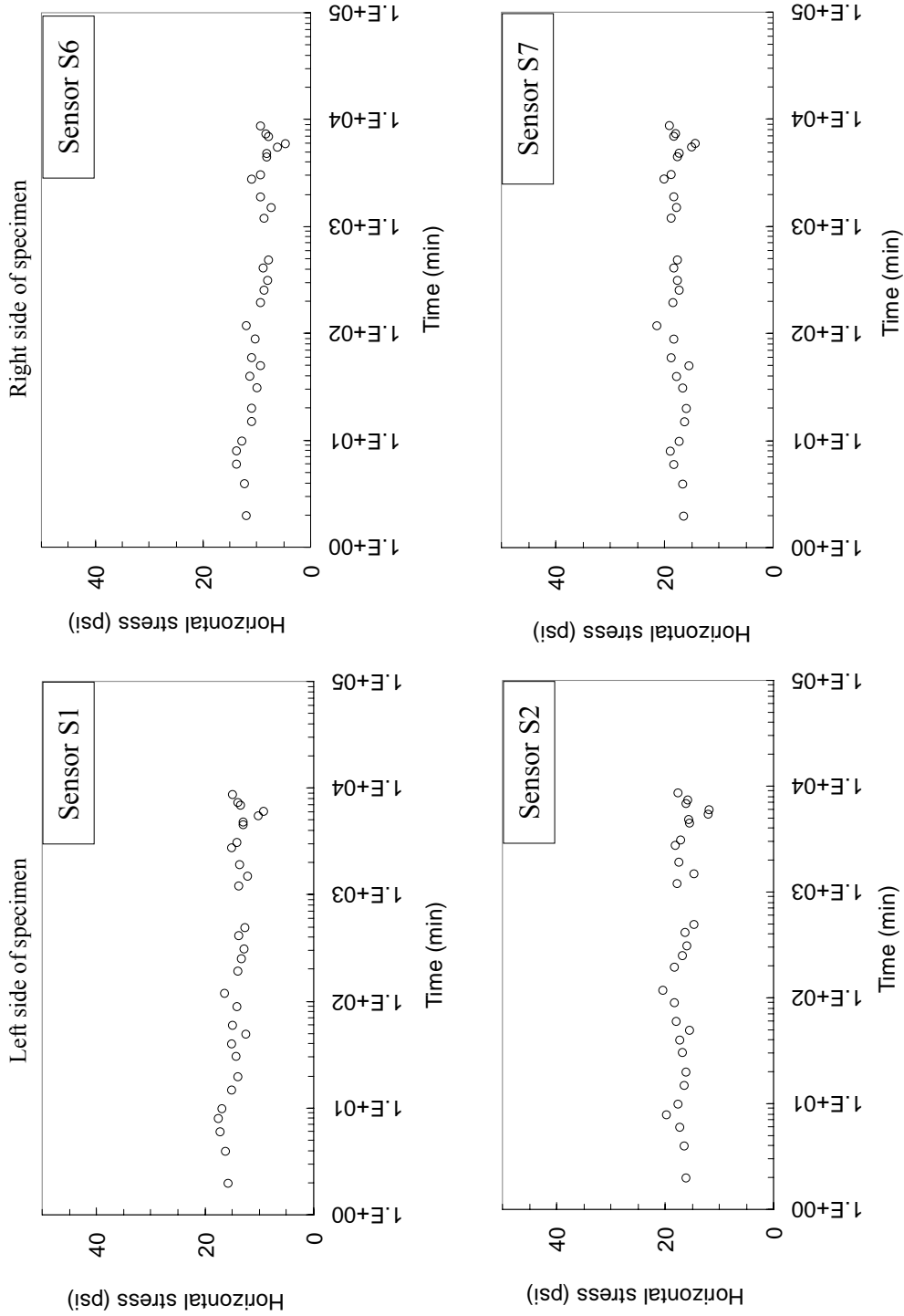


Figure C-41 Horizontal stress versus time from sensors S1, S2 (left) and S6, S7 (right) for Test #5-16

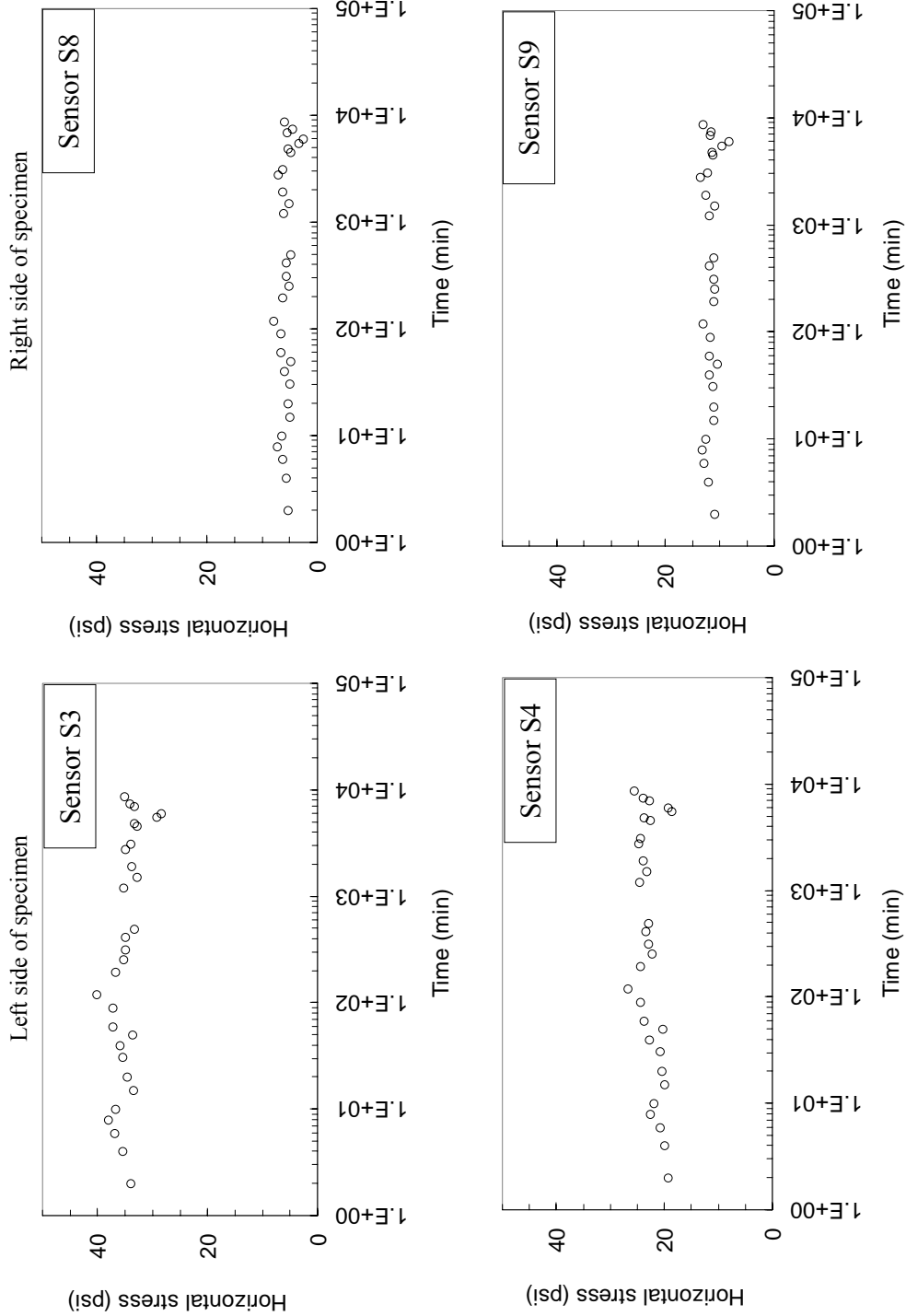


Figure C-42 Horizontal stress versus time from sensors S3, S4 (left) and S8, S9 (right) for Test #5-16

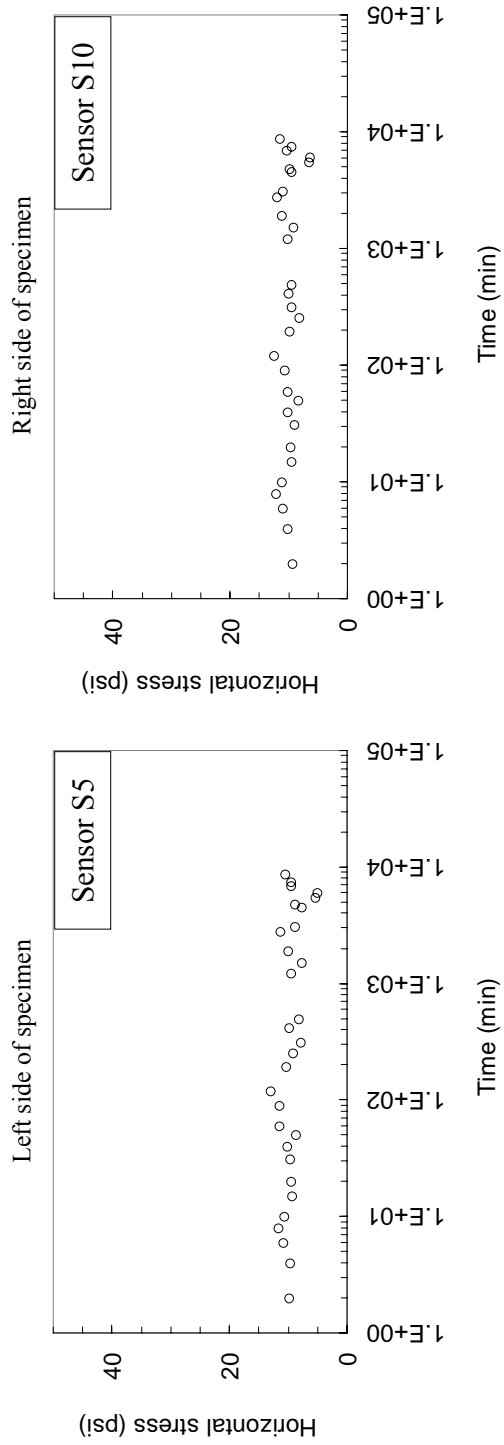


Figure C-43 Horizontal stress versus time from sensors S5 (left) and S10 (right) for Test #5-16

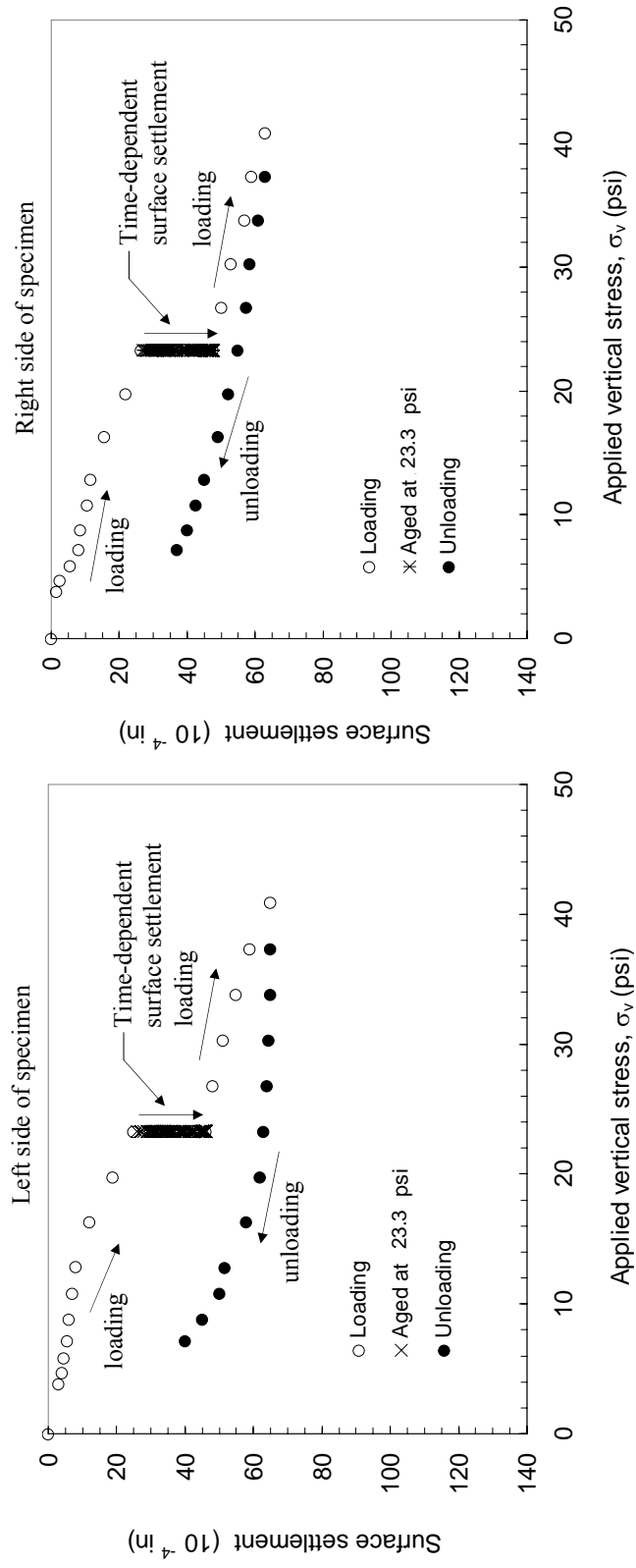


Figure C-44 Surface settlement during loading, under sustained vertical stress of 23.3 psi for 7 days and during unloading for Test #5-16

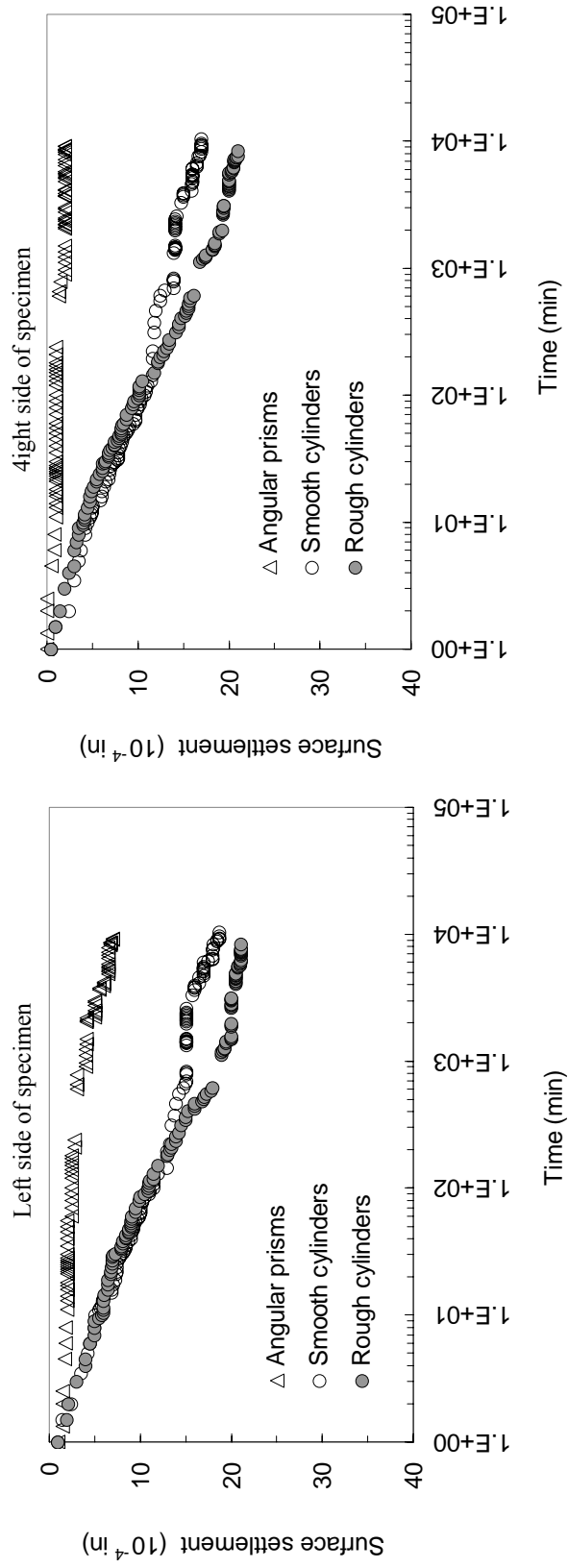


Figure C-45 Surface settlement for 7.5" x 5.0" specimens under a constant vertical stress of 23.3 psi

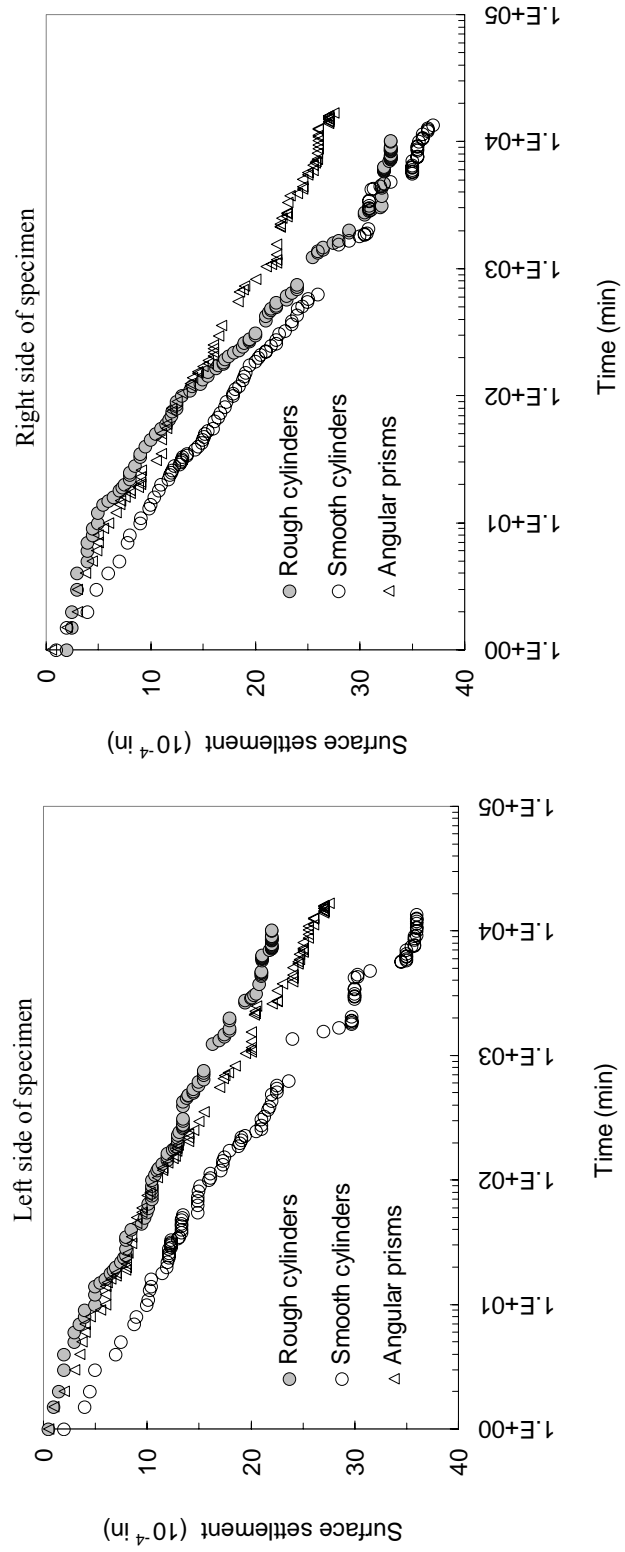


Figure C-46 Surface settlement for 7.5" x 5.0" specimens under a constant vertical stress of 40.9 psi

APPENDIX D
PHOTOS FROM CHAPTER 5

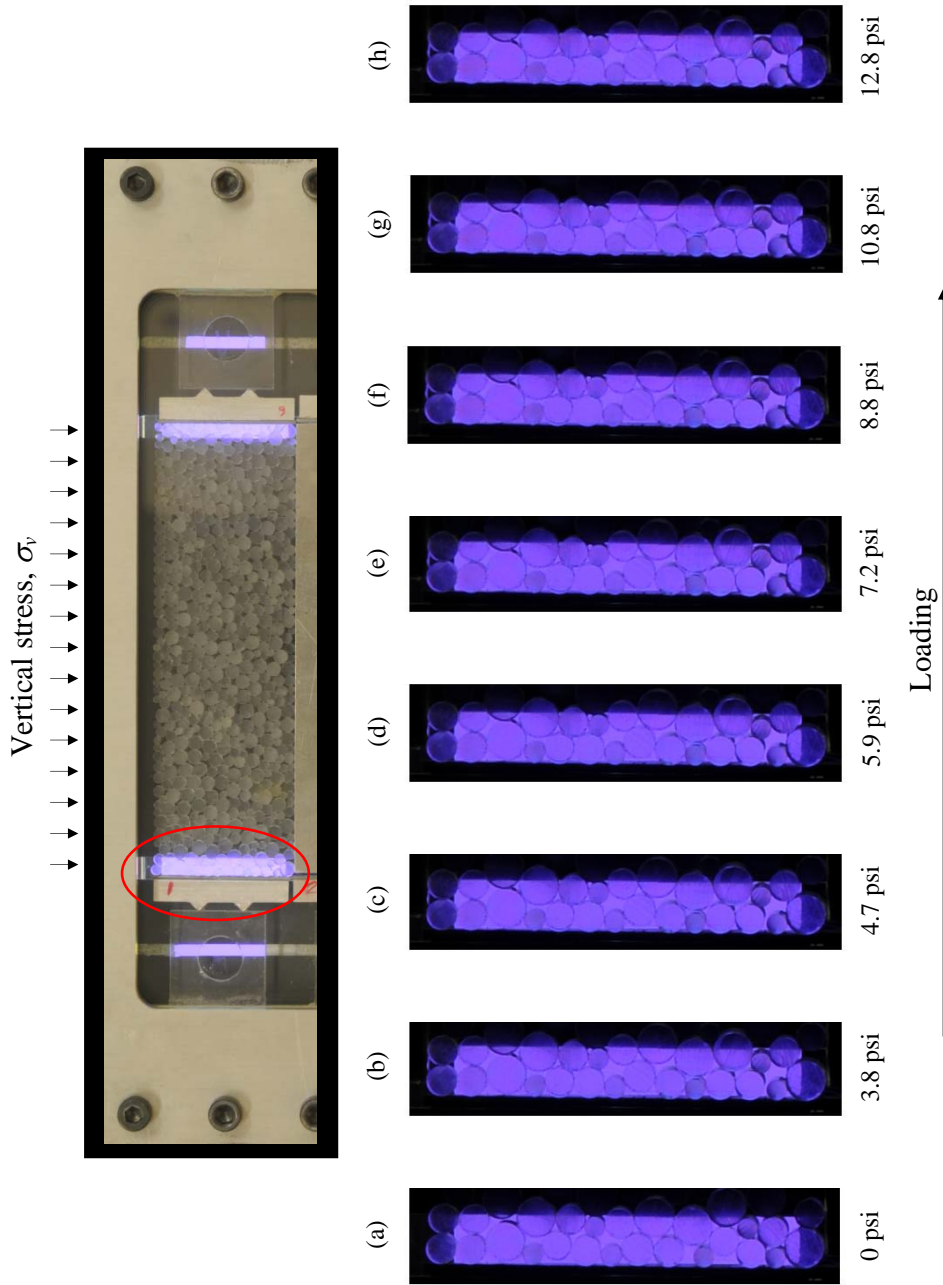


Figure D-1 Photos of particles at the right wall of the specimen during loading for Test #5-2

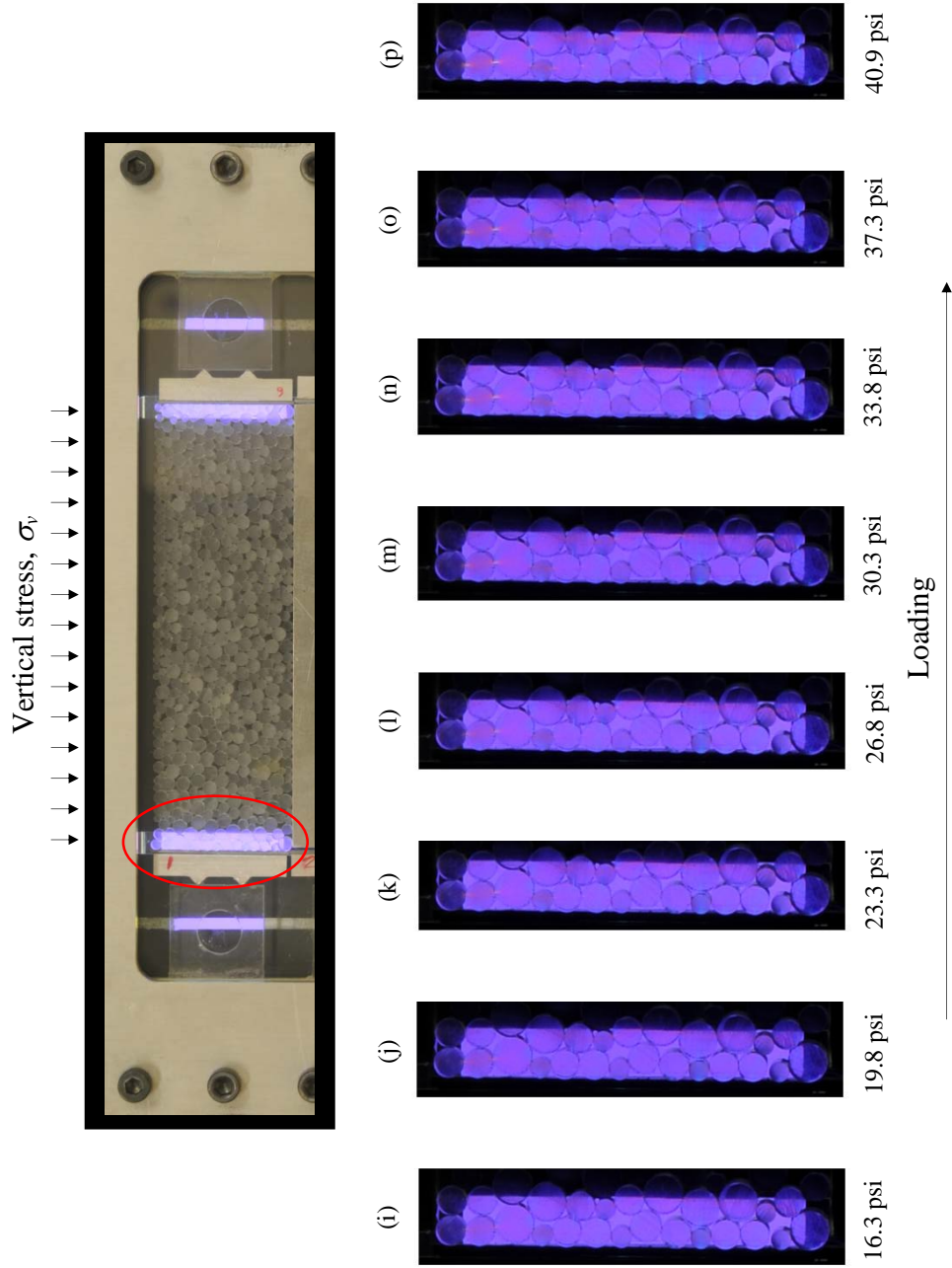


Figure D-1(cont) Photos of particles at the left wall of the specimen during loading for Test #5-2

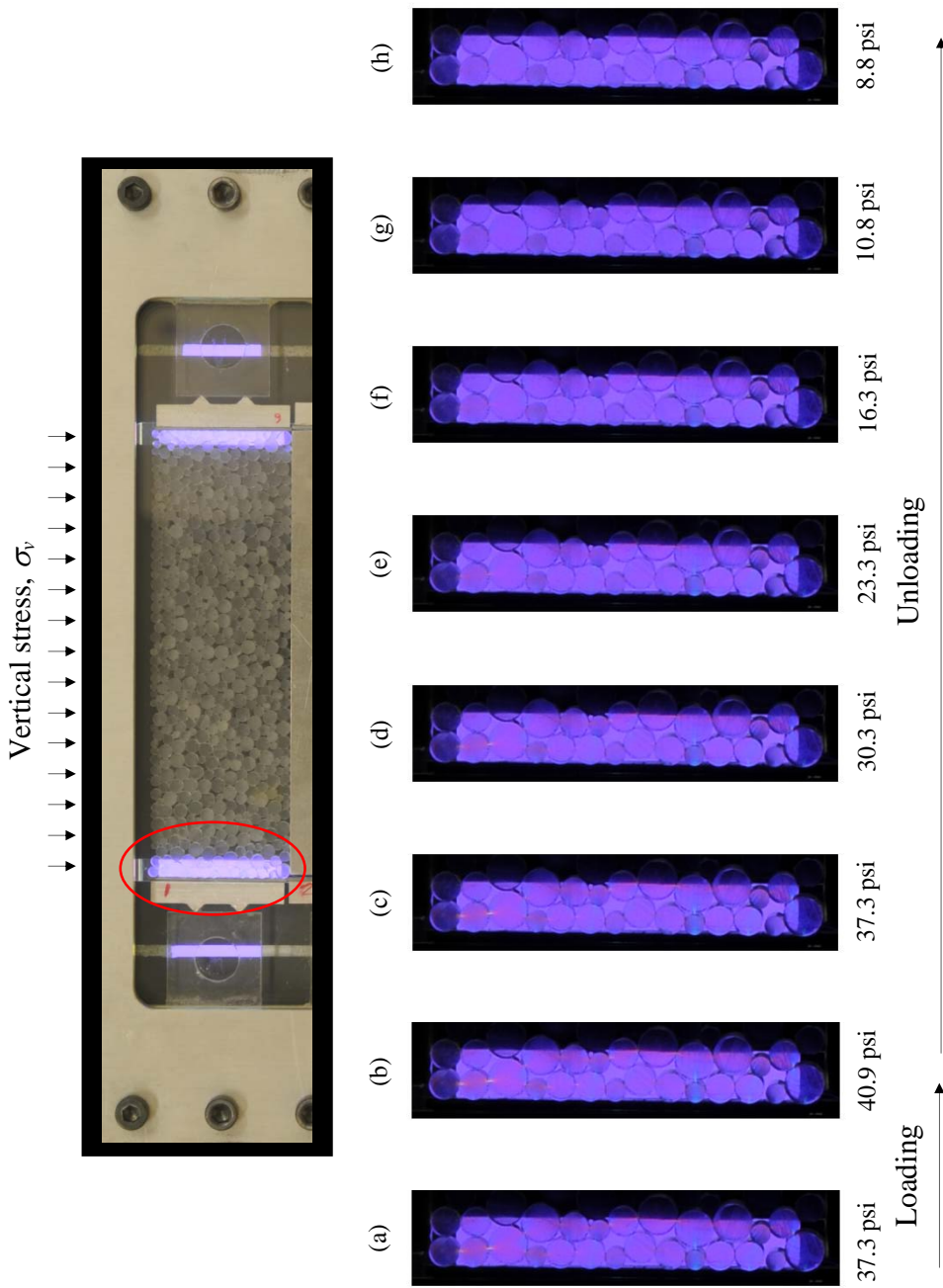


Figure D-2 Photos of particles at the left wall of the specimen during loading and unloading for Test #5-2

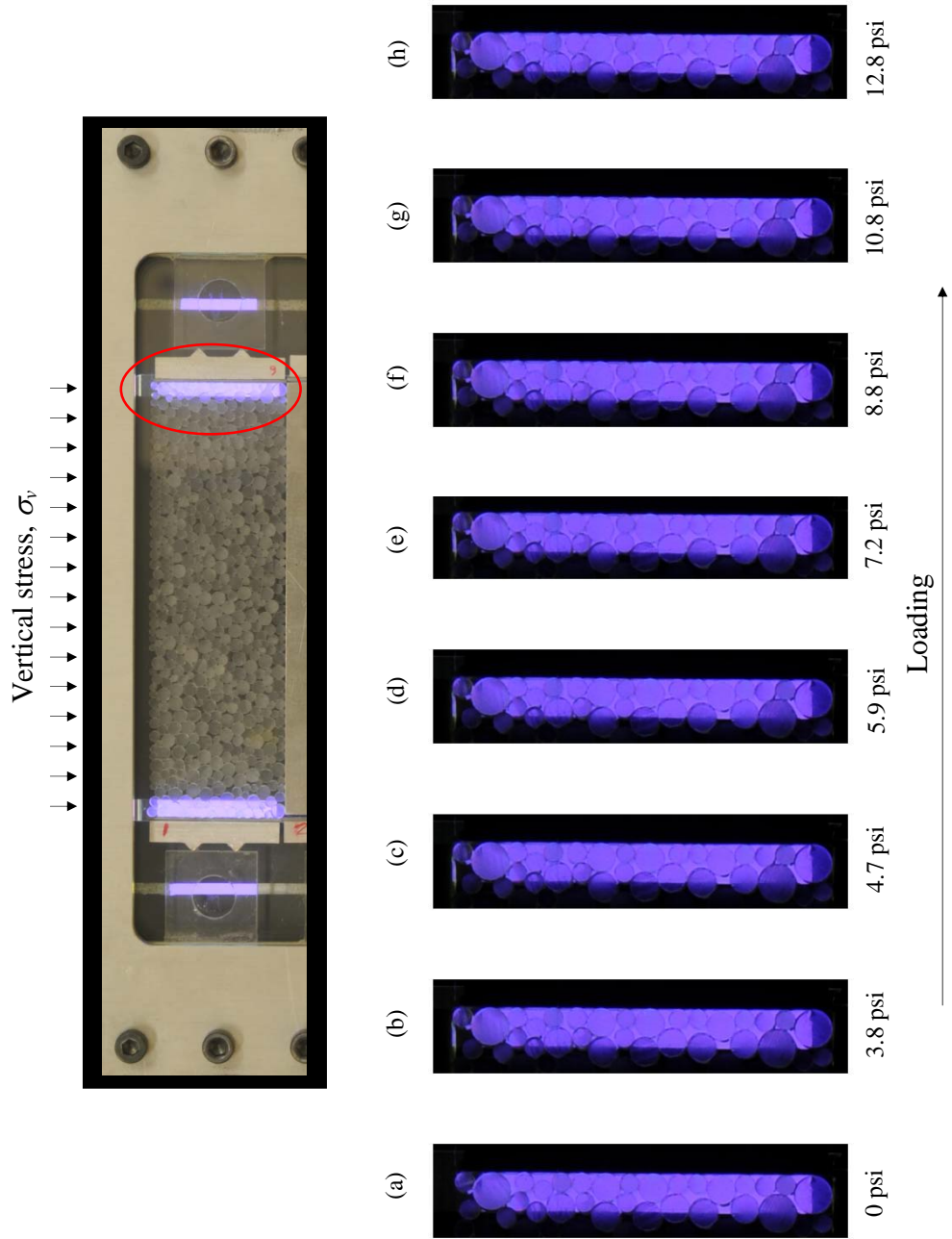


Figure D-3 Photos of particles at the right wall of the specimen during loading for Test #5-2

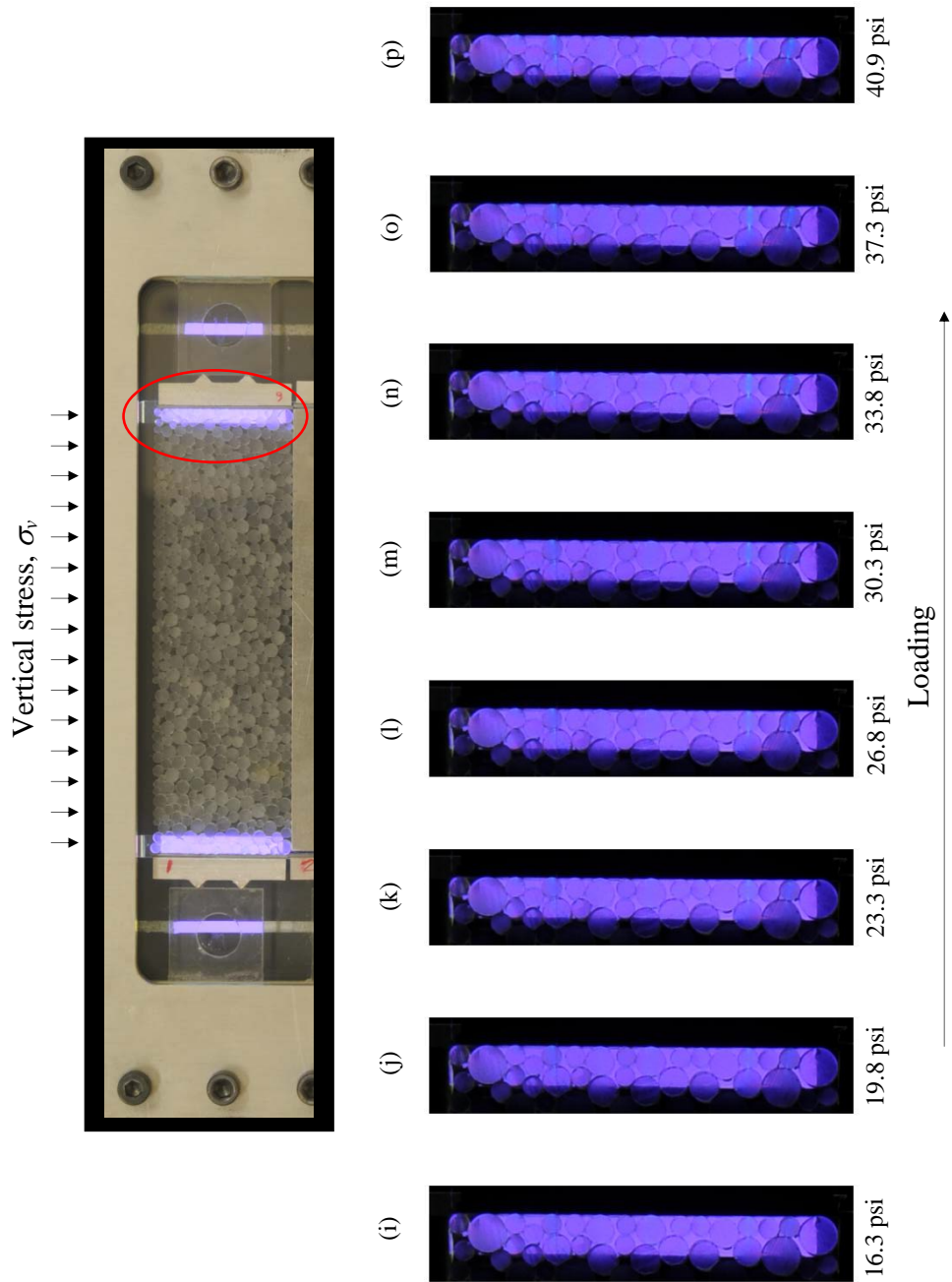


Figure D-3(cont.) Photos of particles at the right wall of the specimen during loading for Test #5-2

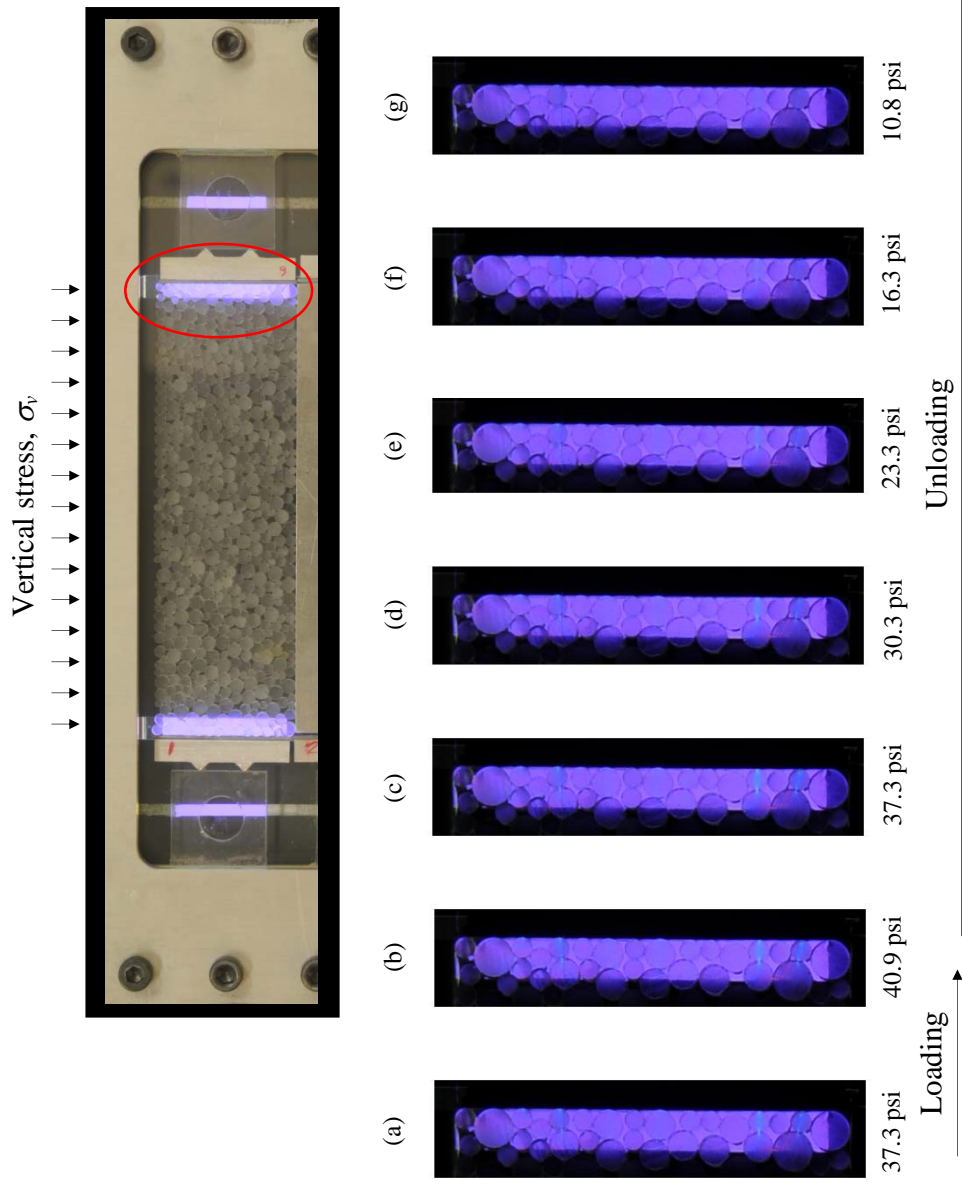


Figure D-4 Photos of particles at the right wall of the specimen during loading and unloading for Test #5-2

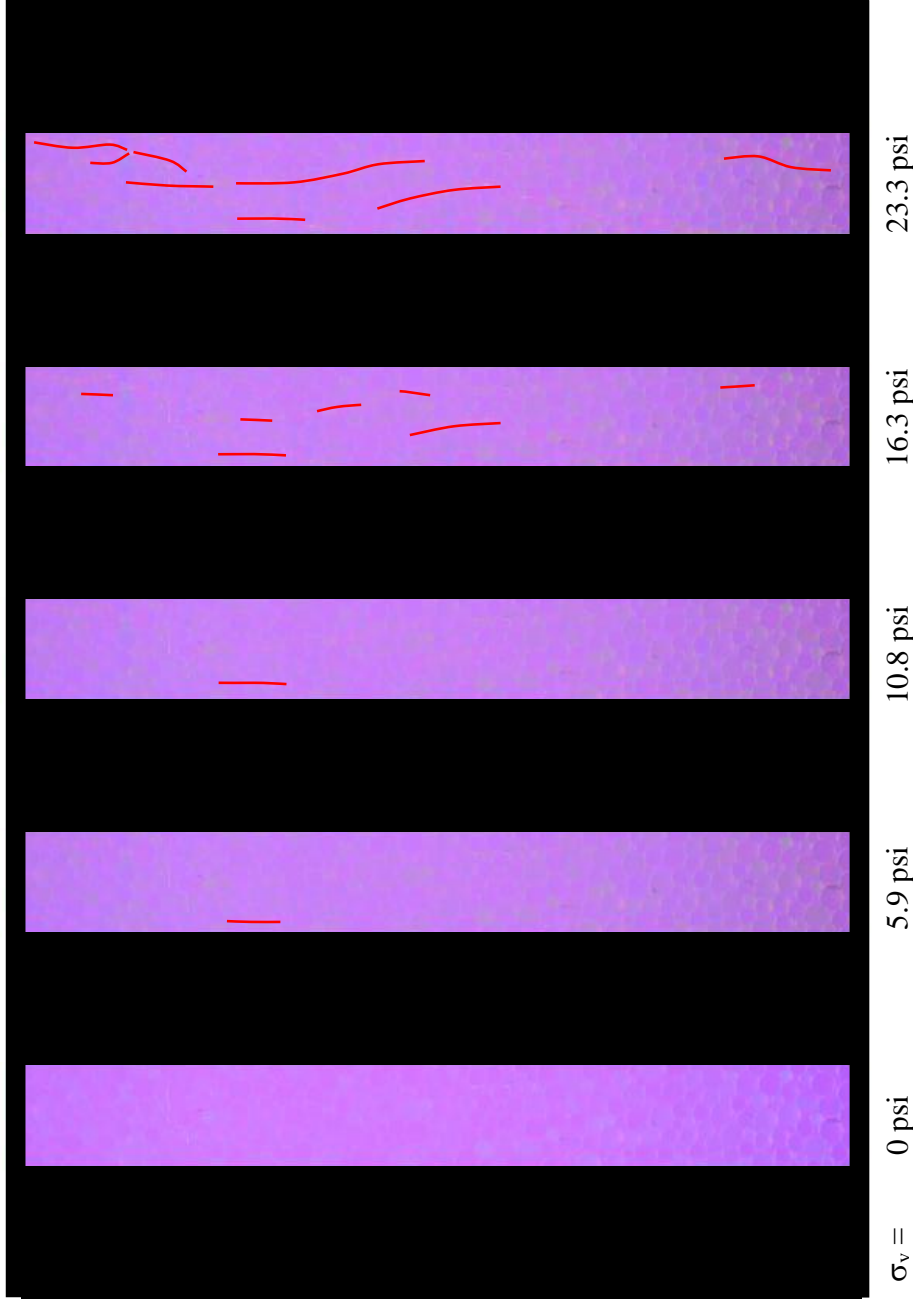


Figure D-5 Formations of force chains in region #2 from the specimen during loading from 0 psi to 23.3 psi (see Figure 5-30 for the location of region #2)

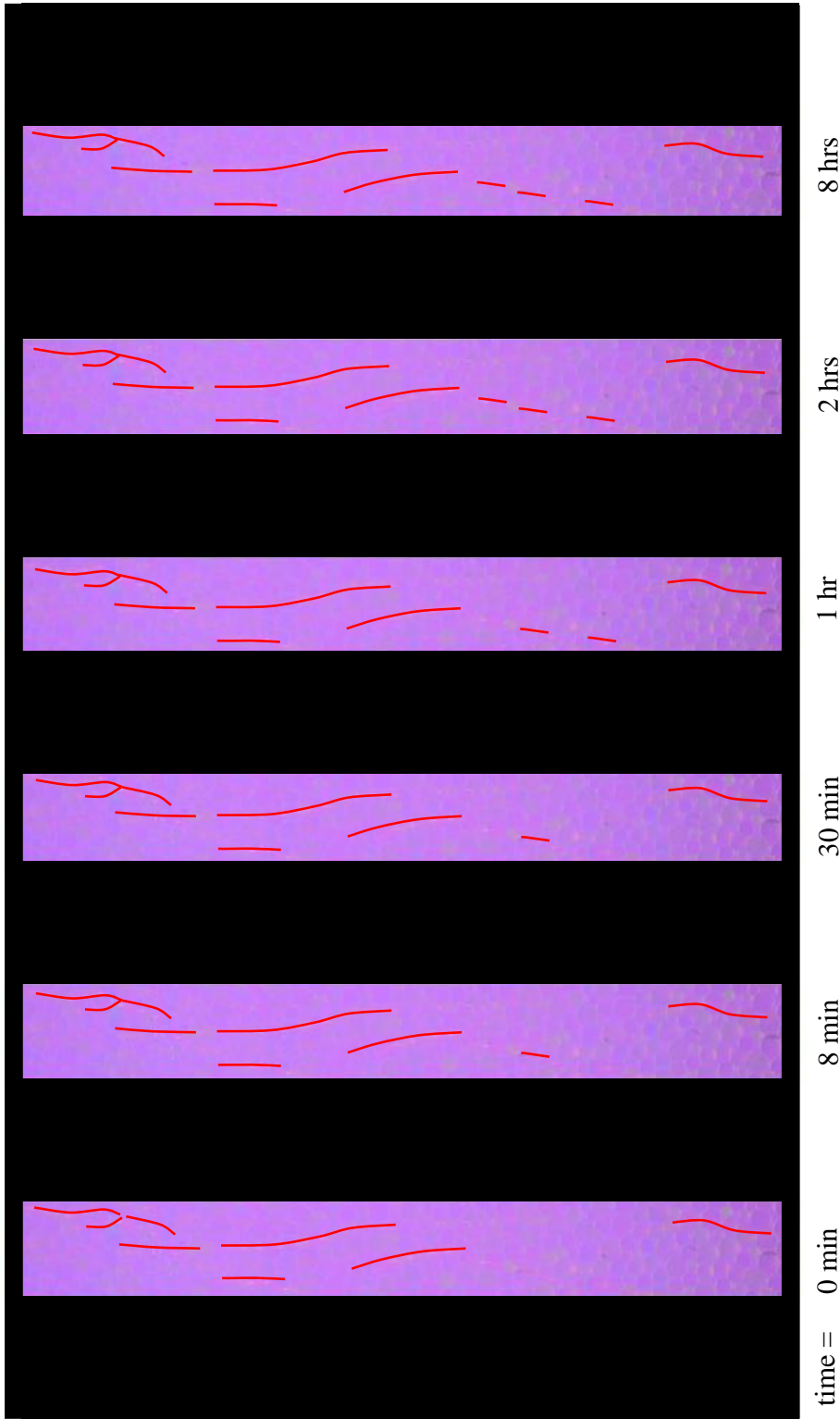


Figure D-6 Force chains versus time in region #2 from the specimen under a constant vertical stress of 23.3 psi (see Figure 5-30 for the location of region #2)

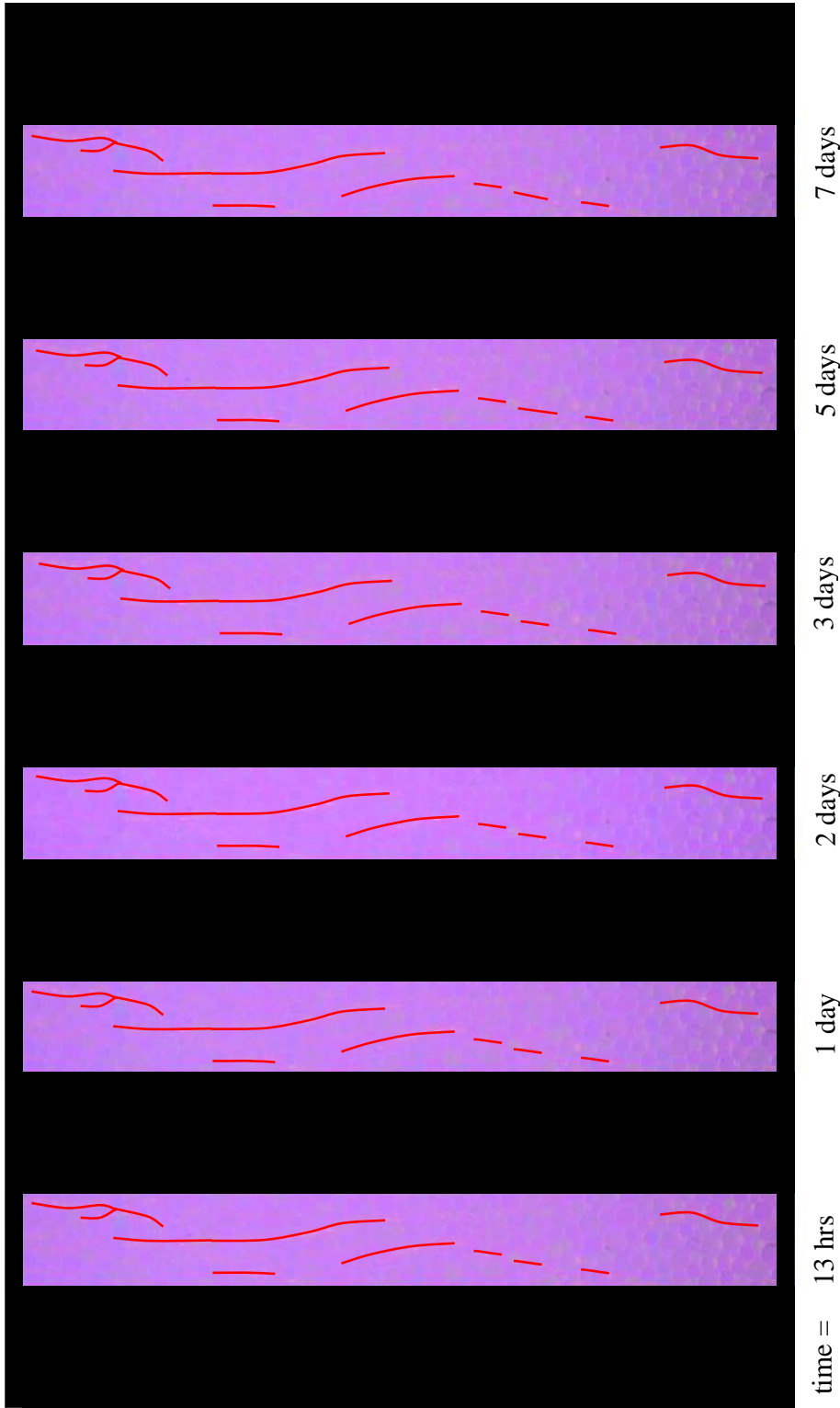


Figure D-6(cont.) Force chains versus time in region #2 from the specimen under a constant vertical stress of 23.3 psi (see Figure 5-30 for the location of region #2)

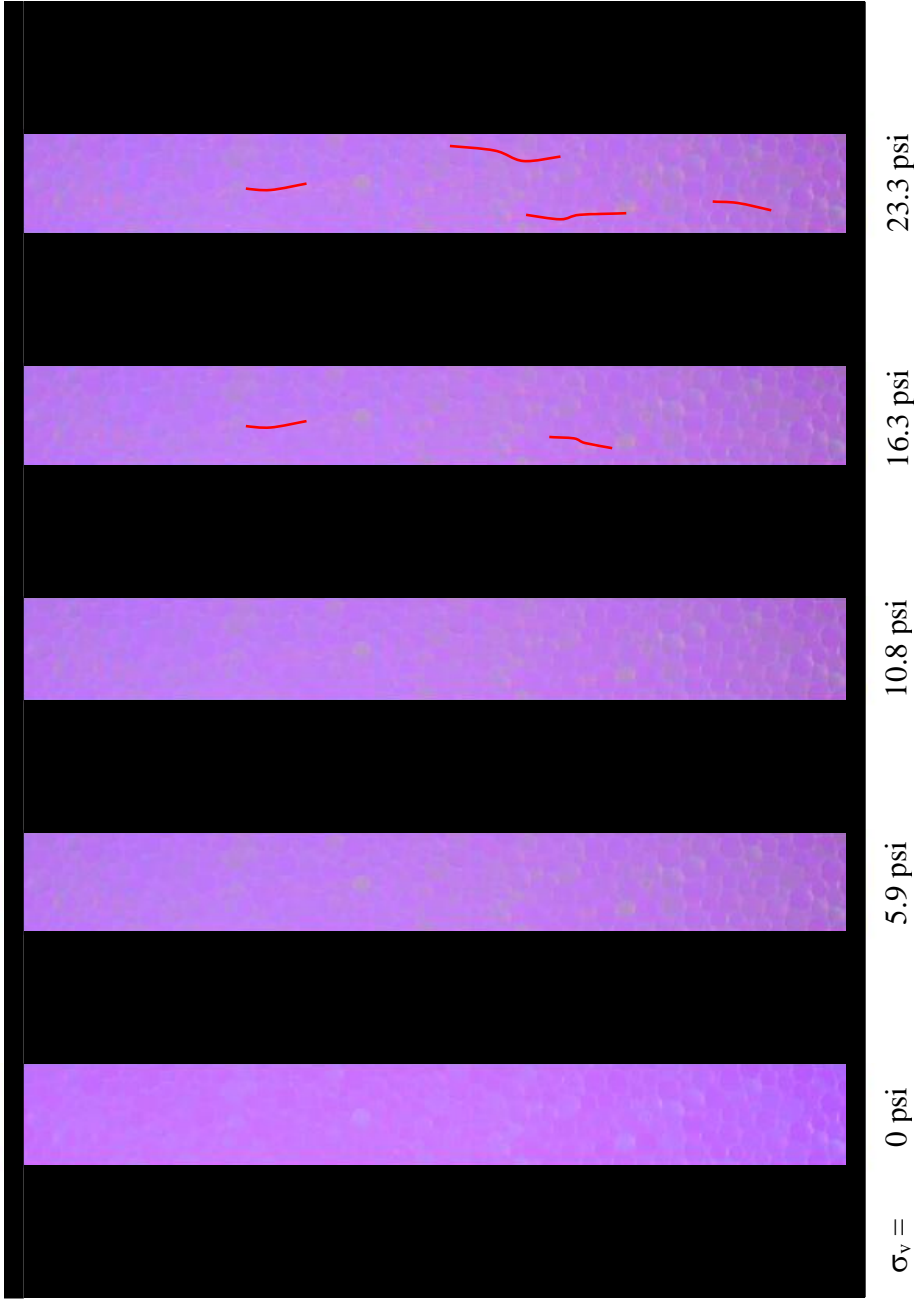


Figure D-7 Formations of force chains in region #3 from the specimen during loading from 0 psi to 23.3 psi (see Figure 5-30 for the location of region #3)

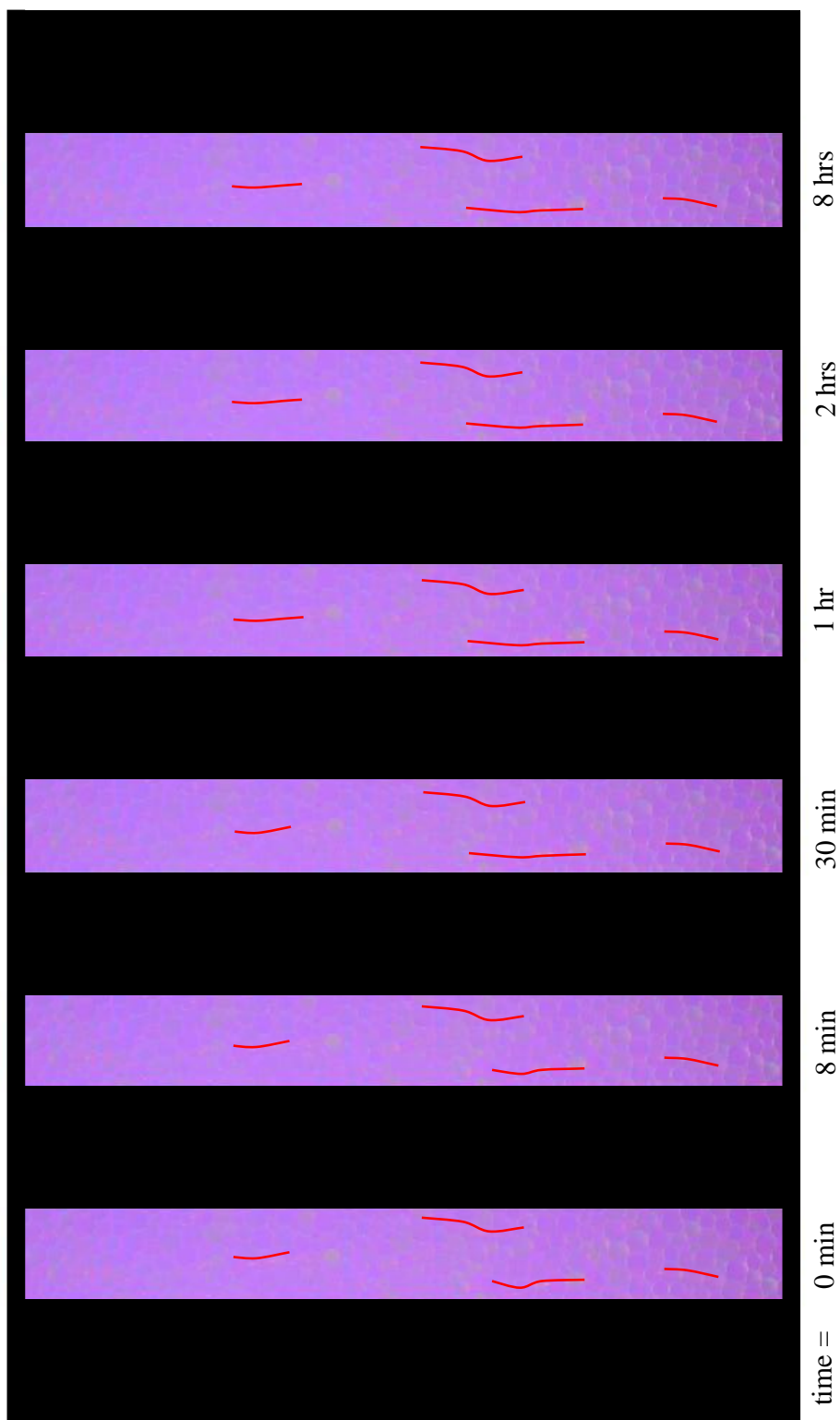


Figure D-8 Force chains versus time in region #3 from the specimen under a constant vertical stress of 23.3 psi (see Figure 5-30 for the location of region #3)

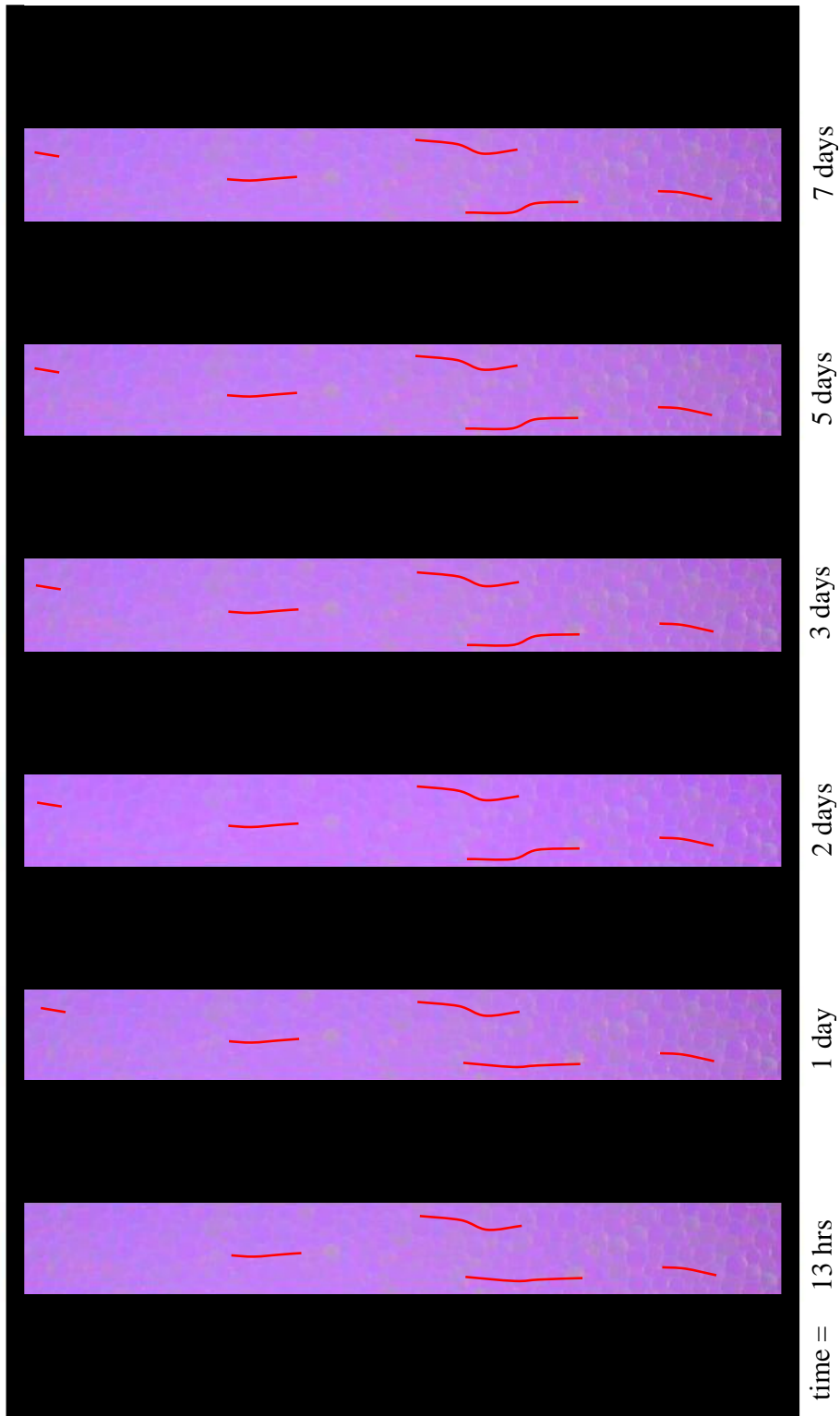


Figure D-8 (cont.) Force chains versus time in region #3 from the specimen under constant vertical stress of 23.3 psi (see Figure 5-30 for the location of region #3)

REFERENCES

REFERENCES

- Aben, H. and Guillemet, C. (1993). "Photoelasticity of Glass," *Springer-Verlag*, 255p.
- Afifi, S.S. and Woods, R.D. (1971). "Long-term Pressure Effects on Shear Modulus of Soils," *Journal of Soil and Foundation Engineering*, ASCE, No. 97 (SM10), 1445-1460.
- Anderson, D.G. and Stokoe, K.H., II (1978). "Shear Modulus, A Time-dependent Soil Property," *Dynamic Geotechnical Testing*, ASTM STP 654, 66-90.
- Allersma, H.G.B. (1987). "Optical Analysis of Stress and Strain in Photoelastic Particle Assemblies," *Ph.D. Dissertation*, Delft University of Technology, The Netherlands, 169p.
- Allersma, H.G.B. (2005). "Optical Analysis of Stress and Strain around Penetrating Elements in A Granular Medium," *Proceedings of The 15th International Offshore and Polar Engineering Conference*, Seoul, South Korea, June 19-24, 590-595.
- Ashford, S., Rollins, K.M., and Lane, D. (2004). "Blast-Induced Liquefaction for Full-Scale Foundation Testing," *Journal of Geotechnical and Geoenvironmental Engineering*, Vol. 130 (8), 798-806.
- Barton, M.E. (1993). "Cohesive Sands: The Natural Transition from Sands to Sandstones," Proceedings of An International Symposium of the International Society for Soil Mechanics and Foundations (ISSMFE), In Anagnostopoulos et al. (eds), *Geotechnical Engineering of Hard Soils – Soft Rocks*, Vol. 1, A.A. Balkema, Rotterdam, 367-374.
- Baxter, C.D.P. (1999). "An Experimental Study on the Aging of Sands," *Ph.D. Dissertation*, Virginia Tech, Blacksburg, Virginia, 303p.
- Baxter, C.D.P. and Mitchell, J.K. (2004) "Experimental Study on the Aging of Sands," *Journal of Geotechnical Engineering and Environmental*, Vol. 130 (10), 1051-1062.
- Bowman, E.T. (2002). "The Aging and Creep of Dense Granular Materials," *Ph.D. Dissertation*, Cambridge University, London, 296p.
- Bowman, E.T. and Soga, K. (2003). "Creep, Aging, and Microstructural Change in Dense Granular Materials," *Soil and Foundation*, Japanese Geotechnical Society, Vol. 43 (4), 107-117.

- Bowman, E.T. and Soga, K. (2005). "Mechanisms of Setup of Displacement Piles in Sand: Laboratory Creep Tests," *Canadian Geotechnical Engineering*, Vol. 42, 1391-1407.
- Brewster, D. (1816). "On the Communication of the Structure of Doubly Refracting Crystals to Glass, muriate of Soda, Flour Spar, and other Substance by Mechanical Compression and Dilation," *Phil. Trans Roy, Soc, London*, 156-178.
- Charlie, W.A., Rwebyogo, M.F.J. and Doehring, D.O. (1992). "Time-dependent Cone Penetration Resistance due to Blasting," *Journal of Geotechnical Engineering*, Vol. 118 (8), 1200-1215.
- Chow, F.C., Jardine, R.J. and Nauroy, J.F. (1988). "Effects of Time on Capacity of Pipe Piles in Dense Marine Sand," *Journal of Geotechnical and Geoenvironmental Engineering*, Vol. 124 (3), 254-264.
- Clark, J.I., Zhu, F. and Paulin, M. (1993). *Discussion on "Time Dependent Cone Penetration Resistance due to Blasting,"* by Charlie, W.A., Rwebyogo, M.F.J. and Doehring, D.O., *Journal of Geotechnical Engineering*, Vol. 119 (12), 2007-2008.
- Dapples, E.C. (1972). "Some Concepts of Cementation and Lithification of Sandstone," *Bulletin American Association of Petroleum Geologists*, 56, 3-25.
- De Boer, R.B. (1977). "On the thermodynamics of Pressure Solution – Interaction between Chemical and Mechanical Forces," *Geochemica et Cosmochimica Acta*, Vol. 41, 249-256.
- Dejong, J.T., Fritzges, M.B. and Nusslein, K. (2006). "Microbially Induced Cementation to Control Sand Response to Undrained Shear," *Journal of Geotechnical and Geoenvironmental Engineering*, Vol. 132 (11), 1381-1392.
- Dowding, C.H. and Hryciw, R.D. (1986). "A Laboratory Study of Blast Densification of Saturated Sand," *Journal of Geotechnical Engineering*, Vol.112 (2), 187-199.
- Drescher, A. (1976). "An Experimental Investigation of Flow Rules for Granular Materials using Optically Sensitive Glass Particles," *Geotechniques*, Vol.26 (4), 591-601.
- Dittes, M. and Labuz, J.F. (2002). "Field and Laboratory Testing of St. Peter Sandstone," *Journal of Geotechnical and Geoenvironmental Engineering*, Vol.128(5), 372-380.
- Dyvik, R., Lacasse, S. and Martic, R. (1985). "Coefficient of Lateral Stress from Oedometer Cell," *Proceedings of the 11th International Conference on Soil Mechanics and Foundation Engineering*, San Francisco, August, 1003-1006.
- Frocht, M.M. (1946). "Photoelasticity," *Wiley*, London, 411p.

- Green, R.A., Hryciw, R.D., Saftner, D.A., Baxter, D.C.P., Jung, Y. and Jirathanathaworn, T. (2008). "Sand Aging Field Study," *Geotechnical Earthquake Engineering and Soil Dynamics IV* (D. Zeng, M.T. Manzari, and D.R. Hiltunen eds.), ASCE GSP 181.
- Hardin, B.O. (1987). "1-D Strain in Normally Consolidated Cohesionless Soils," *Journal of Geotechnical Engineering*, Vol. 113(12), 1449-1467.
- Hendry, A.W. (1948). "An Introduction to Photoelastic Analysis," *Blackie and Son Limited*, 152p.
- Houlsby, G.T. and Hitchman, R (1988). "Calibration Chamber Tests for A Cone Penetrometer in Sands," *Geotechnique* 38 (1), 39-44.
- Hryciw, R.D. (1986). "A Study of the Physical and Chemical Aspects of Blast Densification of Sand," *Ph.D. Dissertation*, Northwestern University, Evanston, 229 p.
- Hryciw, R.D. and Dowding, C.H. (1988). "CPT and DMT in evaluation of blast-densification of sand," *Penetration Testing 1988 edited by De Ruiter*, ISOPT-1, Balkema., Rotterdam, ISBN 9061918014, 521-527.
- Hryciw, R.D. and Thomann, T.G. (1993). "Stress-history–Based Model for G^e of Cohesionless Soils," *Journal of Geotechnical Engineering*, Vol.119(7), 1073-1093.
- Jessop, H.T. and Harris, F.C. (1949). "Photoelasticity: Principles & Methods," *Cleaver-Hume Press Limited*, University College, London, 184p.
- Joshi, R.C., Achari, G., Kanijraj, S. R., and Wijeweera, H. (1995). "Effect of Aging on the Penetration Resistance of Sands," *Canadian Geotechnical Journal*, Vol. 32, 767-782.
- Kuhn, M.R. and Mitchell, J.K. (1993). "New Perspectives on Soil Creep," *Journal of Geotechnical Engineering Division*, Vol. 119 (3), 908-913.
- Kuhn, M.R. (1999). "Structured Deformation in Granular Materials," *Mechanics of Materials*, Vol. 31, 407-429.
- McKenzie, H.W. and Hand, R.J. (1993). "Basic Optical Stress Measurement in Glass," *Society of Glass Technology*, 90p.
- Mesri, G., Feng, T.W., and Benak, J.M. (1990). "Postdensification Penetration Resistance of Clean Sands," *Journal of Geotechnical Engineering*, Vol. 116 (7), 1095-1115.
- Mesri, G. and Hayat, T.M. (1993). "The Coefficient of Earth Pressure at Rest," *Canadian Geotechnical Journal*, Vol. 30, 647-666.
- Mesri G. and Vardhnabhuti, B. (2007). "Coefficient of Earth Pressure at Rest for Sands Subjected to Vibration," *Canadian Geotechnical Journal*, Vol. 44, 1242-1264.

- Mitchell J.K. (2008). "Aging of Sand – A Continuing Enigma?," *Proceedings of the 6th International Conference on Case Histories in Geotechnical Engineering*, Arlington, VA, August 11-16. 21p.
- Mitchell, J.K. and Santamarina, J.C. (2005). "Biological Considerations in Geotechnical Engineering," *Journal of Geotechnical and Geoenvironmental Engineering*, Vol. 131 (10), 1222-1233.
- Mitchell, J.K. and Solymar, Z.V. (1984). "Time-dependent Strength Gain in Freshly Deposited or Densified Sand," *Journal of Geotechnical Engineering*, Vol. 110 (11), 1559-1576.
- Oda, M. (1972). "The Mechanism of Fabric Changes during Compressional Deformation of Sand," *Soils and Foundations*, Vol.12 (2), 1-18.
- Oda, M. and Kazama, H. (1998). "Microstructure of Shear Bands and its Relations to The Mechanism of Dilatancy and Failure of Dense Granular Soils," *Geotechnique*, Vol.48 (4), 465-481.
- Oda, M., Nemat-Nasser, S. and Konichi, J. (1985). "Stress-induced Anisotropy in Granular Masses," *Soils and Foundations*, Vol. 25 (3), 85-97.
- Radjai, F., Wolf, D.E., Jean, M. and Moreau, J. (1998). "Bimodal Character of Stress Transmission in Granular Packings," *Physical Review Letters*, Vol.80, No.1, 61-64.
- Schmertmann, J.H. (1987). "Discussion of 'Time-dependent Strength Gain in Freshly Deposited or Densified Sand,' by J.K. Mitchell and Z.V. Solymar" *Journal of Geotechnical Engineering*, Vol.113 (2), 173-175.
- Schmertmann, J.H. (1991). "The Mechanical Aging of Soils," *Journal of Geotechnical Engineering*, Vol.117 (9), 1288-1330.
- Sheldon, H.A. and Wheeler, J. (2003). "Influence of Pore Fluid Chemistry on the state of Stress in Sedimentary Basins," *Geological Society of America*, Vol. 31, No. 1, 59-62.
- Sheldon, H.A. and Wheeler, J., Worden, R.H., and Cheadle, M.J. (2003). "An Analysis of the Roles of Stress, Temperature, and pH in Chemical compaction of Sandstones," *Journal of Sedimentary Research*, Vol. 73, No.1, 64-71.
- Stocks-Fischer, S., Galinat, J.K. and Bang, S.S. (1999). "Microbiological Precipitation of CaCO₃," *Soil Biology and Biochemistry*, Vol. 31, 1563-1571.
- Strainoptics, Inc. "PS-1011-PL Instruction Manual for Large-field Polarimeter (Plane Polarization)" (user manual for Strainoptics A-100 analyzer and RP-100).

Terzaghi, K. (1934). "Large Retaining Wall Tests," *Engineering News Record*, 112, Feb 1st, 136-140.

Thomann, T.G. (1990). "Stiffness and Strength Changes in Cohesionless Soils due to Stress History and Dynamic Disturbance," *Ph.D. Dissertation*, University of Michigan, Ann Arbor, 183p.

Thomann, T.G. and Hryciw, R.D. (1990). "Laboratory Measurement of Small Strain Shear Modulus under K_0 Conditions," *Geotechnical Testing Journal*, ASTM, 97-105.

Thomann T.G. and Hryciw, R.D. (1992). "Stiffness and Strength Changes in Cohesionless Soils due to Disturbance," *Canadian Geotechnical Journal*, Vol. 29, 853-861.

Weyl, P.K. (1959). "Pressure Solution and the Force of Crystallization – A Phenomenological Theory," *Journal of Geophysical Research*, Vol. 64, No. 11, 2001-2025.

Wilding, L.P., Smeck, N.E. and Dress, L.R. (1977). "Silica in Soils: Quartz, Cristobalite, tridymite, and Opal," Chapter 14, in *Minerals in Soil Environments*, Soil Science Society of America, Madison, Wisc., 471-552.